COLD-FORMED STEEL COMPRESSION MEMBERS WITH PERFORATIONS

By

NABIL MAHMOUD ABDEL-RAHMAN, B.Sc., M.Sc.

A Thesis

Submitted to the School of Graduate Studies

in Partial Fulfilment of the Requirements

for the Degree

Doctor of Philosophy

McMaster University

COLD-FORMED STEEL COMPRESSION MEMBERS

WITH PERFORATIONS

To my dear wife, Elham,

for her love and continuous support

DOCTOR OF PHILOSOPHY (1997) McMaster University

(Civil Engineering) Hamilton, Ontario, Canada

TITLE: Cold-Formed Steel Compression Members with Perforations.

AUTHOR: Nabil Mahmoud Abdel-Rahman, B.Sc. (Cairo University)

M.Sc. (Cairo University)

SUPERVISOR: Dr. K. S. Sivakumaran

NUMBER OF PAGES: xx, 264

ABSTRACT

The research work of this thesis is concerned with the local buckling behaviour and the post-local buckling strength of perforated cold-formed steel (CFS) members subjected to axial compressive loading.

Cold-formed steel sections are widely used nowadays as primary and secondary framing members in low-rise steel buildings. Although CFS members are essentially thin-walled framing elements, with a major susceptibility to local buckling, these members maintain a considerable reserve of post-local buckling strength prior to yielding. The post-local buckling strength of CFS members is largely affected by the sectional non-uniform material properties after the forming operation, the initial imperfections, the large deformation behaviour after buckling, and the possibility of having utility perforations in the plate components of the members.

A finite element-based analytical model has been developed in this thesis to investigate the post-local buckling behaviour and the ultimate strength of non-perforated and perforated CFS compression members. A large deformation degenerated shell finite element was used to model the surface of CFS sections. The kinematic formulation of the degenerated shell element was enhanced using the method of "assumed strain fields", to eliminate any locking problem of the element. Special consideration was given in the finite element model to the geometric

imperfections and the loading technique of CFS compression members.

Tensile coupon tests and residual stress tests were performed on CFS channel sections, in order to determine the effects of the cold forming operation on the distribution of the material properties across CFS sections. Based on the results of these tests, analytical models for the stress-strain relationship, the yield strength distribution, and the residual stress distribution across CFS sections were developed and incorporated in the finite element model of CFS compression members.

A series of CFS channel stub-column tests was performed to verify the deformation and ultimate strength predictions of the proposed finite element model. The tests were also used to investigate the effects of perforations on the behaviour and load capacity of CFS members in compression. The finite element model was then used to assess the axial stress distribution and the effective design width of perforated plates of CFS compression members. This assessment was performed through a parametric study on the perforation and the plate parameters.

Two effective design width equations for stiffened compression plates with square and elongated perforations were developed, based on the analysis of the finite element results. The ultimate load predictions of the two equations were compared to the stub-column test results of this thesis, and several other test results from the literature. The proposed equations proved to give accurate and safe predictions for the effective design width and the ultimate strength of perforated CFS compression members.

ACKNOWLEDGEMENTS

The author wishes to express his sincere appreciation to Dr. K.S. Sivakumaran, the supervisor of this research work, for his valuable guidance, encouragement, and friendly supervision during the course of the study. The valuable comments and suggestions of Dr. R.M. Korol and Dr. M.A. Dokainish, members of the supervisory committee, are also deeply appreciated

The financial support through the Department of Civil Engineering Graduate Assistantship, the C.W. Sherman Scholarship, the CIDA/McMaster Scholarship, and the Ontario Graduate Scholarship are gratefully acknowledged.

Thanks are due to the author's family, wife, and friends at McMaster university, for their encouragement and moral support which made this work a reality.

TABLE OF CONTENTS

LIST OF TABLES

LIST OF FIGURES

LIST OF SYMBOLS

The symbols used in this thesis are defined below. All symbols are also defined at their first appearance in the text:

a	Width of perforation.
$[B]$, $[B_0]$, $[B_L]$, $[B_{NL}]$	Strain-displacement matrices of the shell element.
$[\bar{B}_m]$, $[\bar{B}_s]$	Substitute (assumed) strain-displacement matrices.
b	Effective design width of a stiffened plate.
b_{un}	Effective design width of a non-perforated plate.
Δb	Loss in effective design width of a stiffened plate due to a perforation.
C_{ijkl}	Material property tensor.
$[D]$	Elastic stress-strain relationship matrix.
$[D_{ep}]$	Elasto-plastic stress-strain relationship matrix.
E	Modulus of elasticity of the material.
E_T	Tangent modulus of the material.
F_{cr}	Critical local buckling stress of a plate.
F_{max}	Maximum edge stress of a stiffened plate.
F_p	Proportional limit strength of the material.
F_{rl}, F_{rt}	Longitudinal and transverse residual stresses.
F_y	Yield strength of the material.
$(F_y)_{min}$	Minimum specified yield strength of the material.
F_{yc}	Yield strength of the corner zone of a channel section.
ΔF_y	Corner zone yield strength increase of the section.
F_u	Ultimate strength of the material.

H	Plastic modulus of the material.
h	Height of perforation.
$[K_T]$, $[K_0]$, $[K_L]$, $[K_{NL}]$	Stiffness matrices of the shell element.
k	Buckling coefficient of a plate.
L	Length of a stub-column.
$N^k(\xi, \eta)$	Interpolation functions of the shell element.
P_u, P_w	Total ultimate load and web plate ultimate load.
P_{AISI}, P_{CSA}, P_p, P_t	AISI, CSA, current predicted, and test ultimate loads.
r	Inside bending radius of the section rounded corner.
S_{ij}	Second Piola-Kirchhoff stress tensor.
t	Uniform thickness of plate, or section.
u_i^k	Translational degrees of freedom of the shell element.
V_{1i}^k, V_{2i}^k, V_{ni}^k	Nodal unit vectors of the shell element.
w, w_f, w_l	Flat width of web, flange, and lip of a channel section.
w', w_f', w_l'	Overall width of web, flange, and lip of a section.
x, y, z	Global Cartesian coordinate system.
x', y', z'	Local Cartesian coordinate system.
ξ, η, ζ	Natural coordinate system.
ν	Poisson's ratio.
α^k, β^k	Rotational degrees of freedom of the shell element.
ϵ_m, ϵ_b, ϵ_s	Membrane, bending, and shear strain components.
$\bar{\epsilon}_m$, $\bar{\epsilon}_s$	Substitute (assumed) membrane and shear strains.
ϵ_{ij}	Green-Lagrange strain tensor.
$d\epsilon^e$, $d\epsilon^p$	Elastic and plastic strain increments.
$\gamma_{\xi\zeta}$, $\gamma_{\eta\zeta}$	Transverse shear strains in the natural coordinates.
$\bar{\gamma}_{\xi\zeta}$, $\bar{\gamma}_{\eta\zeta}$	Substitute (assumed) transverse shear strains.
ϕ^{ij}, ψ^{ij}	Two dimensional interpolation functions.
δ, δ_o	Imperfection and imperfection amplitude.

CHAPTER 1

INTRODUCTION

1.1 General

Cold-formed steel (CFS) sections are widely used nowadays as primary and secondary framing members in low-rise steel buildings. The CFS sections are also widely used as open joists, floor decks, sandwich panels, and entrance structures for both low and high-rise buildings. The increasing use of CFS sections in building construction is due to their favourable characteristics, such as high strength-to-weight ratio, high stiffness-to-weight ratio, easy and fast erection, etc., over other traditional structural materials like masonry, timber, and concrete. Other than the applications of CFS sections in the area of building construction, the use of these sections extends to other broader areas, such as the construction of grain bins, storage racks, transmission towers, drainage facilities, car bodies, etc.

The two main forming methods, which are frequently used in manufacturing CFS sections, are the cold roll forming and the press-brake forming. The cold roll forming is the widely used method for the mass production of individual structural framing members, such as channel sections, Z-sections, angles, hat sections, and tubular members. The thickness of the steel sheets generally used in CFS structural members can be as low as 0.4 mm, and as high as 6.4 mm (Yu, 1991). Thus, CFS

members are essentially thin-walled members with moderate to very high width-to-thickness ratios of their plate components. Therefore, the individual plate components of CFS members are susceptible to local buckling at low compressive, shear, bending, or bearing stresses. However, due to the possibility of membrane action of the buckled plates, local buckling does not necessarily mean a failure of the CFS member, and a considerable reserve of post-local buckling strength can be obtained prior to the initiation of yielding. In fact, the ultimate strength of a CFS member can be many times higher than its local buckling strength.

Perforations are often provided in the web and/or flange plates of beams and columns of CFS structural members, in order to facilitate duct work, piping, and bridging. Perforations are also usually provided in CFS storage racks for the purpose of easy assembly. These perforations may take different shapes and dimensions, depending on their purpose.

1.2 Statement of the Problem

The determination of the ultimate strength of non-perforated and perforated cold-formed steel (CFS) members in compression requires a correct evaluation of the post-local buckling strength of these members. To evaluate the post-local buckling strength correctly, the following phenomena have to be taken into consideration:

[1] Type of Local Buckling: Local buckling of individual plate components of CFS compression members may take place elastically or inelastically, depending on the

material properties and the width-to-thickness ratio of the plate components.

[2] Large Deformations: The behaviour of the CFS compression members in the post-local buckling range is associated with large local deformations (lateral displacements and rotations) of the buckled plates. Secondary internal forces and non-uniform stress distributions may result due to these large deformations, even though the member is under uniformly applied loads.

[3] Initial Imperfections: The deformation behaviour of CFS compression members in the pre and post-local buckling ranges is sensitive to the initial out-of-plane deformations (initial imperfections) of the plate components of the members.

[4] Variations of Mechanical Properties: The non-uniformity of the cold work applied to CFS sections during the cold forming operation alters the material properties of the virgin steel sheet. This alteration results in different mechanical properties (yield strength and ultimate strength) across the section, and a nonlinear stress-strain relationship of the CFS material.

[5] Residual Stresses: The restrictions of the shape and length of the CFS section, after its release from the cold forming machine, results in the generation of significant longitudinal and transverse residual stresses within the section.

[6] Perforations: Since the use of perforation reinforcement is impractical in thin-walled steel construction, the existence of the perforations in the plate components of CFS members changes the boundary conditions of these plates, and consequently affects their individual ultimate strengths, and the overall ultimate

strength of the member.

The above mentioned phenomena give a strong indication that the behaviour of CFS members in the post-local buckling range is an interaction of a large deformation behaviour and an elasto-plastic nonlinear material behaviour. Furthermore, the existence of initial imperfections, non-uniform material properties, residual stresses, and perforations causes the problem to be rather complicated for a direct theoretical formulation and analysis of such members. Therefore, one of the primary goals of this thesis is to establish an appropriate nonlinear formulation and an analysis technique for the behaviour of non-perforated and perforated CFS members in compression using the finite element method. The geometry, and the membrane and bending force representation, of shell finite elements are quite suitable to the geometry and the behaviour of CFS members. In fact, a nonlinear finite element formulation using shell elements is perhaps the only analytical tool that may handle such a complex problem in an efficient way.

1.3 Design Approaches for Cold-Formed Steel Members in Compression

Cold-formed steel (CFS) members in compression may fail in an overall buckling mode of the entire member, a local buckling mode of the individual plate components of the cross section, or a combination of the overall and local buckling modes. The design approaches used for CFS members to resist the overall buckling mode are similar to the approaches used for members made of hot-rolled steel

sections. However, in the local buckling design of CFS members, the slenderness ratios (width-to-thickness ratios) of the plate components of the section are first checked for possible local buckling. If the slenderness ratio of a plate component is less than the critical slenderness ratio, the plate component will not buckle, and can be considered fully effective. However, if the slenderness ratio is higher than the critical slenderness ratio, the plate component may locally buckle, and should be considered partially effective. The post-local buckling strength of such plate can be determined using an effective width concept, as will be explained in section 1.3.2. The effective area of the entire CFS section in the post-local buckling range can, then, be evaluated as the summation of the effective widths of the individual plate and corner components of the section, multiplied by the sectional uniform thickness.

1.3.1 Local Buckling and Post-Local Buckling Strength of Plates

The elastic local buckling stress (F_{cr}) of a flat plate component under uniform compression (Figure 1.1) can be determined as follows, based on the solution of the small deflection differential equation of the plate:

$$F_{cr} = k \frac{\pi^2 E}{12\ (1-\nu^2)\ (\frac{w}{t})^2} \qquad (1.1)$$

where (w/t) is the width-to-thickness ratio of the plate, (E) is the modulus of elasticity, and (ν) is the Poisson's ratio. The buckling coefficient (k) is considered equal to 4.0 for a plate simply supported on both unloaded edges (stiffened plate), and

equal to 0.425 for a plate simply supported on one unloaded edge and free supported on the other edge (unstiffened plate) (Yu, 1991). Hence, by assuming that the local buckling stress (F_{cr}) of a stiffened steel plate (k=4, v=0.3) is equal to the yield stress (F_y), a slenderness ratio limit $(w/t)_{lim}$ can be evaluated from Equation 1.1 as follows:

$$(\frac{w}{t})_{lim} = 1.9\sqrt{\frac{E}{F_y}} \qquad (1.2)$$

Equation 1.2 means that if the (w/t) ratio of the plate is less than $(w/t)_{lim}$, then yielding of the plate will occur prior to local buckling. However, if the (w/t) ratio of the plate is larger than $(w/t)_{lim}$, then local buckling of the plate will occur before reaching the yield stress.

The post-local buckling strength of compression plates is obtained due to the membrane action, and the redistribution of compressive stresses across the plate section after buckling, as shown in Figure 1.2(a). The stiffened edges of the plate will continue to resist more compressive loads until the stress at the edges reaches the yield point of the material, then the plate will begin to fail.

1.3.2 Effective Width Concept

The concept of "Effective Width" was first introduced by von Karman, et al. (1932). In this concept, the post-local buckling non-uniform stress distribution over the width of a stiffened compression plate is replaced by a uniform stress distribution,

equal to the plate edge stress (F_{max}), over a fictitious effective width (b) as shown in Figure 1.2(b). The effective width (b) is calculated so that the area under the curve of the actual non-uniform stress distribution is equal to the sum of the two equivalent fictitious areas, with a total width (b) and a uniform edge stress (F_{max}), i.e.:

$$\int_0^w F \, dx = b \, F_{max} \tag{1.3}$$

Therefore, according to the effective width concept, the central part of the plate is considered ineffective, and the two parts along the stiffened edges of the plate are considered fully effective. If the initiation of yielding at the edges of the stiffened plate is taken as the ultimate state, then the effective width (b) can be taken as the particular width of the plate which buckles just at yielding of the plate edges. Hence, the effective width (b) can be evaluated using the concept of Equation 1.2, by replacing the flat width (w) by the effective width (b), as follows:

$$b = 1.9 \, t \sqrt{\frac{E}{F_y}} \tag{1.4}$$

The extensive experimental investigation carried out by Winter (1947) on light-gage cold-formed steel sections led to a generalized empirical formula, to Equation 1.4 of von Karman, for the effective width (b) of stiffened compression plates at any stress level below yielding. The formula proposed by Winter (1947) is:

$$b = 1.9\ t \sqrt{\frac{E}{F_{max}}} \left[1 - 0.475 \left(\frac{t}{w}\right) \sqrt{\frac{E}{F_{max}}} \right] \qquad (1.5)$$

Equation 1.5 was later modified, based on an accumulated experience from the tests of Winter (1970) during the period from 1946 to 1968, as follows:

$$b = 1.9\ t \sqrt{\frac{E}{F_{max}}} \left[1 - 0.415 \left(\frac{t}{w}\right) \sqrt{\frac{E}{F_{max}}} \right] \qquad (1.6)$$

Also, Equation 1.6 was further simplified by Roorda and Venkataramaiah (1979), based on their statistical analysis of the available experimental tests, to take the following form:

$$b = 2\ t \sqrt{\frac{E}{F_{max}}} \left[1 - 0.5 \left(\frac{t}{w}\right) \sqrt{\frac{E}{F_{max}}} \right] \qquad (1.7)$$

1.3.3 Effective Design Width Provisions of Different Standards

The current Canadian Standard for the design of cold-formed steel (CFS) members is the S136-94 "Cold-Formed Steel Structural Members" (CSA, 1994). In this Standard, the procedure for calculating the effective design width (b) for the strength determination of a plate element under uniform compression is given as follows:

$$b = w \qquad \text{for} \quad (w/t) \le (w/t)_{lim} = 0.644 \sqrt{\frac{k\,E}{F_{max}}} \tag{1.8}$$

$$b = 0.95\,t \sqrt{\frac{k\,E}{F_{max}}} \left[1 - 0.208 \left(\frac{t}{w}\right) \sqrt{\frac{k\,E}{F_{max}}} \right] \quad \text{for } (w/t) > (w/t)_{lim} \tag{1.9}$$

In other words, the effective design width (b) can be considered equal to the width of the plate (w) if the slenderness ratio of the plate (w/t) is less than a limiting slenderness value $(w/t)_{lim}$. Otherwise, the effective design width (b) should be less than (w) and can be calculated according to Equation 1.9, based on the maximum stress at the edge of the plate (F_{max}). In fact, Equation 1.9 is the same as Winter's equation (Equation 1.6), with a generalization of the longitudinal edge conditions of the plate where the buckling coefficient (k) is expressed as a variable. However, the $(w/t)_{lim}$ of the Standard is less than the theoretical slenderness limit, as given in Equation 1.2. The Standard recommends using (k) equal to 4.0 for stiffened plate elements on each edge by a web or a flange, and equal to 0.43 for unstiffened plate elements. The Standard also gives a procedure to calculate (k) for plate elements stiffened on one edge by a web or a flange and on the other edge by an edge stiffener (Clause 5.6.2.3 of the Standard), depending on the moment of inertia of the stiffener.

A new 1996 American Specification for the design of CFS members, "Specification for the Design of Cold-Formed Steel Structural Members", was in the

printing process during the time of writing this thesis. However, the reference of the new Specification for the effective design width provisions is the American Specification "Load and Resistance Factor Design Specification (LRFD) for Cold-Formed Steel Structural Members" (AISI, 1991). In the LRFD Specification, a different format of Equations 1.8 and 1.9 is given for calculating the effective design width (b) for the strength determination of a plate element under uniform compression. The LRFD format states that:

$$\begin{aligned} b &= w && \text{for } \lambda \le 0.673 \\ b &= \rho\, w && \text{for } \lambda > 0.673 \end{aligned} \qquad (1.10)$$

where

$$\rho = \frac{1}{\lambda}\left(1 - \frac{0.22}{\lambda}\right) \le 1.0$$

$$, \quad \lambda = \frac{1.052}{\sqrt{k}}\left(\frac{w}{t}\right)\sqrt{\frac{F_{max}}{E}}$$

The assumptions for the buckling coefficient (k) in the American LRFD Specification is similar to that of the Canadian Standard (CSA, 1994).

The Japanese Specification for the design of CFS members is the "Recommendations for the Design and Fabrication of Light Weight Steel Structures" (AIJ, 1985). In this Specification, the effective design width (b) of a plate element under uniform compression is independent of the slenderness ratio (w/t) of the plate,

and is calculated using a procedure similar to Equation 1.4 with a constant of 1.64 instead of 1.9. However, the Australian and the European Specifications give effective design width procedures similar to that of the Canadian and the American design documents (Yu, 1991).

1.4 Review of Literature

In this section, the previous research pertaining to some of the topics discussed in this thesis, namely; [a] shell finite elements, [b] material properties of cold-formed steel (CFS) sections, and [c] testing and analysis of perforated CFS members in compression, is being reviewed

1.4.1 Shell Finite Elements

Since this study involves a nonlinear finite element analysis using shell finite elements to solve the problem of non-perforated and perforated cold-formed steel (CFS) members in compression, this section gives a brief discussion on the development of shell finite elements.

A considerable number of papers devoted to literature surveys on shell finite elements have been published in the technical journals concerned with the numerical analysis techniques. For example, recent papers by Gilewski and Radwanska (1991), and Mackerle (1993) list the publications on moderately thick and thin shell finite elements. Also, Kanok-Nukulchai and Ma (1993) presented an excellent review of

displacement-based degenerated shell elements. Shell finite elements have been developed in the frameworks of displacement, mixed, hybrid stress, and hybrid-mixed methods. However, the displacement-based finite elements are still the most practical, simple and appealing to practicing engineers. The shell elements may be formulated based on a 3-D continuum approach, or based on classical shell theory. However, these elements will not be versatile, since they are tied to a special shell theory, and thus could be applicable to a special class of shell problems only. Recently, preference has been devoted to develop degenerated shell elements. In these elements, fully three-dimensional stress and strain conditions are degenerated to general shell behaviour. This approach has the advantage of being independent of any shell theory, and thus is applicable to very thin, and moderately thick shell structures.

Degenerated shell finite elements were first introduced through the 9-node element of Ahmad, et al. (1970). The element was based on independent quadratic interpolations for the displacement and the rotational degrees of freedom. This degenerated shell element has been used extensively by many researchers since 1970. The element was also used in conjunction with several numerical integration schemes, such as the reduced integration scheme (Zienkiewicz, et al., 1971) and the selective integration scheme (Hughes, et al., 1978), to evaluate the terms of the element stiffness matrix. Degenerated shell elements with additional displacement modes were later developed, as the semi-loof element of Irons (1976), to increase the element capability in representing the bending modes. Moreover, shell elements applying the

Discrete Kirchhoff theory, as the triangular plate and shell elements of Batoz and Lardeur (1989), and shell elements applying modified strain expressions, as the shell element of Huang and Hinton (1986), were developed to achieve the condition of zero transverse shear strain energy in thin shells. A large deformation consistent triangular shell element was recently developed by Koziey (1993) and El Damatty (1995). The element has 13 nodes, cubic displacement interpolation, and special rotational degrees of freedom to obtain a quadratic variation of the transverse shear stresses through the thickness of the shell.

1.4.2 Material Properties of Cold-Formed Steel Sections

The deformations, which occur in cold-formed steel (CFS) sections during their manufacturing operation from steel sheets, induce substantial changes in the characteristics of the CFS material. These changes are usually associated with variations in the mechanical properties, and generation of residual stresses across the CFS sections. Since the material in the rounded corner areas of the sections is cold-worked to a considerably higher degree than the material in the flat areas, significant variations in the mechanical properties and the significant residual stresses are normally found at and around the corner areas.

1.4.2.1 Variations of Mechanical Properties

Chajes, et al. (1963) investigated the effects of various amount of uniform cold

stretching on the stress-strain behaviour of mild carbon structural steel sheets. Tensile and compressive tests of the cold stretched material were performed in the direction of the initial stretching and transverse to it. It was found that the main causes of the changes of the mechanical properties due to the cold work are the strain hardening and the strain aging phenomena of the steel material. These two phenomena are explained in Figure 1.3. The changes in the mechanical properties were also found to depend on the type of steel, and the type and direction of the applied stress. Karren and Winter (1967) and Karren (1967) performed tensile and compressive coupon tests on CFS sections made from different carbon structural steels. A part of the tested sections was formed using the roll forming operation, and the other part was formed using the press-brake operation. It was found that the yield strength and the ultimate strength of the corners of the CFS sections are considerably higher than that of the virgin steel sheets before forming. The stress-strain curves of the rounded corners were found to have gradual yielding and significant reduction in the total elongation. The method of forming of the sections was noticed to have some effects on the results of the coupon tests, specially for the coupons taken from the flat areas of the sections. Similar tensile coupon tests were performed by Coetsee, et al. (1990) on press-brake formed stainless steel channel sections. The response of the stainless steel material to the cold forming operation was found to be similar to that of the carbon structural steel material.

Karren (1967) developed a semi-empirical model to predict the percentage

increase in the rounded corner yield strength due to the forming operation. The model suggested that the increase in the yield strength would depend on the ratio between the ultimate strength and the yield strength of the virgin steel sheet, and on the inside bending radius-to-thickness ratio of the corner. This approach is currently being used in the American LRFD Specification (AISI, 1991). Lind and Schroff (1975) presented another model to evaluate the corner yield strength of CFS sections. Their model assumed a linear hardening relationship of the material in the margin between the yield strength and the ultimate strength, and the hardening constant was determined empirically from the tests of Karren (1967). The final form of the model concluded that the 90° corner yield strength of a CFS section could be evaluated by replacing the virgin yield strength by the virgin ultimate strength over an arc length of the corner of five times the thickness. For other corner angles, the arc length should be increased proportionally. The approach of Lind and Schroff (1975) is currently being used in the Canadian S136-94 Standard (CSA, 1994).

1.4.2.2 Residual Stresses

Alexander (1959) and Korol (1971) presented a progressive theoretical model for the distributions of residual stresses, which result from the operation of cold-bending a wide sheet to a curved profile. An ideally elasto-plastic material behaviour, involving both von Mises and Tresca yield criteria, was assumed in the theoretical model to evaluate the bending stresses, the spring-back stresses, and the net residual

stresses at the curved elements. Figure 1.4(a) shows the two dimensional state of stress of a curved element following the spring back, where the path $A'B'OC'D'$ represents the residual stress state (Korol, 1971). Figure 1.4(b) shows the resulting distributions of the transverse and longitudinal residual stresses. Ingvarsson (1979) carried out an experimental and analytical study to investigate the residual stresses at the rounded corner parts of CFS sections. The study indicated that the magnitudes of the transverse and longitudinal corner residual stresses in CFS sections depended on the external circumstances during the active cold forming. The study also indicated that the existence of residual stresses in CFS sections explains the geometric imperfections usually found in these sections, such as the twisting of Z-shaped sections.

Weng and Pekoz (1990) performed an experimental residual stress investigation on CFS channel sections with different thicknesses. Longitudinal residual stresses were investigated at both the rounded corner parts and flat parts of the sections. Two cutting methods were used to release the residual strains; the saw cutting method, and the electrical discharge machining method. The results indicated that tensile residual stresses exist on the outside surfaces of CFS sections, and compressive residual stresses exist on the inside surfaces of the sections. Uniform magnitudes of residual stresses were recorded at the flat areas of the sections, while higher magnitudes of residual stresses were recorded at the rounded corners. This distribution of longitudinal residual stresses was consistent for all the tested CFS

sections. Roy, et al. (1994) performed similar residual stress study on CFS angle and channel sections. The study was performed through two non-destructive testing methods (the X-ray diffraction method and the Magnetic Barkhausen noise method), and two destructive cutting methods (the hole drilling method and the saw cutting method). However, the presented results of this study gave only the measured residual stresses at the corners of the CFS sections, without much detail about the distribution of the stresses across the sections.

1.4.3 Local Buckling of Perforated Cold-Formed Steel Compression Members

The local buckling behaviour of perforated Cold-formed steel (CFS) members subjected to axial, bending, bearing, and combination loads was studied by many researchers in the past. Some of the recent studies dealing with the effects of perforations on the flexural strength of CFS members were given by Yu and Davis (1973), Schuster (1992), and Shan, et al. (1994). Also, recent studies dealing with the effects of perforations on the web crippling strength of CFS members were given by Yu and Davis (1973), Sivakumaran and Zielonka (1989), and Langan, et al. (1994). However, since this study is concerned with the post-local buckling strength of perforated CFS compression members, this section gives an overview on the previous experimental and analytical studies performed on perforated CFS members subjected to axial compression loading. The section also gives an overview on the available effective design width procedures for perforated compression plates.

1.4.3.1 Experimental and Analytical Studies

The experimental investigation carried out by Yu and Davis (1973) is considered to be one of the first investigations which studied CFS members with perforated elements. Local and post-local buckling strengths were investigated for both stiffened and unstiffened perforated sections. A series of experimental tests on doubly symmetric sections were performed to study the effects of the perforation parameters on the ultimate strength of the sections. Ortiz-Colberg (1981) performed an experimental study on the axial capacity of CFS columns with circular perforations. The study aimed at developing an empirical effective design width equation for perforated web plates of CFS compression members. Loov (1984) studied experimentally the post-local buckling capacity of channel CFS stub-columns with rectangular web perforations. Different cross sections were considered, but with fixed dimensions of the perforation.

Banwait (1987) and Sivakumaran (1987a) presented an experimental investigation, which studied the local buckling and post-local buckling behaviour of axially loaded CFS channel sections. Different sizes and shapes of the perforation were considered. Sivakumaran (1987b) performed a nonlinear finite element analysis to study the local and post-local buckling behaviour of axially loaded perforated CFS members. The finite element model consisted of a four-node isoparametric shell element, and a multi-linear elasto-plastic stress-strain relationship. The model showed good ultimate strength results, but higher stiffness, when compared to the

experimental results. The effects of initial imperfections, residual stresses, and variations of the mechanical properties of the material across the CFS sections were not taken into consideration. Miller and Pekoz (1994) performed an experimental and analytical study to investigate the local buckling behaviour of channel CFS stub-columns with rectangular web perforations. The post-local buckling strength of the stub-columns was determined, and compared to two different design approaches to calculate the resulting ultimate loads.

Rhodes and Schneider (1994), and Rhodes and Macdonald (1996), performed an experimental investigation on the effects of multiple circular and elongated perforations on the ultimate compression strength of CFS channel sections. The multiple perforations were located transversally at the same cross section of the web and flange plates, and in the longitudinal direction of the tested compression members. A main observation from these tests was that the area of the compression member between the multiple perforations tended to buckle individually in a column fashion. The ultimate load results of the tests were compared to the results of different design approaches, in order to find a suitable design procedure for such CFS members with multiple perforations.

1.4.3.2 Current Effective Design Width Procedures of Perforated Plates

For perforated stiffened plates, Yu and Davis (1973) proposed a design approach to predict the effective design width of perforated plates with either central

circular or square perforation. They assumed that the buckling behaviour of a perforated plate is similar to that of a non-perforated plate up to a certain limit of the perforation width-to-plate width ratio (a/w). Above this limit, the perforated plate can be treated as two separate, but identical, unstiffened compression plates. Based on this assumption, an effective design width equation of the following form was proposed:

$$b = 0.95\ t \sqrt{\frac{k\ E}{F_{max}}} \left(1 - A\ \frac{a}{w}\right) \left[\ 1 - 0.208\ \left(\frac{t}{w-a}\right) \sqrt{\frac{k\ E}{F_{max}}} \left(1 - B\ \frac{a}{w}\right)\ \right] \quad (1.11)$$

For a circular perforation, the constants (A) and (B) are 0.226 and 0.0379, respectively and the equation was limited for a perforation of (a/w) ratio less than 0.7. However for a square perforation, the constants (A) and (B) are 0.316 and 0.053, respectively and the equation was limited for a perforation of (a/w) ratio less than 0.5. The effective design width for plates with perforation above these (a/w) ratio limits was to be determined assuming two separate unstiffened plates on both sides of the perforation.

Banwait (1987) presented a design equation for plates with both circular and square perforation. The equation was based on his experimental study on cold-formed steel (CFS) sections with (w/t) ratios of 51.5 and 112.4 for the perforated web plate. The equation states that:

$$b = \sqrt{\frac{w - a}{w}}\, b_{um} \qquad (1.12)$$

where (b_{um}) is the effective design width of the corresponding non-perforated plate, obtained according to Equations 1.8 and 1.9.

Miller and Pekoz (1994) presented a simplified approach for the treatment of perforated plates with any shape of perforation. The approach consists of:

$$\text{If } (w\text{-}b_{um}) > (a), \text{ then } b = b_{um} \qquad (1.13)$$

$$\text{If } (w\text{-}b_{um}) \leq (a), \text{ then } b = w\text{-}a \qquad (1.14)$$

In other words, if the perforation does not extend into the effective portion of the plate (calculated by ignoring the perforation), then it does not affect the effective design width. However, if the perforation extends into the effective portion, then the effective design width can be obtained by deducting the perforation width from the total plate width.

The design procedure given in the American LRFD Specification (AISI, 1991) for stiffened plates with circular perforations is based on the results of the experimental study of Ortiz-Colberg (1981). The procedure (in the format of Equations 1.8 and 1.9) can be expressed as follows:

$$b = w - a \qquad \text{for} \quad (w/t) \le (w/t)_{lim} = 0.644 \sqrt{\frac{k\,E}{F_{max}}} \tag{1.15}$$

$$b = 0.95\,t \sqrt{\frac{k\,E}{F_{max}}} \left[1 - 0.208 \left(\frac{t}{w}\right) \sqrt{\frac{k\,E}{F_{max}}} - 0.8 \frac{a}{w} \right] \quad \text{for} > (w/t)_{lim} \tag{1.16}$$

This design procedure is only applicable for stiffened compression plates with slenderness ratio (w/t) not greater than 70, and having a circular perforation with a diameter less than half the width of the plate.

The design procedure given in the Canadian S136-94 Standard (CSA, 1994) for perforated wall stud assemblies is based on the experimental study of Miller and Pekoz (1994). The procedure states that the effective design width (b) of perforated webs of wall studs can be calculated assuming the web to consist of two unstiffened elements, one on each side of the perforation. This simplified design procedure has some limitations, including the perforation width not to exceed half the depth of the section or 65 mm, and the perforation length not to exceed 115 mm. The procedure is also not applicable for single members in compression (Clause 6.6 of the Standard).

1.5 Objectives and Scope

The current study was motivated by the need for an appropriate analytical technique, which can be used to predict the behaviour and the post-buckling strength

of cold-formed steel (CFS) members in compression.

1.5.1 Objectives

The objectives of the current study are as follows:

[1] Development of a shell finite element to model the large deformation and the elasto-plastic behaviour of thin and moderately thick shell structures, as cold-formed steel (CFS) members.

[2] Experimental evaluation of the typical material properties of CFS sections.

[3] Development of a finite element model suitable for the analysis of CFS compression members

[4] Verification of the developed finite element model with experimental tests of CFS stub-columns.

[5] Performing a finite element investigation to study the effects of perforation parameters on the behaviour and ultimate strength of CFS compression members.

[6] Establishing suitable design equations for perforated CFS compression members.

1.5.2 Scope of Research

The scope and organization of the research achieved in this thesis are presented as follows:

Chapter One: An introduction and review of previous research related to the study topics are presented.

Chapter Two: The nonlinear formulation of a basic degenerated shell finite element is presented. This formulation is modified using the "assumed strain fields" method to eliminate the locking problems associated with the basic element. The "assumed strain fields" method is extended to the large deformation formulation of the shell element.

Chapter Three: The experimental evaluation of the material properties of cold-formed steel (CFS) sections is presented, through two series of tests on the mechanical properties, and the residual stresses across CFS sections. Analytical models for the stress-strain relationship of the CFS material, the variation of the yield strength, and the distribution of residual stresses are developed.

Chapter Four: A finite element analysis model for CFS members in compression is presented. The model is verified with a series of experimental tests on non-perforated and perforated CFS stub-columns. The effects of perforations on CFS members in compression are discussed based on the results of the experimental tests.

Chapter Five: An investigation on the effects of different perforation parameters on the axial stress distributions and the effective design widths of perforated elements is presented. Two proposed effective design width equations for CFS structural elements with square and elongated perforations are also presented and discussed.

Chapter Six: The conclusions and the recommendations of the study are presented.

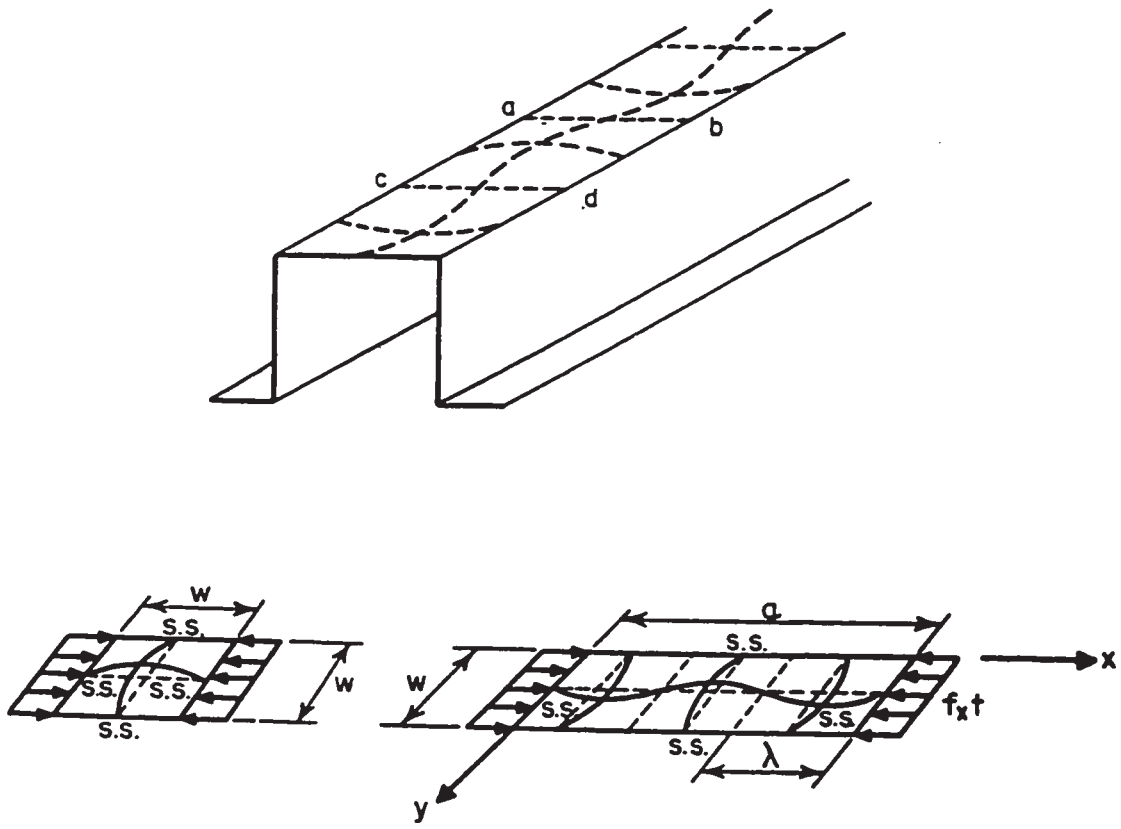

Figure 1.1 Local buckling of stiffened compression plates (Yu, 1991)

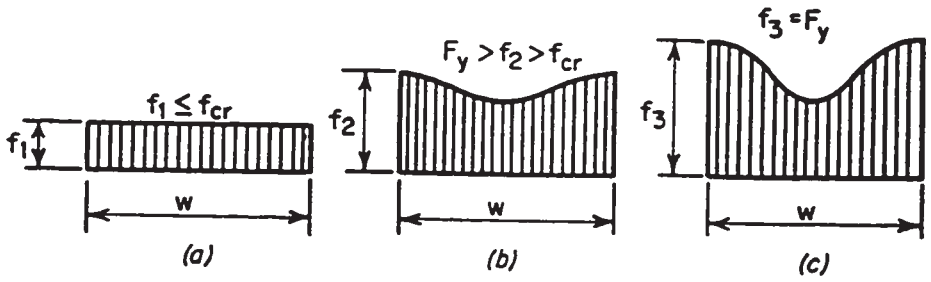

Figure 1.2(a) Stages of stress redistribution in stiffened compression plates (Yu, 1991)

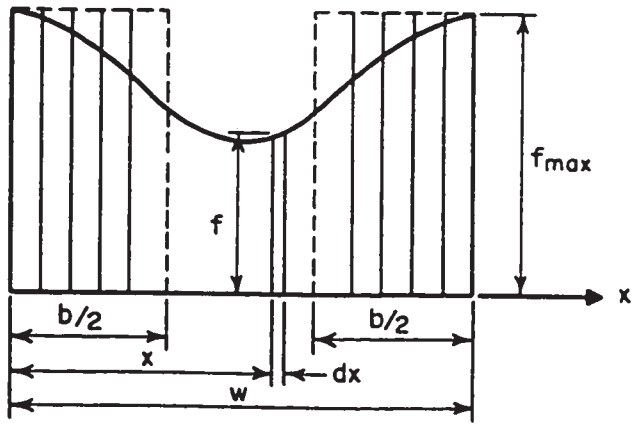

Figure 1.2(b) Effective width of stiffened compression plates

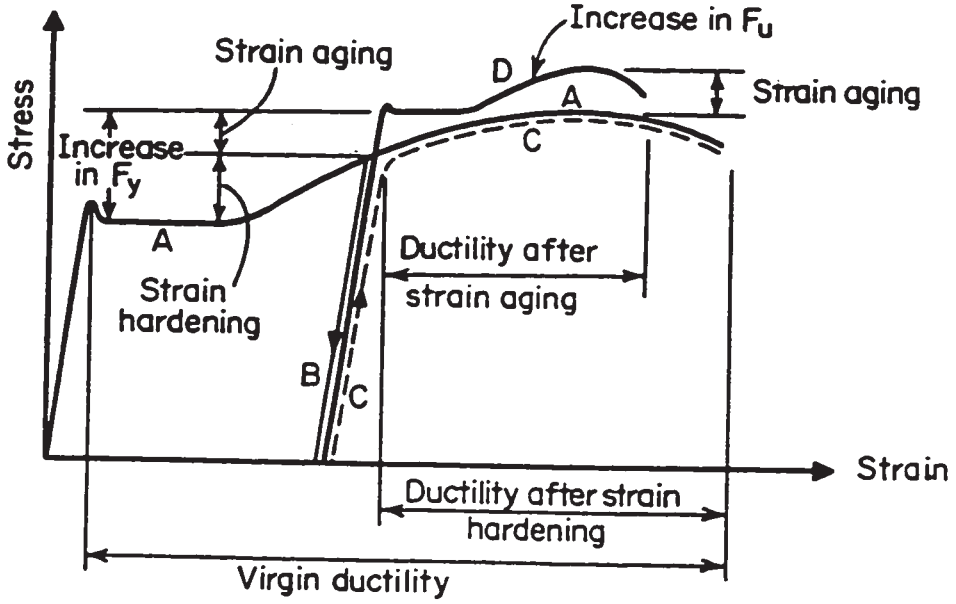

Figure 1.3 Effects of strain hardening and strain aging phenomena on the stress-strain relationship (Chajes, et al., 1963)

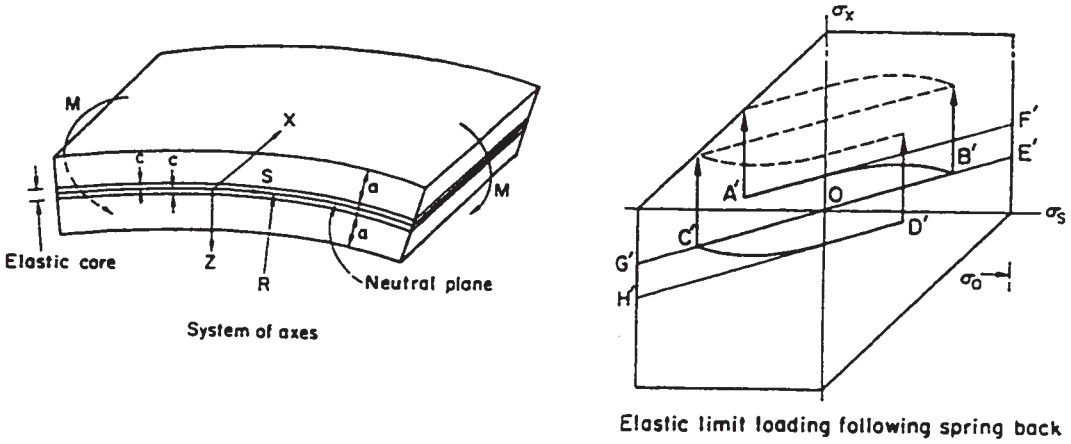

Figure 1.4(a) State of stress of a wide plate in cold-bending (Korol, 1971)

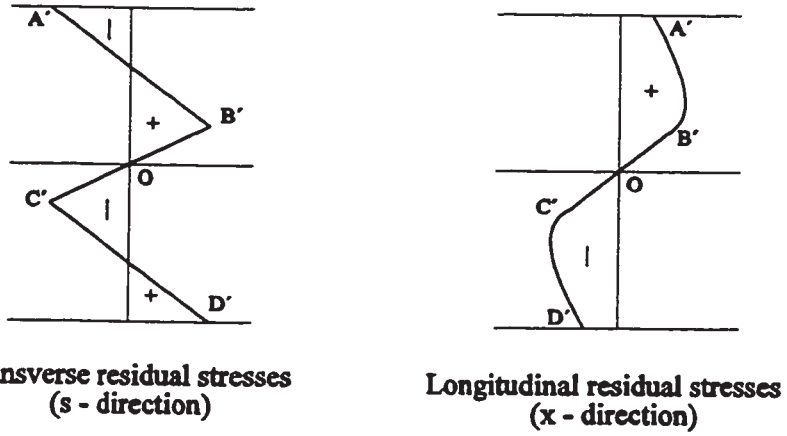

Figure 1.4(b) Residual stresses resulting from cold-bending

CHAPTER 2

NONLINEAR "ASSUMED STRAIN" SHELL FINITE ELEMENT

2.1 Introduction

Degenerated isoparametric shell finite elements, based on independent interpolations for the translational and rotational degrees of freedom, were first introduced by Ahmad, et al. (1970). The degenerated shell elements had the advantage of being independent of any shell theory, therefore they were suitable for modelling both thin and moderately thick shell structures. However, with the increased use of the degenerated shell elements, some problems associated with the analysis of thin shells, and the use of reduced or selective numerical integration schemes, were discovered. These problems are the "transverse shear and membrane locking", and the "spurious zero energy modes", (Parisch, 1979, and Koziey, 1993).

A 9-node degenerated isoparametric shell finite element was considered in the current study to represent the body of the cold-formed steel (CFS) members. The first part of this chapter briefly presents the basic large deformation formulation, and the elasto-plastic material formulation, of the nonlinear degenerated 9-node shell finite element. The large deformation formulation was based on the Total Lagrangian formulation, while the elasto-plastic material formulation consisted of a multi-linear isotropic strain hardening model, based on the Huber-von Mises yield criterion. The

basic 9-node shell element was extracted from the finite element program INDAP (INDAP, 1987), and inserted as a library element in the finite element program XFEAP (XFEAP, 1990). This change was necessary since only the program XFEAP had the advantage of providing several control techniques, that were most suitable for the incremental nonlinear analysis of CFS members under consideration.

As CFS members are essentially thin-walled members, the kinematic formulation of the basic 9-node degenerated shell element was enhanced in the second part of this chapter, by using the method of "assumed strain fields" (Huang and Hinton, 1986), in order to eliminate the locking problems associated with the analysis of thin structures. The implementation of the "assumed strain fields" method was extended in this study, to cover the large deformation formulation of the 9-node degenerated shell element.

The third part of this chapter presents a set of bench mark problems to investigate the efficiency and accuracy of the new 9-node "assumed strain" shell element. The bench mark problems cover the large deformation behaviour and the elasto-plastic behaviour for a wide range of very thin to moderately thick plate and shell structures.

2.2 Nonlinear Formulation of the Degenerated Shell Finite Element

The basic 9-node degenerated shell finite element applies the Reissner-Mindlin theory (Mindlin, 1951), where normals to the mid-surface of the shell before

deformation are assumed to remain straight, but not necessarily normal to the mid-surface after deformation. The stress component normal to the mid-surface of the element is considered equal to zero, and the strain energy associated with this normal stress is neglected.

2.2.1 Coordinate Systems and Element Geometry

Three coordinate systems are used in the formulation of the degenerated shell finite element. These systems are defined as follows:

(i) Global Cartesian Coordinate System (x, y, z): which is used to define the nodal coordinates and displacements of the element.

(ii) Natural Coordinate System (ξ, η, ζ): The mid-surface of the shell element and its interpolation functions are defined in terms of the (ξ) and (η) coordinates. The (ζ) direction is normal to the shell mid-surface in the thickness direction. This coordinate system is called natural since all the coordinates (ξ, η, and ζ) vary from (-1) to (+1).

(iii) Local Cartesian Coordinate System (x′, y′, z′): which is used to define local strains and stresses at any point within the shell element. The (z′) direction is considered to be normal to the surface (ζ) = constant, and (x′ and y′) directions are tangent to that surface.

The degenerated shell finite element has nine mid-surface nodal points as shown in Figure 2.1. Each nodal point (k) of the element has five degrees of freedom; three translational displacements (u^k, v^k, and w^k) defined along the global directions,

and two rotations (α^k and β^k) around the mid-surface axes (local coordinate system). The global Cartesian coordinates (x_i) of any point of the element can be uniquely given in terms of the nodal coordinates (x_i^k) and the element thickness at the nodes (t^k) as follows:

$$x_i = \sum_{k=1}^{9} N^k(\xi,\eta)\, x_i^k + \frac{\zeta}{2} \sum_{k=1}^{9} N^k(\xi,\eta)\, t^k\, V_{n\,i}^k \qquad (i = 1,2,3) \quad (2.1)$$

where, $N^k(\xi,\eta)$ are the interpolation functions at the node k, which are given in Appendix A. The vector (V_{ni}^k) is the vector of the direction cosines (with respect to the global coordinates) of the unit vector normal to the shell mid-surface in the thickness direction at the node k.

2.2.2 Displacement Field

The displacements of any point (u_i) in the shell finite element are defined by quadratic interpolation functions of the three Cartesian components of the nodal displacements (u_i^k), and the two rotations of the nodal vector (V_{ni}^k) about the two orthogonal directions (V_{1i}^k and V_{2i}^k) normal to it. The definition of (u_i) can be written as follows:

$$u_i = \sum_{k=1}^{9} N^k(\xi,\eta)\, u_i^k + \frac{\zeta}{2} \sum_{k=1}^{9} N^k(\xi,\eta)\, t^k\, \delta V_{n\,i}^k \qquad (i = 1,2,3) \quad (2.2)$$

The change in the normal vector (δV_{ni}^k) can be expressed in terms of the unit vectors (V_{1i}^k) and (V_{2i}^k), that are orthogonal to (V_{ni}^k), and the small rotations (α^k) and (β^k) of the normal vector about (V_{1i}^k) and (V_{2i}^k), respectively, as follows:

$$\delta V_{n\,i}^{k} = V_{1\,i}^{k}\ \beta^{k} - V_{2\,i}^{k}\ \alpha^{k} \tag{2.3}$$

Equation 2.2 can, then, be rewritten in a compact form as follows:

$$u_i = \sum_{k=1}^{9} \bar{N}^{k}(\xi,\eta,\zeta)\ d^{k} \tag{2.4}$$

where the matrix $\bar{N}^k(\xi,\eta,\zeta)$ includes the terms of $N^k(\xi,\eta)$ in the (ξ-η) mid-surface, and the additional terms related to the unit vectors (V_{1i}^k and V_{2i}^k) in the (ζ) direction. The vector (d^k) is the degrees of freedom vector at the node k.

2.2.3 Total Lagrangian Formulation

The Total Lagrangian formulation has been considered in the current large deformation analysis. In this formulation, all the current static and kinematic variables (at time T) are referred to the initial configuration before deformation (at time T = 0) as shown in Figure 2.2. The Total Lagrangian formulation includes all kinematic nonlinear effects due to large displacements and rotations, but small strains.

2.2.3.1 Strain and Stress Tensors

The strain and stress tensors incorporated with the Total Lagrangian formulation, as presented by Bathe (1982), are the Green-Lagrange strain tensor (ϵ_{ij}) and the Second Piola-Kirchhoff stress tensor (S_{ij}). The two tensors, relevant to the shell analysis, are of the form:

$$\epsilon_{ij} = \{ \epsilon_{xx} \;\; \epsilon_{yy} \;\; \epsilon_{xy} \;\; \epsilon_{yz} \;\; \epsilon_{xz} \}$$

$$S_{ij} = \{ S_{xx} \;\; S_{yy} \;\; S_{xy} \;\; S_{yz} \;\; S_{xz} \} \qquad (2.5)$$

The Green-Lagrange strain tensor (ϵ_{ij}) is defined as:

$$\epsilon_{ij} = \tfrac{1}{2} (u_{i,j} + u_{j,i} + u_{k,i} \, u_{k,j}) \qquad (2.6)$$

in which ($u_{i,j} = \frac{\partial u_i}{\partial x_j}$) is the derivative of the i^{th} component of the displacement with respect to the j^{th} coordinate of the initial undeformed configuration.

The Second Piola-Kirchhoff stress tensor ($S_{i\,j}$) is related to the Green-Lagrange strain tensor, through the material property tensor (C_{ijkl}), as follows:

$$S_{ij} = C_{ijkl} \; \epsilon_{kl} \qquad (2.7)$$

The Green-Lagrange strain tensor and the Second Piola-Kirchhoff stress

tensor have the advantage of being invariant under rigid body deformations. The two tensors are also conjugate from the energy point of view, which means that the integration of their product over a specified undeformed volume gives the strain energy of this volume. Further information about the properties of these two tensors is given by Bathe (1982).

2.2.3.2 Virtual Work and Finite Element Equations

The equilibrium condition in the finite element analysis is introduced by means of the virtual work equation. The Total Lagrangian formulation, referred to the undeformed configuration (time T=0), results in a virtual work equation with the incremental terms as follows:

$$\int {}_0C_{ijkl}\ {}_0\Delta\epsilon_{kl}\ \delta\ {}_0\Delta\epsilon_{ij}\ {}^0dv + \int {}^T{}_0S_{ij}\ \delta\ {}_0\Delta\eta_{ij}\ {}^0dv = {}^T\delta W - \int {}^T{}_0S_{ij}\ \delta\ {}_0\Delta\epsilon_{ij}\ {}^0dv \tag{2.8}$$

where $({}^T\delta W)$ is the external incremental virtual work at the current time (T). The tensor $({}_0\Delta\epsilon_{ij})$ is the incremental Green-Lagrange strain tensor, which can be divided into a linear part $({}_0\Delta\epsilon_{0\,ij})$, and an initial displacement part $({}_0\Delta e_{ij})$ as follows:

$${}_0\Delta\epsilon_{ij} = {}_0\Delta\epsilon_{0\,ij} + {}_0\Delta e_{ij} = \tfrac{1}{2}\left({}_0\Delta u_{i,j} + {}_0\Delta u_{j,i}\right) + \tfrac{1}{2}\left({}_0u_{k,i}\ {}_0\Delta u_{k,j} + {}_0\Delta u_{k,i}\ {}_0u_{k,j}\right) \tag{2.9}$$

and $({}^T{}_0S_{i\,j})$ is the Second Piola-Kirchhoff stress at time (T) referred to the initial

configuration. The incremental stress tensor (${}_0\Delta S_{ij}$) is expressed as:

$$ {}_0\Delta S_{ij} = {}_0C_{ijkl}\ {}_0\Delta \epsilon_{kl} \tag{2.10} $$

The nonlinear incremental strain (${}_0\Delta \eta_{ij}$), which is not included in the (${}_0\Delta \epsilon_{ij}$) expression, can be expressed as:

$$ {}_0\Delta \eta_{ij} = \tfrac{1}{2} \left({}_0\Delta u_{k,i}\ {}_0\Delta u_{k,j} \right) \tag{2.11} $$

By substituting the expressions of Equations 2.9 to 2.11 into Equation 2.8, and by realizing that the virtual displacements ($\delta \Delta u$) are arbitrary displacements, the incremental virtual work equation can be written in a matrix form as follows:

$$ \left[\int {}_0B^T\, D_{ep}\, {}_0B\ {}^0dv + \int {}_0B_{NL}{}^T\, S\, {}_0B_{NL}\ {}^0dv \right] \Delta d = {}^TR - \int {}_0B^T\, S\ {}^0dv \tag{2.12} $$

The (T) symbol on the top-left position of a variable indicates the current time step, while the (T) symbol on the top-right position of a variable indicates the transpose of the variable. The matrix [D_{ep}] represents the elasto-plastic stress-strain relationship, and will be evaluated in Section 2.2.4 of this chapter. The vector (${}^TR$) is the current external applied loads, and the vector (Δd) is the incremental nodal degrees of freedom. The incremental strain-displacement matrix [${}_0B$] consists of the small

deformation matrix $[{}_0B_0]$ and the initial displacement matrix $[{}_0B_L]$ associated with the strains $({}_0\Delta\epsilon_0)$ and $({}_0\Delta e)$, respectively. Therefore, the matrix $[{}_0B]$ is defined as follows:

$$ {}_0B = {}_0B_0 + {}_0B_L \tag{2.13} $$

The matrix $[{}_0B_{NL}]$ is the incremental nonlinear strain-displacement matrix. The complete expressions for the terms of the matrices $[{}_0B_0]$, $[{}_0B_L]$, and $[{}_0B_{NL}]$ are given by Bathe (1982).

By substituting from Equation 2.13 into 2.12 and collecting the corresponding terms, the finite element incremental equations can be obtained as follows:

$$ [\, K_0 + K_L + K_{NL} \,]\, \Delta d = {}^{T}R - f \tag{2.14} $$

The right-hand side of Equation 2.14 is the residual force vector, which results from subtracting the internal forces (f) of the previous iteration from the current external forces $({}^{T}R)$. The matrix $[K_0]$ is the linear stiffness matrix, the matrix $[K_L]$ is the initial displacement stiffness matrix, and the matrix $[K_{NL}]$ is the nonlinear stiffness matrix. The three stiffness matrices are defined as follows:

$$ K_0 = \int {}_0B_0{}^{T}\, D_{ep}\, {}_0B_0 \; {}^{0}dv \tag{2.15} $$

$$K_L = \int {}_0B_0{}^T D_{ep} {}_0B_L \ {}^0dv + \int {}_0B_L{}^T D_{ep} {}_0B_L \ {}^0dv + \int {}_0B_L{}^T D_{ep} {}_0B_0 \ {}^0dv \quad (2.16)$$

$$K_{NL} = \int {}_0B_{NL}{}^T S \ {}_0B_{NL} \ {}^0dv \quad (2.17)$$

The summation of the three stiffness matrices (K_0, K_L, and K_{NL}) gives the element tangent stiffness matrix $[K_T]$.

The Total Lagrangian formulation presented above gives the main steps in developing the large deformation formulation of the 9-node degenerated shell finite element. Readers who require more detail about the Total Lagrangian formulation are advised to refer to Bathe (1982), or Zienkiewicz and Taylor (1991).

2.2.4 Elasto-Plastic Strain Hardening Model

A multi-linear isotropic strain hardening constitutive model was formulated to represent the stress-strain relationship of the cold-formed steel material. The model was based on the Huber-von Mises yield criterion and its associated flow rule, as presented by Chen and Han (1988). An incremental approach was adopted for the current elasto-plastic analysis, in order to have a compatibility with the large deformation finite element analysis approach presented in Section 2.2.3. The following steps summarize the main procedure followed in the derivation of the constitutive model.

2.2.4.1 The Yield Criterion

The yielding state of an isotropic material in the Huber-von Mises yield criterion is determined by a yield function (F) as follows:

$$F = \sigma_e - \sigma_y = \sqrt{3J_2} - \sigma_y = 0 \qquad (2.18)$$

where (σ_e) is an effective stress function, (σ_y) is the uniaxial yield stress, and (J_2) is the second deviatoric stress invariant. The stress invariant (J_2) is defined as:

$$J_2 = \tfrac{1}{2}\, s_{ij}\, s_{ji} \;, \qquad s_{ij} = \sigma_{ij} - \delta_{ij}\, \sigma_m \qquad (2.19)$$

where (s_{ij}) is the stress deviator tensor, and ($\sigma_m = \tfrac{1}{3}\sigma_{ii}$) is the first invariant of the stress tensor. Based on the definitions of (J_2) and (s_{ij}), the effective stress (σ_e) for the degenerated shell finite element, using the local Cartesian coordinate system (x',y',z'), can be evaluated as follows:

$$\sigma_e = \sqrt{3J_2} = \left[(\sigma_{x'}^2 + \sigma_{y'}^2 - \sigma_{x'}\, \sigma_{y'}) + 3\,(\gamma_{x'y'}^2 + \gamma_{y'z'}^2 + \gamma_{x'z'}^2) \right]^{1/2} \qquad (2.20)$$

The normal stress ($\sigma_{z'}$) does not appear in Equation 2.20, as it was considered negligible in the formulation of the degenerated shell element. The yielding condition in Equation 2.18 occurs when the effective stress (σ_e), given by Equation 2.20, be

equal to the uniaxial yield stress (σ_y).

2.2.4.2 Elasto-Plastic Stress-Strain Relationship

The total strain increment in the local Cartesian coordinate system ($d\epsilon'$) is defined as the sum of the elastic strain increment ($d\epsilon'^e$) and the plastic strain increment ($d\epsilon'^p$) as follows:

$$d\epsilon' = d\epsilon'^e + d\epsilon'^p \tag{2.21}$$

The plastic strain increment ($d\epsilon'^p$) is defined, according to the associated flow rule, as follows:

$$d\epsilon'^p = d\lambda \; F_{,\sigma} \tag{2.22}$$

where ($d\lambda$) is a non-negative scalar, and ($F_{,\sigma}$) is the flow vector $\{\partial F/\partial \sigma\}$. The deferential form of Equation 2.18 can be written as follows:

$$F_{,\sigma}^{T} \, d\sigma' - A \, d\lambda = 0 \tag{2.23}$$

where (A) is the hardening parameter. Using Equations 2.21 to 2.23, and knowing that ($d\sigma' = D \, d\epsilon'^e$), an expression for the scalar ($d\lambda$) can be determined as follows:

$$d\lambda = \frac{F_{,\sigma}^{T} \; D \; d\epsilon'}{A + F_{,\sigma}^{T} \; D \; F_{,\sigma}} \tag{2.24}$$

where [D] is the elastic stress-strain relationship matrix, given as:

$$[D] = \frac{E}{1 - \nu^2} \begin{bmatrix} 1 & \nu & 0 & 0 & 0 \\ . & 1 & 0 & 0 & 0 \\ . & . & \frac{1-\nu}{2} & 0 & 0 \\ \text{Symmetric} & . & . & \frac{\kappa(1-\nu)}{2} & 0 \\ . & . & . & . & \frac{\kappa(1-\nu)}{2} \end{bmatrix} \tag{2.25}$$

and (κ = 5/6) is a shear correction factor. Based on the above expressions, the incremental stress-strain relationship beyond the initial yield stress (proportional limit) can be written as follows:

$$d\sigma' = D_{ep} \; d\epsilon' \tag{2.26}$$

where $[D_{ep}]$ is the elasto-plastic stress-strain relationship matrix defined as :

$$D_{ep} = D - \frac{D \; F_{,\sigma} \; F_{,\sigma}^{T} \; D}{A + F_{,\sigma}^{T} \; D \; F_{,\sigma}} \tag{2.27}$$

2.2.4.3 Multi-linear Strain Hardening

The hardening parameter (A) in Equation 2.27 should be set to zero for the condition of perfect plasticity. However for strain hardening materials, (A) takes the value of the plastic modulus (H), which is the slope of the effective stress (σ_e)-effective plastic strain (ϵ_e^p) curve. The incremental effective plastic strain ($d\epsilon_e^p$) can be calculated as follows, assuming an equivalent amount of plastic work per unit volume to that of the general stress-strain case:

$$d\epsilon_e^p = \frac{1}{\sigma_e}(d\lambda \; F_{,\sigma}^T \; \sigma') \tag{2.28}$$

The plastic modulus (H) is related to the modulus of elasticity (E) and the corresponding tangent modulus (E_T) as follows:

$$H = \frac{E \; E_T}{E - E_T} \tag{2.29}$$

As will be discussed in Chapter Three, the current elasto-plastic constitutive model employs a multi-linear stress-strain relationship to account for the gradual yielding behaviour and the strain hardening of the cold-formed steel material. The gradual yielding was accommodated with a bi-linear plastic representation, with tangent moduli (E_{T1} and E_{T2}) beyond the proportional limit as shown in Figure 2.3. The strain hardening of the material was accommodated with a linear plastic segment with a

tangent modulus (E_{T3}). The uniaxial stress limits of the three plastic segments and the values of the three tangent moduli (E_{T1}, E_{T2}, and E_{T3}) are chosen based on the tensile coupon test results presented in Chapter Three. Equation 2.29 can then be generalized for a plastic modulus (H_i) as follows:

$$H_i = \frac{E\ E_{Ti}}{E - E_{Ti}} \qquad (i = 1, 2, 3) \tag{2.30}$$

Having defined all the terms in Equation 2.27, the elasto-plastic stress-strain matrix $[D_{ep}]$ can be calculated to take part in the nonlinear finite element formulation as presented in Section 2.2.3.2.

2.3 Problems Associated with the Degenerated Shell Finite Element

The analysis problems associated with the basic 9-node degenerated shell finite element arise from the Mindlin assumption (that a constant transverse shear strain is considered through the thickness of the element), and from the representation of the membrane strains. Parisch (1979) performed a critical survey on the 9-node degenerated shell element to study the performance of the element. It was found that the element performs very well for moderately thick shells, and for general loading conditions. However, for very thin shells, and shells in pure bending, over stiff erroneous solutions were usually obtained when full integration is used to evaluate the stiffness matrices of the element. This problem is known as "transverse shear and

membrane locking" of degenerated shell elements. The use of a reduced integration scheme to under-integrate the stiffness matrix of the degenerated shell element, in order to reduce the locking effects, may result in the generation of spurious zero energy modes.

2.3.1 Transverse Shear and Membrane Locking

The phenomenon of the "transverse shear and membrane locking" may be explained as follows:

The total potential energy (Π), based on the Reissner-Mindlin theory, for a degenerated shell element may be given by:

$$\Pi = \tfrac{1}{2} \int_V \epsilon_m^T D_m \epsilon_m \, dV + \tfrac{1}{2} \int_V \epsilon_b^T D_b \epsilon_b \, dV + \tfrac{1}{2} \int_V \epsilon_s^T D_s \epsilon_s \, dV - W \quad (2.31)$$

where (ϵ_m), (ϵ_b), and (ϵ_s) are the membrane, bending, and transverse shear strain tensors, respectively. The matrices [D_m], [D_b], and [D_s] are the corresponding stress-strain relationship matrices. After the integration through the element thickness, the element strain energy terms can be separated into the bending strain energy [S.E.$_b$], the membrane strain energy [S.E.$_m$], and the transverse shear strain energy [S.E.$_s$]. These strain energy terms can be written as follows :

$$S.E._b = \tfrac{1}{2}\left[\frac{E\,t^3}{12(1-\nu^2)}\right]\int\left[k_{xx}^2 + k_{yy}^2 + 2\nu k_{xx}k_{yy} + \frac{(1-\nu)}{2}k_{xy}^2\right]dx\,dy$$

$$S.E._m = \tfrac{1}{2}\left[\frac{E\,t}{(1-\nu^2)}\right]\int\left[\epsilon_{mxx}^2 + \epsilon_{myy}^2 + 2\nu\epsilon_{mxx}\epsilon_{myy} + \frac{(1-\nu)}{2}\epsilon_{mxy}^2\right]dx\,dy$$

$$S.E._s = \tfrac{1}{2}\left[\frac{E\,t}{2(1+\nu)}\right]\int\left[\gamma_{xz}^2 + \gamma_{yz}^2\right]dx\,dy \qquad (2.32)$$

where (k_{xx}), (k_{yy}), and (k_{xy}) are the shell curvatures, (ϵ_{mxx}), (ϵ_{myy}), and (ϵ_{mxy}) are the membrane strains, and (γ_{xz}) and (γ_{yz}) are the transverse shear strains. It can be deduced from Equation (2.32) that:

$$\|S.E._s\| \;\alpha\; \|S.E._b\| \,/\, \left(\frac{t}{\Delta L}\right)^2 \quad ; \quad \|S.E._m\| \;\alpha\; \|S.E._b\| \,/\, \left(\frac{t}{\Delta L}\right)^2 \qquad (2.33)$$

where (ΔL) denotes a characteristic length of the element. When the $(t/\Delta L)$ ratio in Equation (2.33) tends to zero at the limit, the transverse shear strains will not tend to zero as they should be according to the thin plate theory. In fact, when the shell thickness becomes very small, the strain energy associated with the transverse shear strains and the membrane strains will magnify, compared to the bending strain energy, and, thus, they will dominate the total stiffness of the element. Therefore, an over stiff solution will result, (Parisch, 1979, Huang and Hinton, 1986).

2.3.2 Spurious Zero Energy Modes

When the "reduced integration" scheme for the stiffness matrix of plate and shell finite elements was first introduced by Zienkiewicz, et al. (1971), the scheme

showed good results in overcoming the locking problems. However, a later understanding of this scheme indicated that the under-integration of all the terms of the element stiffness matrix may result in a rank deficiency of the matrix. Therefore, a better integration scheme "selective integration" was introduced by Hughes, et al. (1978). In the "selective integration" scheme, a reduced integration rule was used to evaluate the terms of the stiffness matrix associated with the troublesome transverse shear strain energy and membrane strain energy only. A full integration rule was used to evaluate the remaining terms of the stiffness matrix (namely the bending stiffness terms) in order to maintain its overall required rank.

The study of Parisch (1979) on degenerated shell finite elements proved that both the "reduced integration" scheme and the "selective integration" scheme may result in the generation of spurious (extra) zero energy modes in excess of the shell six rigid body modes. This would mean then, an instability condition of the element may occur unless sufficient boundary conditions are introduced. The study indicated that up to four spurious zero energy modes were located in the basic 9-node degenerated shell element when a 2x2 integration scheme, in the mid-surface plane, was used to evaluate the transverse shear and membrane terms of the element stiffness matrix. Furthermore, up to seven spurious zero energy modes were located when the 2x2 integration scheme was used to evaluate all the terms of the stiffness matrix. The 9-node degenerated shell element needs, at least, a 3x3 integration scheme in the mid-surface plane to obtain the exact terms of the elastic stiffness matrix (Bathe, 1982).

2.4 "Assumed Strain Fields" Method

The "assumed strain fields" method, proposed by Huang and Hinton (1986) and Huang (1987a), was used in the current study to modify the kinematic formulation of the 9-node degenerated shell finite element. The purpose of using the "assumed strain fields" method was to overcome the analysis problems of the basic 9-node shell element, which were discussed in Section 2.3. These problems are the transverse shear and membrane locking, and the spurious zero energy modes.

The "assumed strain fields" method is based on the idea of introducing substitute consistent transverse shear and membrane strain fields, instead of the strain fields that may be evaluated from the displacements and rotations expressions of the basic 9-node shell element. However, a link between the original strain fields and the substitute strain fields is established at a set of appropriately located points in the mid-surface of the shell element, called the "sampling points". The sampling points are the points in the shell element, where the original strain fields of the basic element give the correct values of the transverse shear and membrane strains. As a result, the transverse shear and membrane strains will be the same for the original strain fields and the substitute strain fields at the sampling points, however, they may be different at other points. The substitute transverse shear and membrane strain fields are then used to evaluate the corresponding terms of the stiffness matrix of the shell element.

2.4.1 Elimination of the Transverse Shear Locking

The condition of zero transverse shear strains for very thin shell situations in the natural coordinate system (ξ,η,ζ) may be written as follows:

$$\begin{bmatrix}\gamma_{\xi\zeta}\\ \gamma_{\eta\zeta}\end{bmatrix} = \begin{bmatrix}w_{,\xi} - \alpha_{\xi}\\ w_{,\eta} - \beta_{\eta}\end{bmatrix} = 0 \qquad (2.34)$$

where $(\gamma_{\xi\zeta})$ and $(\gamma_{\eta\zeta})$ are the two transverse shear strains in the thickness direction (ζ), and (α_{ξ}) and (β_{η}) are the rotations associated with the transverse shear strains $(\gamma_{\xi\zeta})$ and $(\gamma_{\eta\zeta})$, respectively. The shear strains $(w_{,\xi})$ and $(w_{,\eta})$ are calculated as the derivatives of the lateral displacement (w) with respect to the mid-surface directions. The polynomial terms for (α_{ξ}) and $(w_{,\xi})$ of the basic 9-node degenerated shell element are given by:

$$\alpha_{\xi} = \alpha_{\xi}\,(\,1,\ \xi,\ \eta,\ \xi\eta,\ \xi^2,\ \eta^2,\ \xi^2\eta,\ \xi\eta^2,\ \xi^2\eta^2\,)$$

$$w_{,\xi} = w_{,\xi}\,(\,1,\ \xi,\ \eta,\ \xi\eta,\ \eta^2,\ \xi\eta^2\,) \qquad (2.35)$$

Similar expressions can be given for (β_{η}) and $(w_{,\eta})$ as well. As the polynomial terms for (α_{ξ}) and $(w_{,\xi})$ [and for (β_{η}) and $(w_{,\eta})$] do not match, substitute fields for the transverse shear strains can be assumed as follows:

$$\bar{\gamma}_{\xi\zeta} = b_1 + b_2\,\xi + b_3\,\eta + b_4\,\xi\eta + b_5\,\eta^2 + b_6\,\xi\eta^2$$

$$\bar{\gamma}_{\eta\zeta} = c_1 + c_2\,\xi + c_3\,\eta + c_4\,\xi\eta + c_5\,\xi^2 + c_6\,\xi^2\eta \qquad (2.36)$$

where the constants b_1 through b_6, and c_1 through c_6, will be determined such that the strains at the "sampling points" are the same as the strains evaluated from the original strain fields. The substitute shear strain ($\bar{\gamma}_{\xi\zeta}$) is linear in (ξ) direction and quadratic in (η) direction, while the substitute shear strain ($\bar{\gamma}_{\eta\zeta}$) is quadratic in (ξ) direction and linear in (η) direction. The shape of the interpolation functions for ($\bar{\gamma}_{\xi\zeta}$) and ($\bar{\gamma}_{\eta\zeta}$) are shown in Figure 2.4. If the substitute strain fields are expressed as polynomials of a lower degree than those in Equation 2.36, the spurious zero energy modes will appear.

To determine the locations of the sampling points, which link the original transverse shear strain fields and the substitute transverse shear strain fields, the following procedure was implemented:

At the sampling points, the original strain fields should give the exact strain results. Thus, the original transverse shear strains ($\gamma_{\xi\zeta}$ and $\gamma_{\eta\zeta}$) should satisfy the following conditions for thin shell situations:

$$\gamma_{\xi\zeta} - \gamma^R{}_{\xi\zeta} \to 0\,, \quad \gamma_{\eta\zeta} - \gamma^R{}_{\eta\zeta} \to 0 \qquad (2.37)$$

where ($\gamma^R{}_{\xi\zeta}$) and ($\gamma^R{}_{\eta\zeta}$) are the transverse shear strains obtained from the exact

analytical solution. Although Equation 2.37 can not be satisfied at all the element points when Reissner-Mindlin theory is applied, it can be satisfied in an average sense as follows:

$$\int_{\Delta A} \gamma_{\xi\zeta}\, d\xi\, d\eta = \int_{\Delta A} \gamma^{R}_{\xi\zeta}\, d\xi\, d\eta \;\rightarrow 0$$
$$\int_{\Delta A} \gamma_{\eta\zeta}\, d\xi\, d\eta = \int_{\Delta A} \gamma^{R}_{\eta\zeta}\, d\xi\, d\eta \;\rightarrow 0 \qquad (2.38)$$

where (ΔA) is a particular area in an individual finite element. For the 9-node shell element, it may be assumed that Equation 2.38 can take the following form:

$$\int_{-1}^{0} \gamma_{\xi\zeta}\, d\xi = 0\,, \quad \int_{0}^{1} \gamma_{\xi\zeta}\, d\xi = 0\,,$$
$$\int_{-1}^{0} \gamma_{\eta\zeta}\, d\eta = 0\,, \quad \int_{0}^{1} \gamma_{\eta\zeta}\, d\eta = 0 \qquad (2.39)$$

The condition of zero transverse shear in Equation 2.34 can then be solved, with the help of the assumptions of Equation 2.39 and the interpolation functions listed in Appendix A, to find the values of (ξ) where the shear strain $(\gamma_{\xi\zeta})$ equals to zero, and the values of (η) where the shear strain $(\gamma_{\eta\zeta})$ equals to zero. The solution results in the sampling points at (ξ) equals to $\pm(1/3)^{1/2}$ for $(\gamma_{\xi\zeta})$, and at (η) equals to $\pm(1/3)^{1/2}$ for $(\gamma_{\eta\zeta})$. However, by referring to Equation 2.36, it can be noticed that six sampling points are required for the representation of the substitute shear strains $(\bar{\gamma}_{\xi\zeta})$ and $(\bar{\gamma}_{\eta\zeta})$. Therefore, the six sampling points for $(\bar{\gamma}_{\xi\zeta})$ were considered at the two lines $(\xi = \pm\, a)$ with $(\eta = +1, 0, -1)$, where "a" equals to $(1/3)^{1/2}$, as shown in Figure 2.5.

This choice insured the continuity of the transverse shear strain across the edges of adjacent elements. Similarly, the six sampling points for ($\bar{\gamma}_{\eta\zeta}$) were considered at the two lines ($\eta = \pm a$) with ($\xi = +1, 0, -1$).

If the substitute transverse shear strains ($\bar{\gamma}_{\xi\zeta}$ and $\bar{\gamma}_{\eta\zeta}$) are replaced by their corresponding terms of the incremental Green-Lagrange strain tensor (${}_0\Delta\bar{\epsilon}_{\xi\zeta}$ and ${}_0\Delta\bar{\epsilon}_{\eta\zeta}$) for the incremental nonlinear analysis, then the substitute fields for the transverse shear strains in Equation 2.36 can be interpolated as follows:

$$
\begin{aligned}
{}_0\Delta\bar{\epsilon}_{\xi\zeta} &= \sum_{i=1}^{3} \sum_{j=1}^{2} \phi^{ij}(\xi,\eta) \; {}_0\Delta\epsilon^{ij}_{\xi\zeta} \\
{}_0\Delta\bar{\epsilon}_{\eta\zeta} &= \sum_{i=1}^{3} \sum_{j=1}^{2} \psi^{ij}(\xi,\eta) \; {}_0\Delta\epsilon^{ij}_{\eta\zeta}
\end{aligned}
\qquad (2.40)
$$

where the terms (${}_0\Delta\epsilon^{ij}_{\xi\zeta}$) and (${}_0\Delta\epsilon^{ij}_{\eta\zeta}$) are the incremental transverse shear strains at the sampling points, evaluated directly from the displacement field in the natural coordinate system. The interpolation functions (ϕ^{ij}), correspond to the sampling points (1,1) through (3,2) associated with ($\bar{\gamma}_{\xi\zeta}$) in Figure 2.5, can be written as follows:

$$
\begin{aligned}
\phi^{(1,1)} &= \tfrac{1}{4}\left(1 + \frac{\xi}{a}\right)\eta\,(\eta + 1) \quad , \quad \phi^{(1,2)} = \tfrac{1}{4}\left(1 - \frac{\xi}{a}\right)\eta\,(\eta + 1) \\
\phi^{(2,1)} &= \tfrac{1}{2}\left(1 + \frac{\xi}{a}\right)(1 - \eta^2) \quad , \quad \phi^{(2,2)} = \tfrac{1}{2}\left(1 - \frac{\xi}{a}\right)(1 - \eta^2) \\
\phi^{(3,1)} &= \tfrac{1}{4}\left(1 + \frac{\xi}{a}\right)\eta\,(\eta - 1) \quad , \quad \phi^{(3,2)} = \tfrac{1}{4}\left(1 - \frac{\xi}{a}\right)\eta\,(\eta - 1)
\end{aligned}
\qquad (2.41)
$$

Similar interpolation functions (ψ^{ij}), correspond to the sampling points (1,1) through (3,2) associated with ($\bar{\gamma}_{\eta\zeta}$) in Figure 2.5, can be written by simply replacing (ξ) by (η), and (η) by (ξ) in the expressions of (ϕ^{ij}) in Equation 2.41.

2.4.2 Elimination of the Membrane Locking

The membrane and transverse shear stiffness terms of the degenerated shell finite element were found to be of the same order of magnitude, as discussed in Section 2.3.1. Therefore, it was expected that the procedure of the elimination of the membrane locking would be similar to that of the transverse shear locking. Furthermore, as the membrane strains can only be separated from the bending strains in the local Cartesian coordinate system (x′, y′, z′), the elimination of the membrane locking should be performed in this coordinate system, (Huang, 1987b).

The in-plane displacements of the shell element can be expressed in the local Cartesian coordinate system as follows:

$$u' = u_0' + z'\,\alpha_{x'}, \qquad v' = v_0' + z'\,\beta_{y'} \tag{2.42}$$

where (u_0') and (v_0') are the displacements in the mid-surface of the element in directions (x′) and (y′), respectively. The rotations ($\alpha_{x'}$) and ($\beta_{y'}$) are the rotations around the local axes (x′) and (y′), respectively. The membrane strains can then be expressed in three terms ($\epsilon_{mx'x'}$, $\epsilon_{my'y'}$, and $\epsilon_{mx'y'}$) as follows:

$$\epsilon_{mx'x'} = \epsilon_{mx'x'}(1,x',y',x'y',x'y'^2,y'^2)$$

$$\epsilon_{my'y'} = \epsilon_{my'y'}(1,x',y',x'y',x'^2y',x'^2) \qquad (2.43)$$

$$\epsilon_{mx'y'} = \epsilon_{mx'y'}(1,x',y',x'y',x'^2,x'^2y',x'y'^2,y'^2)$$

It can be noticed, from Equation 2.43, that the substitute field for the membrane strain ($\epsilon_{mx'x'}$) should be linear in (x′) direction and quadratic in (y′) direction. Similarly, the substitute field for the membrane strain ($\epsilon_{my'y'}$) should be quadratic in (x′) direction and linear in (y′) direction. However, the substitute field for the membrane strain ($\epsilon_{mx'y'}$) should be quadratic in both (x′) and (y′) directions. Higher order components of the membrane strain terms were considered of negligible effect on the substitute membrane strain fields. Therefore, the substitute fields for the incremental membrane strains of the Green-Lagrange strain tensor (${}_0\Delta\bar{\epsilon}_{mx'x'}$, ${}_0\Delta\bar{\epsilon}_{my'y'}$ and ${}_0\Delta\bar{\epsilon}_{mx'y'}$) can be interpolated as follows:

$$\begin{aligned}
{}_0\Delta\bar{\epsilon}_{mx'x'} &= \sum_{i=1}^{3}\sum_{j=1}^{2} \phi^{ij}(\xi,\eta)\ {}_0\Delta\epsilon^{ij}_{mx'x'} \\
{}_0\Delta\bar{\epsilon}_{my'y'} &= \sum_{i=1}^{3}\sum_{j=1}^{2} \psi^{ij}(\xi,\eta)\ {}_0\Delta\epsilon^{ij}_{my'y'} \\
{}_0\Delta\bar{\epsilon}_{mx'y'} &= \tfrac{1}{2}\sum_{i=1}^{3}\sum_{j=1}^{2} \phi^{ij}(\xi,\eta)\ {}_0\Delta\epsilon^{ij}_{mx'y'} \\
&\quad + \tfrac{1}{2}\sum_{i=1}^{3}\sum_{j=1}^{2} \psi^{ij}(\xi,\eta)\ {}_0\Delta\epsilon^{ij}_{mx'y'}
\end{aligned} \qquad (2.44)$$

where the interpolation functions (ϕ^{ij}) and (ψ^{ij}) are as defined in the previous section (section 2.4.1). The terms (${}_0\Delta\epsilon^{ij}_{mx'x'}$, ${}_0\Delta\epsilon^{ij}_{my'y'}$ and ${}_0\Delta\epsilon^{ij}_{mx'y'}$) are the incremental

membrane strains at the sampling points, evaluated directly from the displacement field in the local Cartesian coordinate system.

The locations of the sampling points for the membrane strains were determined by considering a shallow cylindrical shell element subjected to pure bending (Huang, 1987b), where the shell element should possess zero membrane strains in this situation. It was found that when the angle of the element rotation due to the pure bending condition is small enough, the locations of the sampling points would be the same as for the transverse shear strains. The locations of the sampling points are shown in Figure 2.5. The substitute incremental membrane strains ($_0\Delta\bar{\epsilon}_{mx'x'}$ and $\frac{1}{2}\,{}_0\Delta\bar{\epsilon}_{mx'y'}$) would be interpolated linearly in (ξ) direction and quadratically in (η) direction. On the other hand, the substitute incremental membrane strains ($_0\Delta\bar{\epsilon}_{my'y'}$ and $\frac{1}{2}\,{}_0\Delta\bar{\epsilon}_{mx'y'}$) would be interpolated quadratically in (ξ) direction and linearly in (η) direction.

2.5 Solution Techniques

The current finite element analysis employs two important solution techniques, which are discussed in this section; [a] the technique for solving the nonlinear equilibrium equation, and [b] the technique for implementing the assumed strain fields method through the nonlinear solution.

2.5.1 Solving the Nonlinear Equilibrium Equation

Two sources of the nonlinear response were introduced in the current finite element analysis; the large deformation representation, and the elasto-plastic material representation. The Newton-Raphson technique was adopted for the incremental iterative procedure of the finite element solution (Bathe, 1982). In the Newton-Raphson technique, the solution for the general finite element equation (Equation 2.14) at the previous discrete time (T-ΔT) is assumed known and the solution at the current discrete time (T) is required, where (ΔT) is a suitably chosen time increment. As the tangent stiffness matrix [K_T] and the internal force vector (f) are not known at the current time (T), an iterative procedure should be followed to obtain the solution at time (T) as shown in Figure 2.6. In this iterative procedure, the tangent stiffness matrix [K_T] was updated at every solution iteration by updating the strain displacement matrix [B] and the stress-strain relationship matrix [D_{ep}]. The solution at the current time (T) would be achieved when the residual force vector (^TR - f) converges to zero. Otherwise, a displacement increment solution from the last iteration should be calculated and added to the total displacement vector, and the iterative procedure should be continued.

A displacement convergence criterion was used to accept the solution at the end of the finite element iterative procedure. The criterion required that the displacement increments resulting from a solution iteration to be within a prescribed tolerance of the total displacement increments for that particular solution step, i.e.:

$$\sqrt{\frac{\sum(\Delta d^{T,i})^2}{\sum(d^{T,i} - d^{T-\Delta T})^2}} \leq TOL \qquad (2.45)$$

where $(\Delta d^{T,i})$ is the displacement increment vector of the current solution iteration, $(d^{T,i})$ is the total displacement vector of the current solution iteration, and $(d^{T-\Delta T})$ is the displacement vector of the last converged solution step. The prescribed convergence tolerance (TOL) was generally chosen equal to 0.001.

The tangent stiffness matrix $[K_T]$ and the internal force vector (f) of the 9-node shell finite element were evaluated using the Gauss Quadrature integration scheme (Bathe, 1982). The number of the integration points in the mid-surface plane and through the thickness direction of the element was variable, depending on the type of the considered problem. However, a minimum integration scheme of 3x3x2 was considered, as it is the minimum recommended scheme for the 9-node shell element.

2.5.2 Implementation of the Assumed Strain Fields Method

As discussed in Sections 2.4.1 and 2.4.2, the method of "assumed transverse shear strain fields" had to be implemented in the natural coordinate system (ξ,η,ζ), while the method of "assumed membrane strain fields" had to be implemented in the local Cartesian coordinate system (x', y', z'). The iterative procedure of the finite element analysis made it necessary to implement the "assumed strain fields" method

on the components of the strain-displacement matrix [B] and the strain vector (ϵ) at every solution iteration. As [B] is usually calculated in the global Cartesian coordinate system (x, y, z) and (ϵ) is usually calculated in the local Cartesian coordinate system (x′, y′, z′), appropriate transformation matrices were established to perform the transformations between these two coordinate systems and the natural coordinate system (ξ,η,ζ). The required transformation matrices are given in Appendix B.

The procedure performed to modify the strain-displacement matrix [B] and the strain vector (ϵ) of the 9-node shell element, in a typical solution iteration, is explained in the following steps. Note that a subscript (s) denotes the transverse shear component of the variable, while a subscript (m) denotes the membrane component of the variable:

1. At the mid-surface of the element (ζ=0), [B_s] and [B_m] were calculated at the sampling points in the global (x, y) directions, and (ϵ_s) and (ϵ_m) were calculated at the sampling points in the local (x′, y′) directions. The transverse shear components [B_s] and (ϵ_s) were then transformed to the natural (ξ, η) directions, while the membrane component [B_m] was transformed to the local (x′, y′) directions.

2. The membrane component [B_m] was calculated at the Gaussian integration points in the mid-surface (ζ=0) in the global (x, y) directions, then transformed to the local (x′, y′) directions. The membrane strain (ϵ_m) was calculated directly at the same integration points in the local (x′, y′) directions.

3. Using the interpolation functions in Equations 2.40 and 2.44, the substitute transverse shear and membrane fields for [B] and (ϵ) from step (1) were interpolated from the sampling points to the Gaussian integration points in the mid-surface (ζ=0), to give the assumed transverse shear components $[\bar{B}_s]$ and $(\bar{\epsilon}_s)$, and the assumed membrane components $[\bar{B}_m]$ and $(\bar{\epsilon}_m)$.

4. By looping over the Gaussian integration points in the thickness direction of the element (variable ζ), the assumed transverse shear and membrane components in step (3) were implemented in [B] and (ϵ) as follows:

4.(a) The matrix [B] was first calculated in the global (x, y) directions. [B] was transformed to the natural (ξ, η) directions, and its original transverse shear component $[B_s]$ was replaced by the assumed component $[\bar{B}_s]$ from step (3).

4.(b) The matrix [B] was then transformed to the local (x′, y′) directions, and the membrane component $[B_m]$ from step (2) was deducted, while the assumed membrane component $[\bar{B}_m]$ from step (3) was added. [B] was transformed back to the global (x, y) directions.

4.(c) The vector (ϵ) was first calculated in the local (x′, y′) directions. (ϵ) was transformed to the natural (ξ, η) directions, and its original transverse shear component (ϵ_s) was replaced by the assumed component $(\bar{\epsilon}_s)$ from step (3).

4.(d) The vector (ϵ) was then transformed back to the local (x′, y′)

directions, and the membrane component (ϵ_m) from step (2) was deducted, while the assumed membrane component ($\bar{\epsilon}_m$) from step (3) was added. No transformation was done afterwards.

2.6 Verification Problems for the Assumed Strain Shell Element

A set of bench mark problems were chosen to test the efficiency and accuracy of the 9-node degenerated assumed strain shell element. The bench mark problems cover the large deformation, and the elasto-plastic, nonlinear behaviour for a range of very thin to moderately thick plate and shell structures. In all these problems, the stiffness matrix of the element was evaluated using a 3x3x2 Gauss Quadrature integration scheme.

Problem (1) Large Deflection of an Elastic Thin Plate Under Uniform Pressure

A square clamped plate subjected to a uniformly increasing transverse pressure was analyzed using the assumed strain shell finite element. The plate was clamped in the in-plane and the transverse directions. The material of the plate was considered to be isotropic and elastic. The configuration of the plate and its elastic properties are shown in Figure 2.7. These conditions and values correspond to the theoretical problem considered by Way (1938). The plate had a width-to-thickness ratio (L/t) of 500, which puts it in the category of extremely thin structures. Only one quarter of the plate was considered in the analysis due to the symmetry of the geometry and

the loading. This quarter plate was modelled using 3x3 (total of nine) assumed strain shell finite elements.

The deflection of the plate at its central point was plotted against the uniform pressure in Figure 2.7. The load-deflection behaviour obtained using the assumed strain shell element, over 20 load increments, was compared to; [a] the behaviour obtained using the basic (original) degenerated shell element, prior to the application of the assumed strain fields method, and [b] the nonlinear theoretical solution given by Way (1938). The nonlinear theoretical solution was based on the "classical Rayleigh-Ritz" approach. From the comparison, it can be noticed that the load-deflection behaviour based on the assumed strain shell element has good agreement with the theoretical solution. This behaviour indicates that the element is not affected by the locking problem, even in a case of an extremely thin structure. The behaviour of the original degenerated shell element is over stiffened at high load levels, which clearly indicates that it is affected by the locking problem.

Problem (2) Large Deflection of an Elastic Thin Plate Under Concentrated Load

An elastic square plate subjected to a concentrated load was analyzed using the assumed strain shell finite element. The plate had two opposite edges clamped in the in-plane and the transverse directions, and the other two edges free as shown in Figure 2.8. The figure also shows the dimensions and the material properties of the plate. These conditions and values correspond to the experiment performed by Kawai

and Yoshimura (1969). The width-to-thickness ratio (L/t) of this plate is 202. A 4x2 mesh (total of eight elements) was used to model one half of the plate due to symmetry.

The deflections at two points (A and B) within the plate were monitored and plotted in Figure 2.8, where the load-deflection behaviour was obtained over 10 load increments. The figure compares the results of the assumed strain shell element and two other different finite element solutions; [a] the solution given by the basic (original) degenerated shell element, and [b] the solution given by the "selective integration" shell element. The selective integration element used 3x3x2 Gaussian integration points for the bending and membrane terms of the stiffness matrix, while used 2x2x2 points for the transverse shear terms. This integration scheme for the selective integration element was thought to help in overcoming the over stiff solution of thin structures by under-integrating the troublesome transverse shear strain terms. Figure 2.8 also shows the experimental data for the problem, given by Kawai and Yoshimura (1969). By first comparing the three finite element solutions to each others, particularly at the highest load level, it can be noticed that the solution obtained using the assumed strain shell element shows about 25% extra displacement over the original shell element, and about 9% extra displacement over the selective integration shell element. When the experimental data is considered, it can be concluded that the solution obtained using the assumed strain shell element agrees very well with most of the experimental data.

Problem (3) Deflection of an Elastic Clamped Cylindrical Panel Under Uniform Pressure

An elastic fully clamped cylindrical panel, subjected to a uniformly increasing normal pressure, was analyzed using the assumed strain shell finite element. The dimensions of the panel are shown in Figure 2.9. These dimensions were the same as the dimensions considered by El Damatty (1995). The panel was considered a relatively thin structure as its length-to-thickness ratio (L/t) equals to 160. Only one quarter of the panel was considered in the analysis due to the double symmetry of the geometry and the loading. This quarter panel was modelled using 2x2 (total of four) assumed strain shell elements.

The relationship between the value of the uniform pressure and the central deflection of the panel, obtained using the assumed strain shell element over 15 load increments, is plotted in Figure 2.9. The figure also shows the results of the same relationship obtained by El Damatty (1995) using consistent subparametric triangular shell elements. The triangular shell element, developed by Koziey (1993) and El Damatty (1995), had 13 nodes and 54 active degrees of freedom. The displacements of this element had cubic interpolation functions, while the rotations had quadratic interpolation functions. The element also had special rotational degrees of freedom to obtain a quadratic variation of the transverse shear stress through the thickness of the shell. El Damatty (1995) used a mesh of eight and 32 triangular elements to model one quarter of the panel. He stated that both meshes gave the same results

shown for the pressure-deflection relationship. An excellent agreement can be noticed between the results of El Damatty and the results of the assumed strain shell element using only four elements. The results obtained using the "selective integration" shell element, described in Problem (2), is also shown in the same figure. A non-consistent behaviour is observed from the results of this element. The element shows stiff behaviour (locking) at the levels of low pressure, but started to soften considerably at the levels of high pressure. This behaviour can be attributed to the under-integration scheme used for the transverse shear strain terms of the stiffness matrix of the element. While the pressure is low, it is mainly transmitted to the edges as membrane forces due to the geometry of the cylindrical panel. However, as the pressure and the deflection increase, transverse shear forces generate and form a high transverse shear stiffness. This transverse shear stiffness is under-integrated incorrectly, so the softening behaviour of the element occurs.

Problem (4) Snap-Through Buckling of an Elastic Cylindrical Panel Under Concentrated Load

The cylindrical panel described in Problem (4) was analyzed again using the assumed strain shell finite element, but with different thickness, loading ,and boundary conditions. The panel was analyzed with a thickness of 12.7 mm under a single concentrated load at the central point as shown in Figure 2.10. The two straight edges of the panel were simply supported, while the two curved edges were free.

These dimensions and boundary conditions were the same as those considered by Horrigome (1977) and Crisfield (1981). One quarter of the panel was modelled using 2x2 (total of four) shell elements. To be able to detect the snap-through buckling of the cylindrical panel, a "displacement control" algorithm was used. The displacement control algorithm enables passing the limiting point of the first ultimate load as shown in Figure 2.10. The algorithm is based on the unified constraint procedure, which enables different control methods to be implemented according to the definition of the control parameters (Kanok-Nukulchai, 1990). A description of the unified constraint algorithm is presented in Appendix C.

The equilibrium condition load of the cylindrical panel is plotted against the incremented central deflection in Figure 2.10. A total of 25 displacement increments were used, with an increment of one mm per solution step. The load-deflection relationship obtained using the assumed strain shell element was compared to the results given by Crisfield (1981). Crisfield modelled one quarter of the panel using 5x5 (total of 25) rectangular elements, with quadratic shape functions for the in-plane displacements, and quartic non-conforming shape functions for the out-of-plane displacements. Good agreement could be noticed between the current results and the results given by Crisfield (1981) for the whole range of the load-deflection relationship. The same figure also shows the results given by Horrigome (1977), up to the first ultimate load level only, who employed hybrid elements to model the cylindrical panel.

Problem (5) Post-Buckling of Elastic Plates Under Uniform Edge Displacement

The post-buckling behaviour of an elastic square simply supported plate was investigated using the assumed strain shell finite element. The configuration of the plate and its material properties are shown in Figure 2.11(a). The dimensions and the material properties were the same as considered in the nonlinear theoretical analysis of Yamaki (1959). The plate was subjected to a uniform edge displacement condition, as shown in the figure. Two cases of the geometry of the plate were considered; [a] a perfect flat plate, and [b] an imperfect plate with a double sine-wave curvature and a central imperfection of 0.1t (where t is the plate thickness). One quarter of the plate was modelled using 3x3 (total of nine) shell elements.

Figures 2.11(a) and (b) show the relationships between both the lateral central displacement and the axial shortening of the plates, versus the ratio of the average edge stress to the critical buckling stress (F / F_{cr}). The solutions obtained using the assumed strain shell element over 20 load increments were compared to the nonlinear theoretical solutions given by Yamaki (1959). Yamaki solved the fundamental equations for large deflections of thin plates by expressing both the initial and additional deflections as double Fourier series. The unknown coefficients of the series were obtained by applying the "Galerkin energy" method. Excellent agreement can be found between the present solutions and the nonlinear theoretical solutions. It is worth noting that the nonlinear theoretical solution in Figure 2.11(a) predicted similar behaviour for the flat and the imperfect plates far beyond local buckling, with slightly

more displacements for the flat plate. It was interesting to find that the present finite element solution had exactly the same prediction.

Problem (6) Elasto-plastic Buckling of Plates Under Uniform Edge Displacement

The elasto-plastic buckling of an imperfect simply supported rectangular plate was investigated using the assumed strain shell finite element. The dimensions of the plate are shown in Figure 2.12. The plate was subjected to a uniform edge displacement condition. The finite element modelling of the plate was performed as for the plate in Problem (5). The material of the plate had a yield strength (F_y) equals to 250 MPa. The dimensions and the material properties of the plate were the same as in the problem considered by Moxham (Crisfield, 1975). The material behaviour was modelled using a bi-linear elastic-perfectly plastic stress-strain relationship. The "displacement control" algorithm was used with 24 displacement increments to obtain the complete behaviour of the plate as shown in Figure 2.12. The solution obtained for the elasto-plastic behaviour of the plate using the assumed strain shell element was compared to the solution given by Moxham (Crisfield, 1975). Moxham used a "Ritz procedure" in which eight unknown coefficients were used to represent the plate deflections. Plasticity was included by means of a volume integration after dividing the plate into thickness layers. Excellent agreement can be noticed in the sub-ultimate and post-ultimate behaviour of the plate. It should be noted here that the plate experienced inelastic local buckling, as the magnitude of the critical buckling stress

(F_{cr}) was greater than the yield stress of the material. The inelastic buckling was also well predicted by using the assumed strain shell element.

Further verification problems of the efficiency of the assumed strain shell element in the elasto-plastic range are presented in Chapter Four, where the element was used to model cold-formed steel members in compression. The performance of the element was compared to the results of the laboratory tests presented in the same chapter, and the element proved to be very efficient as well.

2.7 Summary

The nonlinear incremental formulation of the 9-node degenerated shell finite element has been presented in this chapter. The formulation includes a "Total Lagrangian" procedure for the large deformation formulation, and a multi-linear isotropic strain hardening model for the elasto-plastic behaviour representing the cold-formed steel (CFS) material. The strain hardening model was based on the Huber-von Mises yield criterion and its associated flow rule. The multi-linear stress-strain relationship was considered to account for the gradual yielding and the strain hardening of the CFS material.

The problems associated with the use of the basic 9-node degenerated shell element, for the modelling of thin shell structures, were discussed. These problems are; [a] the "transverse shear and membrane locking", and [b] the "spurious zero energy modes". The kinematic formulation of the 9-node degenerated shell element

has been enhanced by using the method of "assumed transverse shear and membrane strain fields", in order to eliminate the above problems. Full numerical integration for the 9-node element can now be reliably employed, and always recommended, in order to eliminate the possibility of the generation of spurious zero energy modes. The implementation of the "assumed strain fields" method has been extended to cover the large deformation formulation of the 9-node shell element.

The solution technique for the incremental nonlinear finite element analysis, based on the iterative Newton-Raphson method, was presented. A displacement convergence criterion was set to accept the solution at the end of the finite element iterative procedure. Also, the procedure performed to modify the strain-displacement matrix [B] and the strain vector (ϵ) in the "assumed strain fields" method, in a typical solution iteration, was presented. Finally, a set of bench mark problems was used to verify the large deformation and the elasto-plastic behaviour of the new implemented 9-node assumed strain shell element. The deformation behaviour of the new shell element was compared to the behaviour of other shell elements, and the results of experimental investigations. Excellent performance was obtained from the new shell element for a wide range of very thin to moderately thick plate and shell structures.

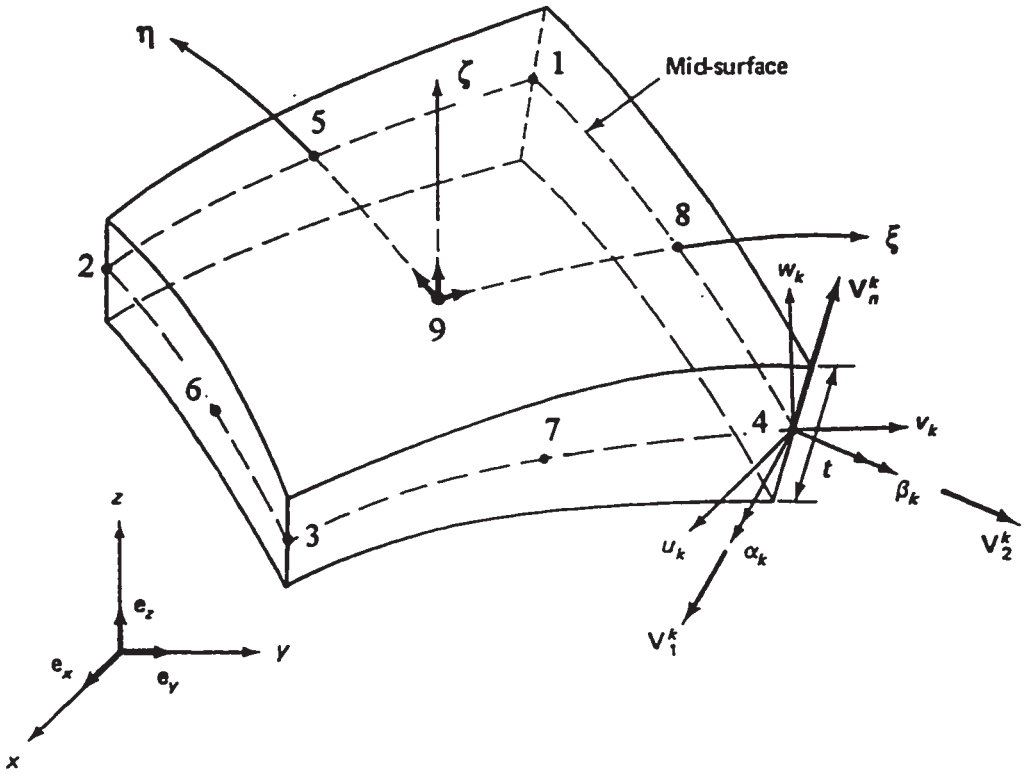

Figure 2.1 The 9-node degenerated shell finite element

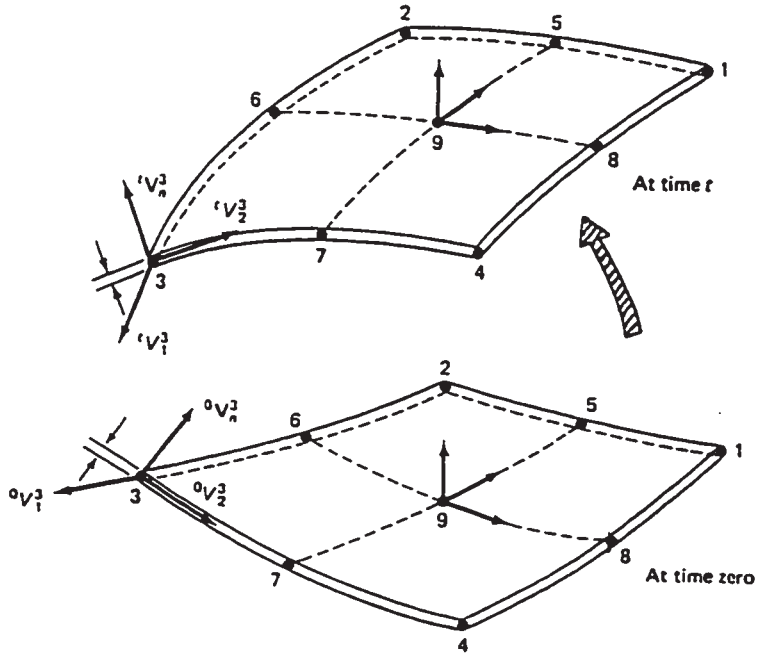

Figure 2.2 The 9-node shell element undergoing large deformations (Bathe, 1982)

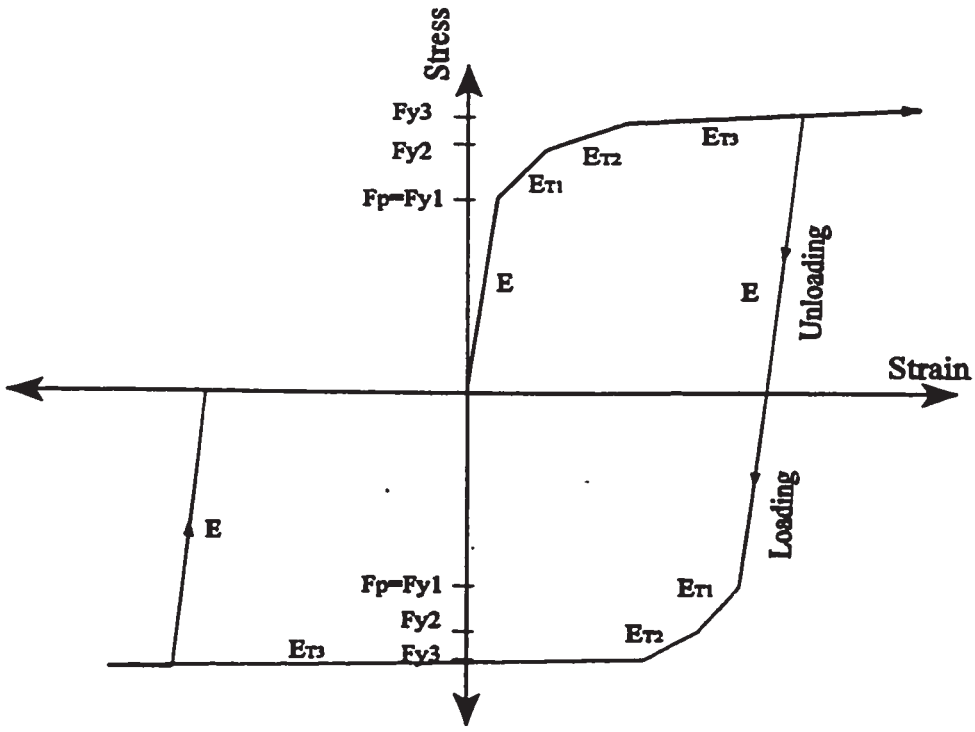

Figure 2.3 Elasto-plastic isotropic stress-strain relationship
with multi-linear strain hardening

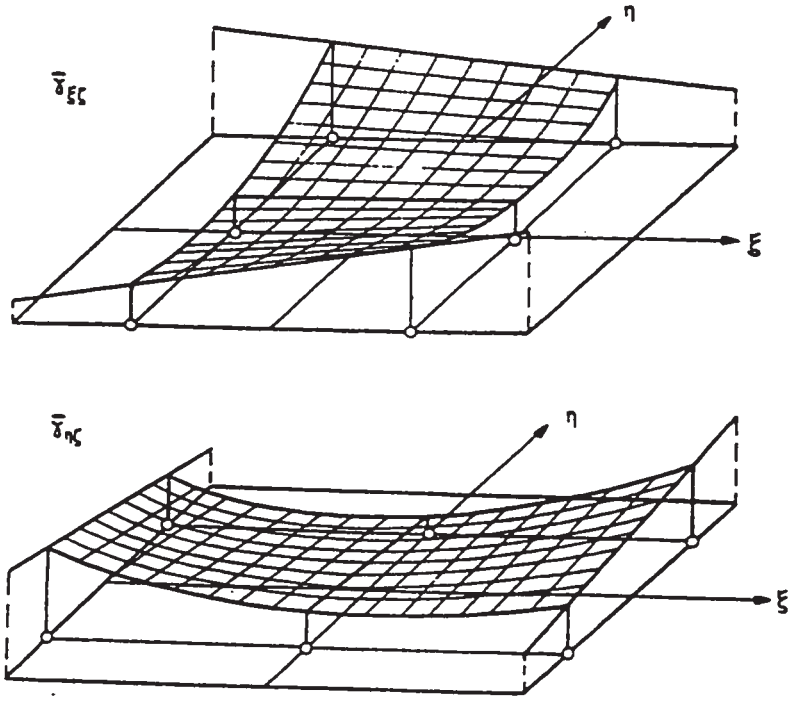

Figure 2.4 Interpolation functions for assumed strain fields (Huang and Hinton, 1986)

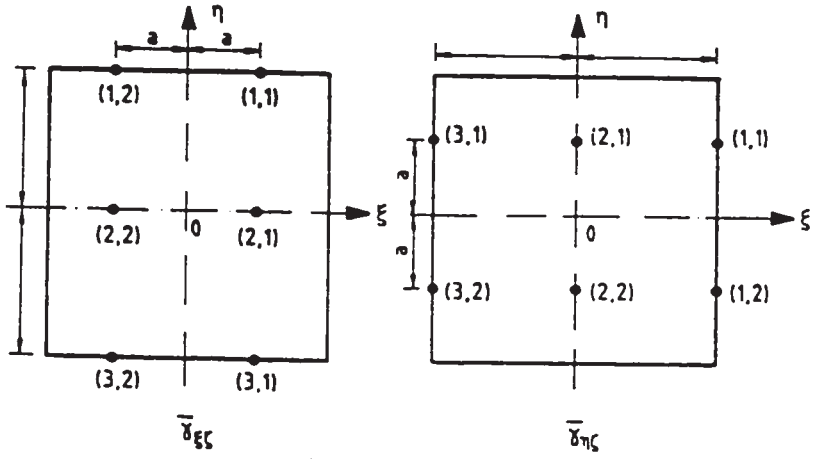

Figure 2.5 Sampling points for assumed strain fields (Huang, 1987a)

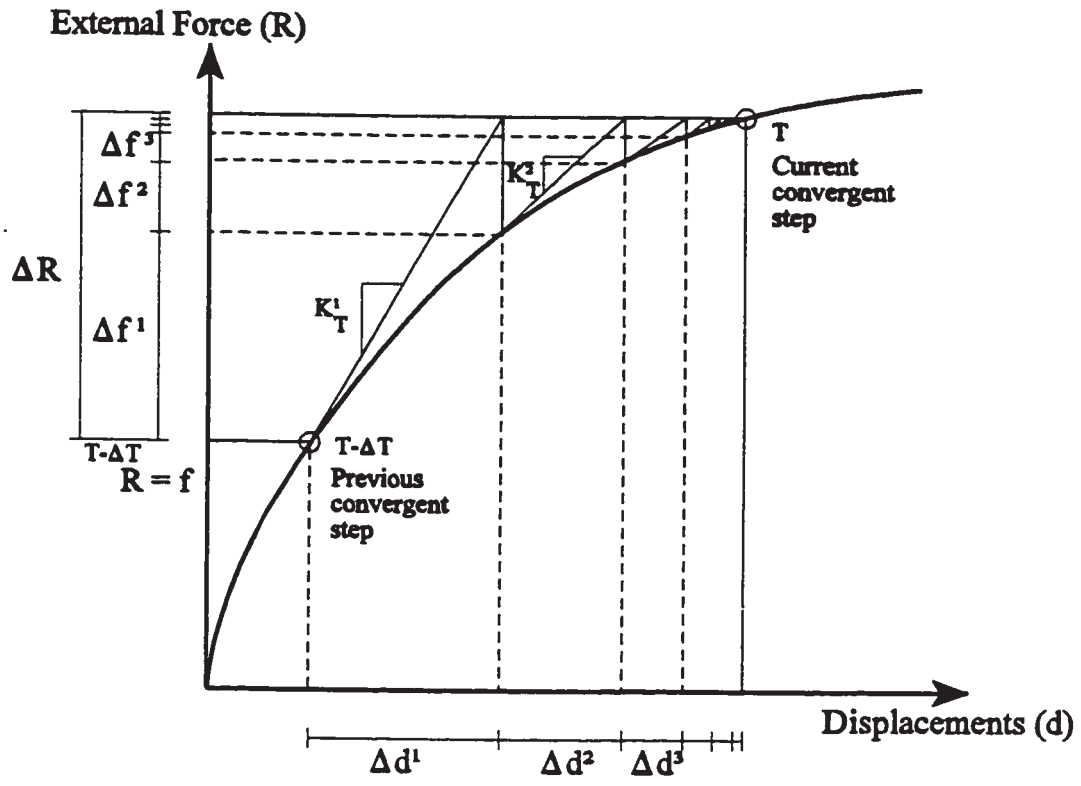

Figure 2.6 Iterative procedure for solving the nonlinear equilibrium equations

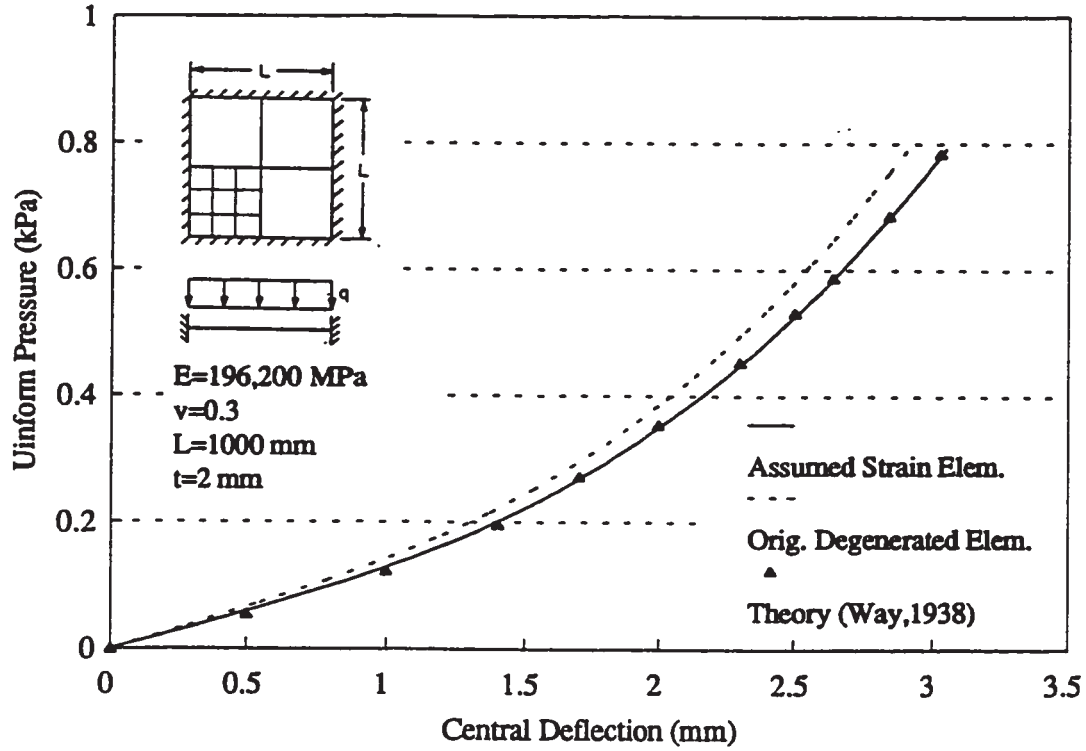

Figure 2.7 Large deflection of a thin plate under uniform pressure

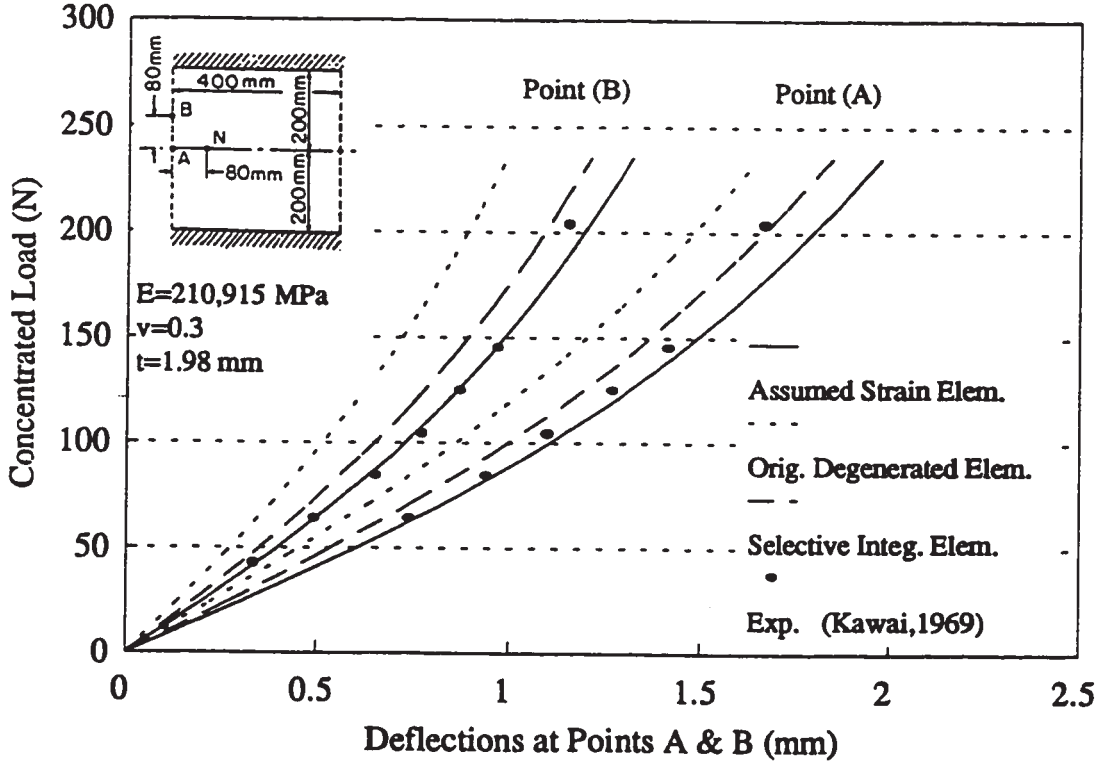

Figure 2.8 Large deflection of a thin plate under concentrated load

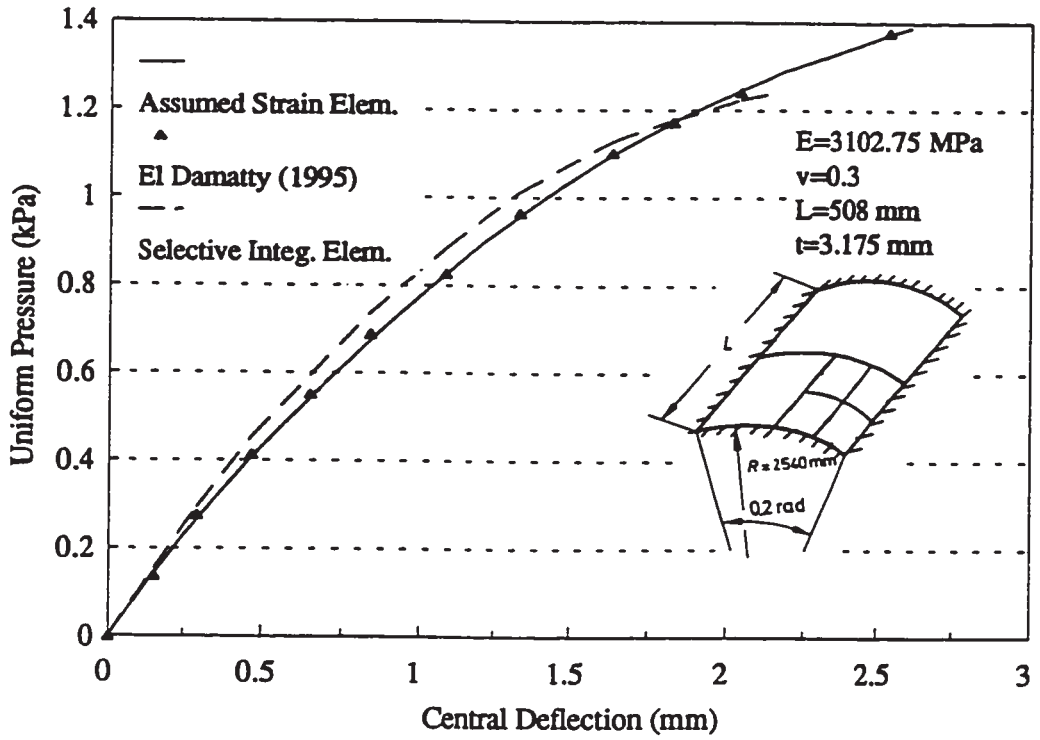

Figure 2.9 Deflection of a clamped cylindrical panel under uniform pressure

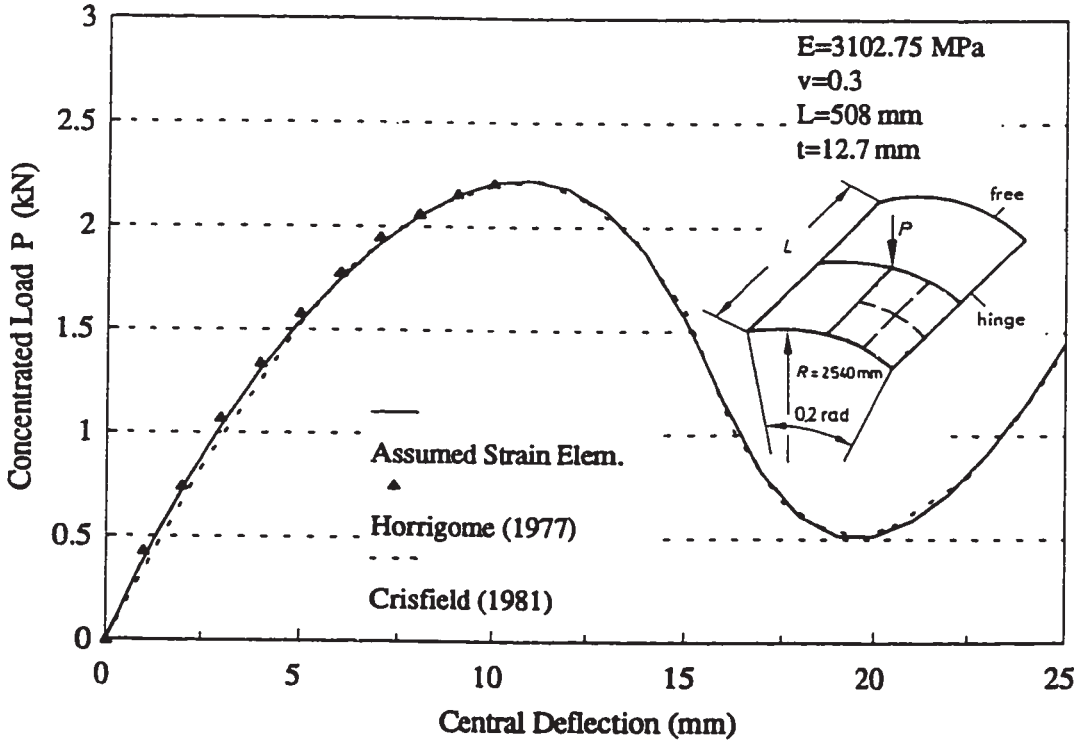

Figure 2.10 Snap-through buckling of a cylindrical panel under concentrated load

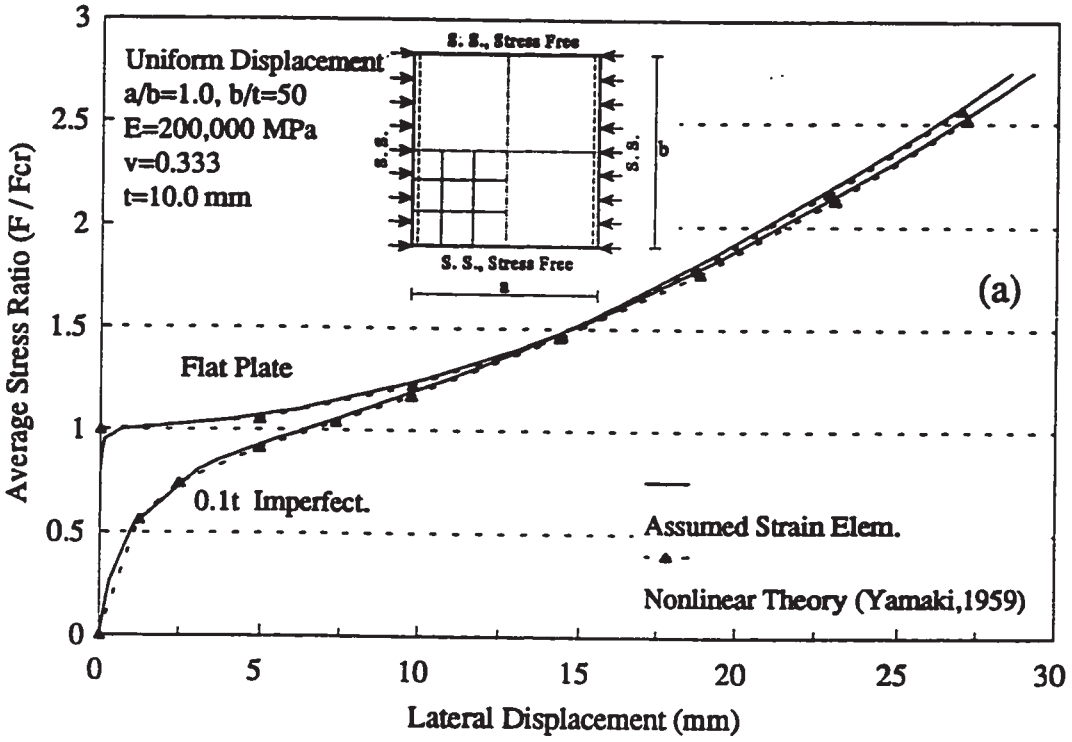

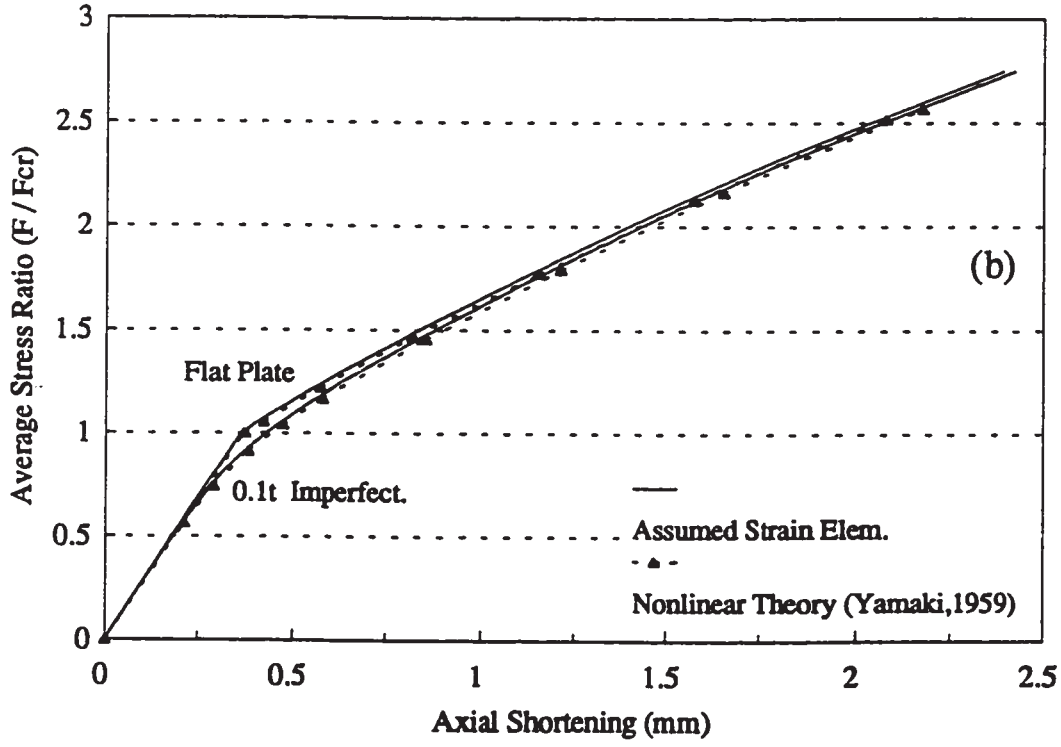

Figure 2.11 Post-buckling of a plate under uniform edge compression

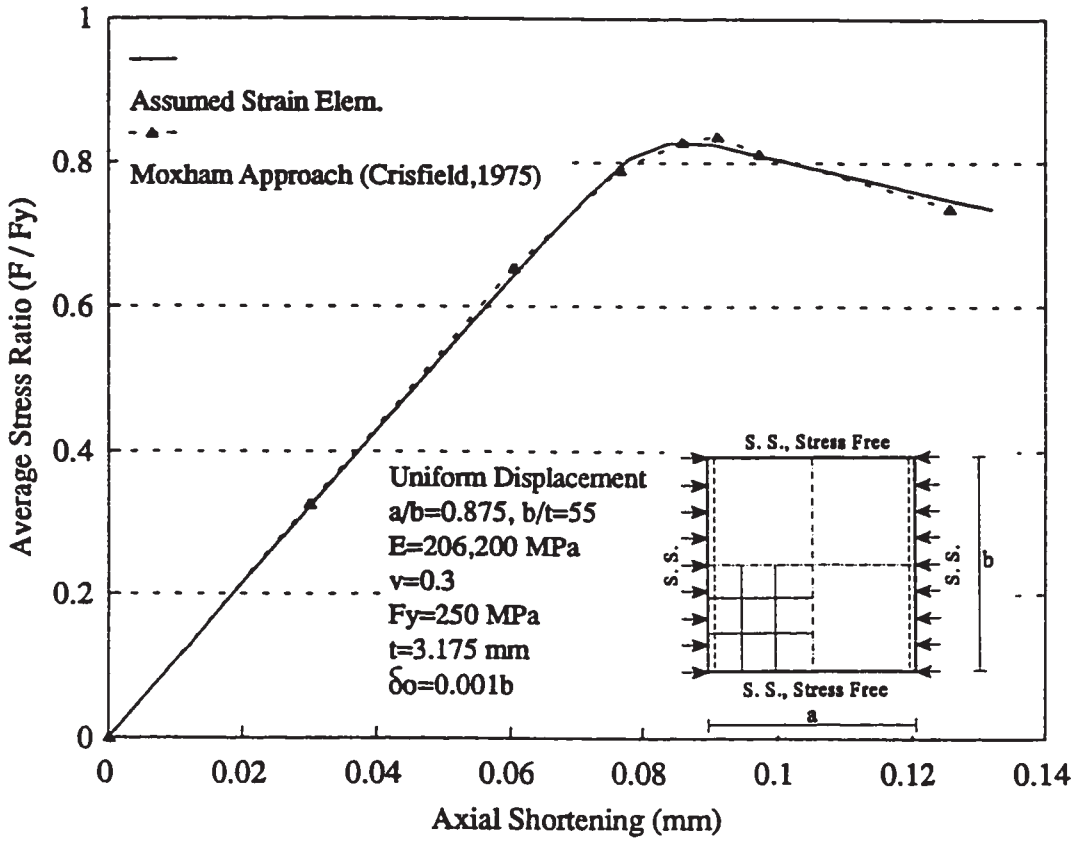

Figure 2.12 Elasto-plastic buckling of a plate under uniform edge compression

CHAPTER 3

MATERIAL PROPERTIES OF COLD-FORMED STEEL SECTIONS: EXPERIMENTAL EVALUATION

3.1 Introduction

The development of an appropriate analytical model to predict the behaviour of cold-formed steel (CFS) structural members requires a correct representation of the corresponding material characteristics. The steel characteristics that are of interest include; [a] the mechanical properties (uniaxial stress-strain behaviour, including values for the proportional limit, yield strength, ultimate strength, yielding plateau, and strain hardening), and [b] the residual stress state (initial pre-loading state of stress).

The two well-known cold-forming methods, the cold-roll forming and the press-brake forming, are expected to induce substantial changes in the characteristics of the CFS material, as compared to the virgin sheet steel. Large deformations are expected to occur in the section due to the cold bending operation. The deformations expected at the flat parts of the section may be elastic deformations, however, the deformations expected at the corner parts are essentially plastic deformations. Once the cold bending operation is completed and the formed section is released, the elastic deformations at flat parts and the released elastic strains at corner parts can not

recover due to the shape restrictions. This behaviour results in the generation of trapped longitudinal, and transverse residual stresses in the section. Meanwhile, the unreleased plastic strains at corner parts result in significant changes in the mechanical properties of the material due to the "strain aging" phenomenon (Chajes et al., 1963). In general, the non-uniformity of the cold work applied to a CFS section results in different mechanical properties and different magnitudes of residual stresses across the section. Thus, in order to develop a suitable CFS material model, the distributions and magnitudes of these mechanical properties and residual stresses need to be evaluated first through experimental tests.

In this chapter, the results of two series of experimental investigations to evaluate the mechanical properties, and the residual stresses of CFS sections are reported. The investigations were performed on CFS channel sections manufactured using the cold-roll forming method. Two different zinc-coated lipped channel sections of steel A 446/A 446M (ASTM, 1994a) were considered in the study. The first section was a 203 mm (8 in.) deep, 1.91 mm (0.075 in.-14 gauge) thick, Grade D steel with a minimum specified yield strength of 345 MPa. The second section was a 101.5 mm (4 in.) deep, 1.22 mm (0.048 in.-18 gauge) thick, Grade A steel with a minimum specified yield strength of 228 MPa. Tensile coupon tests were used to evaluate the mechanical properties at different positions of the channel sections. Electrical resistance strain gauges with an "Electrical Discharge Machining" cutting technique were used to establish the magnitudes and distributions of residual stresses

within the channel sections. The techniques used to idealize the variations of the mechanical properties and the residual stresses of CFS channel sections are also presented.

3.2 Tensile Coupon Tests

The mechanical properties of cold-formed steel (CFS) channel sections were evaluated based on a total of 41 tensile coupons. The coupons were cut along the longitudinal direction of the two channel sections. The exact positions of the coupons in the web, flanges, corners, and lips of the sections are shown in Figure 3.1. For each position, a minimum of two coupons were tested.

3.2.1 Tensile Coupons

The tensile coupons consisted of [a] 13 standard flat coupons (positions A-4, A-8, A-9, B-4, and B-8, length 200 mm, width 12.5 mm), [b] 19 non-standard flat coupons (positions A-1, A-3, A-5, A-7, B-1, B-3, B-5, and B-7, length 200 mm, width 6.25 mm), and [c] 9 non-standard curved coupons (positions A-2, A-6, B-2, and B-6, length 300 mm, corner width). The standard flat coupons were cut from flat parts of the sections, and dimensioned according to the guidelines provided by the ASTM Standards A370-92, "Standard Test Methods and Definitions for Mechanical Testing of Steel Products", (ASTM, 1994b) for sheet-type materials. The non-standard flat coupon were cut from near-to-corner parts of the sections. These

coupons had the same dimensions as the standard coupons except of the narrower width within the gage length and the grip section. The narrower width was chosen to obtain coupons that are as close as possible to the corners of the tested sections. The non-standard curved coupons were cut from corner parts of the sections. These coupons were dimensioned longer than the standard coupons to minimize the bending effects at the centre of the specimen during testing. The width of a curved coupon included the complete corner area at its position. The grip sections of all the curved coupons were not flattened to keep the centre of the applied tensile force during the test aligned with the centre of the specimen within the gage length.

3.2.2 Test Procedure

The tensile coupons were tested in a 250-kN capacity MTS (Material Test System) machine. The MTS machine had a maximum voltage output of 10 volts for both the load and the strain readings, with a readability of 0.004 volts. A load range of 10% (load capacity of 25 kN) was adopted for the test. The coupons were mounted in the testing machine using the gripping devices and aligned with respect to the vertical axis of the machine. The axial load was then applied at a constant rate of 3.0 mm/min. A calibrated extensometer of 50.0 mm gage length was attached to the centre of the tensile coupons, to measure the axial elongation of the coupons during the test. A strain range of 10% (maximum readable strain of 0.1) was adopted during the initial part of the test. Beyond an equivalent strain limit of 0.02, the strain

range was increased to 50% (maximum readable strain of 0.5), in order to monitor the subsequent behaviour of the coupons up to failure. This change of the strain range during the test affected only the recorded numerical values of the elongation and did not affect the continuity of the test itself. The voltage readings of both the axial load and the axial elongation during the test were recorded using a two-channel data acquisition system. A real time display of the load-elongation relationship during the test was monitored by connecting a personal computer with a "Lab-Tech Notebook" computer software to the data acquisition system.

3.2.3 Test Results

As the calibrated extensometer was attached to the centre of the tensile coupons during the test, it was desirable to have the failure within the gage length of the extensometer. All the standard flat coupons failed within the extensometer gage length, well away from the grips of the testing machine. Most of the non-standard flat and curved coupons also failed within the gage length. However, three non-standard flat coupons and two non-standard curved coupons failed in the reduced section but outside the gage length. Figure 3.2 shows a sample of the typical failed coupons, where the failure occurred within the gage length.

The stress-strain relationship of a tensile coupon was derived from the load-elongation relationship using its initial cross-sectional area and the gage length. The initial cross-sectional area of a flat coupon was determined by measuring the actual

minimum width, and the minimum metal thickness within the gage length, to the nearest 0.01 mm using a digital micrometer. The minimum base metal thickness was determined by excluding the average thickness of the zinc coating layer. The thickness of the coating layer was determined using the provision A 90/A 90M "Standard Test Method for Weight of Coating on Iron and Steel Articles with Zinc or Zinc-Alloy Coatings" of the American testing standards (ASTM, 1994c). The average thickness of the zinc coating layer was found to be 0.04 mm and 0.031 mm for sections (A) and (B), respectively. The initial cross-sectional area of a curved coupon was determined from the geometry of the corner part of the section, knowing the base metal thickness and the manufacturer inside and outside specified radii.

3.2.3.1 Test Results for Section (A)

The results of the stress-strain relationships for different positions across the test section (A) (203 x 1.91 mm) are shown in Figures 3.3 through 3.6. As indicated before, a minimum of two coupons were tested at each position. In these figures, graph (a) shows the overall stress-strain curves of the coupons up to failure, and graph (b) shows the initial portion of the stress-strain behaviour up to a strain of 0.02. The stress-strain curve of only one coupon for each of the flat positions (A-4, A-8, and A-9) is presented in Figure 3.3, as no major differences were found between the results of the typical tensile coupons at these three positions. The stress-strain curves of two coupons are presented for each of the other positions in Figures 3.4 through

3.6. However, only one coupon is presented for position A-3, as the second coupon failed just outside the gage length.

Table 3.1 summarizes the average results for the mechanical properties of the test section (A). The yield strength (F_y) was determined based on the 0.2% offset strength method. This is due to the fact that all the tensile coupons experienced a gradual yielding, as opposed to the sharp yielding associated with mild-carbon structural steel. The proportional limit (F_p), which is the starting point of gradual yielding, was determined using the 0.01% offset strength method. The calculated modulus of elasticity (E) at all the tested positions (except for position A-6) was generally less than of 203 x 10^3 MPa, the value recommended by both the American and Canadian design specifications (AISI, 1991 and CSA, 1994) for the design of CFS structures.

The stress-strain curves of all the flat and next-to-corner coupons (except of position A-7) typically have a yielding plateau following the gradual yielding and then a strain hardening up to the ultimate strength (F_u). The coupons representing positions A-1 and A-7 have no yielding plateau, and the gradual yielding is followed directly by the strain hardening. The flat coupons of positions A-4, A-8, and A-9 have approximately the same stress-strain relationship with an equal yield strength of 385 MPa, and an equal ultimate strength of 475 MPa. The lip coupons of position A-1 and the next-to-corner coupons of positions A-3, and A-5 show an increase in the yield and ultimate strengths between 1% and 5% compared to the strengths of the flat

coupons. The coupons of position A-7 show an equivalent increase in the ultimate strength, but suffer a loss of 2% in the yield strength. The total elongation of the lip and the next-to-corner coupons are generally less than that for the flat coupons.

The stress-strain curves of the corner coupons (positions A-2 and A-6) do not show the yielding plateau and the strain hardening behaviour. Instead, the gradual yielding extends sharply up to the ultimate strength (F_u) at an equivalent strain of about 0.02 only. The total elongation of these coupons do not exceed a value of 9%. The increase in the yield strength of the corner coupons has a maximum value of 47% compared to the strength of the flat coupons. The equivalent increase in the ultimate strength of corner coupons has a maximum value of only 29%.

Figure 3.7 shows the variation of the recorded yield and ultimate strengths across the test section (A). It can be observed from the figure that the increase in both the yield strength (F_y) and the ultimate strength (F_u) is concentrated at and around the corner areas of the section. The percentage increase in (F_y) is generally more pronounced than that of (F_u). As a result, the yield strength value becomes close to the ultimate strength value at the corner areas. The flat areas in the web and the flanges of the section have equivalent values of (F_y) and (F_u). The experimental yield strength is noticed to be higher than the minimum specified yield strength (345 MPa) across the section.

3.2.3.2 Test Results for Section (B)

The results of the stress-strain relationships for different positions across the test section (B) (101.5 x 1.22 mm) are shown in Figures 3.8 through 3.12. The results of two coupons are presented for each position, except for position B-1 where the second coupon failed just outside the gage length, and for position B-6 where the second coupon failed away from the gage length.

Table 3.2 summarizes the average results for the mechanical properties of the test section (B). The yielding behaviour varies from a position to another across the test section (B) as shown in Figures 3.8 through 3.12 (graph (b)). All the lip coupons of position B-1 and the next-to-corner coupons of positions B-5 and B-7 experienced a sharp yielding behaviour. As a result, the yield strength (F_y) for these positions was calculated as the average yield stress of the yielding plateau. The corner coupons of positions B-2 and B-6 experienced a gradual yielding behaviour. The yield strength (F_y) for these positions was determined based on the 0.2% offset strength method as for the test section (A). The yielding behaviour for the flat coupons of positions B-4 and B-8 and the next-to-corner coupons of position B-3 could not be clearly defined, as one tested coupon showed a sharp yielding and the other tested coupon showed a gradual yielding. The yield strength (F_y) for these positions was determined based on the strength of the sharp yielding coupon. The calculated modulus of elasticity (E) at all positions (except for position B-6) was also less than the recommended design value (AISI, 1991 and CSA, 1994) of 203×10^3 MPa.

The stress-strain curves of the lip, flat, and next-to-corner coupons show a yielding plateau followed by a strain hardening up to the ultimate strength (F_u). The flat coupons have an average total elongation of 36%, while the next-to-corner coupons have an average total elongation of 32%. The yielding plateau of the lip coupons of position B-1 is very short and the total elongation is only about 22%. The flat coupons of positions B-4 and B-8 have approximately the same stress-strain relationship and an equal ultimate strength (F_u) of 362 MPa. The recorded yield strengths (F_y) of positions B-4 and B-8 are also very close (320 MPa and 318 MPa, respectively). The lip coupons of position B-1 show an increase in the yield and ultimate strengths of 12% and 13%, respectively, compared to the strengths of the flat coupons. The next-to-corner coupons of positions B-3, B-5, and B-7 show an equivalent increase in the yield and ultimate strengths up to 6% only.

The stress-strain curves of the corner coupons (positions B-2 and B-6) show a similar behaviour as the corner coupons of the test section (A). The gradual yielding behaviour of B-2 and B-6 extends up to the ultimate strength at an equivalent strain of about 0.06. the total elongation of these coupons has a value of 12%. The increase in the yield and ultimate strengths of the corner coupons ranges between 23% and 26%.

Figure 3.13 shows the variation of the recorded yield and ultimate strengths across the test section (B). It can be observed from the figure that the primary increase in both the yield strength (F_y) and the ultimate strength (F_u) is concentrated

at and around the corner areas of the section, including the lip area. However, the flat areas of the web and the flanges also have some increase in (F_y) and (F_u). The percentage increase in (F_y) was found to be generally equivalent to that of (F_u). The experimental yield strength is noticed to be considerably higher than the minimum specified yield strength (228 MPa) across the section.

3.2.4 Significant Observations

The following observations can be drawn from the test results of sections (A) and (B):

[a] The results for the flat web and flange areas showed that the tensile coupons from flat parts have approximately the same stress-strain relationship, yield strength, ultimate strength, and elongation. Although actual data about the properties of the virgin steel sheet is not available, this behaviour of the flat parts suggests that the cold-roll forming operation has little effect on the flat parts of the section. Therefore, virgin sheet properties may be used as the corresponding properties of the flat parts of the section.

[b] The substantial changes in the material behaviour were noticed at and around the corner parts of the sections, as a result of the large plastic deformations of the cold forming operation. A considerable increase in the yield and ultimate strengths (F_y and F_u) occurred at the corner parts. This increase was accompanied by a severe decrease in the total elongation, and a disappearance of the yielding plateau

and the strain hardening ranges.

[c] The changes in the material properties adjacent to the corner parts (represented by the next-to-corner coupons) were not as high as for the corner parts, but generally higher than flat parts.

[d] The steel grade of the test sections is found to have an effect on the percentage increase in (F_y) at the corner parts of the test sections. This percentage for the test section (A) was almost double that of the test section (B). This indicates that as the specified yield strength (F_y) increases, the percentage increase in (F_y) at the corner parts also increases.

[e] The steel grade is also found to have an effect on the yielding behaviour of the tensile coupons. While all the coupons of the test section (A) (Grade D steel) experienced a gradual yielding behaviour, only the corner coupons of the test section (B) (Grade A steel), experienced the same behaviour. All the other coupons of section (B) showed either a sharp yielding or a non-defined yielding behaviour.

[f] Using the 0.2% offset method to determine the yield strength (F_y) can be generally applied for the tensile coupons experiencing both gradual yielding and sharp yielding. It was noticed that using this method for sharp yielding coupons of section (B) would give the same results as presented in Table 3.2.

3.3 Model for the Variation of Yield Strength

The results of the tensile coupon tests show that the significant variations of

the yield strength (F_y) in cold-formed steel (CFS) channel sections occur at the corner areas and at the flat areas adjacent to corners. These observations are comparable to the results given by Karren and Winter (1967) and Coetsee, et al. (1990). In order to incorporate these variations into an analytical model of the CFS material, it is proposed that a lipped channel CFS section, with a small (r/t) ratio of its rounded corners, to be divided into two zones; a corner zone and a flat zone. The corner zone is proposed to include all the four curved areas of the section, two equivalent flat areas on both sides of each curved area, and the two lips of the section. The flat zone includes the rest of the flat area of the web and flanges of the section. Each zone will be assigned appropriate, but different, mechanical properties. Figure 3.14 identifies the suggested corner zone, and the flat zone of a lipped channel section with small (r/t) ratio.

Based on the experimental results of the tensile coupons presented earlier, the yield strength of the flat zone (F_y) is proposed to be uniform, and represented by the value of the minimum specified yield strength of the steel grade used for the section. This means that no increase in (F_y) need to be considered in the flat zone of the section. The yield strength of the corner zone (F_{yc}) is, however, proposed to have higher value than the corresponding strength of the flat zone. Karren (1967) developed a semi-empirical model to predict the increase in the corner yield strength (ΔF_y) as follows:

$$\Delta F_y \left(\underline{\text{Corner Area}}\right) = \left[\frac{B_c}{(r/t)^m} - 1.0\right] F_y \qquad (3.1)$$

where,

$$B_c = 3.69 \left(\frac{F_u}{F_y}\right) - 0.819 \left(\frac{F_u}{F_y}\right)^2 - 1.79 \;, \quad m = 0.192 \left(\frac{F_u}{F_y}\right) - 0.068$$

The main parameters in Karren's model are the ultimate strength-to-yield strength ratio (F_u/F_y) of the virgin steel material, and the corner inside radius-to-sheet thickness ratio (r/t). This model is currently being used in the American LRFD Specification (AISI, 1991). Lind and Schroff (1975) proposed another model to predict the increase in the corner yield strength, and their model is currently included is the Canadian S136-94 Standard (CSA, 1994). This model suggests (ΔF_y) as follows:

$$\Delta F_y \left(\underline{\text{Corner Area}}\right) = (5t / 1.57r)\,(F_u - F_y) \qquad (3.2)$$

Both models can be used to predict the yield strength increase of the corner areas only, and are not valid for areas adjacent to corners, which showed increased yield strength as well. Therefore, as shown in Table 3.3, the current test results, as well as the results given by Karren and Winter (1967) for different shapes of roll-formed sections, were compared to Equations 3.1 and 3.2 to investigate which of the two models is more consistent with the test results. It was observed that the ratio between the average increase in the yield strengths (ΔF_y) measured within the corner zone and the increase predicted by Equation 3.1 ranges between 0.49 and 0.74, with an average

equal to 0.63. It was also observed that this ratio increases, approximately, with the decrease of the yield strength. As for Equation 3.2, the same ratio was observed to range between 0.57 and 1.05, and no trend is noticed with the increase of the yield strength. Hence, it is proposed to use Karren's model to predict the yield strength of the corner zone (F_{yc}), however, a factor of 0.6 is added to Equation 3.1 as follows:

$$\Delta F_y \text{ (Corner Zone)} = 0.60 \left[\frac{B_c}{(r/t)^m} - 1.0\right] F_y \qquad (3.3)$$

Figure 3.15 shows the proposed idealization for the distribution of the yield strength across the lipped channel section and the measured distribution given by the tensile coupon tests for both sections (A) and (B). The total area of increase of the yield strength can be defined in the figure as the area under the distribution of (F_y). It can be noticed that this area under the idealized distribution is equivalent to the area under the measured distribution. This equivalency further shows that the idealized yield strength distribution can represent the same total strength of the section as the real distribution. Moreover, the idealized distribution is simple and can be easily incorporated within an analytical material model for CFS channel sections.

3.4 Model for the Stress-Strain Relationship

The stress-strain curves, displayed in Figures 3.3 to 3.6 and 3.8 to 3.12, show that all the tensile coupons of the test section (A) (Grade D steel) and most of the

tensile coupons of the test section (B) (Grade A steel) experienced a gradual yielding behaviour with no definite yield point. Therefore, an idealized elasto-plastic stress-strain model with a multi-linear isotropic strain hardening rule is used to account for the gradual yielding behaviour. The idealized multi-linear stress-strain model (Figure 3.16) is based on the Huber-von Mises elasto-plastic stress-strain model (Chen and Han, 1988), and its mathematical formulation has been presented in Chapter Two. In the idealized model, the elastic stress-strain behaviour is represented by an initial linear segment with a slope equal to the modulus of elasticity (E) up to a proportional strength limit (F_p) which is equivalent to the initial point of the material non-linearity. The gradual yielding behaviour is idealized using a bi-linear representation between the proportional limit (F_p) and the yield strength (F_y) passing through an intermediate yielding strength (F_{ym}) as shown in Figure 3.16. This intermediate strength (F_{ym}) is taken as the half-way point strength between the proportional strength (F_p) and the yield strength (F_y). Two different tangent moduli (E_{T1} and E_{T2}) are defined for the bi-linear representation. The strain hardening behaviour is represented by a linear segment with a tangent moduli (E_{T3}). The limit strengths of the idealized stress-strain relationship (F_p, F_{ym}, and F_y) are different for the corner zone than that for the flat zone of the channel section according to the idealization of the variation of the yield strength for CFS channel sections presented in section 3.3. However, the test results indicate that the ratio (F_p / F_y) has a range between 0.66 and 0.88 for all the gradual yielding tensile coupons. A ratio of (F_p / F_y) equal to 0.75 is considered appropriate

for both the flat zone, and the corner zone of the section. The modulus of elasticity (E) is considered equal to 203,000 MPa, which is the value recommended in the North American design codes (CSA, 1994 and AISI, 1991). The proposed values for the tangent moduli (E_{T1}, E_{T2}, and E_{T3}) are 100,000 MPa, 20,000 MPa, and 1,000 MPa, respectively, which are the best approximations of the results of the tested tensile coupons.

3.5 Residual Stress Tests

The magnitudes and distributions of longitudinal and transverse residual surface strains at different positions of cold-formed steel (CFS) channel sections were investigated in the current study. The surface strains represent the trapped residual stresses in the sections. The surface strains were released by slicing the sections into strips using the method of Electrical Discharge Machining (EDM), and the strains were measured using electrical resistance strain gauges.

3.5.1 Electrical Discharge Machining Method

The Electrical Discharge machining (EDM) is a non-traditional machining process of metals using sparks (electrical discharges). The conventional EDM system is illustrated schematically in Figure 3.17. The sparks occur between the cutting tool (electrode) and the test specimen (workpiece) in an environment of a dielectric fluid. The cutting tool does not physically contact the test specimen. Instead, the dielectric

fluid creates a path for the sparks as the fluid becomes ionized between the tool and specimen. The initiation of the sparks occurs when a sufficient amount of voltage is applied across the machining gap, and the dielectric fluid becomes ionized to cause a flow of electric current between the cutting tool and the test specimen through the gap (Weller and Haavisto, 1984). The use of the EDM method for a CFS residual stress test is considered a relatively new technique, as most of the work done before was based on conventional saw cutting. The only reported test which used this method was performed by Weng and Pekoz (1990). The advantages of using the EDM method over the saw method are; [a] avoiding permanent deformations of the tested section, as excessive clamping is not needed, [b] avoiding vibrations during the cutting process, as there is no contact between the cutting tool and the test specimen, and [c] cutting is done under the surface of the dielectric fluid, where the fluid works as a coolant and also as an insulator between the tool and the specimen.

The EDM machine used in the current investigation was a knee-type, quill-head TQH-31 compact electrical discharge machine, manufactured by ELOX Corporation, Troy, Michigan. The TQH-31 machine works through three systems; a hydraulic system, an electrical system, and a coolant system. The quill-head of the machine has a vertical travel of 6" (152 mm) and can be manually or hydraulically operated. The workpan of the machine has a size of 42" length, 14" width, and 10" depth (approximately 1000 x 350 x 250 mm). The cutting tool was made of brass, as it is an excellent conduction material, and was shaped as a rectangular plate with

a thickness of 1 mm. Since the brass cutting tool erodes during the cutting process, the tool had to be changed after every 3 or 4 cuttings with a new one. A hydrocarbon oil was used as a dielectric fluid and was continuously circulated during the cutting process to flush away the removed material particles.

3.5.2 Preparation of Test Specimens and Data Acquisition

Two identical residual stress tests were performed for each of section (A) (203 x 1.91 mm) and section (B) (101.5 x 1.22 mm). The test specimens were saw-cut from long CFS columns away from the ends to exclude any end damage of the columns. The length of the specimens of sections (A) and (B) was 600 mm and 300 mm, respectively. The length of each specimen was approximately three times the width of the section to insure that the specimen be sufficiently long, so that it has the same residual stress pattern as a much longer column from the same stock (Column Research Council, 1976). The specimens were then prepared for mounting the strain gauges by removing the zinc coating layer at the positions of the gauges using a 50% solution of the hydrochloric acid. Fourteen strain gauges were mounted on each test specimen of section (A), and 12 strain gauges were mounted on each test specimen of section (B). The positions of the strain gauges on the specimens of sections (A) and (B) are shown in Figures 3.18(a) and 3.19(a), respectively. As shown in the figures, the strain gauges were mounted on both the inside and outside surfaces of the specimens at each position, except at the lip and at the adjacent corner where no

gauges were mounted on the inside surface as it was difficult to reach. All the strain gauges were of 5 mm length, and were mounted in the longitudinal direction of the section at the mid-length of the test specimen. One 5 mm rosette strain gauge was also mounted at position (8) of the second test specimen of section (A) in order to measure the released outside surface strains in the longitudinal, transverse, and 45° directions of the specimen. The strain gauges were glued to the test specimens according to the procedure provided by the manufacturing company. The gauges were then wired and coated with a thick layer of protective coating in order to prevent any damage during handling and cutting process.

The reading of released strain data was achieved by connecting the strain gauges of a single test specimen to a strain indicator (Model P-3500) through two switch and balance units (Model SB-1). The strain indicator had a range of ±20,000 $\mu\epsilon$ with a readability of 1 $\mu\epsilon$, and the switch and balance units had a resolution of less than 1 $\mu\epsilon$. Two switch and balance units were used as each unit had a capacity of 10 channels only. The units were connected in parallel, so either of them can be switched "open" to enable taking readings on the other unit.

3.5.3 Test Procedure

Once the preparation of each test specimen was completed, the specimen was placed inside the workpan of the TQH-31 machine and lightly clamped to the bed of the pan at its edges. The workpan was then filled with the hydrocarbon oil and the

brass cutting tool was mounted in its place. The reading of each strain gauge was initialized to zero using the switch and balance units.

The cutting sequence for the test specimens of sections (A) and (B) around the strain gauges is as shown in Figures 3.18(b) and 3.19(b), respectively. The specimen was supported underneath each cutting path to prevent any local deformations in the surrounding area of the cut. After the transverse cut paths (1) and (2) were completed, the outer parts of the specimen were removed from the workpan and the longitudinal cutting sequence was done on the middle part only (75 mm). This procedure insured that any released membrane strains during the cut paths (1) and (2) were also taken into consideration. When the whole cutting sequence was completed, the cut strips were taken out of the workpan and were left for about three minutes in order to cool down to the normal room temperature. The readings of all the strain gauges were then recorded using the strain indicator. Figure 3.20(a), (b) show a test in progress for section (A) and the sliced strips of the specimen after the test was completed.

3.5.4 Test Results

The measured values of the released surface strains for section (A) and section (B) are given in Tables 3.4 and 3.5, respectively. All the strain values shown are longitudinal surface strains, except for position (8) in Table 3.4 where the surface strains in three directions are reported for the second test specimen. The unreported

data at positions (1) and (2) in Tables 3.4 and 3.5 represent locations where strain gauges could not be attached. It has to be mentioned that a measured negative surface strain corresponds to a positive (tensile) residual surface stress, and a measured positive surface strain corresponds to a negative (compression) residual surface stress. Tables 3.4 and 3.5 also show the ratios between the measured strains and the yield strains of the materials of sections (A) and (B). The yield strains were calculated from the flat area yield strengths presented in section 3.2.3 using a modulus of elasticity (E) equal to 203,000 MPa. The variations of the measured longitudinal surface strains are also shown in a graphical form for one-half of sections (A) and (B) in Figures 3.21(b) and 3.22(b), respectively.

The results of the measured surface strains of CFS channel sections indicate that surface residual stresses exist in these sections due to the cold roll-forming operation. Tensile residual stresses are found on the outside surface of the channel sections, and compression residual stresses are found on the inside surface of the channel sections. This behaviour is consistent with all the tested specimens of sections (A) and (B). The magnitudes of the surface residual stresses, which corresponds to the magnitudes of the released strains, vary across the same section. The variation of the ratio between the measured strains and the yield strain of the material ranges between 2% and 72% for section (A), and between 5% and 45% for section (B). The major effects of the forming operation, at the location of the highest magnitudes of residual stresses, is found at the web area next to the curved corner

(position 6) for all the tested specimens. The lip area (position 1) and the flange-lip corner area (position 2) also show relatively high magnitudes of residual stresses. The web-flange corner area (position 5) shows low magnitudes of residual stresses compared to the flange-lip corner area (position 2). This behaviour may be attributed to the forming technique and the arrangement of the forming rolls. Unfortunately, information about the actual forming technique and the arrangement of rolls used by the manufacturer is not available. The minor effects of the forming operation is found at the flanges of the sections (positions 3 and 4) for all the tested sections.

An important phenomenon observed from the test results is that the magnitudes of longitudinal residual stresses on the outside surface of a section at every location are very close to the corresponding magnitudes on the inside surface, however with an opposite sign. The same phenomenon was observed in the tests performed by Weng and Pekoz (1990). Also, the theoretical residual stress model, presented by Alexander (1959) and Korol (1971), concluded that the longitudinal residual stress distribution through the thickness of a curved profile reverses sign through the thickness, and has a zero magnitude at the centre line of the profile (see Figure 1.4 of Chapter One).

The residual stresses in both the longitudinal and transverse directions were investigated in the current study at one location on the web plate of section (A). The principal strains at this location were calculated using stress analysis procedures (Dally and Riley, 1978) and were found to be -286.5 $\mu\epsilon$ and +13.5 $\mu\epsilon$, respectively.

It can be noticed that the difference between the first principal strain and the recorded longitudinal strain (-284 $\mu\epsilon$) is less than 1%. This suggests that the longitudinal direction of a CFS section is the principal residual stress direction. The longitudinal residual stress (F_{rl}) and the transverse residual stress (F_{rt}) at the same location can be calculated, for a plane stress condition, as follows :

$$F_{rl} = \frac{E}{(1 - \nu^2)} (\epsilon_l + \nu \epsilon_t) = -62.6 \text{ MPa} \quad (3.4)$$

$$F_{rt} = \frac{E}{(1 - \nu^2)} (\epsilon_t + \nu \epsilon_l) = -16.6 \text{ MPa} \quad (3.5)$$

where (E), equal to 203,000 MPa, is the modulus of elasticity, and (ν), equal to 0.3, is Poisson's ratio of steel, (ϵ_l and ϵ_t) are the longitudinal and the transverse strains, respectively. The ratio between the longitudinal residual stress and the yield strength (F_{rl} / F_y) at this location equals to 0.163, which is within 10% higher than the ratio of (ϵ_l / ϵ_y) at the same location (0.150). This suggests that the ratio between the longitudinal strain and the yield strain can be used to represent the magnitude of longitudinal residual stress compared to the yield strength of the material.

3.6 Model for the Residual Stress Distribution

The current results of the residual stress tests, and also the results given by Weng and Pekoz (1990), show that significant longitudinal residual stresses exist at and around the corner areas of the channel sections. The results also indicate that

the magnitudes of the residual stresses depend on the steel grade and the web width of the section. Based on these results, the idealized longitudinal residual stress distributions for section (A) (Grade D steel) and section (B) (Grade A steel) may be as shown in Figures 3.23(a) and 3.23(b), respectively. It is found that a ratio (F_{rl} / F_y) equal to 40% for the corner zone (which is defined in section 3.3) represents the average of the residual stresses in this zone for all the test specimens in the current study. This ratio is less than the ratio of 50% suggested by Weng and Pekoz (1990). For the flat zone, an average ratio (F_{rl} / F_y) equal to 12% is found to represent the flat areas of section (A) (which has a total width of 203 mm), and an average ratio (F_{rl} /F_y) equal to 18% is found to represent the flat areas of section (B) (which has a total width of 101.5 mm). These ratios indicate that the cold work, and consequently the longitudinal residual stresses, tend to increase on the flat areas of shallow (short web) sections. The effect of the cold work on the flat areas will also increase with the increase of the inside corner bending radius (r) of the section. Hence, it is suggested that the ratio (F_{rl} / F_y) in the flat zone of any roll-formed channel section can be assumed based on the overall web width (w′) and the inside corner bending radius (r). The following simple formulae can be used to determine the longitudinal residual stress ratio (F_{rl} / F_y) for the corner zone and the flat zone of CFS channel sections:

$$(F_{rl} / F_y) \text{ corner zone } = 0.4 \tag{3.6}$$

$$(F_{rl} / F_y) \text{ flat zone } = 0.4 - 0.005 \left(\frac{w'}{r}\right) \tag{3.7}$$

where (F_y) is the measured (or specified) yield strength of the section.

Due to the lack of the magnitudes and directions of the residual stress data through the thickness of CFS sections, the longitudinal residual stress distribution through the thickness of CFS channel sections is assumed linear, with a zero magnitude at the centre line, for the corner and flat zones of the section. A tensile residual stress is assumed on the outside surface, and equal compression residual stress is assumed on the inside surface at the same location. This longitudinal residual stress distribution through the thickness is similar to the distribution proposed by Weng and Pekoz (1990).

3.7 Summary

The results of 41 tensile coupon tests to evaluate the mechanical properties of cold-formed steel (CFS) channel sections have been presented in this chapter. Also the results of four residual stress tests to establish the magnitudes and distributions of residual stresses within the channel sections have been presented. Both series of tests showed that the cold bending operation alters the virgin material properties of the steel sheet. The major changes of the material properties were found at and around the sections corners as a result of the large plastic deformations at these areas.

The tensile coupon tests showed that a considerable increase in the yield and ultimate strengths occur at the corner areas of CFS channel section. The increase in the yield and ultimate strengths at areas adjacent to the corners were not as high as for the corner areas, but generally higher than flat parts. It was also noticed that the percentage increase in the yield strength at the corner areas increases with higher values of the specified yield strength. Analytical models for the distribution of yield strength and the stress-strain relationship across channel sections have been developed based on the observations of the tensile coupon tests. The models propose that channel sections be divided into two zones, with each zone be assigned appropriate yield strength and stress-strain relationship.

The residual stress tests were performed using the method of Electrical Discharge Machining. The tests showed that tensile residual stresses exist on the outside surfaces of CFS channel sections, and equivalent compression residual stresses exist on the inside surfaces of the sections. It was found that the magnitudes of residual stresses depend on the yield strength and the web width of the section. The tests also indicated that residual stresses in the longitudinal direction of the channel section are the main residual stresses due to the cold bending operation. An Analytical model for the distribution of longitudinal residual stresses across CFS channel sections have been presented based on the current test results.

Table 3.1 Mechanical properties of tensile coupons for section (A)

Position	A-1	A-2	A-3	A-4	A-5	A-6	A-7	A-8	A-9
Pos. Type	Lip	Corner	Next to corner	Flat	Next to corner	Corner	Next to corner	Flat	Flat
E (GPa)	196.7	194.9	193.7	195.2	188.2	214.1	191.8	195.2	195.2
F_p (MPa) [a]	277.8	362.5	290.6	292.8	286.8	383.3	286.0	292.8	292.8
F_y (MPa) [b]	405.1	552.3	397.9	385.2	397.1	565.0	379.4	385.2	385.2
Yielding Type [c]	G	G	G	G	G	G	G	G	G
F_u (MPa)	495.3	604.9	481.8	475.0	477.2	614.8	479.3	475.0	475.0
Elong. % [d]	25.9	8.2	25.0	30.1	26.0	6.5	28.1	30.1	32.2
F_p / F_y	0.69	0.66	0.73	0.76	0.72	0.68	0.75	0.76	0.76
F_u / F_y	1.22	1.10	1.21	1.23	1.20	1.09	1.26	1.23	1.23
$F_y / F_{y\,flat}$	1.05	1.43	1.03	1.0	1.03	1.47	0.98	1.0	1.0
$F_u / F_{u\,flat}$	1.04	1.27	1.02	1.0	1.01	1.29	1.01	1.0	1.0

[a] F_p is the 0.01% offset strength.

[b] F_y is the 0.2% offset strength.

[c] G represents gradual yielding.

[d] Total elongation at fracture.

Table 3.2 Mechanical properties of tensile coupons for section (B)

Position	B-1	B-2	B-3	B-4	B-5	B-6	B-7	B-8
Pos. Type	Lip	Corner	Next to corner	Flat	Next to corner	Corner	Next to corner	Flat
E (GPa)	184.6	185.8	197.3	183.7	192.7	210.4	189.6	187.8
F_p (MPa)[a]	--	352.4	--	--	--	342.5	--	--
F_y (MPa)[b]	357.2	400.1	333.9	320.0	328.3	392.0	335.7	318.1
Yielding Type[c]	S	G	N	N	S	G	S	N
F_u (MPa)	410.0	453.3	364.5	362.0	362.3	450.2	371.7	362.0
Elong. %[d]	21.9	12.1	33.2	35.8	32.0	12.3	30.0	36.1
F_p / F_y	--	0.88	--	--	--	0.87	--	--
F_u / F_y	1.15	1.13	1.09	1.13	1.10	1.15	1.11	1.14
$F_y / F_{y\,flat}$[e]	1.12	1.26	1.05	1.0	1.03	1.23	1.06	1.0
$F_u / F_{u\,flat}$[e]	1.13	1.25	1.01	1.0	1.0	1.24	1.03	1.0

[a] F_p is the 0.01% offset strength for gradual yielding materials.

[b] F_y is the 0.2% offset strength for gradual yielding materials and the yield stress for sharp yielding materials.

[c] S represents sharp yielding, G represents gradual yielding, and N represents non-defined shape of yielding.

[d] Total elongation at fracture.

[e] The flat properties are considered that of position B-8.

Table 3.3 Comparison of the increase in corner yield strength of roll-formed sections

Section	$\Delta F_y / F_y$ (corner area)			$\Delta F_y / F_y$ (corner zone)	(5)/(3)	(5)/(4)
	Test results	Karren Eq. 3.1 (AISI)	Lind Eq. 3.2 (CSA)	Test results		
(1)	(2)	(3)	(4)	(5)	(6)	(7)
(a) Current study						
C-385[a]	0.45	0.35	0.30	0.17	0.49	0.57
C-318	0.25	0.21	0.17	0.13	0.61	0.76
(b) Karren and Winter (1967)						
Track-259	--	0.57	0.37	0.39	0.68	1.05
C-255	--	0.84	0.70	0.54	0.64	0.77
Joist-212	1.07	0.93	1.17	0.69	0.74	0.59

[a] Measured yield strength in MPa.

Table 3.4 Measured released surface strains for section (A)

Measured position[a]	Surface strain ($\mu\epsilon$) (ϵ_y = 1898 $\mu\epsilon$)							
	Outside surface				Inside surface			
	Specimen (1)		Specimen (2)		Specimen (1)		Specimen (2)	
	ϵ	ϵ/ϵ_y	ϵ	ϵ/ϵ_y	ϵ	ϵ/ϵ_y	ϵ	ϵ/ϵ_y
1	-857	-0.452	-892	-0.470	--	--	--	--
2	-1188	-0.626	-1252	-0.660	--	--	--	--
3	-243	-0.128	-250	-0.132	+44	0.023	+75	0.040
4	-141	-0.074	-324	-0.171	+84	0.044	+111	0.058
5	-129	-0.068	-84	-0.044	+200	0.105	+126	0.066
6	-1366	-0.720	-1219	-0.642	+1272	0.670	+1342	0.707
7	-257	-0.135	-302	-0.159	+150	0.079	+220	0.116
8	-404	-0.213	-284	-0.150	+246	0.130	+180	0.095
			+11 (trans.)					
			-164 (45°)					

[a] Refer to Figure 3.21(a)

Table 3.5 Measured released surface strains for section (B)

Measured position[a]	Surface strain ($\mu\epsilon$) (ϵ_y = 1567 $\mu\epsilon$)							
	Outside surface				Inside surface			
	Specimen (1)		Specimen (2)		Specimen (1)		Specimen (2)	
	ϵ	ϵ/ϵ_y	ϵ	ϵ/ϵ_y	ϵ	ϵ/ϵ_y	ϵ	ϵ/ϵ_y
1	-474	-0.302	-356	-0.227	--	--	--	--
2	N/A[b]	N/A	-388	-0.248	--	--	--	--
3	-149	-0.095	-152	-0.097	+79	0.050	+117	0.075
4	-157	-0.100	-171	-0.109	+221	0.141	+82	0.052
5	-236	-0.151	-252	-0.161	+258	0.165	N/A	N/A
6	-698	-0.445	-614	-0.392	+568	0.362	+609	0.389
7	N/A	N/A	-462	-0.295	N/A	N/A	+401	0.256

[a] Refer to Figure 3.22(a)

[b] Defective strain gauge during the cutting process

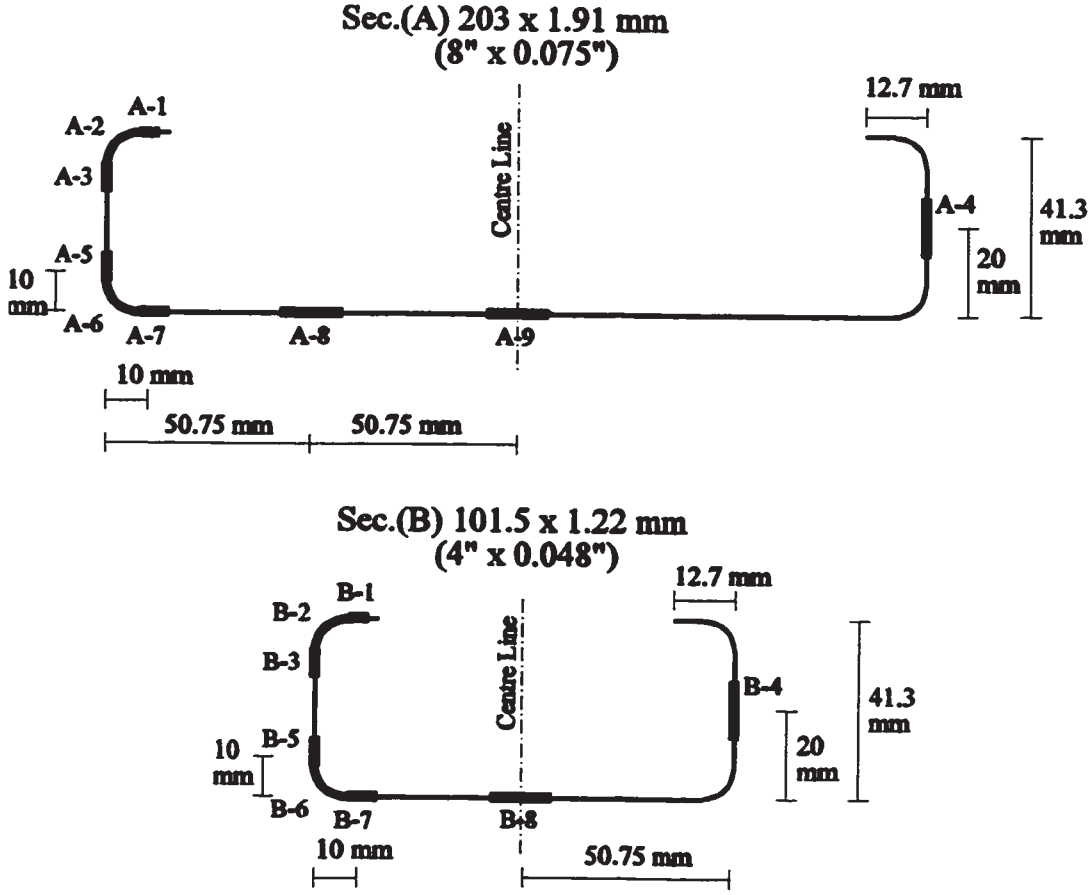

Figure 3.1 Positions of tensile coupons for sections (A) and (B)

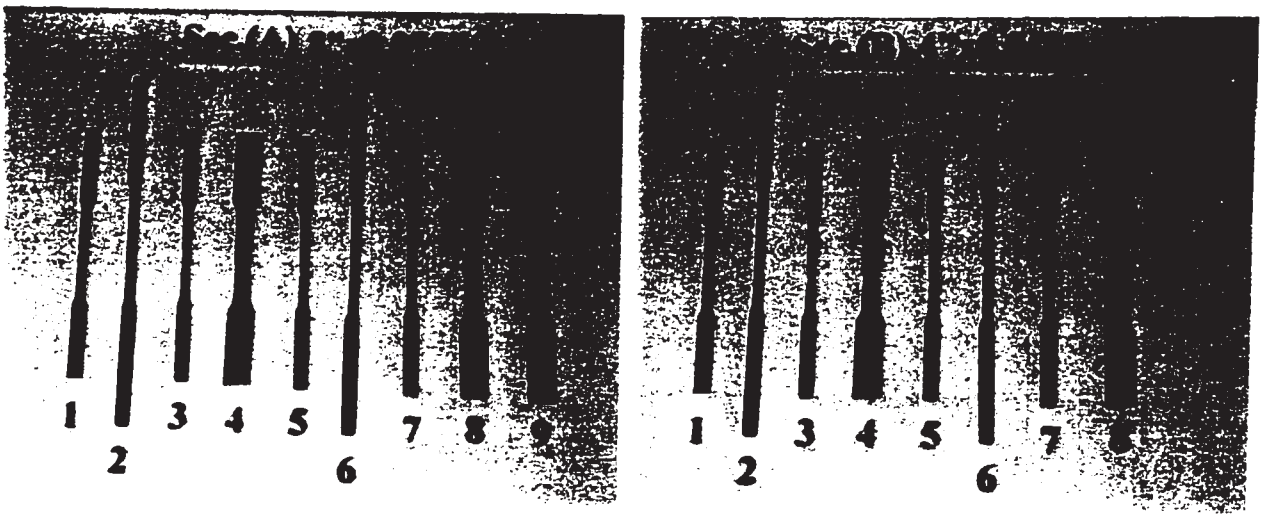

Figure 3.2 Tensile coupons for sections (A) and (B) after failure

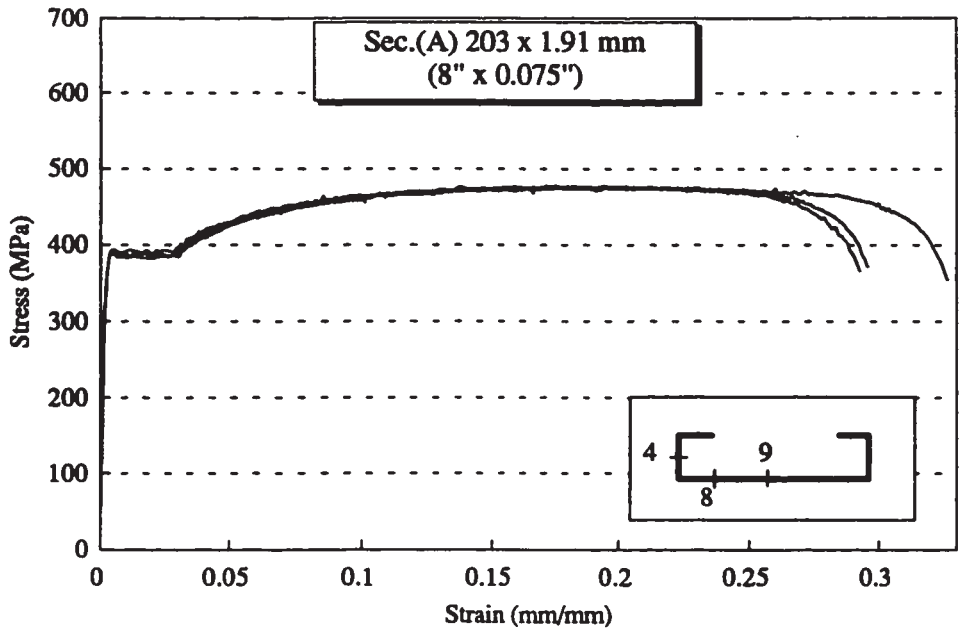

(a)

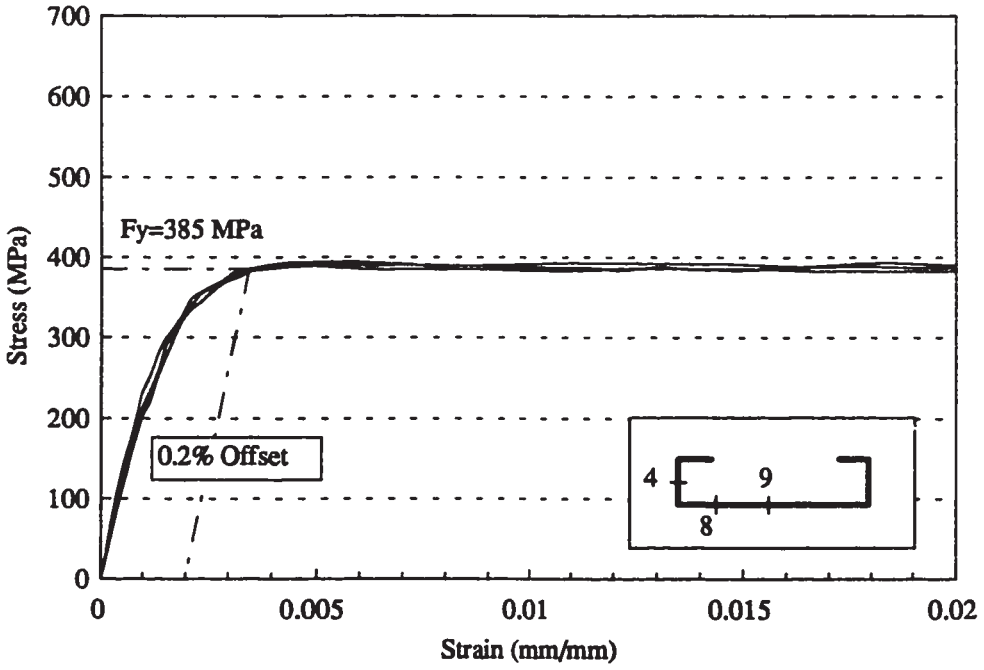

(b)

Figure 3.3 Stress-strain curves of tensile coupons for section (A)
(Specimens A-4, A-8, and A-9)

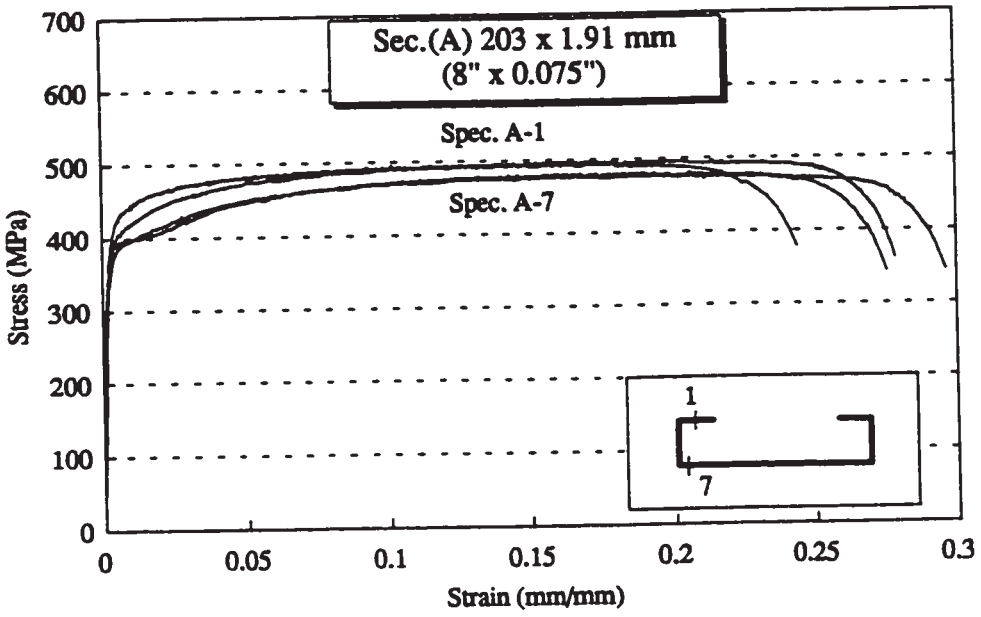

(a)

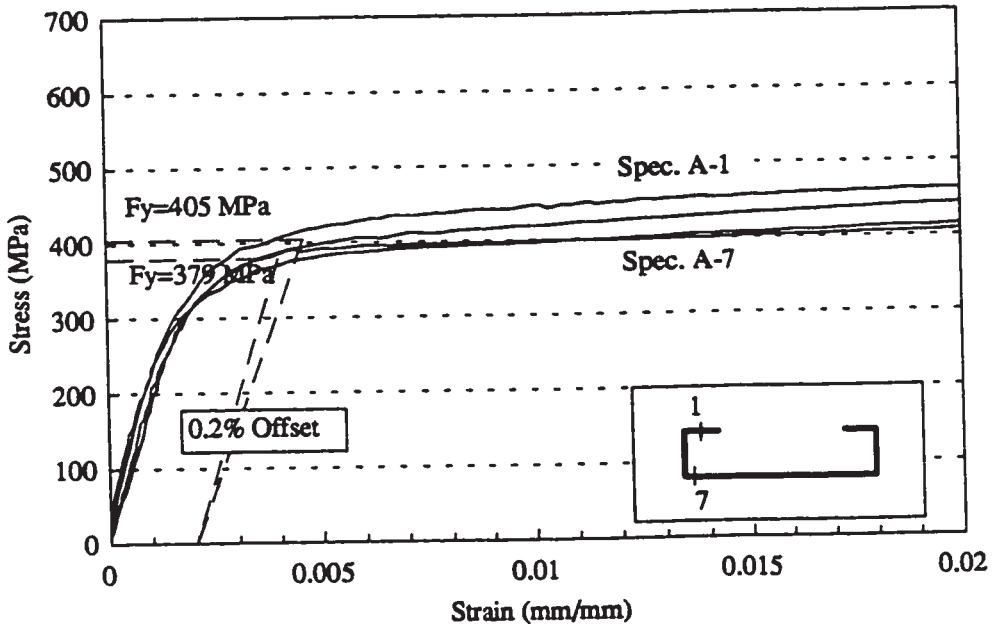

(b)

Figure 3.4 Stress-strain curves of tensile coupons for section (A)
(Specimens A-1 and A-7)

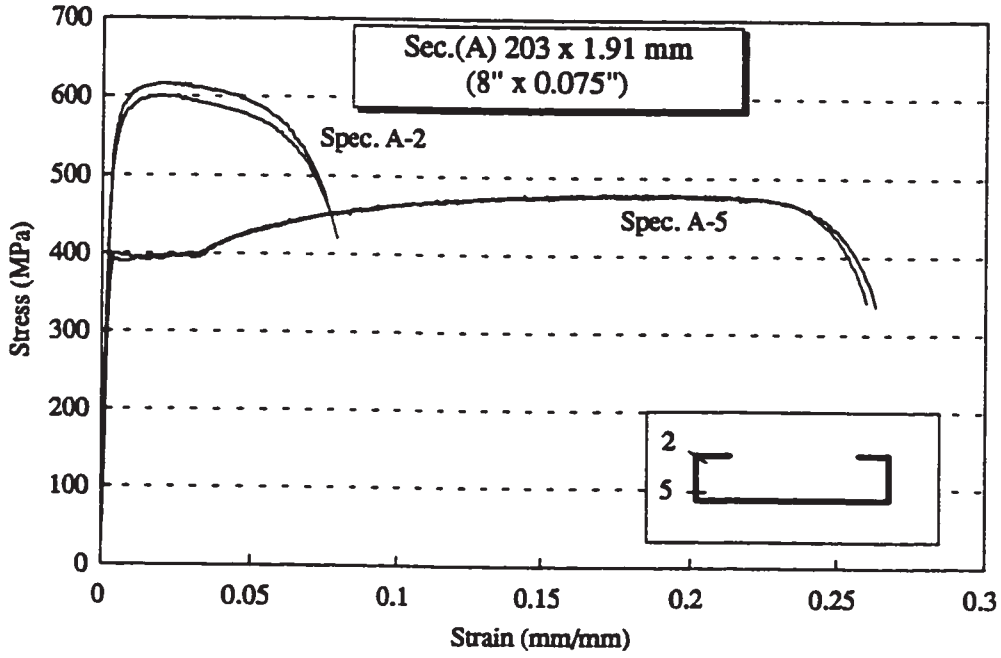

(a)

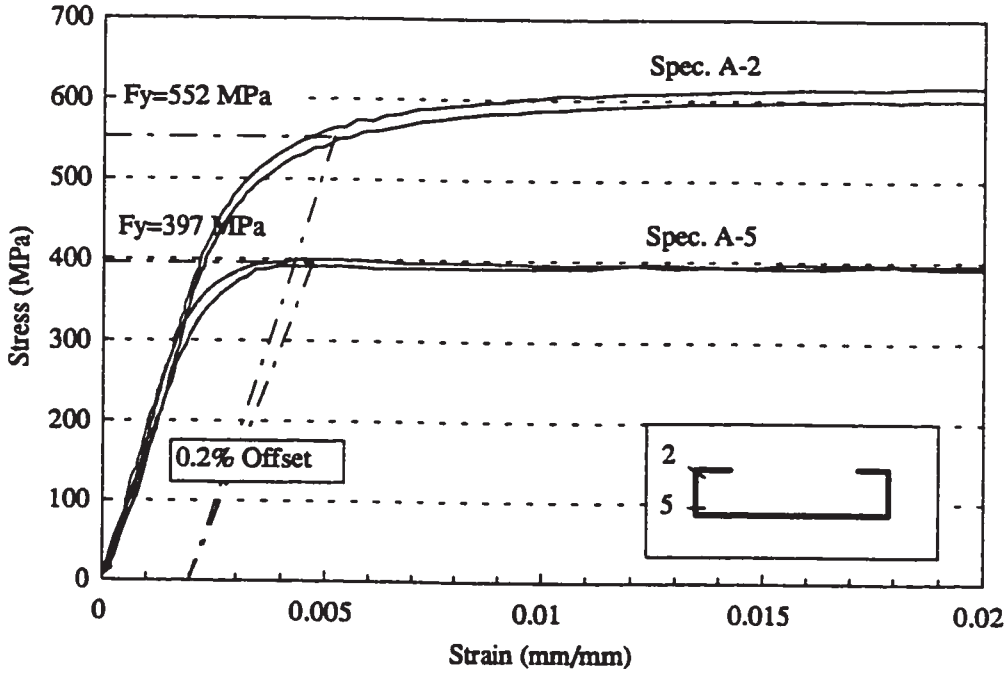

(b)

Figure 3.5 Stress-strain curves of tensile coupons for section (A)
(Specimens A-2 and A-5)

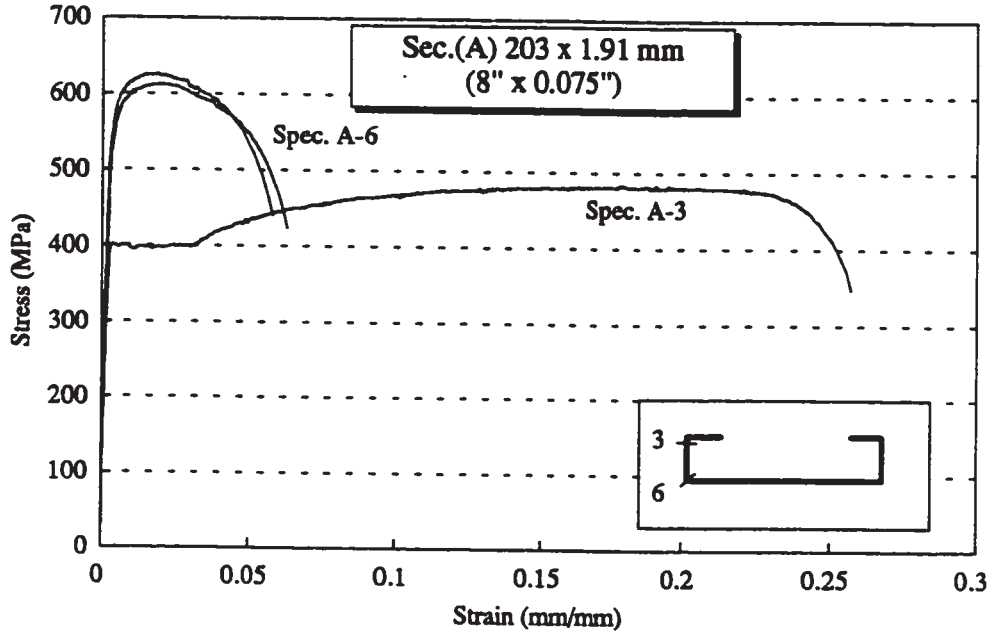

(a)

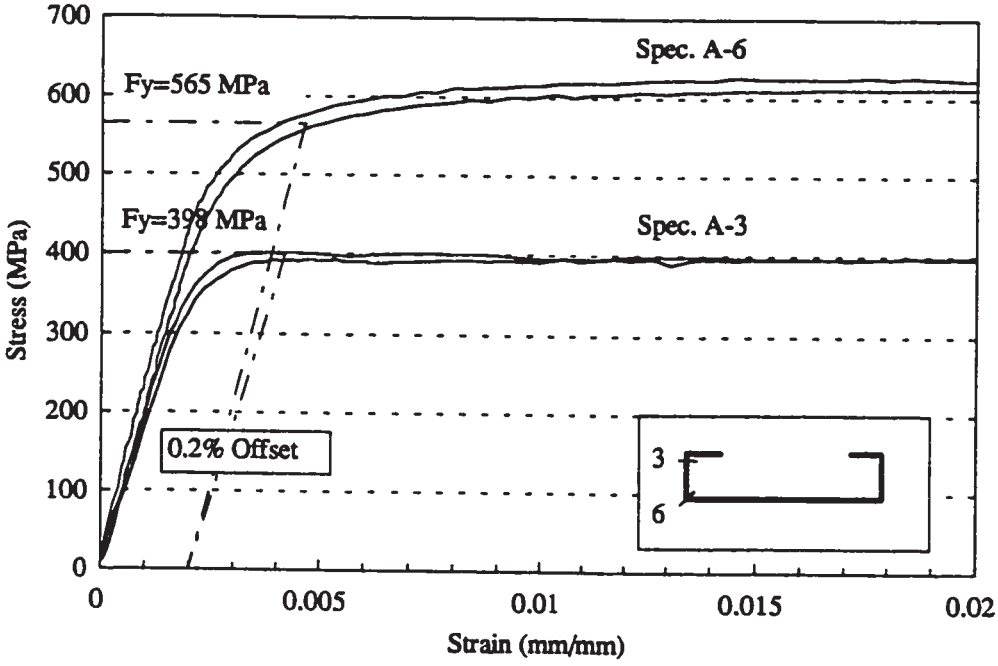

(b)

Figure 3.6 Stress-strain curves of tensile coupons for section (A)
(Specimens A-3 and A-6)

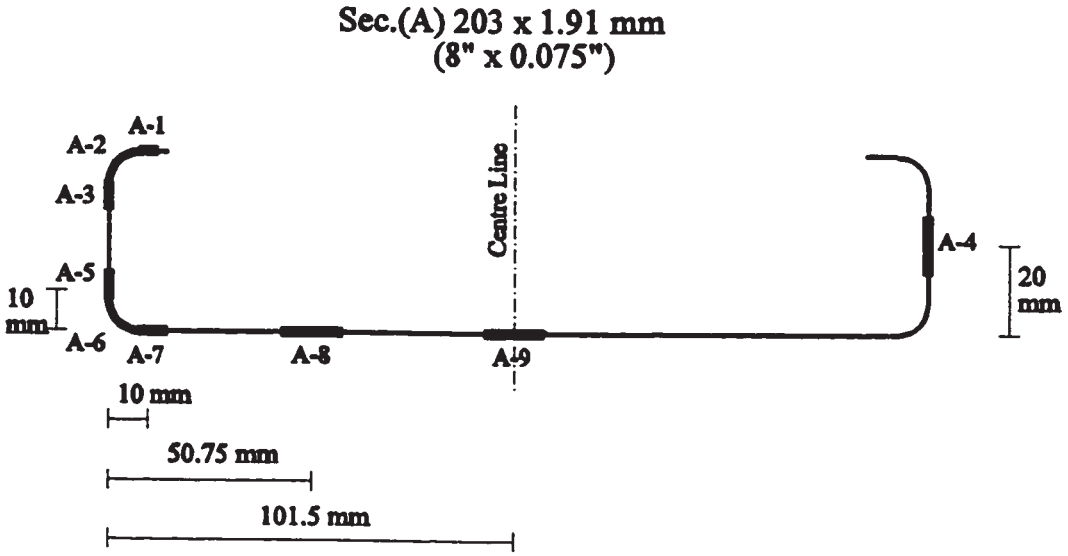

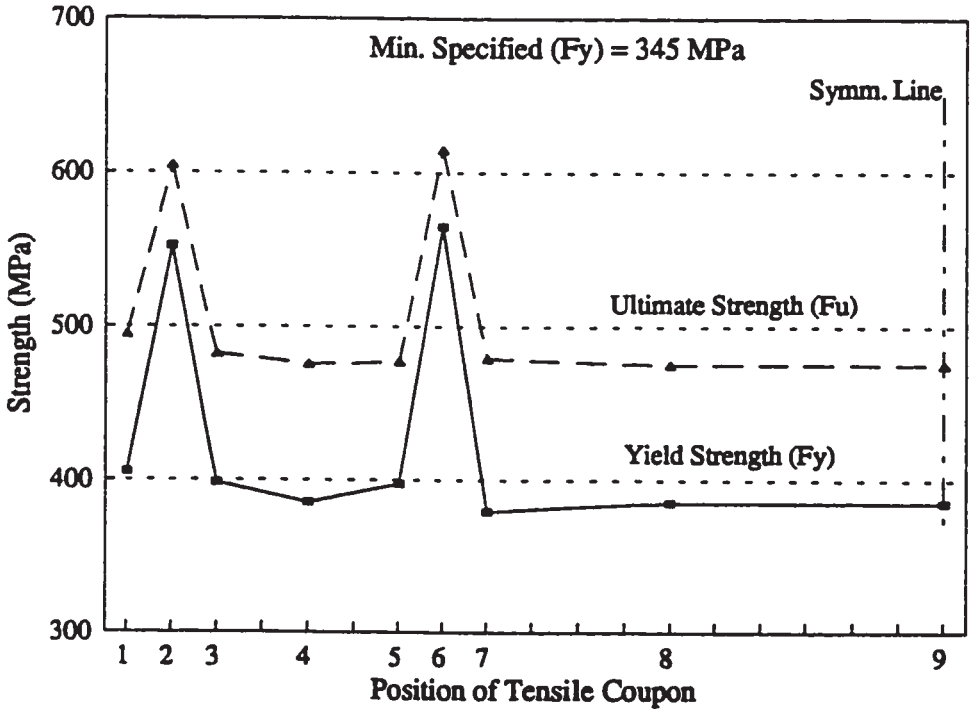

Figure 3.7 Variation of the yield and ultimate strengths across section (A)

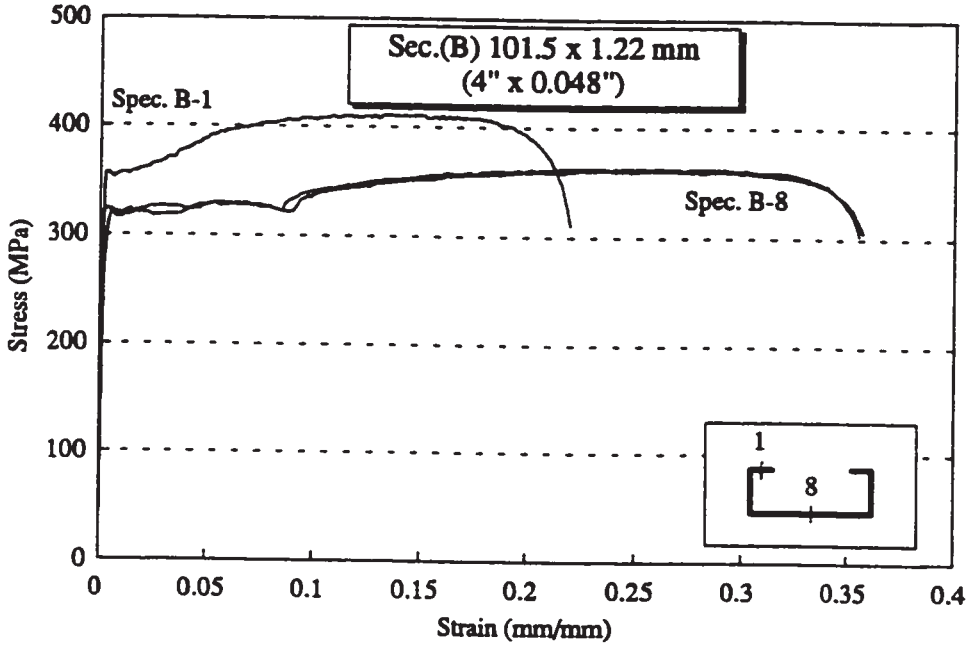

(a)

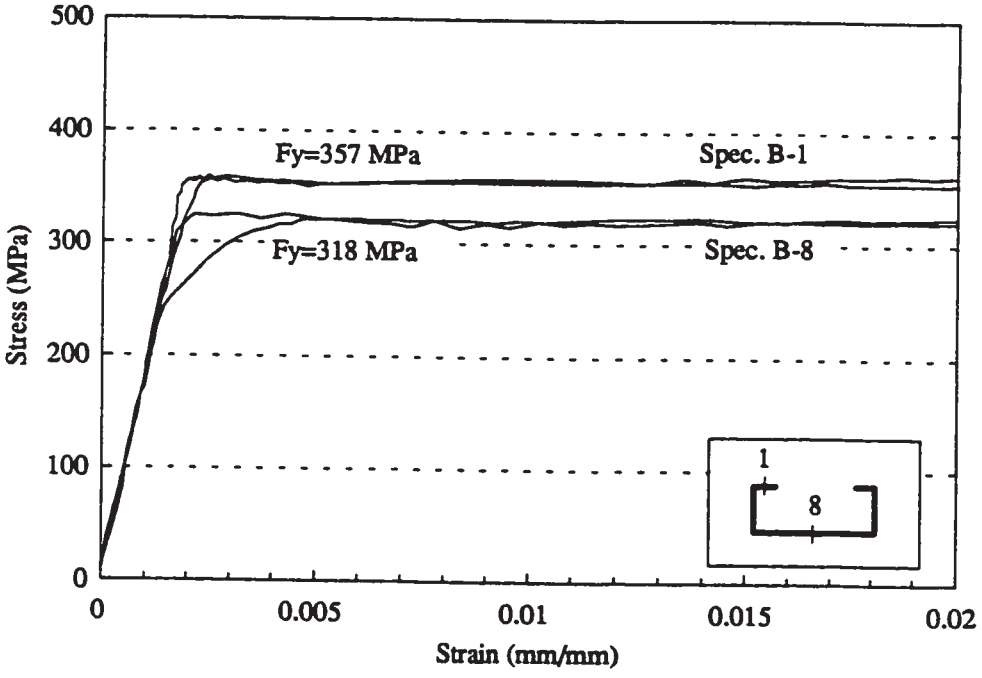

(b)

Figure 3.8 Stress-strain curves of tensile coupons for section (B)
(Specimens B-1 and B-8)

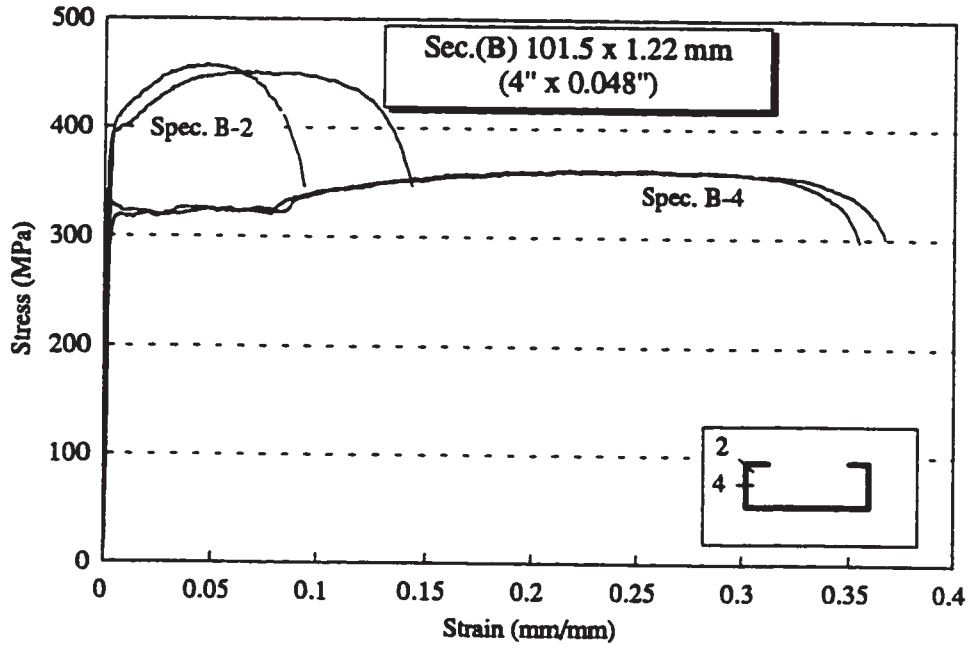

(a)

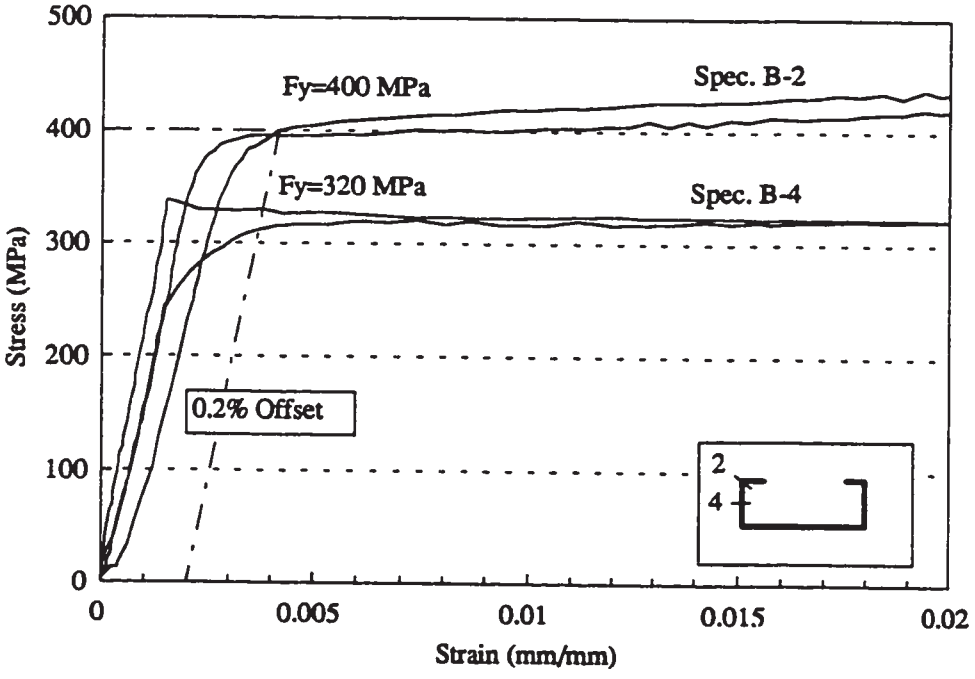

(b)

Figure 3.9 Stress-strain curves of tensile coupons for section (B)
(Specimens B-2 and B-4)

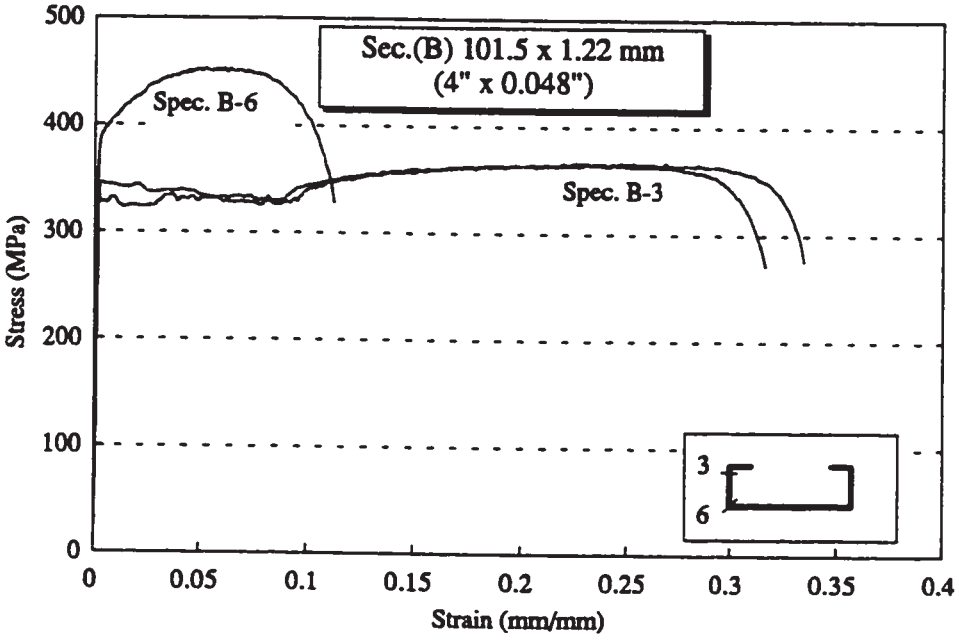

(a)

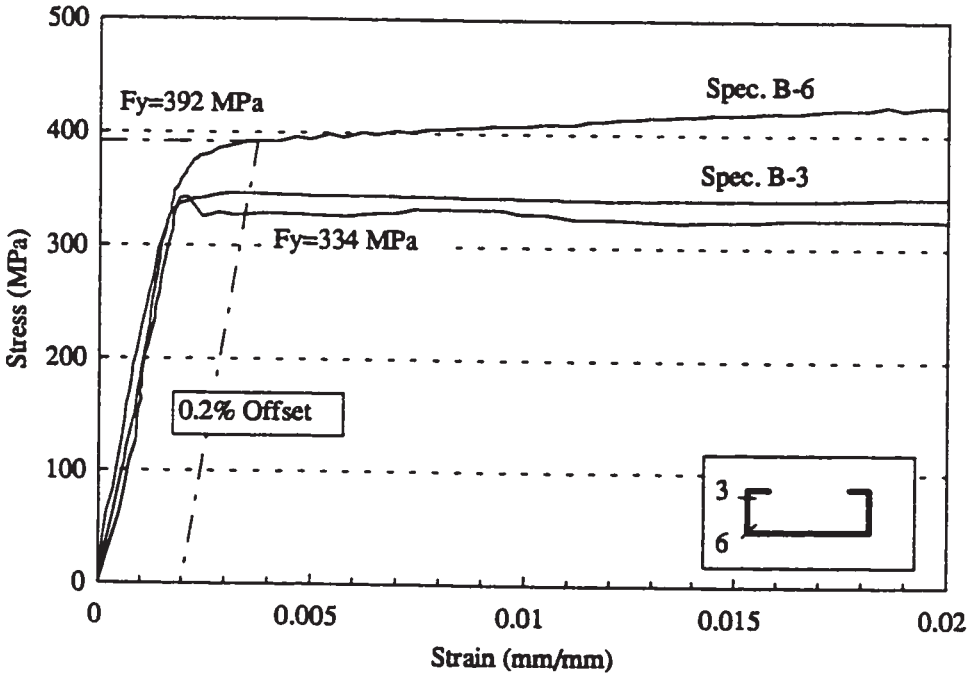

(b)

Figure 3.10 Stress-strain curves of tensile coupons for section (B)
(Specimens B-3 and B-6)

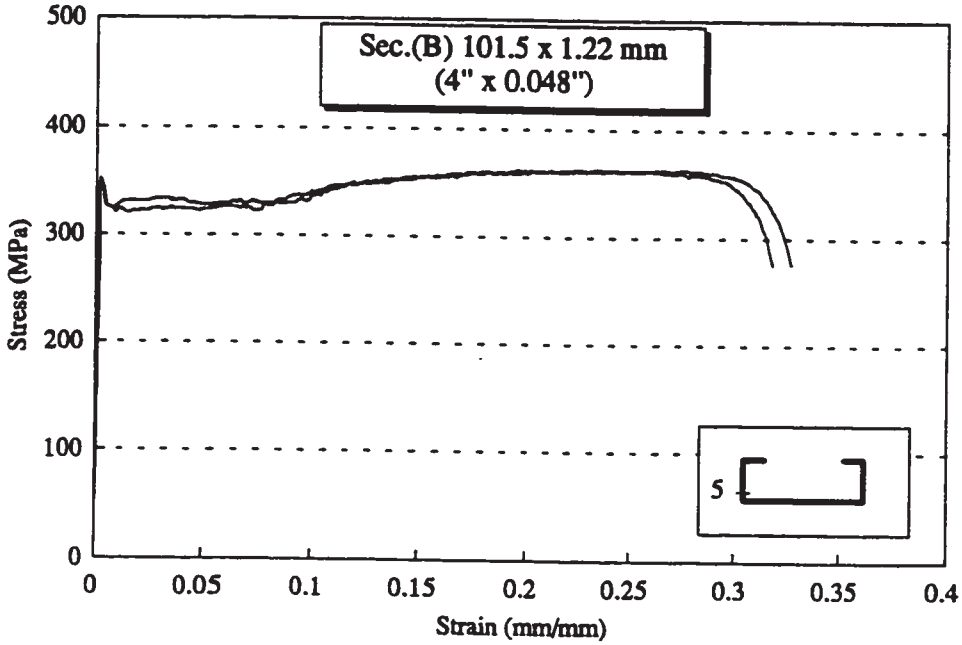

(a)

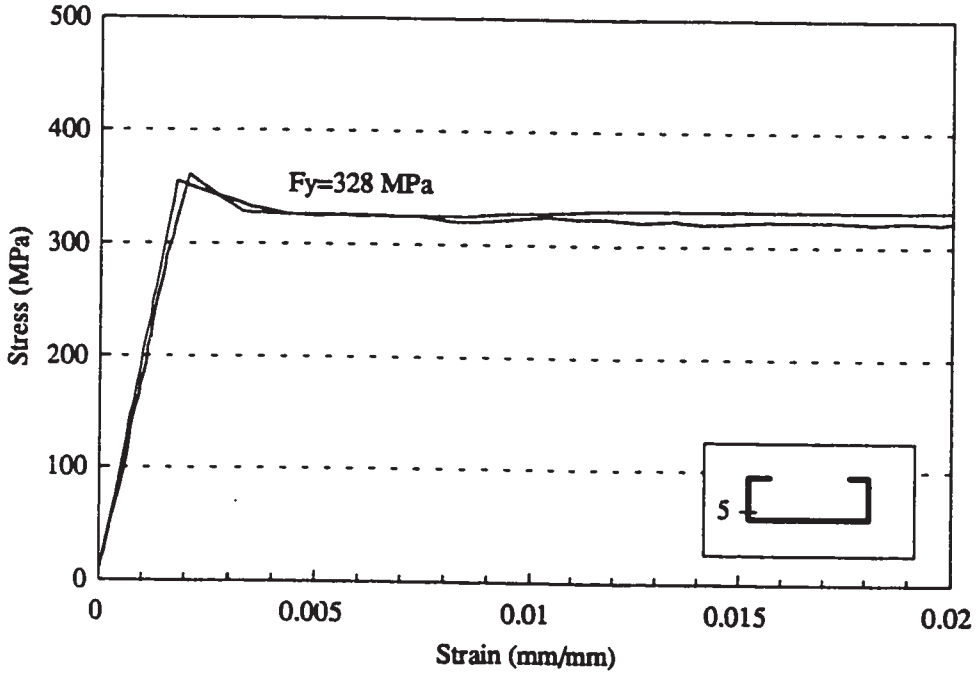

(b)

Figure 3.11 Stress-strain curves of tensile coupons for section (B) (Specimen B-5)

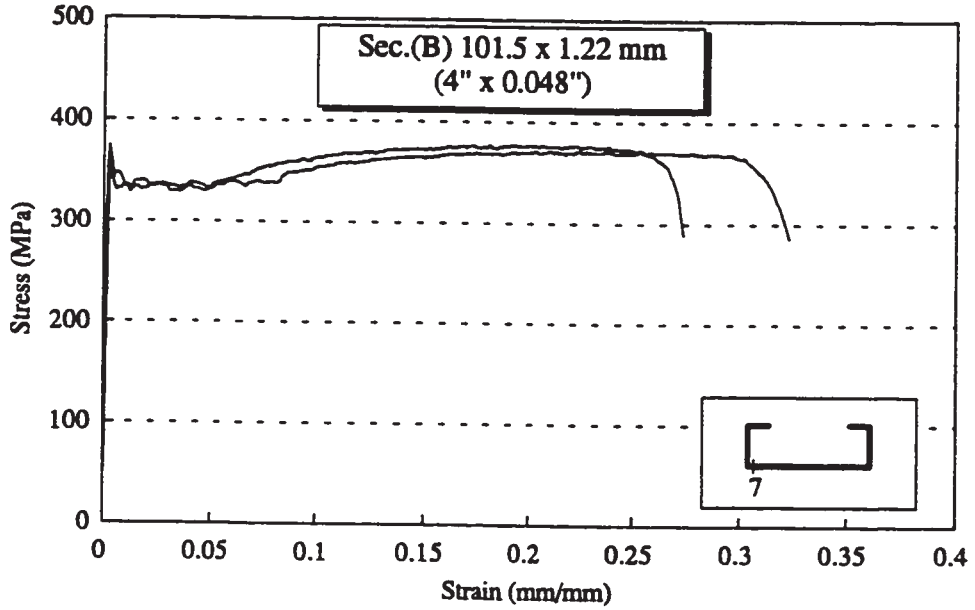

(a)

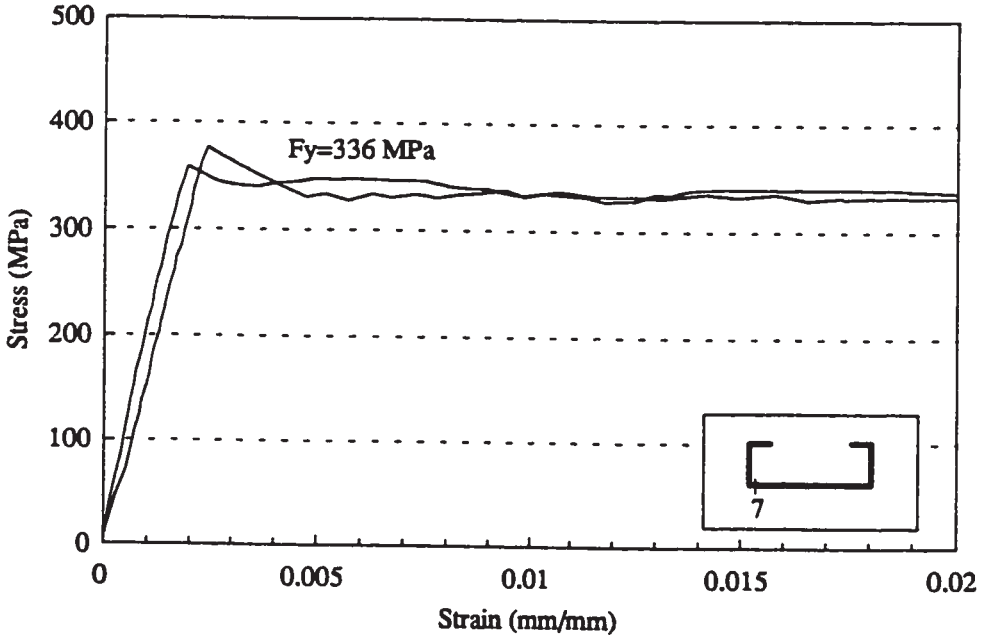

(b)

Figure 3.12 Stress-strain curves of tensile coupons for section (B)
(Specimen B-7)

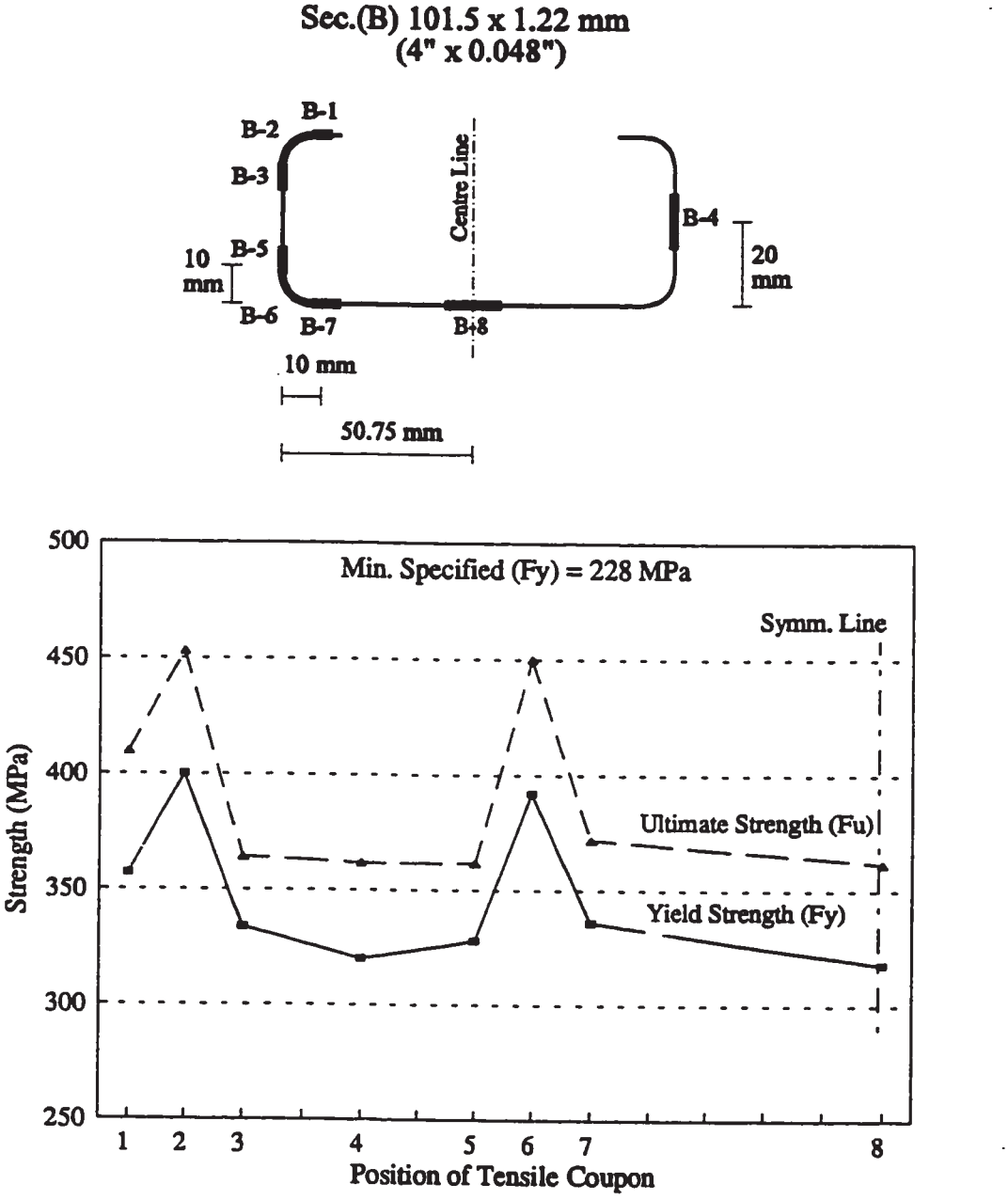

Figure 3.13 Variation of the yield and ultimate strengths across section (B)

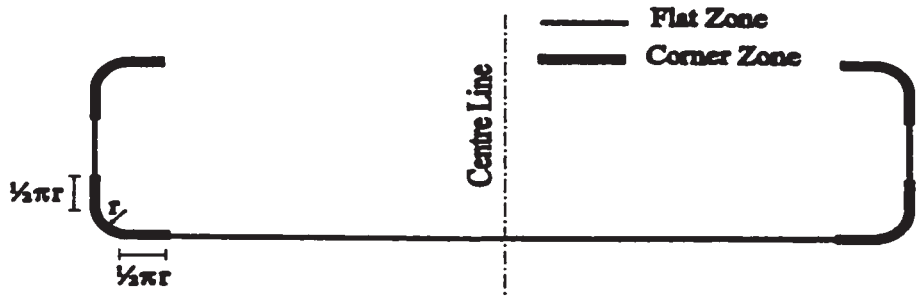

Figure 3.14 Definition of flat and corner zones of a lipped channel section

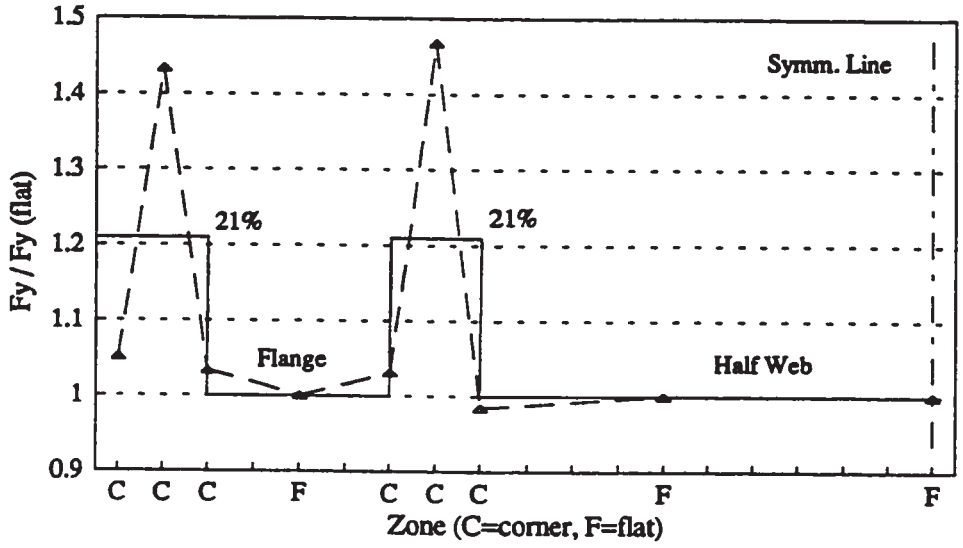

(a) Sec. (A) - Grade D Steel

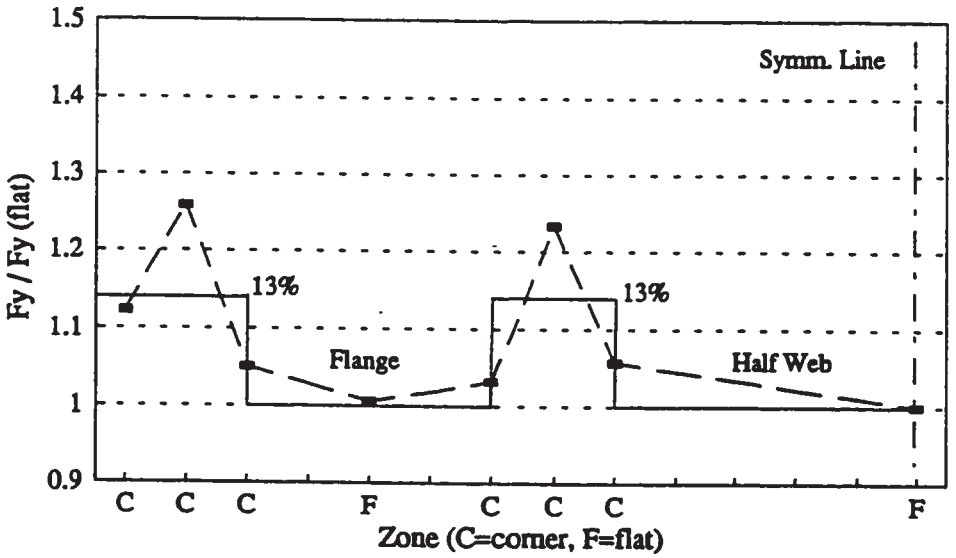

(b) Sec. (B) - Grade A Steel

Figure 3.15 Measured and idealized yield strength
for channel sections of Grades D and A steels

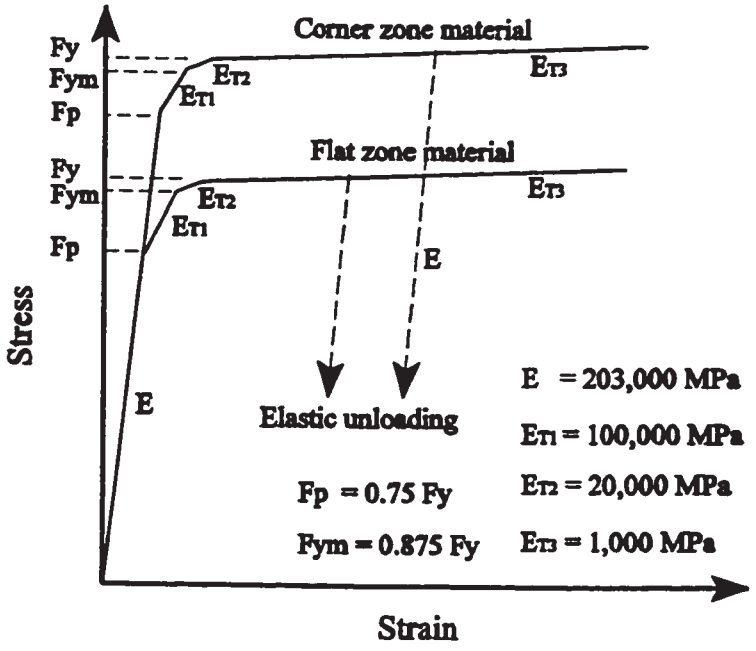

Figure 3.16 Idealized stress-strain relationship for cold-formed steel

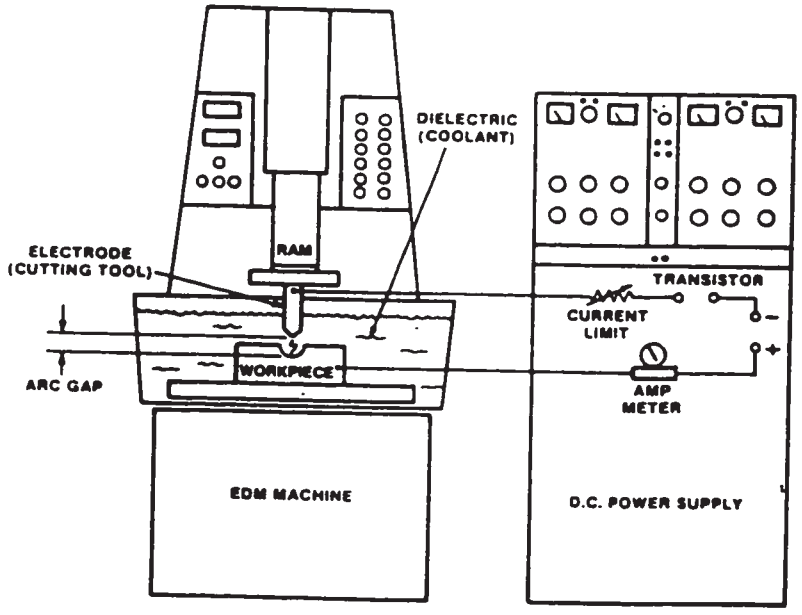

Figure 3.17 Schematic diagram of an EDM system (Weller and Haavisto, 1984)

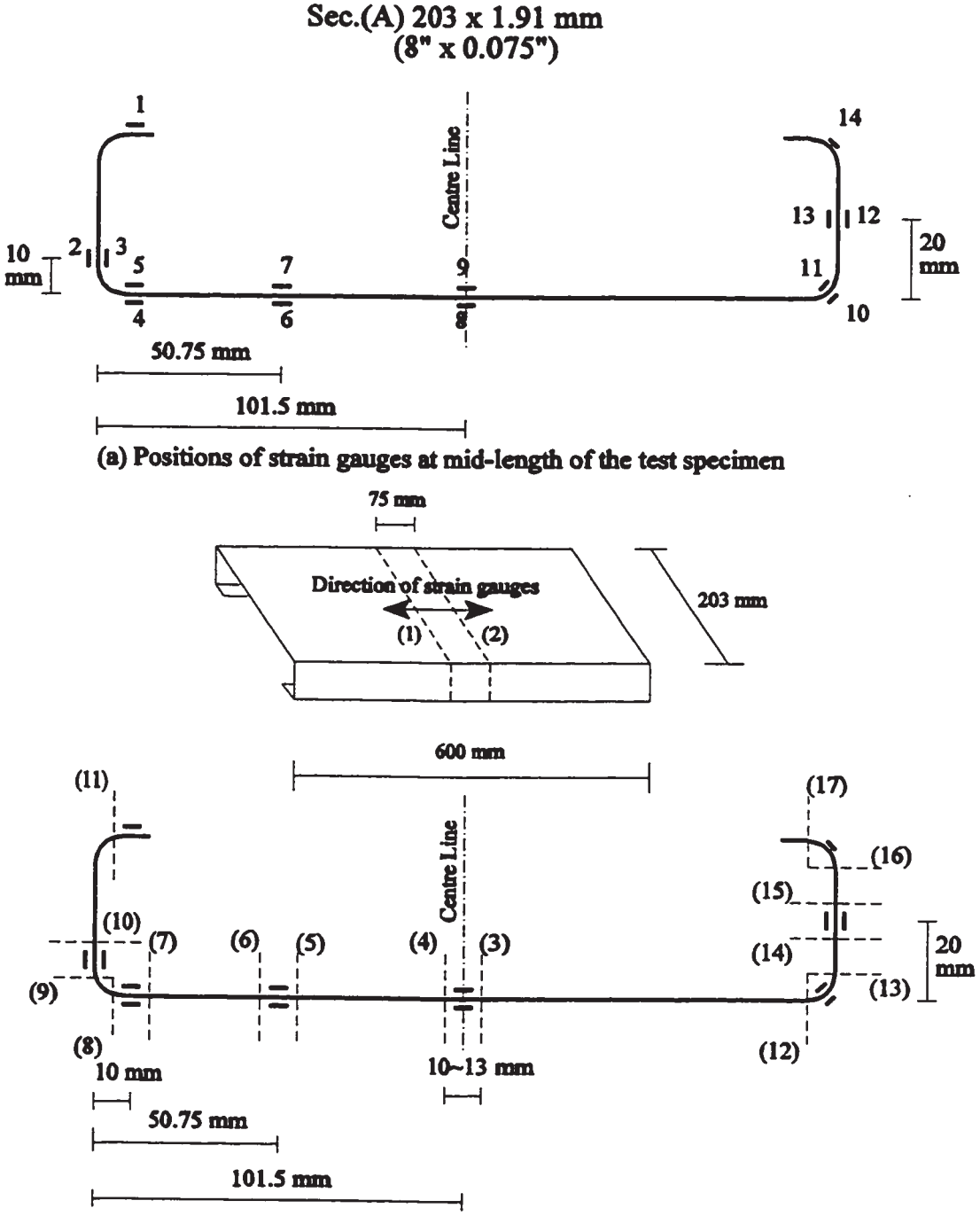

(a) Positions of strain gauges at mid-length of the test specimen

(b) Cutting sequence using the EDM method

Figure 3.18 Positions of strain gauges for residual strains and cutting sequence for section (A)

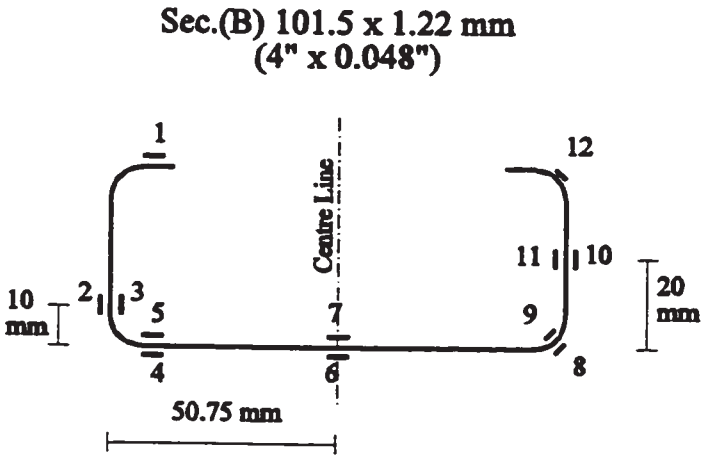

(a) Positions of strain gauges at mid-length of the test specimen

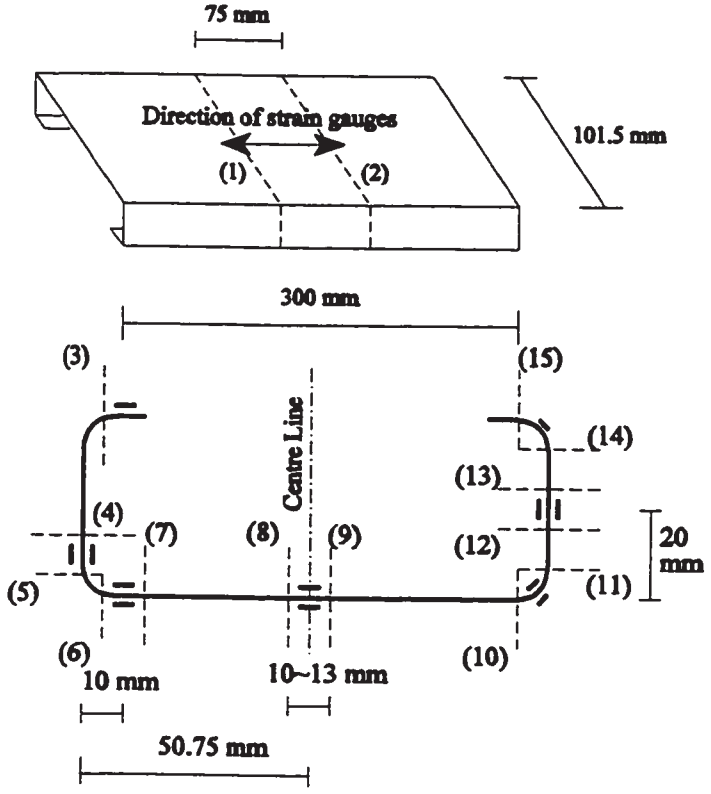

(b) Cutting sequence using the EDM method

Figure 3.19 Positions of strain gauges for residual strains and cutting sequence for section (B)

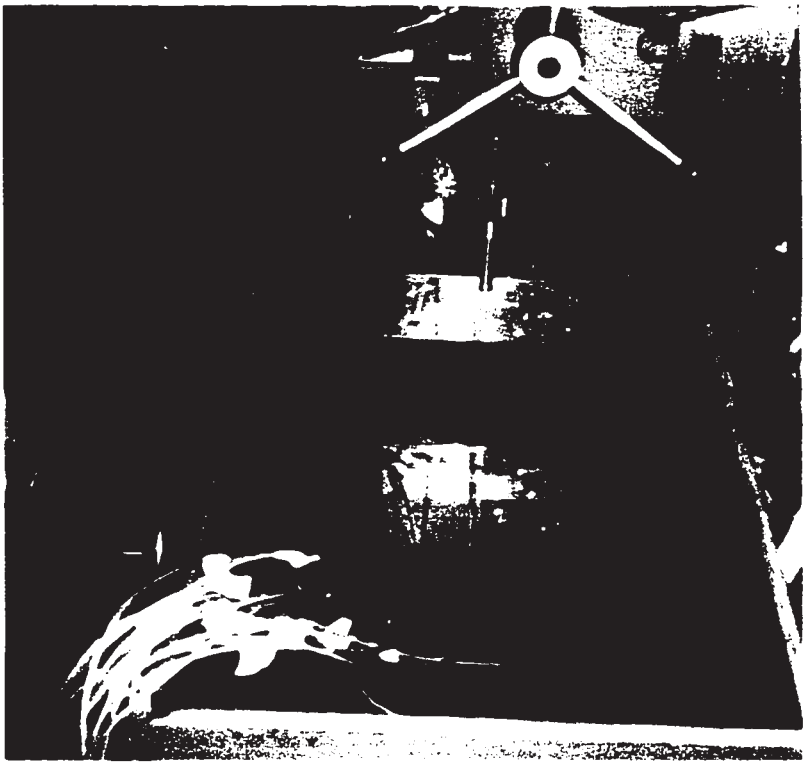

(a) Specimen during the cutting operation

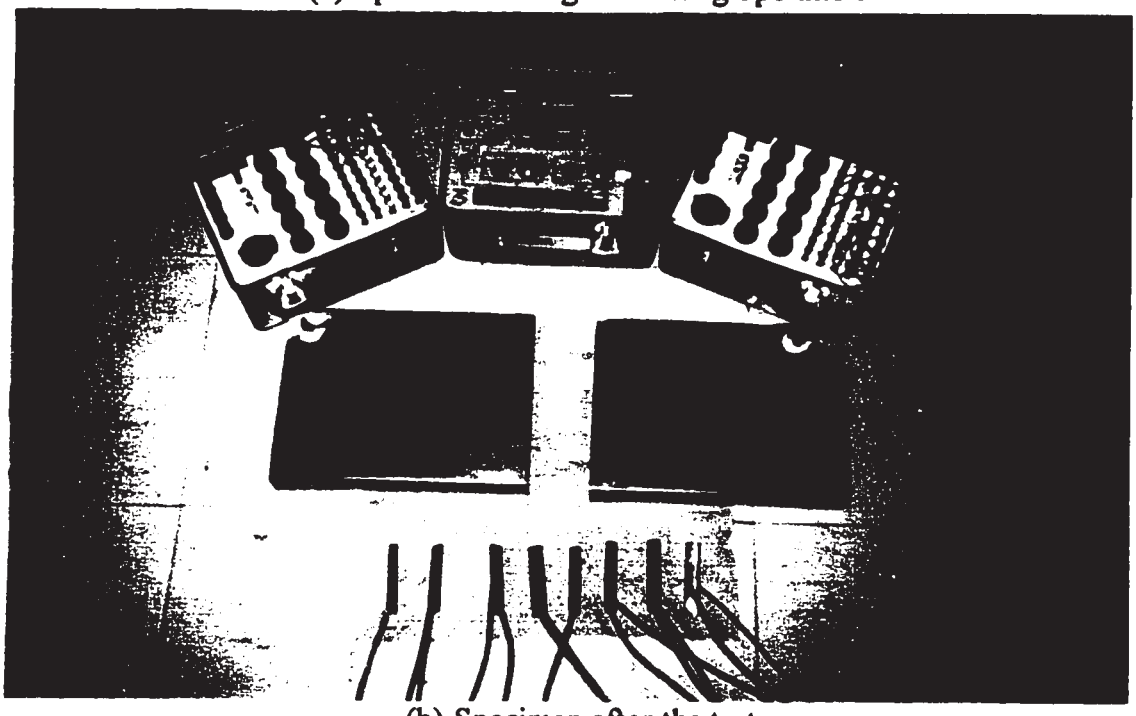

(b) Specimen after the test

Figure 3.20 Residual stress test specimen of section (A)

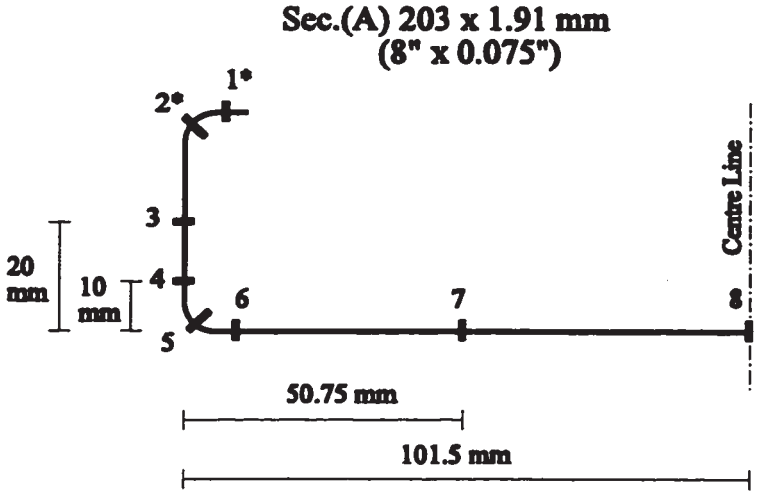

(a) Measured positions on the test specimen
(* represents outside gauge only)

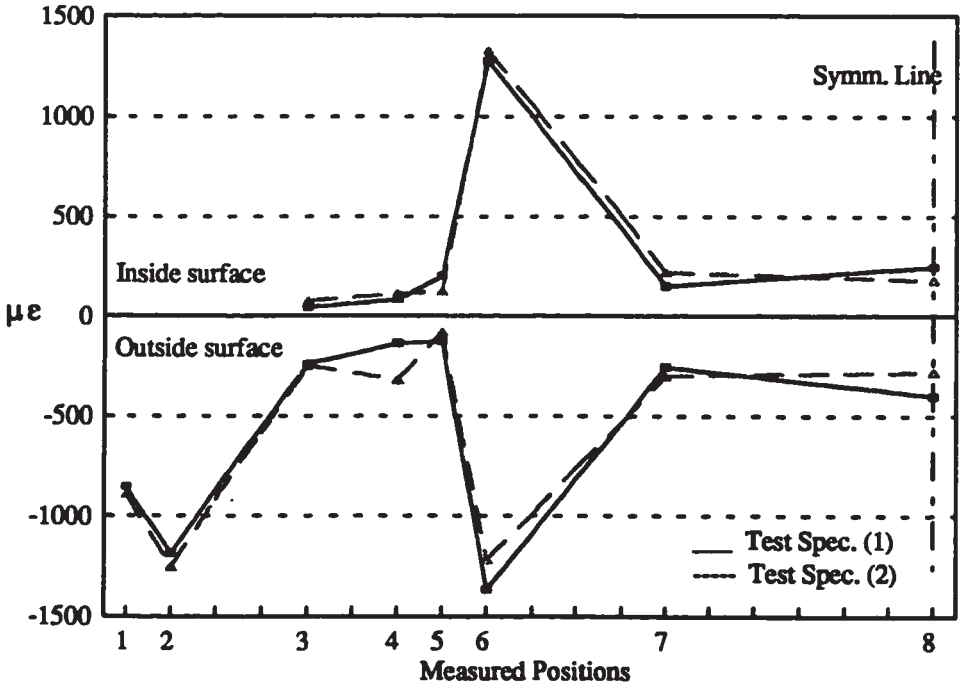

(b) Outside and Inside strain distributions

Figure 3.21 Measured longitudinal surface strains for section (A)

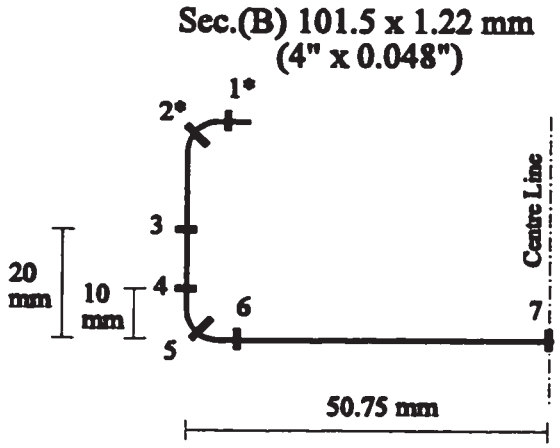

(a) Measured positions on the test specimen
(* represents outside gauge only)

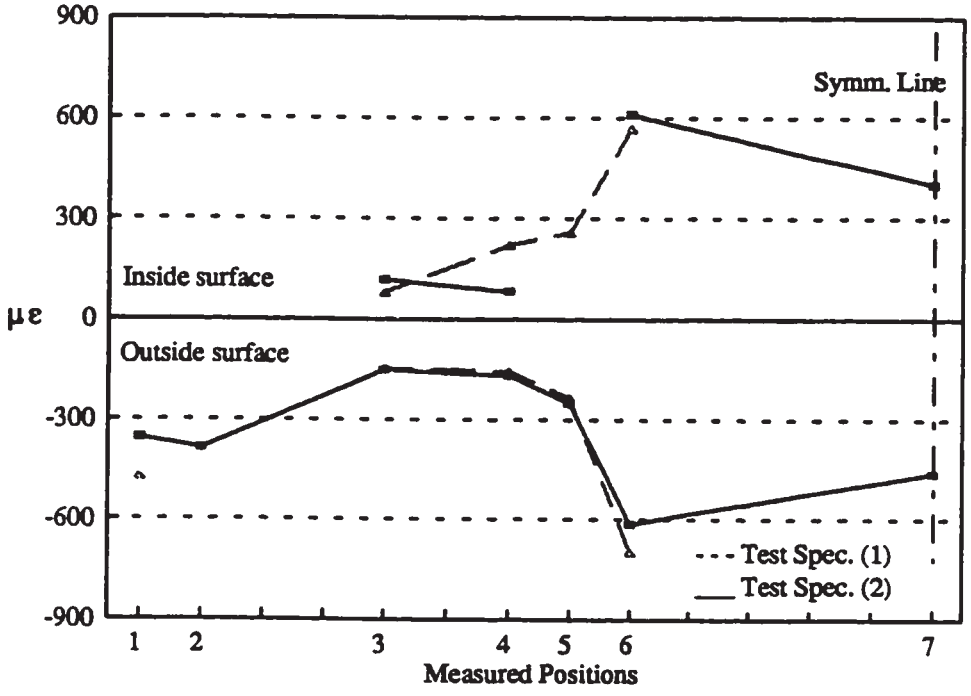

(b) Outside and Inside strain distributions

Figure 3.22 Measured longitudinal surface strains for section (B)

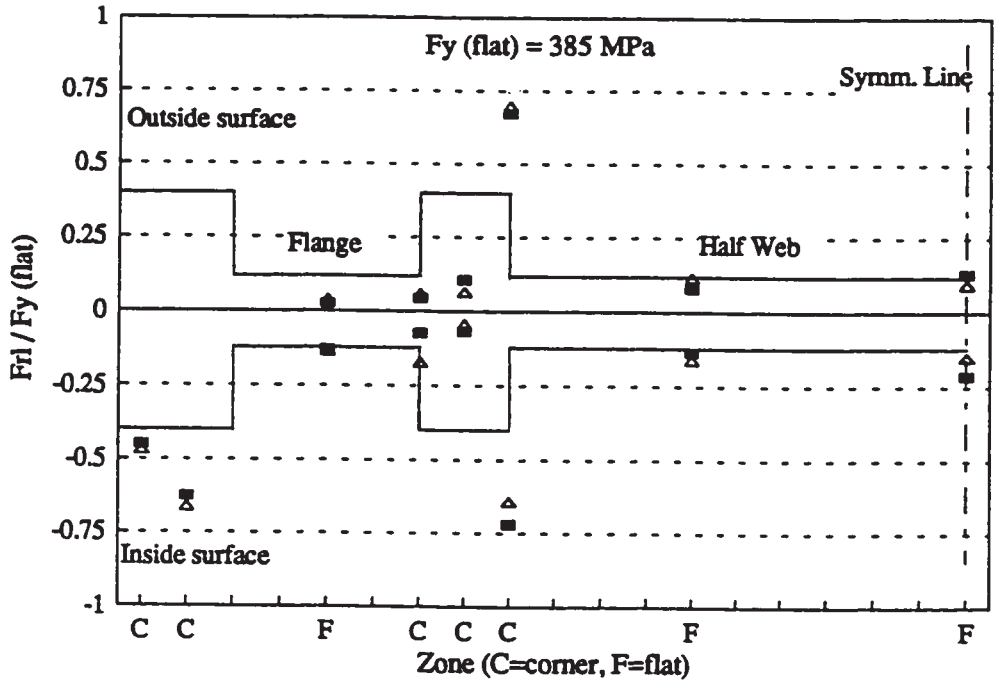

(a) Sec. (A) - Grade D Steel

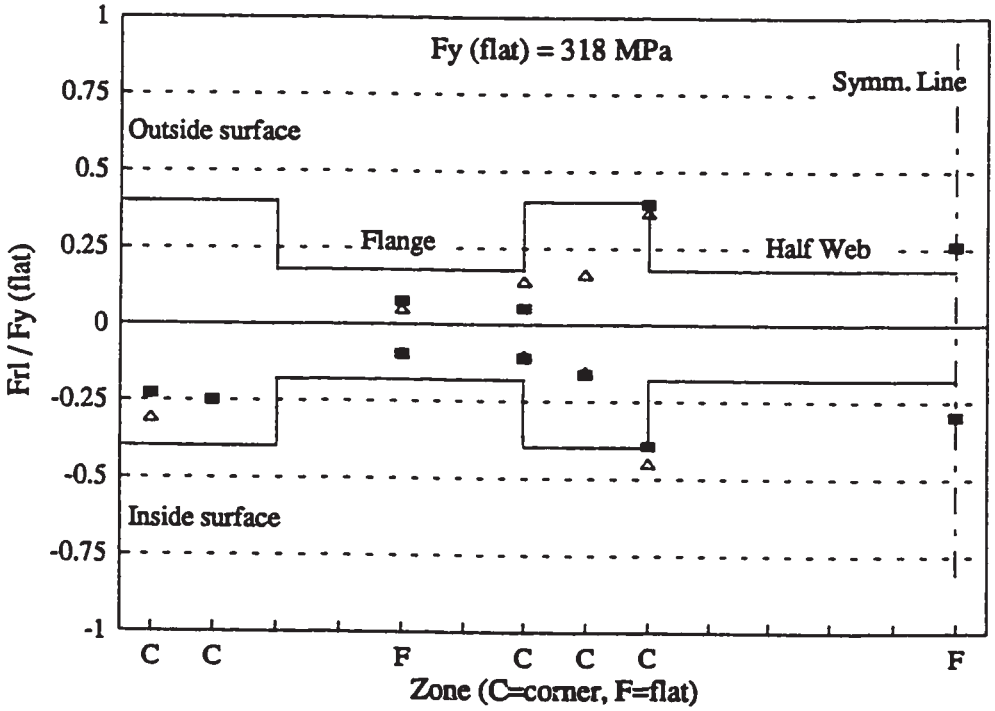

(b) Sec. (B) - Grade A Steel

Figure 3.23 Measured and idealized residual stresses for channel sections of Grades D and A steels

CHAPTER 4

LOCAL BUCKLING MODELLING AND EXPERIMENTAL VERIFICATION OF MEMBERS IN COMPRESSION

4.1 Introduction

A finite element-based analytical model has been developed in the first part of this chapter to predict the local buckling and the post-local buckling behaviour of cold-formed steel (CFS) members in axial compression. The finite element model utilizes the 9-node assumed strain isoparametric shell finite element presented in Chapter Two to represent the body of CFS sections. The shell finite element includes both geometric and material non-linearities, so that local buckling behaviour and ultimate strength of CFS members can be correctly predicted. The finite element model is also capable of simulating different material properties, geometric imperfections, and residual stresses, which result due to the cold-forming operation. The model is flexible enough to accommodate different shapes of perforations within the CFS members.

The second part of this chapter presents an experimental study which includes a series of 20 CFS stub-column tests. The series had four non-perforated specimens and 16 perforated specimens having different shapes of perforation. The stub-column tests were primarily performed to verify the results of the proposed finite element

model. Moreover, the tests were also used to investigate the effects of perforation on the deformation behaviour, buckling loads, ultimate loads, and stress behaviour of CFS members in compression.

4.2 Modelling Requirements for Members in Compression

In order to use the finite element method to study the local buckling and post-local buckling behaviour of cold-formed steel (CFS) members in compression, specific requirements have to be satisfied in both modelling and loading of CFS sections.

Cold-formed steel structural sections are generally composed of flat flanges, webs, lips, and rounded intersection corners. The wide thickness range of CFS sections puts these sections in a category of very thin to moderately thick sections. As a result, the finite element chosen to model CFS sections should be able to model flat surfaces as well as smooth curved surfaces. The finite element should also be able to represent both thin and moderately thick structures. The 9-node assumed strain isoparametric shell finite element, presented in Chapter Two, satisfies the requirement of representing flat and curved surfaces, as the element is isoparametric and defined locally in curvilinear coordinates. The finite element also satisfies the requirement of representing a wide thickness range by using the "assumed strain fields" method to eliminate the locking phenomenon associated with the analysis of very thin shells.

Large out-of-plane deformations usually occur in the post-local buckling range of relatively thin CFS compression members. This behaviour results in local bending

stresses as well as membrane stresses in the buckled plates. Therefore, the finite element chosen to model CFS sections should be able to represent both membrane behaviour and flexural behaviour, and should accommodate large displacements and rotations. The isoparametric shell finite element, introduced in Chapter Two, is a large deformation element as its displacement formulation takes into consideration geometric non-linearity. The element can represent membrane and flexural behaviour by having a stress field of five stress components, in the form of three in-plane stresses and two transverse shear stresses.

Cold-formed steel compression members may buckle in a local mode, an overall mode, or an interaction of local and overall modes. As the current study is interested in local buckling only, it was required to eliminate completely the overall member buckling. The American LRFD Specification (AISI, 1991) indicates that in order to eliminate the overall buckling mode in an experiment of a compression member, the length of the member should be limited to 20 times the minimum radius of gyration (20 r_{min}) of the cross section. Although this condition can also be applied to a finite element analysis model, the overall buckling mode can also be eliminated by controlling the lateral deformations of the compression member. As will be presented in the next section, a combination of the two ways to eliminate the overall buckling mode was used in the current finite element model.

Lateral imperfections are generally required to initiate the local buckling mode in the finite element analysis of compression members. These imperfections may be

in the form of a small lateral load at a central point of the member, or in the form of a geometric imperfection distribution of the member shape. A geometric imperfection distribution was used in the current finite element model to avoid the effects of a lateral load on the ultimate strength of the compression member. Moreover, a geometric imperfection distribution was found easy to generate for different plates composing the compression member.

Concentric compression members are usually loaded through bearing plates, which provide uniform displacements over the loading edge of the member. The finite element model was required to satisfy that the loading edge of the compression member is kept flat throughout the analysis history. A uniform axial load condition and a uniform axial displacement condition at the loading edge are expected to satisfy the requirement prior to the local buckling of individual plate elements of the member. However as local buckling develops, a uniform axial load condition will no longer satisfy the flat edge requirement, and the analysis has to be continued using a uniform axial displacement condition. As will be explained later when describing the loading technique, a uniform axial displacement condition was employed in the current finite element model throughout the analysis.

4.3 The Finite Element Model

4.3.1 Mesh Selection and Boundary Conditions

Stub-columns of channel sections were considered in the current finite element

study to represent cold-formed steel (CFS) members in compression. The length of the stub-column should be short enough to eliminate the overall buckling mode of the column. The condition that the length should not exceed (20 r_{min}) of the cross section was not possible to satisfy for every study case. It was found out that when applying the above condition to channel sections with short flanges, it results in a short length of the stub-column that can not accommodate the desired height of perforation. Hence, it was decided to use a stub-column length equal to three times the web width of the cross section to study cases where (20 r_{min}) of the cross section is less than three times the web width. This length was considered suitable to accommodate different heights of perforation, and to allow local buckling mode to propagate in the longitudinal direction of the stub-column. The overall buckling mode of all the study cases was eliminated by locking the out-of-plane displacement of discrete edge nodes of the web plate of the section.

Due to the symmetry of the geometry and the loading conditions of the stub-columns, only one quarter of every stub-column was modelled using the assumed strain shell finite element as shown in Figure 4.1(a). The width of the lip plate and each curved corner was modelled using one shell finite element. The isoparametric quadratic curvature of the shell element fitted well with the geometry of the curved corners of the channel CFS section. The width of the flange plate was divided into three shell elements. Seven shell finite elements were used in the height direction of the flange and lip plates of the one quarter stub-column. This discretizations was

deemed to be sufficient to provide reasonable accuracy for the finite element results, due to the quadratic displacement field of the shell finite element and the limited deformations expected to occur in the flange and lip plates. The discretization of the web plate was finer than that for other plates of the stub-column as large deformations were expected to occur in the web plate following the initiation of local buckling. A central web perforation was usually introduced in the finite element model by providing an equivalent quarter area to be free of finite elements, as shown in Figure 4.1(b). The sides of the perforation were considered to be free edges. Seven shell finite elements were considered to represent half the width and height of the web plate in the one quarter stub column, away from the perforation. However, the number of shell finite elements in the width and height directions of the web plate was increased adjacent to the perforation, according to the dimensions of the perforation itself. Figure 4.1(b) shows a sample finite element discretizations of the web plate around the perforation.

The normal vectors at the nodal points of the shell finite elements were not an input for the program. Instead, the program generated these normal vectors at each node. In the evaluation of the stiffness matrix and load vector of each element, a 3x3x3 Gauss Quadrature integration scheme was used in the mid-surface plane and through the thickness direction. The order of the integration scheme was enough to integrate exactly the elastic matrices of the 9-node shell finite element (Bathe, 1982). The largest total number of shell finite elements analyzed for a model of one quarter

CFS stub-column was 108 elements. The corresponding total number of nodal points was 594 nodes.

Symmetric boundary conditions were imposed at the symmetry lines of the quarter stub-column as shown in Figure 4.1(a). The symmetry lines indicated in the figure were assumed to have zero rotations around the centre lines, and zero in-plane displacements across the centre lines. Simply supported conditions were assumed at the bottom loaded edge of the stub-column. Therefore, this edge was assumed to have free displacement along the Y-direction and free out-of-plane rotations, but zero displacements along the X and Z-directions.

4.3.2 Material Properties

The results of the tensile coupon tests of cold-formed steel (CFS) sections, presented in Chapter Three, indicated that cold-formed steel material exhibits a gradual yielding behaviour, rather than a sharp yielding behaviour, and a considerable range of strain hardening. The results also indicated that a significant increase in the yield strength (F_y) occur at and around the corner areas of CFS sections. As a result of these observations, appropriate models for the stress-strain relationship and the distribution of yield strength across CFS channel sections were developed in Chapter Three. The developed stress-strain relationship represents an idealized elasto-plastic multi-linear strain hardening model to account for the gradual yielding and the strain hardening phenomena of CFS material. The developed yield strength distribution

represents an idealized non-uniform distribution model to account for the increased yield strength at the corner zones of CFS sections. The models were described in detail in Sections 3.3 and 3.4 of Chapter Three. The developed stress-strain relationship was incorporated in the current finite element analysis as a part of the elasto-plastic strain hardening model presented in section 2.2.4 of Chapter Two. Also, the developed yield strength distribution was incorporated in the finite element analysis by assigning appropriate yield strength values for the shell finite elements across the one quarter stub-column. These appropriate yield strength values followed the developed non-uniform yield strength distribution.

The assumed properties of CFS material for the finite element analysis were as follows: modulus of elasticity (E) of 203,000 MPa, two tangent moduli (E_{T1} and E_{T2}) of 100,000 MPa and 20,000 MPa representing the gradual yielding, tangent modulus (E_{T3}) of 1,000 MPa representing the strain hardening, and Poisson's ratio (ν) of 0.3. Different values of the yield strength (F_y) could be utilized in the finite element analysis according to the measured, or specified, yield strength of the CFS section.

4.3.3 Loading Technique

The cold-formed steel (CFS) stub-column was required to be centrally loaded to eliminate the effects of any eccentricity on the resulting deformations and stresses. Therefore, uniform compressive line loading was applied at the loading edge of the CFS stub-column. The modelling requirement of having the loading edge of the stub-

column flat and straight throughout the analysis was satisfied by employing a uniform axial displacement condition. This uniform displacement condition was achieved by applying the compressive loading through rigid plate elements, which were attached to the loading edge as shown in Figure 4.2. The rigid plate elements were restricted to undergo axial longitudinal displacement only in the Y-direction. The interface between the rigid loading plate elements and the loaded edge of the stub-column was modelled using short rigid truss elements. The out-of-plane rotations at the nodal points of these truss elements were fixed at the side of the rigid plate elements and kept free at the edge side of the stub-column. This would mean then, the nodal points at the loaded edge of the stub-column were kept under the condition of uniform displacement throughout the analysis by using the proposed loading system of rigid plate and truss elements. However, the distribution of load over the loaded edge of the CFS member was not necessarily uniform and could take any shape depending on the level of loading.

In fact, the proposed loading system simulates the case of having a bearing plate welded to the loaded edge of the stub-column. The bearing plate would keep the whole loaded edge at the same magnitude of axial displacement at any load level, but may distribute the load in a non-uniform sense. The bearing plate would also allow the loaded edge to rotate freely in the out-of-plane direction.

4.3.4 Imperfections

4.3.4.1 Geometric Imperfections

The application of geometric imperfections in the finite element model of cold-formed steel (CFS) compression members was required to initiate the local buckling mode of individual plate panels of the cross section. Although a local imperfection distribution may not have a great effect on the ultimate load of the member, it was found, from the current finite element study, that geometric imperfections have significant effects on the deformation behaviour up to the ultimate load.

Hancock (1981) suggested that the distribution of local plate imperfections in a CFS column may be assumed similar to the expected local buckling shape of the plate. The expected local buckling shape of a compression plate is a half wave in the transverse direction and a series of longitudinal waves, with half-wave lengths approximately equal to the plate width, in the longitudinal direction. For CFS lipped channel sections, which are composed of relatively deep webs connected to short flanges, numerical trials on channel stub-columns showed that the longitudinal half-wave length of the web plate is less than its width and is approximately equal to the average width of the web and the flange plates. Therefore, a double sine-wave distribution was used in the current finite element model for the geometric imperfection shape of the web plate of CFS channel stub-columns. The imperfection distribution (δ) in the transverse and the longitudinal directions is:

$$\delta = \delta_o \sin\left(\frac{\pi x}{w}\right) \sin\left(\frac{\pi y}{\bar{w}}\right) \qquad (4.1)$$

where (δ_o) is the imperfection amplitude at the central point of the web plate, (w) is the width of the web plate, and ($\bar{w}$) is the average width of the web and flange plates. The imperfection distribution is as shown in Figure 4.3. This form of distribution was used extensively by many researchers in the past to study imperfect compression steel plates (Korol and Sherbourne, 1972, Narayanan and Chow, 1984).

Kwon and Hancock (1991) investigated the magnitude of the imperfection amplitude (δ_o) on CFS channel sections. Amplitudes from 0.4 mm to 1.5 mm were measured for the web and flange plates of the channel sections. The examined sections had a web plate width of 120 mm, a flange plate width of 90 mm, an overall thickness of 1.1 mm, and a yield strength (F_y) of 590 MPa. The imperfection distributions were also noticed to have a wave-like shape on both sides of the straight plane of the plate. The British Steel Design Code suggests the use of the following formula as an upper limit for the imperfection amplitude (δ_o) of compression steel plates (Narayanan and Chow, 1984):

$$\frac{\delta_o}{t} = 0.145 \left(\frac{w}{t}\right) \sqrt{\frac{F_y}{E}} \qquad (4.2)$$

This formula gives the imperfection amplitude (δ_o) as a ratio of the plate thickness (t). The ratio (δ_o/t) is a function of the slenderness ratio (w/t) and the material properties

(E and F_y) of the plate. By comparing the experimental measurements of Kwon and Hancock (1991) to the predictions of Equation 4.2, the equation was found to predict reasonable limits for imperfection amplitudes. Hence, as Equation 4.2 gives an upper limit for the imperfection amplitude, a value of (δ_o/t) equal to half the value predicted by Equation 4.2 was used in the current finite element model to obtain the amplitude (δ_o) of the web plate of CFS stub-columns.

Similar imperfection distributions were not generated for the flange and lip plates of CFS lipped channel sections. The reason was that the short width of these plates usually makes the initiation of local buckling mode to occur in the web plate. However, the integrity of the channel section was maintained in the finite element model by keeping the right angle at the intersection of different plates of the section as shown in Figure 4.3.

4.3.4.2 Residual Stresses

The results of the residual stress tests of cold-formed steel (CFS) sections, presented in Chapter Three, showed that tensile residual stresses exist on the outside surfaces of CFS channel sections, and equivalent compression stresses exist on the inside surfaces of the sections. The results also showed that residual stresses in the longitudinal direction are the main residual stresses in the sections. A longitudinal residual stress distribution model was developed in Chapter Three based on the above observations. The proposed model represents a non-uniform distribution of

longitudinal residual stresses across a channel section, and a linear distribution through the thickness. The model was described in detail in section 3.6 of Chapter Three.

The developed longitudinal residual stress distribution was employed in the current finite element analysis. The residual stress distribution satisfied both force and moment equilibrium requirements within the finite element model. Residual stresses were treated as initial applied stresses within each shell element of the finite element model. The residual stress values were applied directly at the 3x3x3 Gaussian integration points for each shell element. As a linear variation was assumed for residual stresses through the thickness of CFS sections, the two surface sets of integration points of each shell finite element were assigned equal, but opposite, values of residual stresses. The mid-plane set of integration points had zero residual stresses. Figure 4.4 shows the integration points and the distribution of longitudinal residual stresses for a typical shell element. The resulting residual stress vector (σ_0) for each shell finite element was transformed into an initial load vector (f_0), which contributes to the equilibrium equations, as follows :

$$f_0 = \int_v B_0^T \sigma_0 \, dV \tag{4.3}$$

where $[B_0]$ is the linear strain-displacement matrix of the shell finite element.

4.3.5 Method of Analysis

The general solution technique for the large deformation elasto-plastic finite element analysis was described in section 2.5.1 of Chapter Two. However, this section is concerned with the particular method of analysis employed for cold-formed steel (CFS) members in compression.

A cold-formed steel stub-column was subjected to incremental uniform axial displacements over the loading edge. A constant axial displacement increment was chosen in the range of 5% of the displacement corresponding to the expected ultimate load of the stub-column. This displacement increment allowed the ultimate load to be reached in about 20 solution steps. A displacement control algorithm was included in the general finite element program, and used to perform the incremental analysis. The algorithm is based on the unified constraint procedure, which enables different control methods to be implemented according to the definition of the control parameters (Kanok-Nukulchai, 1990). A description of the unified constraint algorithm and its use to solve a set of equilibrium equations of a discrete finite element system is presented in Appendix C. The displacement control algorithm allowed the incrementation of the axial displacement at one control node within the finite element mesh. This control node was selected at the edge of the CFS stub-column. According to the loading technique described in Section 4.3.3, the utilized rigid plate elements at the edge of the stub-column maintained all the edge nodes at the same axial displacement value for every solution step.

A displacement convergence criterion was used, as discussed in section 2.5.1 of Chapter Two, to accept the solution at the end of each solution step of the nonlinear finite element analysis. The criterion required that the displacement increments resulting from a solution iteration to be within a prescribed tolerance of the total displacement increments for that particular solution step. The prescribed tolerance was set to 0.001 in the current analysis. The solution for each displacement step generally needed three to six iterations to reach that prescribed tolerance.

The solution of the governing equilibrium equations resulted in the load intensity at load/support nodes, and the displacement vector at other nodes for each solution step. The incrementation of axial displacements was continued until the load intensity started to decrease, which indicated that the ultimate load of the stub-column has been reached. The use of the displacement control algorithm enabled the finite element analysis to extend beyond the ultimate load, where the load capacity decreases while axial displacements increase. This gave the current solution the advantages of: [a] predicting the magnitude of the ultimate load precisely, and [b] predicting the descending load-deformation behaviour (post-ultimate behaviour) of the stub-column.

Before proceeding further with the analysis of CFS members in compression, the accuracy and the efficiency of the developed finite element model was verified using experimental results of stub-column tests. The following section presents the setup and procedure of the stub-column tests, and the next section presents the test

results and the comparison with the finite element results.

4.4 Stub-Column Tests

A set of 20 non-perforated and perforated stub-column tests were performed in order to verify the results of the finite element model for cold-formed steel (CFS) channel sections in compression. Two different zinc-coated lipped channel sections of steel Grade A 446/A 446M (ASTM, 1994a) were used in the study. The first section (Sec. A) was 203 mm (8 in.) deep, Grade D steel (345 MPa), and the second section (Sec. B) was 101.5 mm (4 in.) deep, Grade A steel (228 MPa). The two sections used in the stub-column tests were the same sections used for the material properties study presented in Chapter Three. The measured flat material yield strength for sections (A) and (B) were 385 MPa and 319 MPa, respectively.

The measured flat widths of the plate elements of the test sections (A) and (B) (w, w_f, and w_l as shown in Figure 4.5) and their base metal thickness (t) are given in Table 4.1. The minimum base metal thickness for a section was obtained by excluding the average thickness of the zinc coating layer. The thickness of the coating layer was determined using the provision A 90/A 90M of the American testing standards (ASTM, 1994c). The average thickness of the zinc coating layer was found to be 0.04 mm and 0.031 mm for sections (A) and (B), respectively.

4.4.1 Preparation of Stub-Column Specimens

The non-perforated and perforated stub-columns were cut to the specified lengths as shown in Table 4.2. The length of the non-perforated stub-columns was first based on three times the overall web width (3w′) in some experimental trials. It was found that the length had to be reduced in order to locate the failure of the stub-columns at their mid-height section. Hence, the length of non-perforated stub-columns in Table 4.2 represents three times the average overall width of the web and the flange of the cross section ($3\ [\frac{w' + w_f'}{2}]$). The length of perforated stub-columns was chosen to be more than that for non-perforated stub-columns, with an increase proportional to the increase of the perforation height. This was done in order to avoid any end loading effects on the capacity of the perforated stub-columns.

Wood blocks were inserted into the channel sections during the cutting process in order to prevent any sectional deformations. The ends of the stub-columns were filed and levelled at right angle to the longitudinal axis of the column. Whenever needed, perforations were then machined into the webs of the stub-columns (except of oval perforations which were made by the manufacturer). The shapes and dimensions of perforations are also given in Table 4.2. The perforation width (a) was selected equal to the available width of the oval perforation of the manufacturer. However, three other shapes of perforations (circular, square, and rectangular) were selected to investigate the effects of the perforation shape and height on the ultimate capacity and behaviour of the stub-columns.

Two steel bearing plates (thickness 12 mm) were centrally connected to both ends of each stub-column. The bearing plates were needed to distribute the load uniformly on both ends of the stub-column. The connection between the stub-column and the bearing plates was established using the epoxy bonding material, Sikadur 31 Hi-Mod Gel, provided by Sika Canada Inc. The Sikadur 31 Hi-Mod Gel is a two-component high strength structural adhesive which gains its full strength after three to seven days. This epoxy material was used as a replacement for welding, as the initial trials showed that welding heat causes substantial permanent damages and distortions to cold-formed steel sections. The epoxy material helped filling any minor gaps between the specimen edges and the bearing plates, plus providing full contact loading on the two ends of the stub-column. The zinc coating layer at the positions of the strain gauges were then removed using a 50% solution of the hydrochloric acid, and cleaned carefully with fine sand paper and alcohol solution.

4.4.2 Data Acquisition

One of the objectives of the stub-column tests was to obtain the deformation behaviour and stress distribution of individual plate components of the specimens. In order to do that, six Linear Variable Displacement Transducers (LVDT) were used to measure the axial and lateral displacements at different locations of the stub-column. Also, electrical resistance strain gauges were mounted, according to the manufacturer procedure, at the mid-height level of each stub-column to monitor the

strain change throughout the test. Figure 4.6 shows the test setup along with the locations of the displacement transducers and the strain gauges.

As two identical specimens for each stub-column were tested, the first specimen had only four strain gauges (Gauges 1 to 4) to check the loading uniformity at the early stage of the test, as further explained in the next section . However, the second specimen had ten strain gauges (Gauges 1 to 10) for the same above-mentioned purpose and also to obtain the strain distribution across the section. The displacement transducers and the strain gauges were connected to a 40 channel data acquisition system, Autodata Nine 3A, which was set to read the displacement and strain data at a rate of 12 readings /min. A real time display of the load-deformation behaviour and the stress distribution across the test specimen was obtained by connecting a personal computer with a "Lab-Tech Notebook" computer software to the data acquisition system.

4.4.3 Test Setup and Procedure

The stub-column specimens were tested in a 600-kN capacity Tinius-Olsen Universal Testing Machine. However, load ranges of 300 kN and 120 kN were used for the specimens of section (A) and section (B), respectively. A 15 mm layer of quick setting grout was first placed on the bed of the testing machine and left to harden. The stub-column specimen, with the attached bearing plates, was then geometrically centred in the testing machine over the grout layer. Another 15 mm

grout layer was placed between the top bearing plate and the moving head of the machine. The bottom grout layers worked as a bed for the stub-column specimen, while the top grout layer helped to distribute the load uniformly and correct any out-of-parallelism of the ends of the specimen. The readings of all the strain gauges were then initialized.

The centring of the specimen was checked by loading the stub-column gradually to a load of about 20% of the expected ultimate load and the reading differences between the four corner strain gauges were verified to be less than 10%. If this condition was not met, the position of the specimen was shifted and a thin layer of cement powder was inserted between the top grout layer and the moving machine head to redistribute the load. When the four corner readings were within 10% of each others, the specimen was unloaded to a small load (about 1 kN) and the displacement transducers were attached to it. All the readings were then initialized in order to start the test.

The test was conducted at a continuous displacement rate of 0.038 mm/min. (0.0015 in./min.) up to the ultimate load of the stub-column. At a load of about 5 kN, steel wedges were inserted between the moving head and the frame of the testing machine to prevent the rotation of the moving head, which may occur when the specimen starts to locally buckle. Loading was continued at the constant displacement rate until the specimen failed and the load started to drop. The displacement rate was then increased to 0.076 mm/min. (0.003 in./min.), and the test

was continued until the load dropped to about half the failure load in order to magnify the failure shape.

Figure 4.7 shows a typical stub-column specimen of section (A) with an oval perforation. The figure shows the stub-column specimen with the attached strain gauges and displacement transducers before testing and after failure inside the testing machine. Figure 4.8 shows the real time display of the load-axial displacement and the load-lateral displacement relationships on the computer screen. Numerical values of the machine axial load and the readings of different strain gauges were also shown on the screen during the test. Figure 4.9 shows eight test specimens of sections (A) and (B) after failure. It can be noticed in the figure that local buckling and complete failure of the perforated specimens occurred generally at the perforation location, and at the mid-height section of the specimens. The non-perforated specimens were noticed to have local buckling to start at the mid-height section, however, complete failure of the specimens was sometimes shifted marginally from that mid-height section.

4.5 Test Results and Comparison with Finite Element Results

The readings of the two axial displacement transducers were averaged to obtain one set of axial displacement readings for each stub-column test. The same procedure was also done for the two lateral web displacement transducers around the perforation. The two axial displacement reading sets were normally found similar

without significant differences. However, the two lateral web displacement reading sets of section (B) specimens were sometimes found to be different as failure around the perforation was not symmetric (specimens B-S2, B-O1, B-R1, and B-R2). Nevertheless, the displacement readings were also averaged for such cases.

Finite element models representing the ten different test cases of stub-column specimens were analyzed. The exact lengths and dimensions of the specimens were used in the finite element models. The modelling techniques for boundary conditions, material properties, imperfections, loading, and method of analysis were described earlier in section 4.3. The yield strength (F_y) of the stub-column specimens was used according to the measured values from the tensile coupon tests presented in Chapter Three (385 MPa for section (A) and 319 MPa for section (B)). The increased yield strength (F_{yc}) at the corner zones of the stub-columns was calculated as 464 MPa for the (F_y) of 385 MPa, and 358 MPa for the (F_y) of 319 MPa, according to Equation 3.3. The calculations are based on a measured ratio of the ultimate tensile strength to the yield strength (F_u / F_y) of 1.23 for section (A) and 1.13 for section (B).

The shape of the stub-column specimens after failure indicated that the epoxy material, which was used to connect the bearing plates to the stub-columns, minimized the out-of-plane rotations at the stub-column edges. The applied epoxy layer was thick enough to fasten the plates to the stub-column edges and minimize these rotations. Therefore, this situation was simulated in the finite element model by locking the out-of-plane rotational degrees-of-freedom between the loaded edge of

the stub-columns and the rigid loading truss elements. Hence, the loading system of the finite element model, which consists of the rigid plate and truss elements, imposed a uniform displacement condition and prevented the out-of-plane rotations at the loading edge of the stub-columns.

4.5.1 Deformation Behaviour

The deformation behaviour of the stub-column specimens is shown in Figures 4.10 through 4.13. The deformations predicted by the finite element analysis are also shown in the same figures. Figures 4.10(a) to (f) show the load-axial displacement behaviour, the load-lateral web displacement behaviour, and the load-lateral flange displacement behaviour for section (A). Figures 4.11(a) and (b) show the load-axial strain behaviour for section (A). Figures 4.12(a) to (f) and 4.13(a) and (b) show the same above mentioned behaviour, but for section (B).

4.5.1.1 Axial Displacement

The two identical specimens of each stub-column test resulted in a consistent axial displacement behaviour as shown in Figures 4.10 and 4.12 for sections (A) and (B), respectively. The finite element analysis also predicted a consistent behaviour with the test specimens throughout the full loading range, including the post-ultimate range where the load started to drop. The total magnitudes of axial displacement experienced by the stub-column specimens of section (A) were as much as double the

corresponding magnitudes of the specimens of section (B). This is due to the fact that the specimens of section (A) are longer, and exhibited more lateral displacements than the specimens of section (B).

A comparison between the behaviour of the non-perforated specimens (marked D) and the specimens with circular and square perforation (marked C and S), for both sections (A) and (B), show a reduction in the stiffness of the perforated specimens. This stiffness reduction is demonstrated by a drop in the initial slope of the load-displacement curve. The reduction in the stiffness associated with the specimens with oval and rectangular perforation (marked O and R) is higher than that for specimens with circular and square perforation. This indicates that not only the width of perforation is a main factor in reducing the stiffness of the stub-columns, but also the height of perforation is another factor in reducing that stiffness.

4.5.1.2 Lateral Web and Flange Displacement

The lateral web displacement was recorded at two different positions of the stub-columns; the central point of the web (or the side of perforation) at the mid-height section, and the quarter-height point from the top end. The load-lateral displacement behaviour at the two positions is plotted on the same figure for each of the stub-column test cases. This behaviour is shown in Figure 4.10 for section (A) and Figure 4.12 for section (B). It can be noticed from the figures that, in some cases, the lateral displacement behaviour of the two identical stub-column specimens

is not consistent with each other, and with the predictions of the finite element analysis. One reason for these differences is that failure of the test specimen may take place at a section near the middle section of the stub-column, but not exactly at the mid-height section. This causes the crests of the buckled specimens to occur at locations other than the locations where the displacement transducers were attached. Another reason is that the lateral displacement behaviour depends largely on the actual geometric imperfections shape of the stub-column specimen.

The figures show that lateral displacements at both of the central point and the quarter point started to increase initially in the same outward direction of the web. Then, with the initiation of local buckling, the quarter point displacement changed to the inward direction while the central point displacement kept propagating in the outward direction. This is a clear indication that the webs of the stub-columns buckled in a series of longitudinal waves with a half-wave length value between the web width and the flange width.

Figure 4.10 shows that perforated stub-column specimens of section (A) achieved more lateral displacements at the central point of the web than the non-perforated ones. Specimens with oval and rectangular perforation showed more lateral displacements than specimens with circular and square perforation. The same behaviour can be noticed for section (B) in Figure 4.12, except for the specimens with rectangular perforation (B-R) which showed little lateral displacements up to the failure load.

The lateral flange displacement was recorded at the central point of the flange at the mid-height section of the stub-columns. The typical flange behaviour of the specimens of section (A) and section (B) are shown in Figures 4.10(f) and 4.12(f), respectively. The figures indicate that the lateral flange displacement of section (A) increased gradually, in the inward direction of the section, up to about 1.5 mm at ultimate load. However, section (B) showed very little lateral flange displacement, only up to about 0.3 mm at ultimate load, but the displacement increased significantly as failure propagated in the section.

4.5.1.3 Axial Strain

The typical strain behaviour of the specimens of section (A) and section (B) are shown in Figures 4.11 and 4.13, respectively. The positions of the strain gauges at the mid-height cross-section of the stub-column specimens are shown in Figure 4.6.

The figures indicate that the corner strain gauges showed a consistent compressive strain increase at the four corners of both sections (A) and (B) up to complete failure. Web strain gauges showed a starting compressive strain increase on the outside and inside surfaces of the web. However, with the initiation of local buckling, the strain on the outside surface (Gauges 5 and 7) changed to tension while the strain on the inside surface (Gauges 6 and 8) kept increasing in compression. Flange strain gauges did not show any evidence of local flange buckling similar to that of the web, as the two gauges on the outside and inside surfaces (Gauges 9 and 10)

showed a consistent strain behaviour up to complete failure.

4.5.2 Buckling Loads

The experimental and finite element buckling loads of the stub-column specimens are reported in Table 4.3. The experimental buckling loads were obtained using two classical methods; [a] the "Inflection Point" method which is based on load versus lateral deflection readings, and [b] the "Strain Reversal" method which is based on load versus strain readings. In the Inflection Point method, the buckling load is defined as the load corresponding to a point with a maximum rate of increase of lateral deflection with respect to load; i.e., minimum slope (Schlack, 1968). In the Strain Reversal method, the buckling load is the load corresponding to the maximum compressive strain on the convex side of the buckled plate (Stowell, et al., 1951). The finite element buckling loads were obtained using the Inflection Point method only, as no strain output was recorded from the finite element analysis.

The reported buckling loads in Table 4.3 indicate that the estimation of the buckling load depends largely on the method used. The Strain Reversal method generally predicted lower buckling loads than the Inflection Point method. This is due to the plate geometric imperfections which cause strain reversal to occur well before reaching a complete buckling of the plate. The effects of geometric imperfections were more pronounced in the results associated with section (A) than section (B), as the former has larger slenderness ratio of the web plate.

The buckling loads of perforated stub-column specimens were found to be less than the corresponding buckling loads of non-perforated specimens. Similar behaviour was noticed by Yu and Davis (1973), Narayanan and Chow (1984), and Banwait (1987). This is due to the fact that the perforation in the centre of the web plate changes its local buckling condition from one stiffened plate to two unstiffened plates from the side of the perforation. The unstiffened plates caused the web plate to locally buckle at a stress value less than that for one stiffened web plate. No definite effects were noticed for the perforation shape on the buckling loads. The change in the buckling loads with various shapes of perforation was different for section (A) than section (B). The effects of the perforation size on buckling loads were not investigated in the current study, as all perforated specimens for each section had the same perforation width.

It has to be mentioned here that, despite of all the difficulties associated with the determination of the buckling loads of cold-formed steel members in compression, the magnitude of the buckling load may not be a valuable quantity when ultimate design is considered. Perhaps the buckling load can be merely considered as the load at which excessive lateral deflections occur in the compression member.

4.5.3 Ultimate Loads

The experimental and finite element ultimate loads of the stub-column specimens are reported in Table 4.3. The experimental ultimate load is the largest

load value reached during the test before the load started to drop. It can be noticed from the table that the ultimate loads of perforated stub-column specimens were less than the corresponding ultimate loads of non-perforated specimens. This is due to the loss of material at the central sections of perforated stub-columns. It can also be noticed that the ultimate loads decreased with the increase of the height of perforation. However, there were little differences (less than 2.5%) between the ultimate load results of specimens with circular and square perforation. Also, there were little differences between the ultimate load results of specimens with oval and rectangular perforation (larger height). This indicates that the shape of perforation had little effect on the expected ultimate loads. This behaviour can be concluded clearly from the finite element results rather than the experimental results, as the former results are more consistent than later ones.

The drop in the ultimate load due to a 33% web perforation width of section (A) was 3% for circular and square perforation, and was 6% for oval and rectangular perforation. The drop in the ultimate load due to a 41% web perforation width of section (B) was 6% for circular and square perforation, and was 11% for oval and rectangular perforation. The loss in the ultimate load of perforated stub-column specimens of section (B) is more pronounced than that of section (A). This behaviour was expected as the slenderness ratio (w/t) of the web plate of section (B) is lower than (w/t) for section (A). A stocky compression plate having a certain perforation is expected to lose more strength than a corresponding slender compression plate

having the same perforation.

4.5.4 Axial Stress Distribution

The axial stress distributions at the mid-height section of the stub-column specimens are shown in Figures 4.14(a) to (e) for section (A), and in Figures 4.15(a) to (e) for section (B). The stress distributions shown correspond to the buckling load and the ultimate load levels for each test case. The experimental results are shown in the figures, at the locations where they have been recorded, using data marks, while the finite element results are shown using continuous lines. The experimental axial stress results were obtained by transferring the recorded axial strains to stresses using the corresponding experimental stress-strain relationships displayed in Chapter Three. Although this procedure is not exact since the axial strains only are not enough to predict axial stresses, the stresses so obtained were approximately correct as stub-column specimens were primarily subjected to axial loading. This axial loading produced major strains in the axial direction and minor strains in other directions.

The stress distributions for section (A) show a consistent agreement between the test results and the finite element results. The consistency is better at the buckling load level than at the ultimate load level. This behaviour is due to that some unpredicted deformations may occur at the ultimate load level, where failure start to take place. Stress concentrations are noticed at locations adjacent to the perforation at the buckling load level for perforated specimens, compared to the non-perforated

specimen (A-D). These stress concentrations can be interpreted as a transfer of the stresses which were supported by the area of the perforation. The stress concentrations disappeared at the ultimate load level, due to the large lateral web displacements which occur at that load level. The large lateral displacements usually cause the web to support less compression stresses, and consequently less axial load. The stress peaks at the ultimate load level correspond to the corner zones of the stub-column specimens. The corner zones of cold-formed steel (CFS) compression members are generally expected to support higher compression stresses, than flat zones, as a result of their higher yield strength and ultimate strength. This behaviour was incorporated in the current finite element model of the stub-column specimens.

The stress distributions for section (B) show a similar behaviour for that of section (A). A consistent agreement was found between the test results and the finite element results. However in few test cases (particularly B-D and B-S), some discrepancy is noticed in the test results. The reason was that failure occurred away from the mid-height section of the stub-column specimens. As a result, the readings of the strain gauges, located at the mid-height section, were different than the readings at the failure section. The stress distributions at the buckling load level for section (B) are not uniform as observed for section (A). This is because the buckling stress value of the web plate of section (B) was close to its yield strength value, while the buckling stress value of section (A) was about 30% of its yield strength value. The stress distribution results for section (B) show stress concentrations similar to the

concentrations mentioned for section (A). The stress concentrations disappeared at the ultimate load level, and the stresses adjacent to the perforation dropped significantly due to the large lateral web displacements.

4.6 Summary

The modelling requirements for a finite element model of cold-formed steel (CFS) members in compression have been presented and discussed. These requirements included the properties for the finite element chosen to represent the CFS sections, the different methods to eliminate the overall buckling mode of the compression members, the lateral imperfection shapes to initiate the local buckling mode, and the loading techniques to obtain a uniform displacement condition over the compression members. A finite element model was then developed for channel-shaped CFS compression members based on the discussed modelling requirements. The model utilized the 9-node large deformation elasto-plastic shell finite element to represent the body of CFS sections. The model also utilized the idealizations of the CFS material mechanical properties and residual stresses presented in Chapter Three. Special loading system and displacement solution algorithm were employed to obtain a uniform displacement condition at the loading edges of the compression members. A double sine-wave distribution was used for the geometric imperfections shape of the web plates of the members to initiate the local buckling mode of individual plate panels. The finite element model of CFS compression members was flexible enough

to accommodate different shapes of web perforations.

The testing procedure and the results of 20 non-perforated and perforated CFS stub-column tests have been presented. The tests were performed to verify the results of the finite element model and to investigate the behaviour of perforated CFS stub-columns. The comparison between the test results and the finite element results was performed for axial and lateral displacement behaviour, axial strain, buckling loads, ultimate loads, and axial stress distribution. The comparison indicated that the finite element analysis generally gave consistent agreement with the test results. The finite element model was capable of predicting the same deformation behaviour of the test results. Predictions for the buckling loads, ultimate loads, and stress distribution were also comparable to the test results. Perforated stub-column specimens showed lower axial stiffness than the non-perforated specimens. The perforation width and height were main factors in reducing the stiffness of the specimens. Perforated stub-column specimens also showed lower buckling and ultimate loads than the non-perforated specimens.

Table 4.1 Measured flat cross-sectional dimensions of test specimens[a]

Section	w (mm)	w_f (mm)	w_l (mm)	t (mm)	w / t	w_f / t	w_l / t
(A)	191.7	30.3	7.4	1.88	102.0	16.1	3.9
(B)	93.9	34.0	9.4	1.27	73.9	26.8	7.4

[a] Refer to Figure 4.5 for notations

Table 4.2 Dimensions of stub-columns[a]

Section	Specimen	Perforation shape	Length L (mm)	Perforation dimensions		
				a (mm)	h (mm)	R (mm)
(A)	A-D1 , A-D2	-None-	365.0	---	---	---
	A-C1 , A-C2	Circle	425.0	63.5	63.5	31.8
	A-S1 , A-S2	Square	425.0	63.5	63.5	---
	A-O1 , A-O2	Oval	475.0	63.5	114.3	31.8
	A-R1 , A-R2	Rectangle	475.0	63.5	114.3	---
(B)	B-D1 , B-D2	-None-	215.0	---	---	---
	B-C1 , B-C2	Circle	250.0	38.1	38.1	19.1
	B-S1 , B-S2	Square	250.0	38.1	38.1	---
	B-O1 , B-O2	Oval	300.0	38.1	101.6	19.1
	B-R1 , B-R2	Rectangle	300.0	38.1	101.6	---

[a] Refer to Figure 4.5 for notations

Table 4.3 Experimental and finite element results of test specimens

Sec.	Specimen	Experimental buckling load (kN)		F. E. buckling load (kN)	Experimental ultimate load (kN)	F. E. ultimate load (kN)
		Inflection point	Strain reversal	Inflection point		
(A)	A-D1	76.2	---	61.8	130.3	125.3
	A-D2	86.6	46.8		126.8	
	A-C1	70.6	---	53.8	114.3	121.9
	A-C2	80.1	43.6		121.5	
	A-S1	69.3	---	59.2	114.3	121.0
	A-S2	72.4	45.5		123.8	
	A-O1	---	---	53.0	117.3	119.1
	A-O2	---	34.0		119.0	
	A-R1	70.9	---	57.6	111.8	117.1
	A-R2	74.9	40.9		117.3	
(B)	B-D1	54.4	---	48.2	64.5	60.9
	B-D2	53.5	47.2		66.0	
	B-C1	43.4	---	46.0	58.1	58.4
	B-C2	42.6	35.6		55.3	
	B-S1	51.5	---	45.1	59.2	56.7
	B-S2	47.8	44.1		53.6	
	B-O1	36.7	---	47.8	57.4	54.8
	B-O2	39.0	25.8		54.8	
	B-R1	45.9	---	47.3	56.7	53.8
	B-R2	48.9	44.6		57.1	

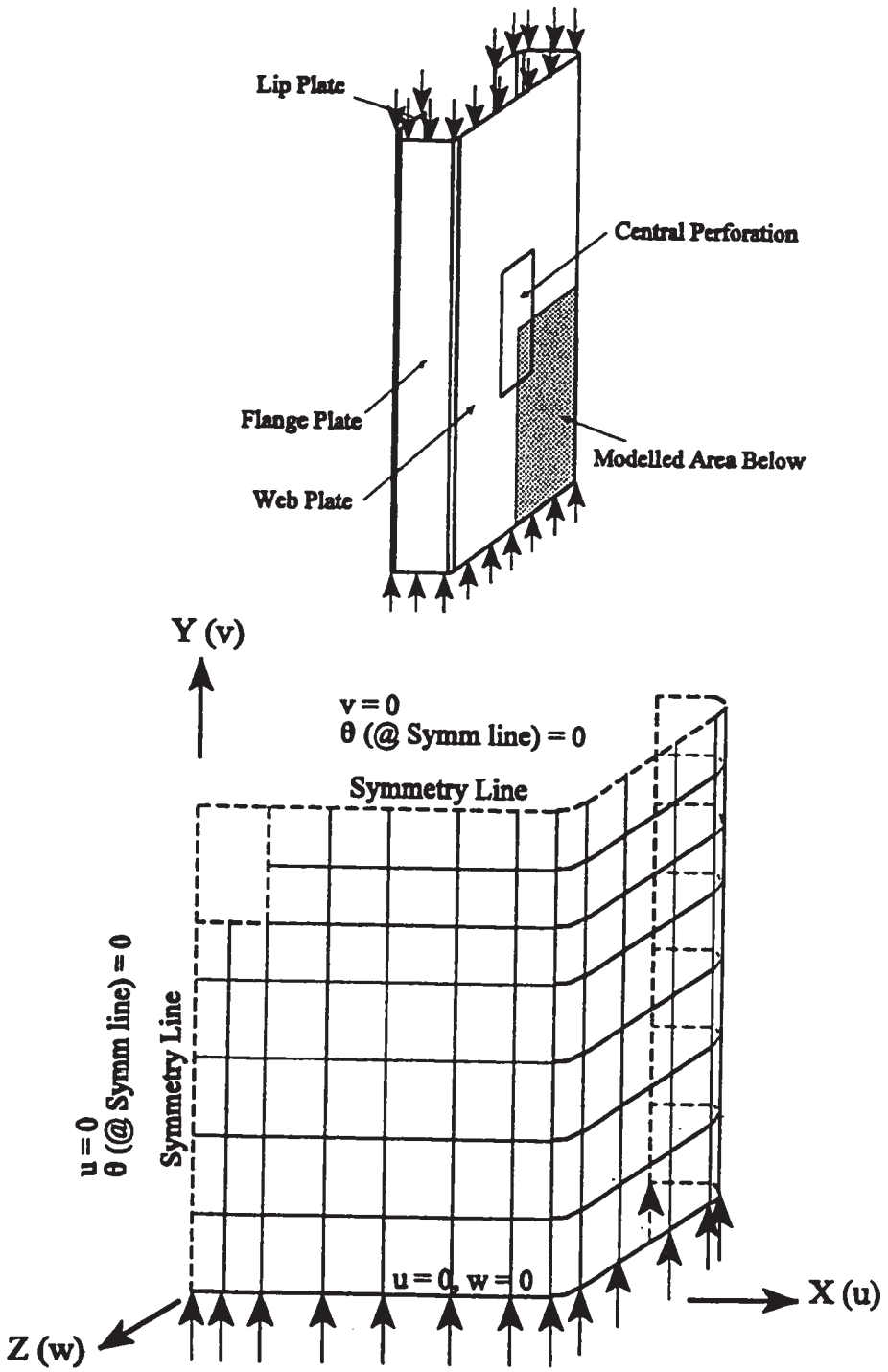

Figure 4.1(a) The finite element model of one-quarter of a stub-column

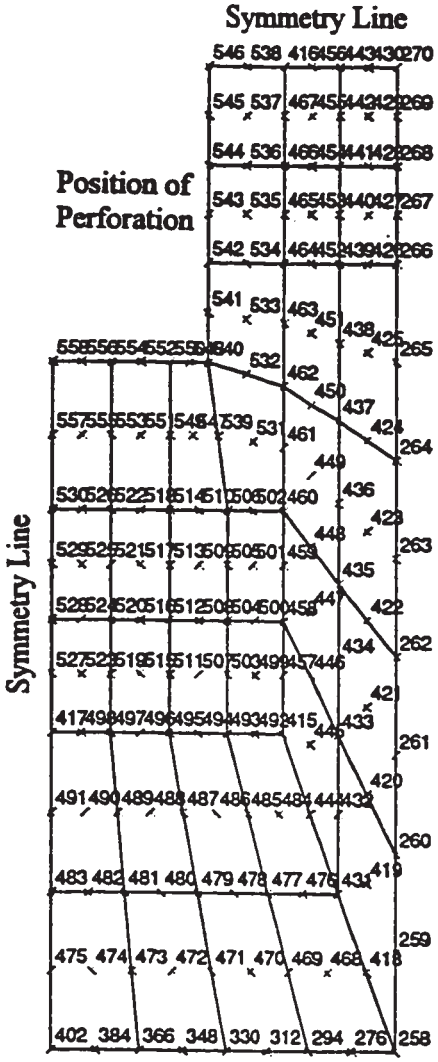

Figure 4.1(b) Typical finite element discretization around the perforation in a stub-column

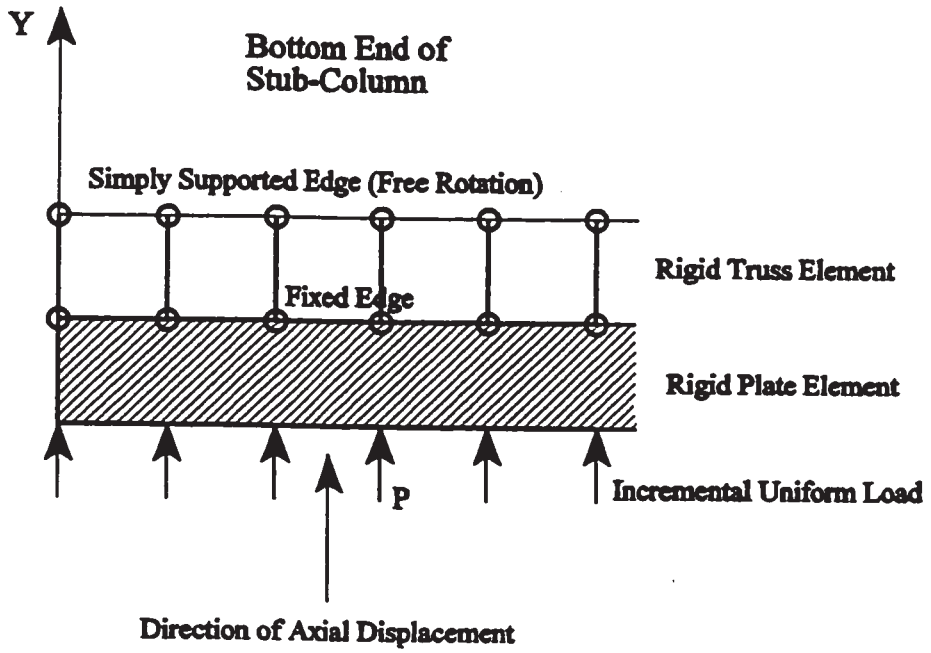

Figure 4.2 Loading technique at the edges of the stub-column

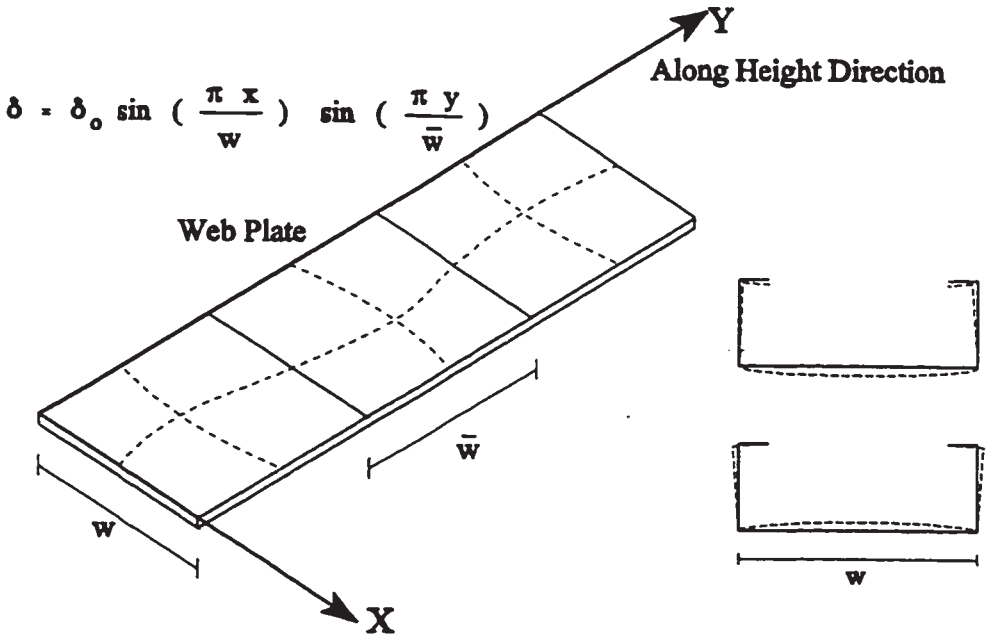

Figure 4.3 Geometric imperfection shape of different plates of a stub-column

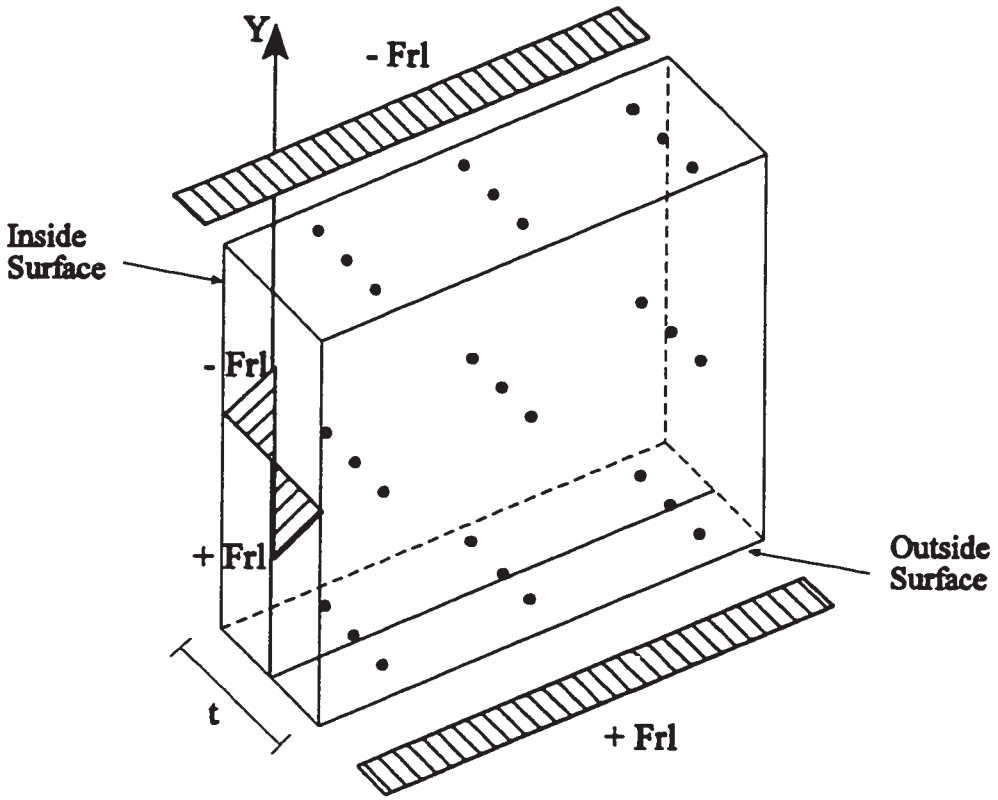

Figure 4.4 Distribution of integration points and longitudinal residual stresses within a shell finite element

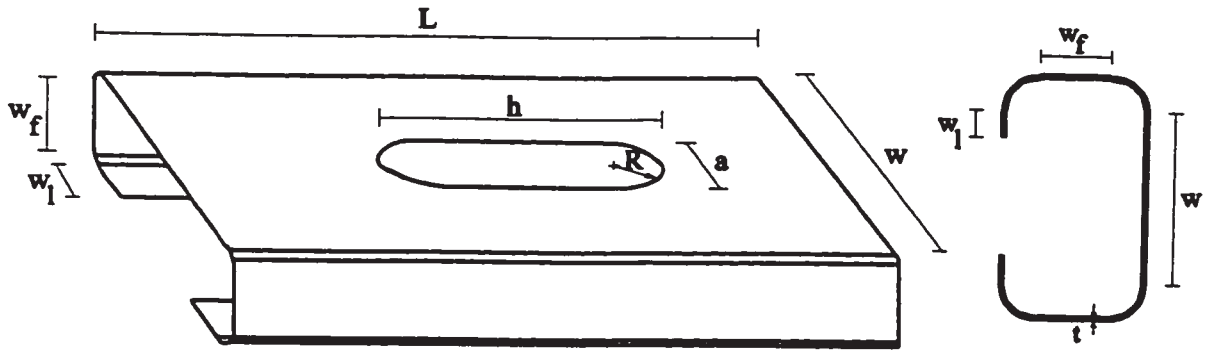

Figure 4.5 Typical dimensions of a stub-column

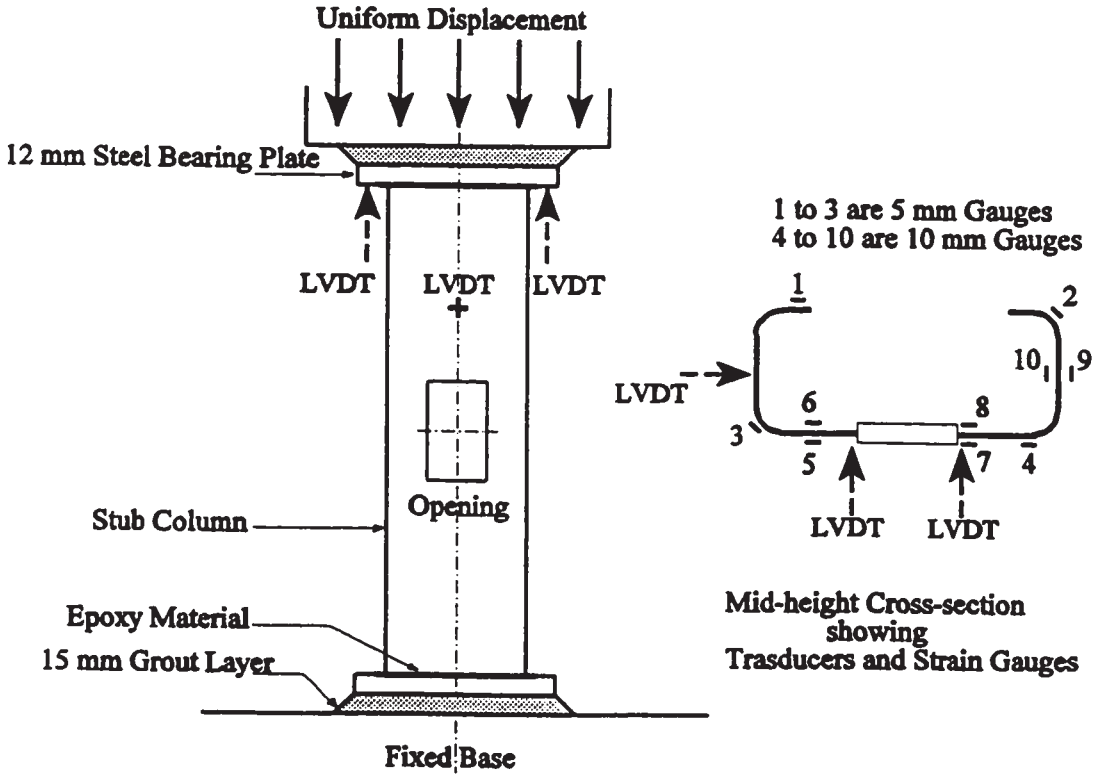

Figure 4.6 Setup and measuring devices of the stub-column test

(a) Specimen ready for testing (b) Specimen after failure

Figure 4.7 Stub-column specimen of section (A) with oval perforation

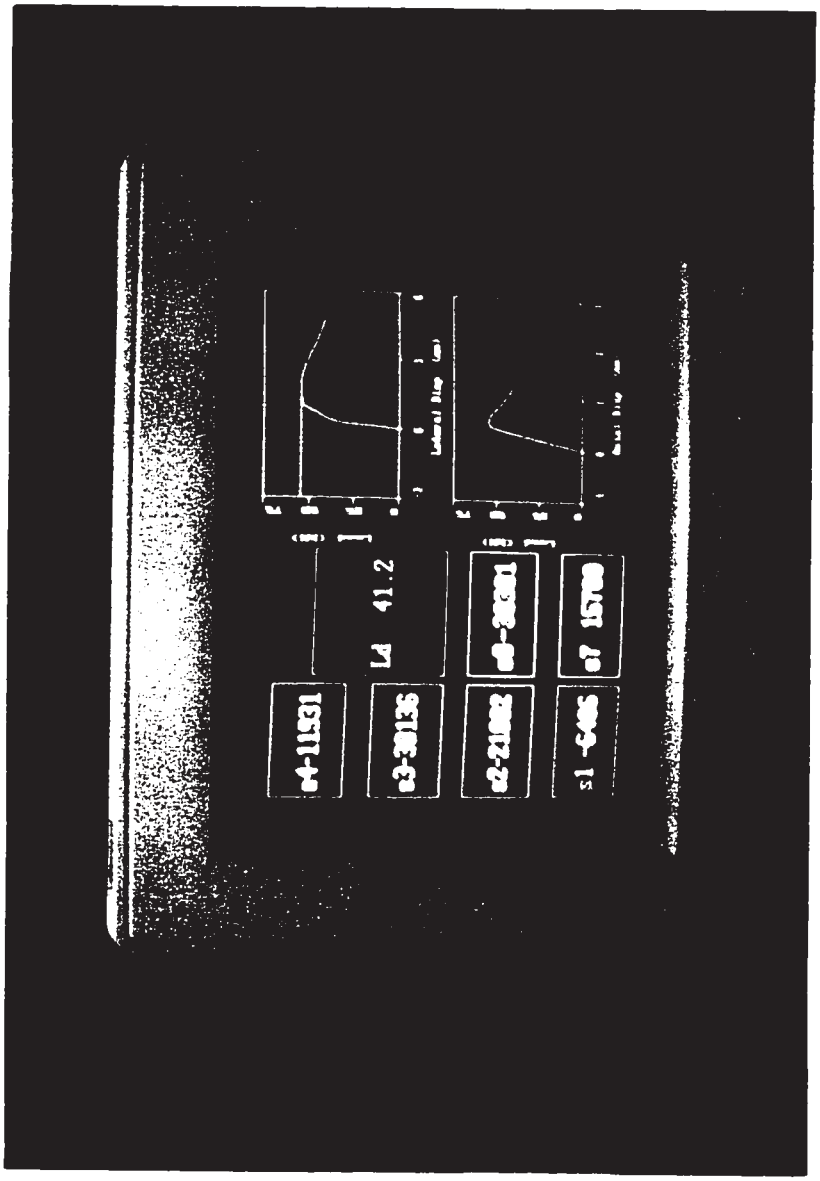

Figure 4.8 Real time display of the load-displacement behaviour and axial strains of a cold-formed steel specimen

Figure 4.9 A sample of cold-formed steel test specimens after failure

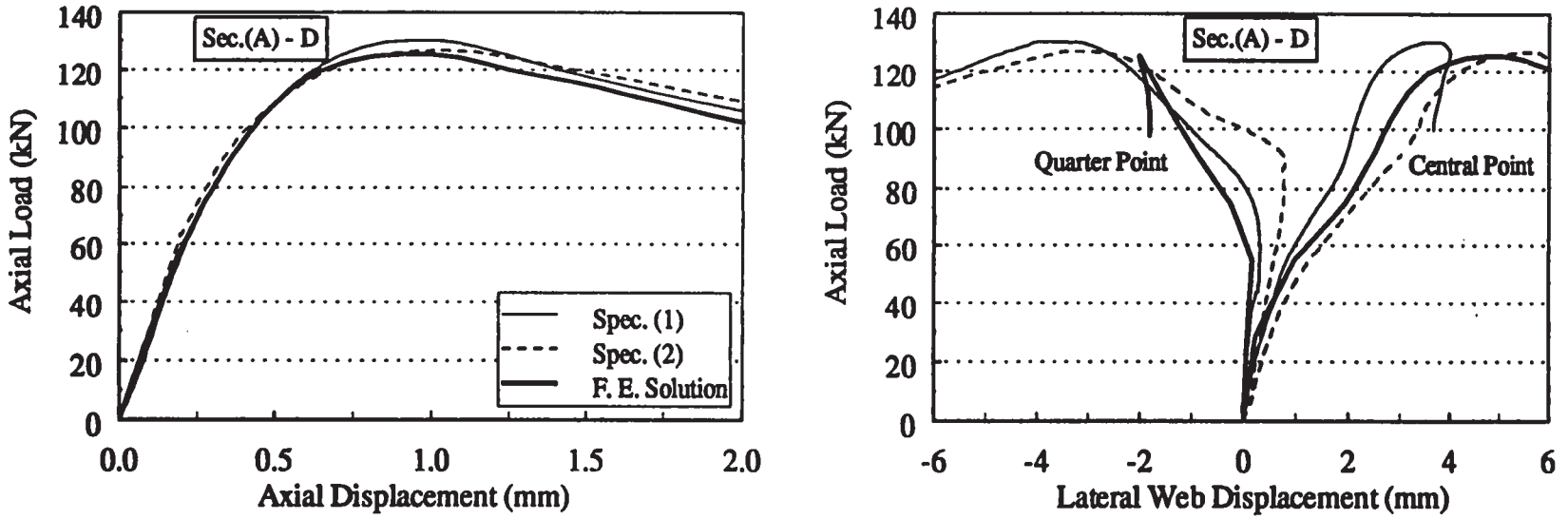

Figure 4.10(a) Measured and predicted F.E. sec. (A) deformation (No perforation)

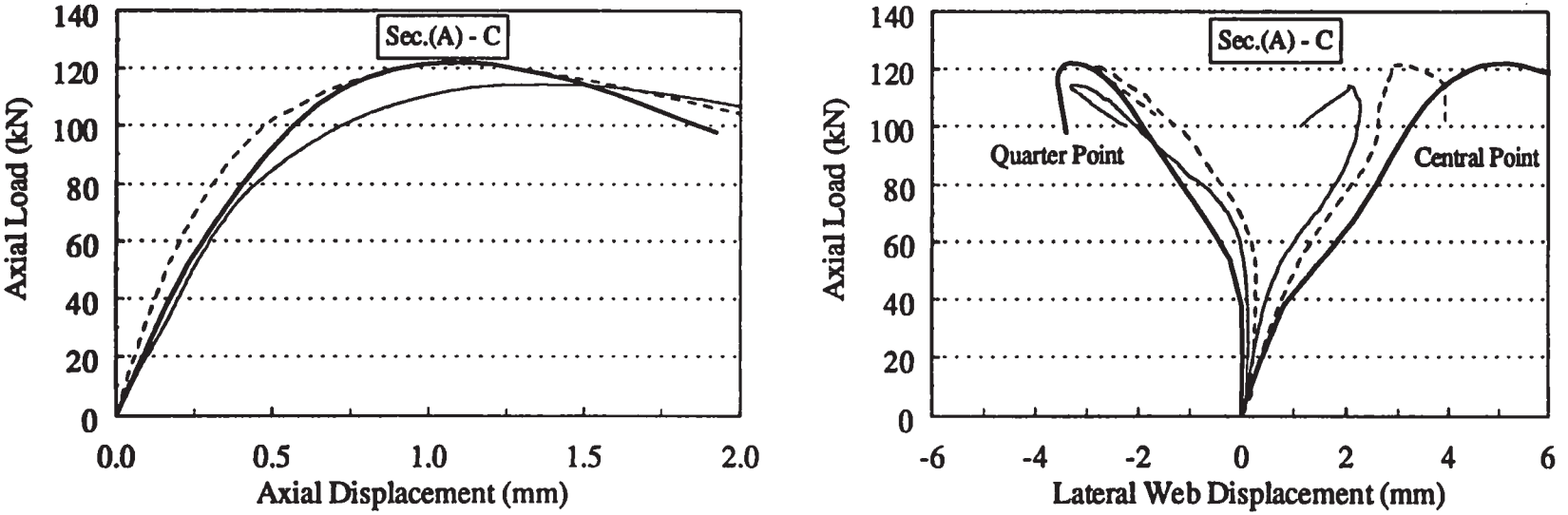

Figure 4.10(b) Measured and predicted F.E. sec. (A) deformation (Circular perforation)

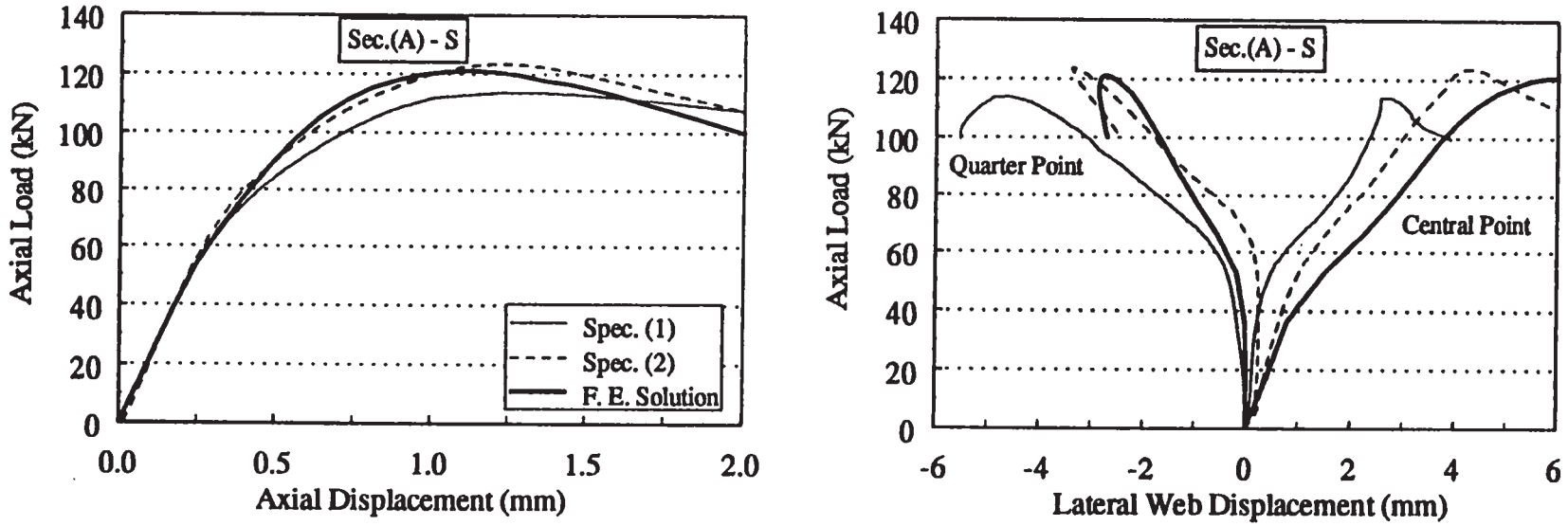

Figure 4.10(c) Measured and predicted F.E. sec. (A) deformation (Square perforation)

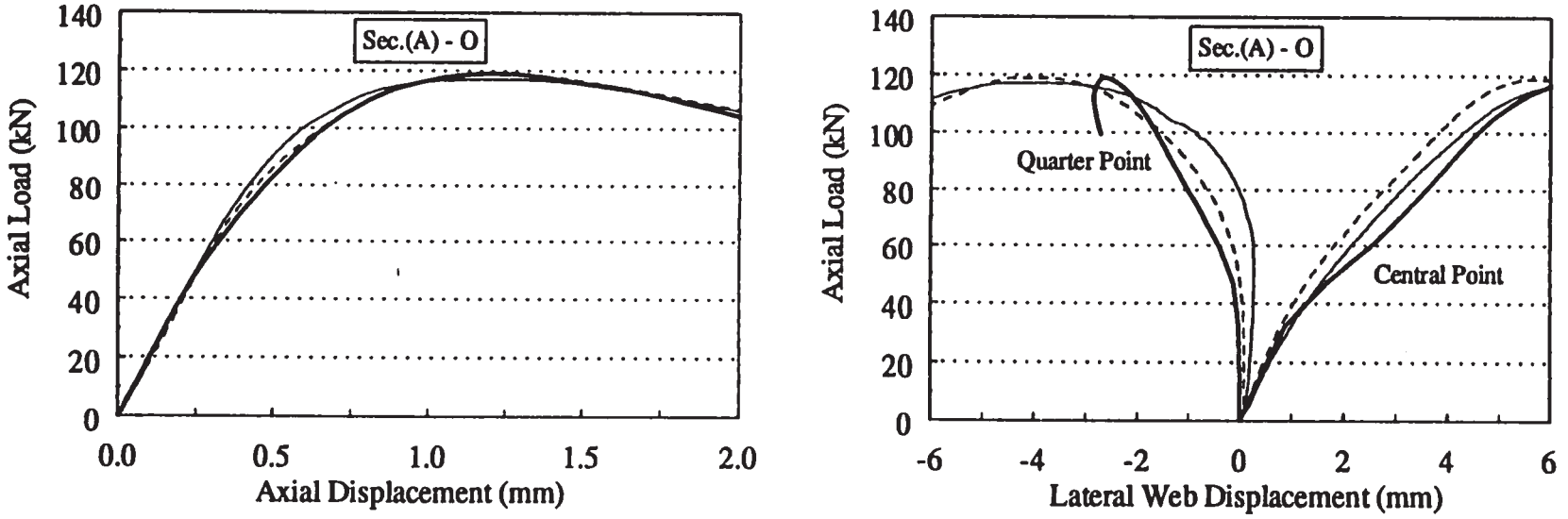

Figure 4.10(d) Measured and predicted F.E. sec. (A) deformation (Oval perforation)

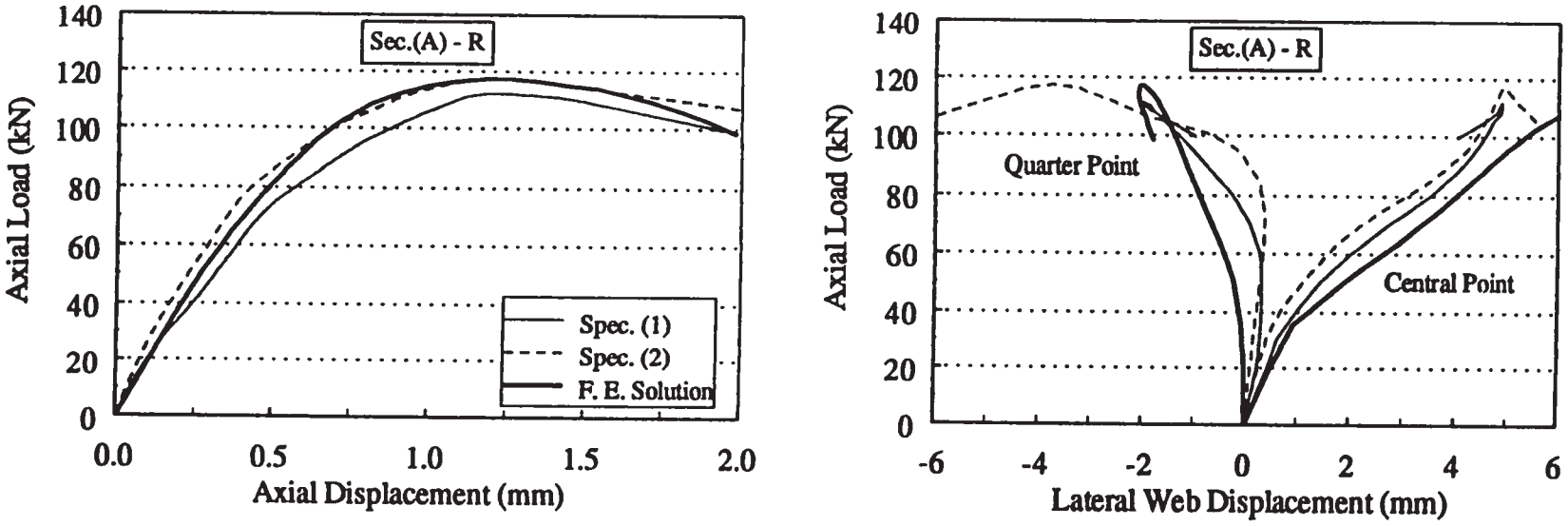

Figure 4.10(e) Measured and predicted F.E. sec. (A) deformation (Rectangular perforation)

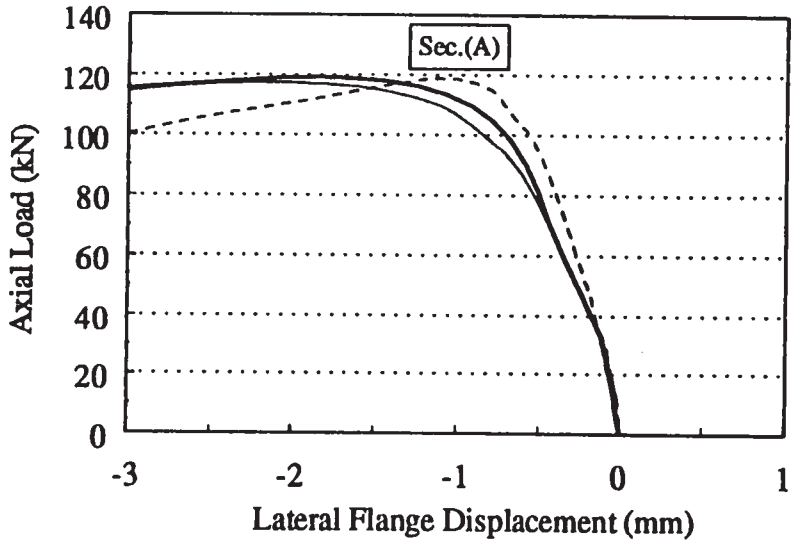

Figure 4.10(f) Typical measured and predicted F.E. sec. (A) flange deformation

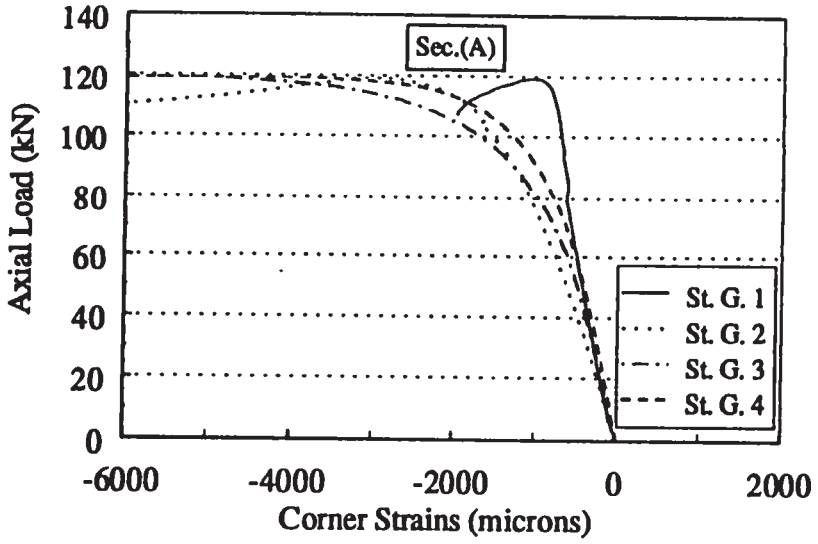

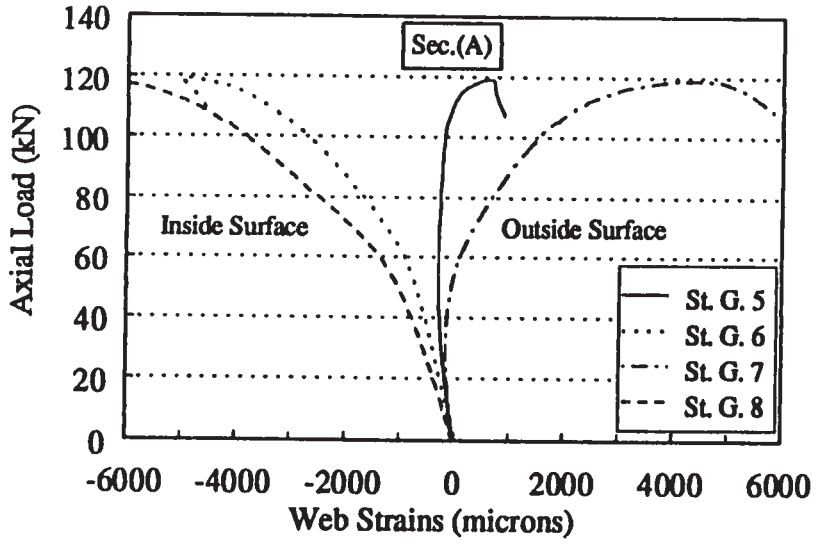

Figure 4.11(a) Typical measured corner and web strains for sec. (A)

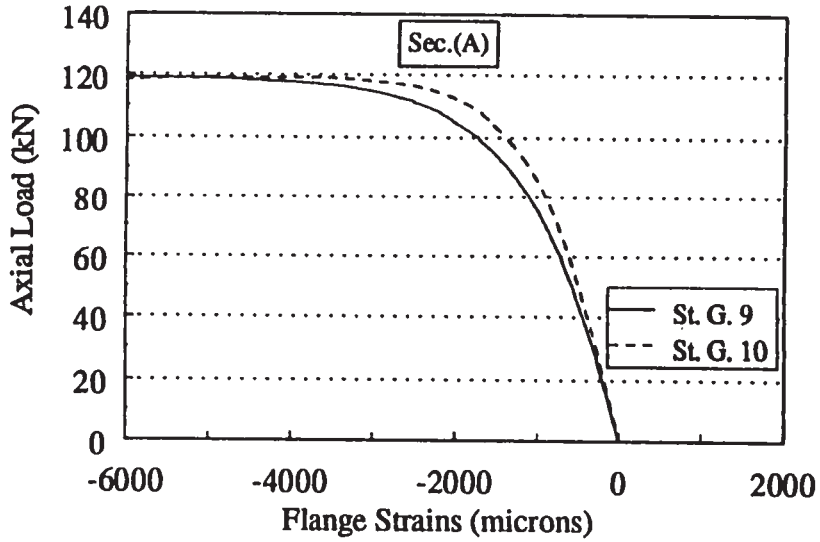

Figure 4.11(b) Typical measured flange strains for sec. (A)

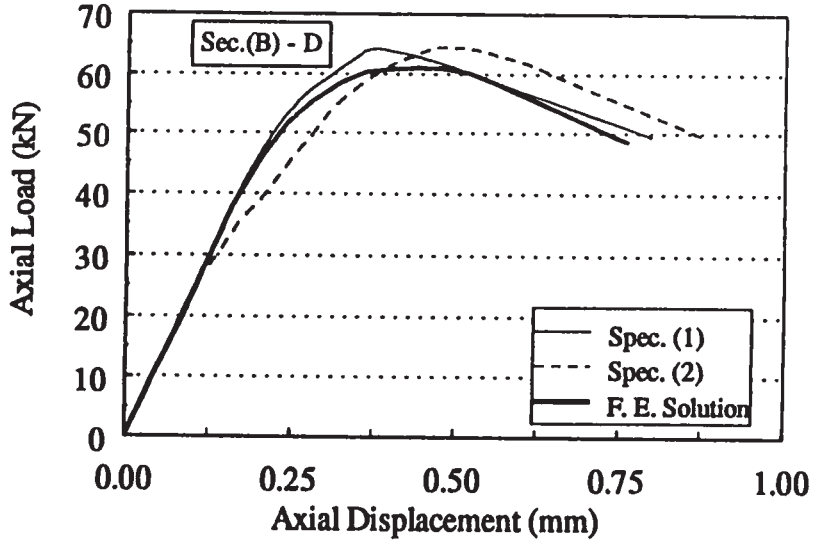

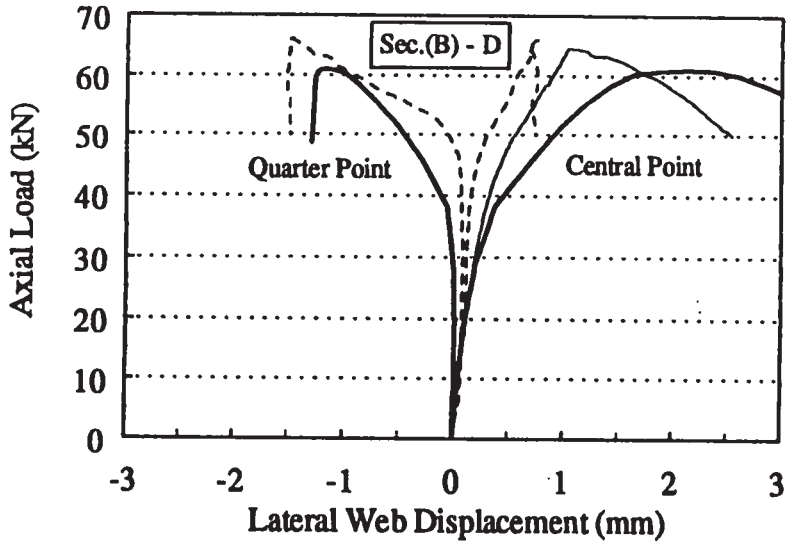

Figure 4.12(a) Measured and predicted F.E. sec. (B) deformation (No perforation)

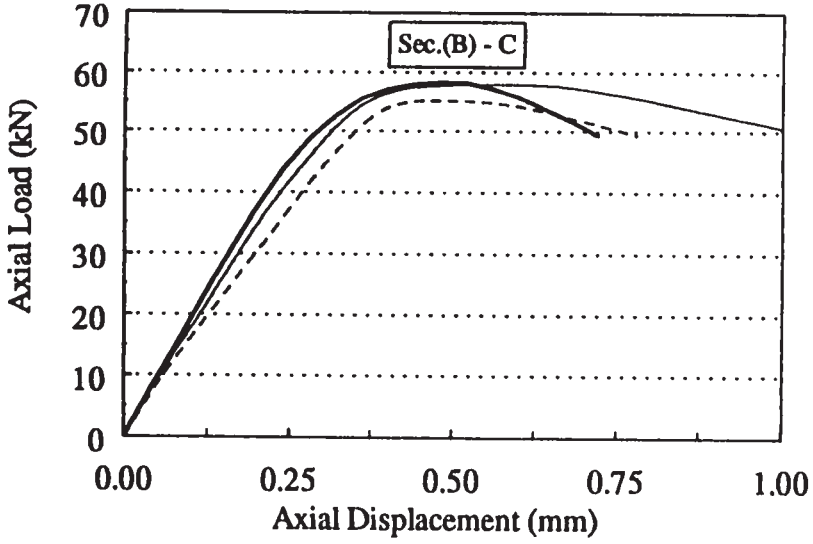

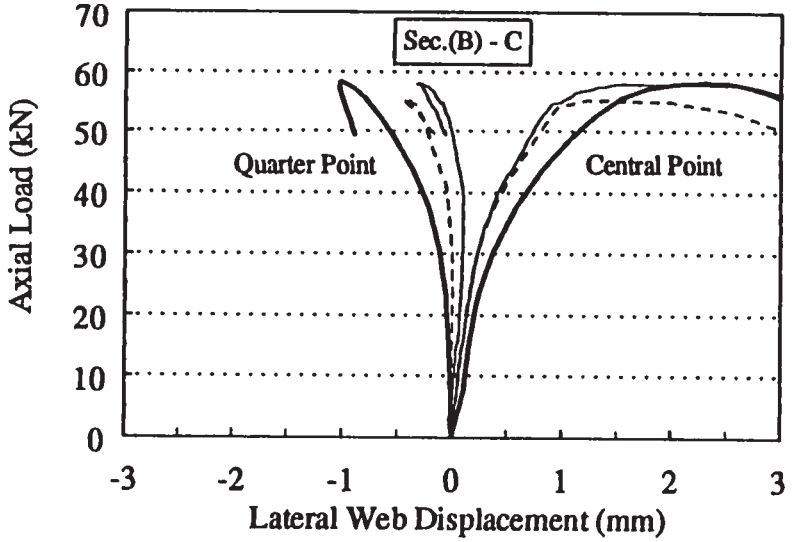

Figure 4.12(b) Measured and predicted F. E. sec. (B) deformation (Circular perforation)

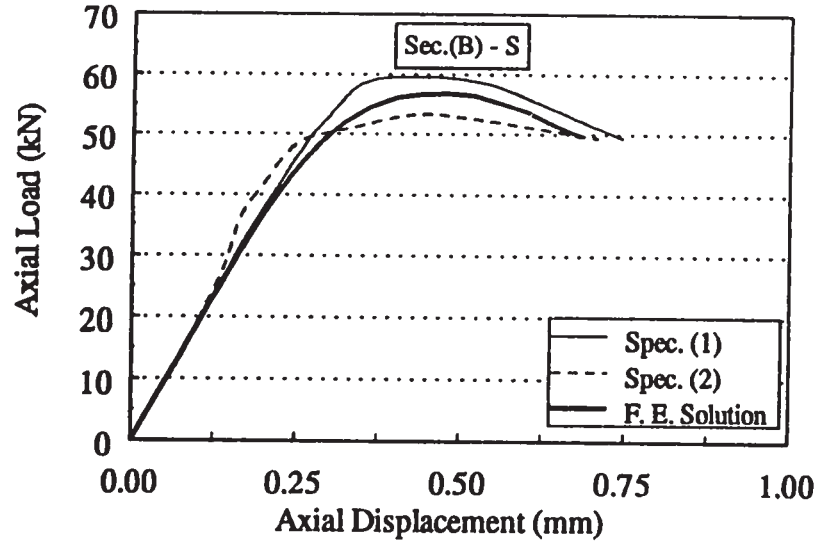

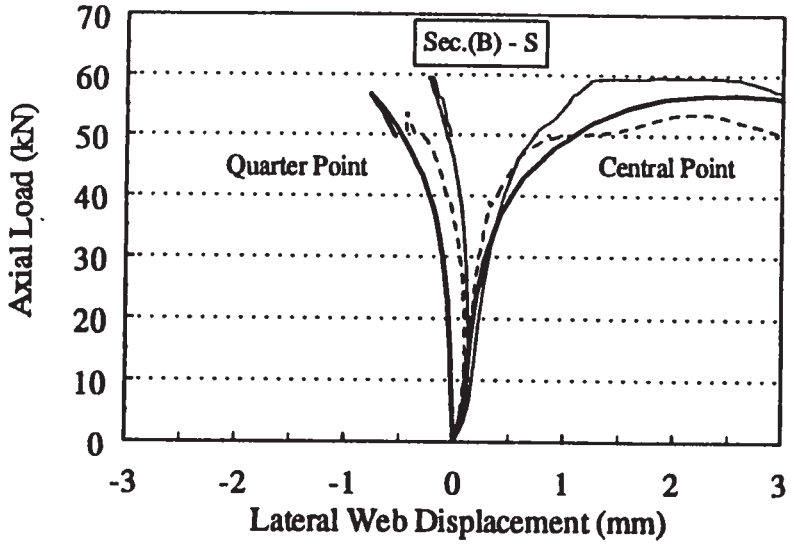

Figure 4.12(c) Measured and predicted F.E. sec. (B) deformation (Square perforation)

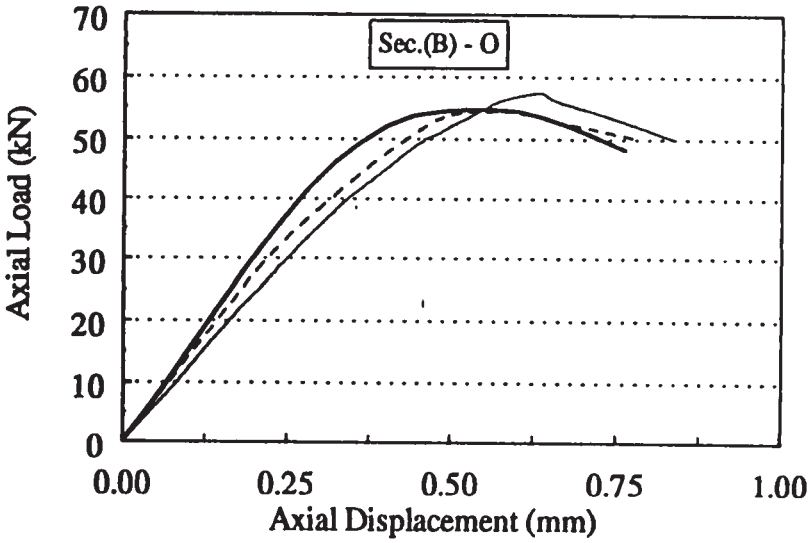

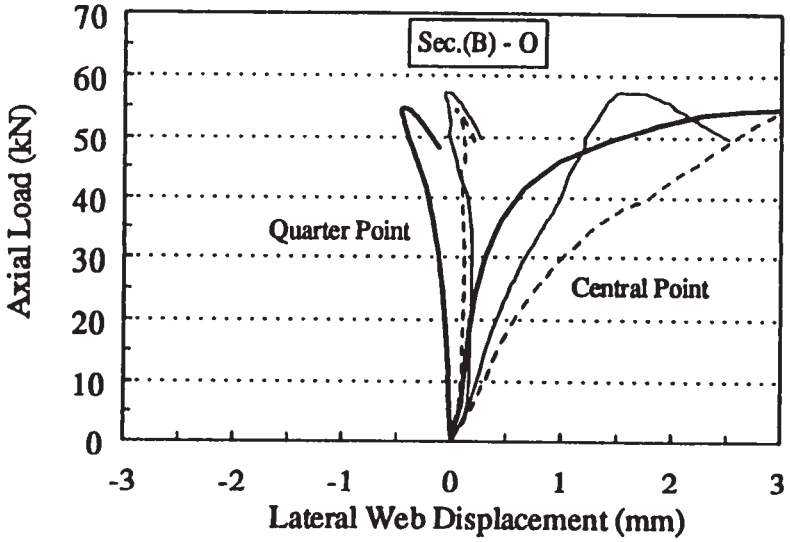

Figure 4.12(d) Measured and predicted F.E. sec. (B) deformation (Oval perforation)

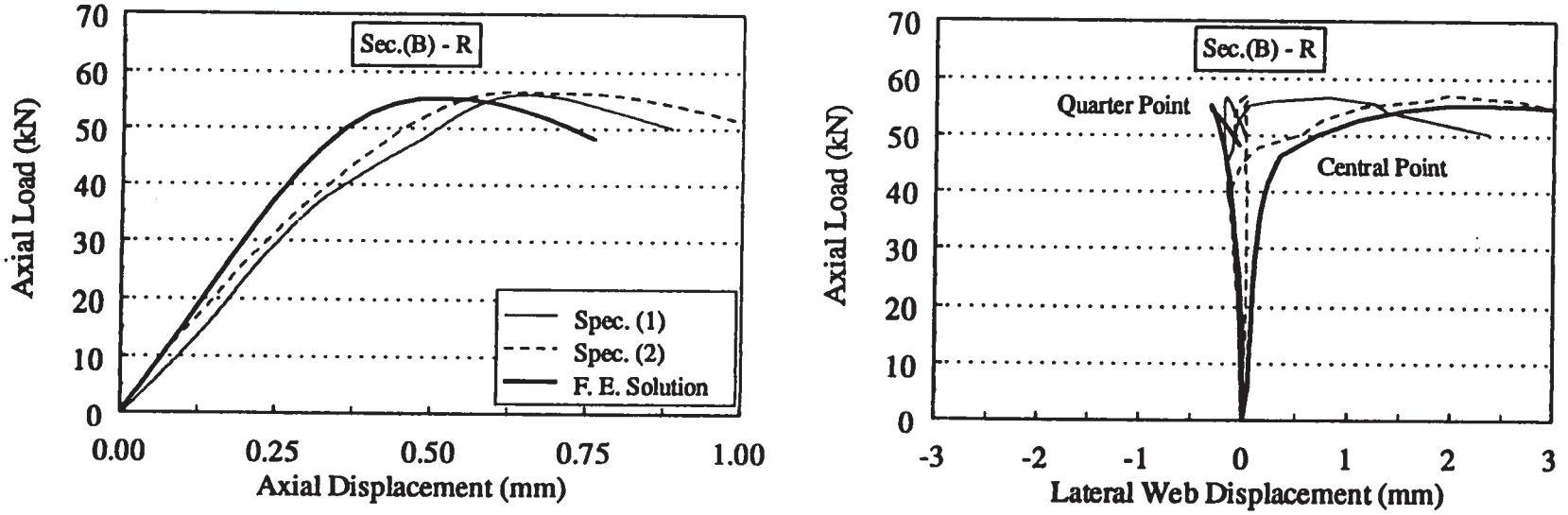

Figure 4.12(e) Measured and predicted F.E. sec. (B) deformation (Rectangular perforation)

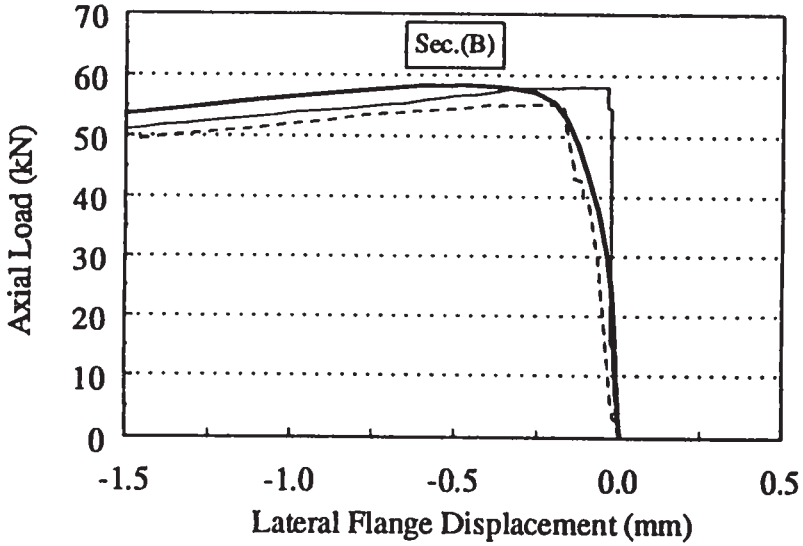

Figure 4.12(f) Typical measured and predicted F.E. sec. (B) flange deformation

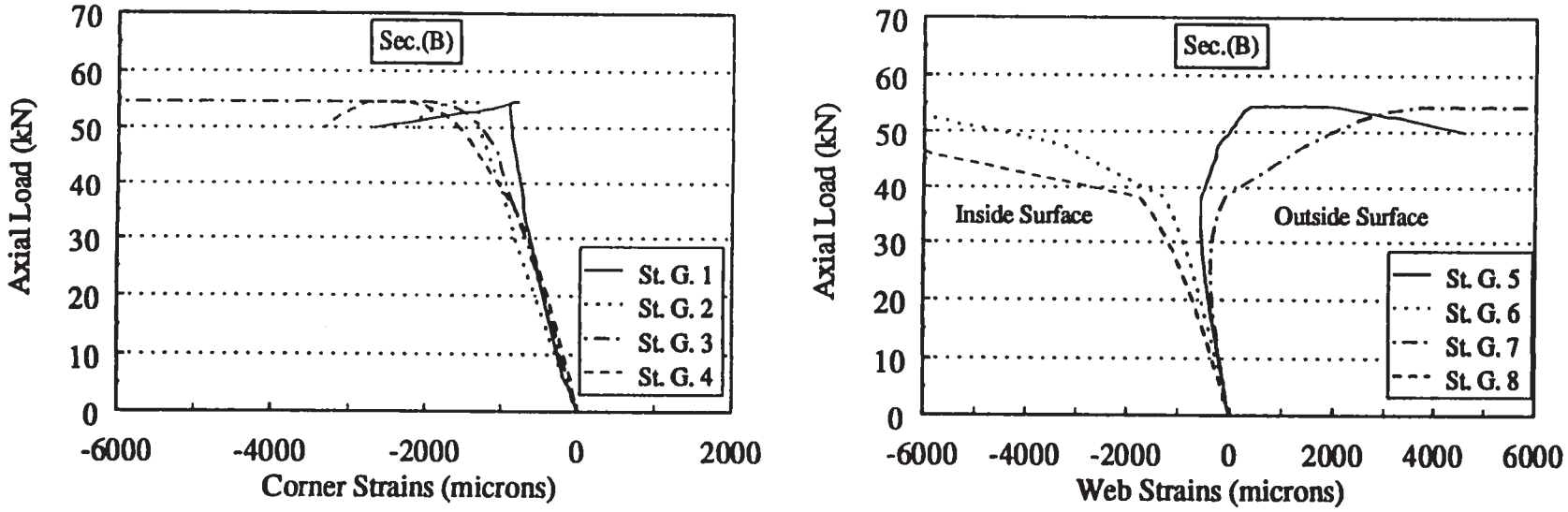

Figure 4.13(a) Typical measured corner and web strains for sec. (B)

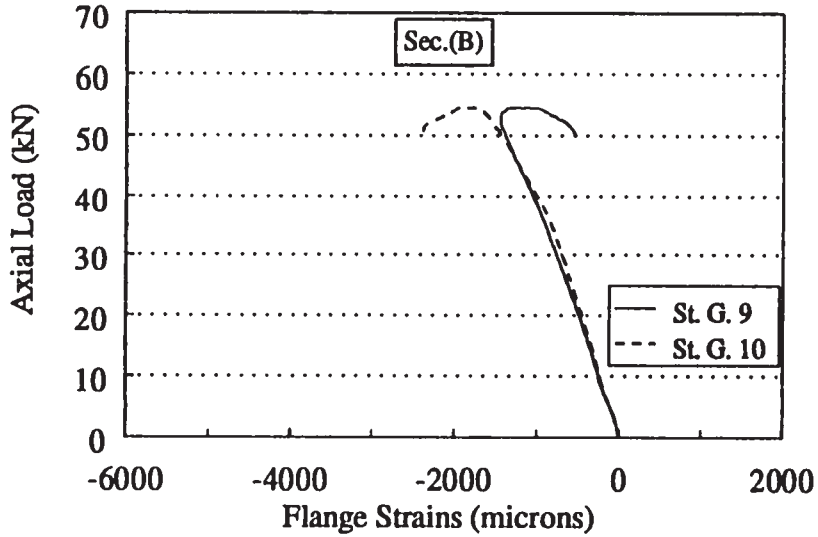

Figure 4.13(b) Typical measured flange strains for sec. (B)

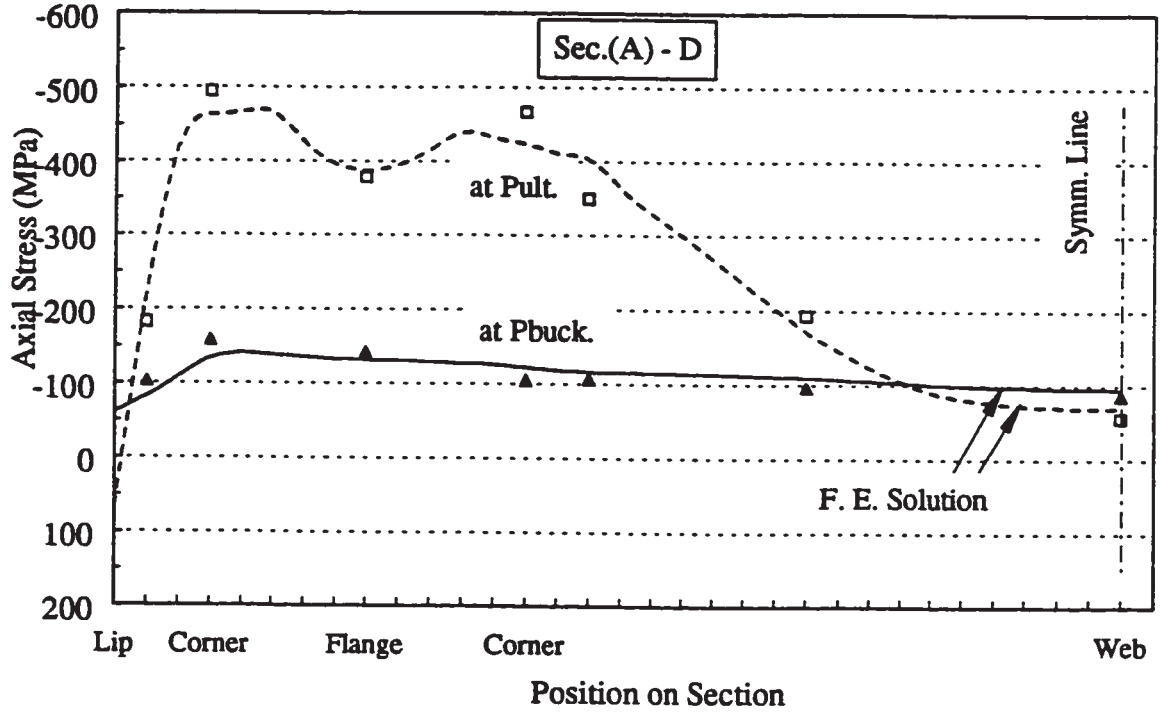

Figure 4.14(a) Measured and predicted F.E. sec. (A) stress distribution (No perforation)

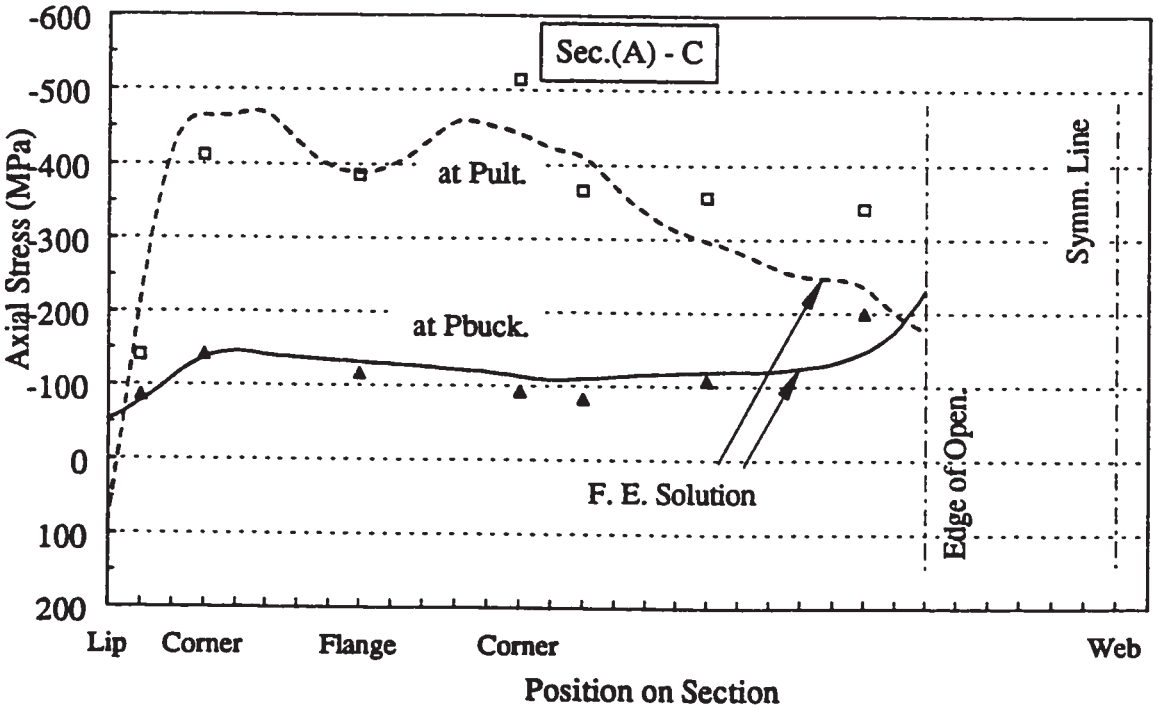

Figure 4.14(b) Measured and predicted F.E. sec. (A) stress distribution (Circular perforation)

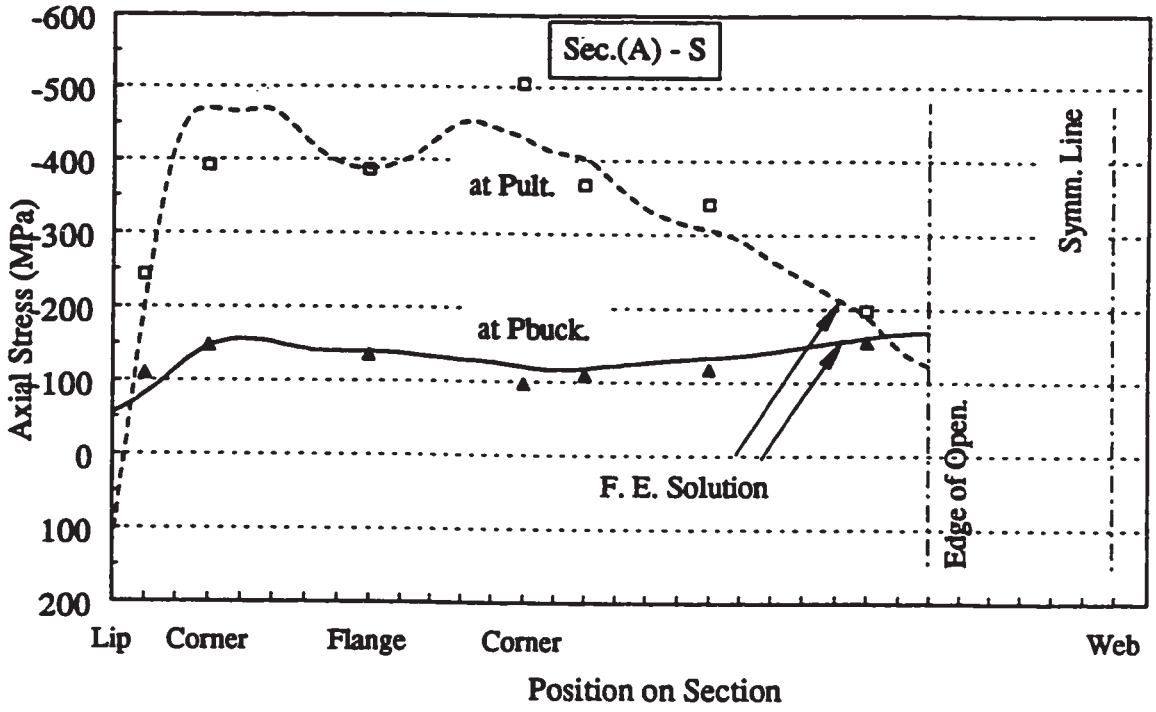

Figure 4.14(c) Measured and predicted F.E. sec. (A) stress distribution (Square perforation)

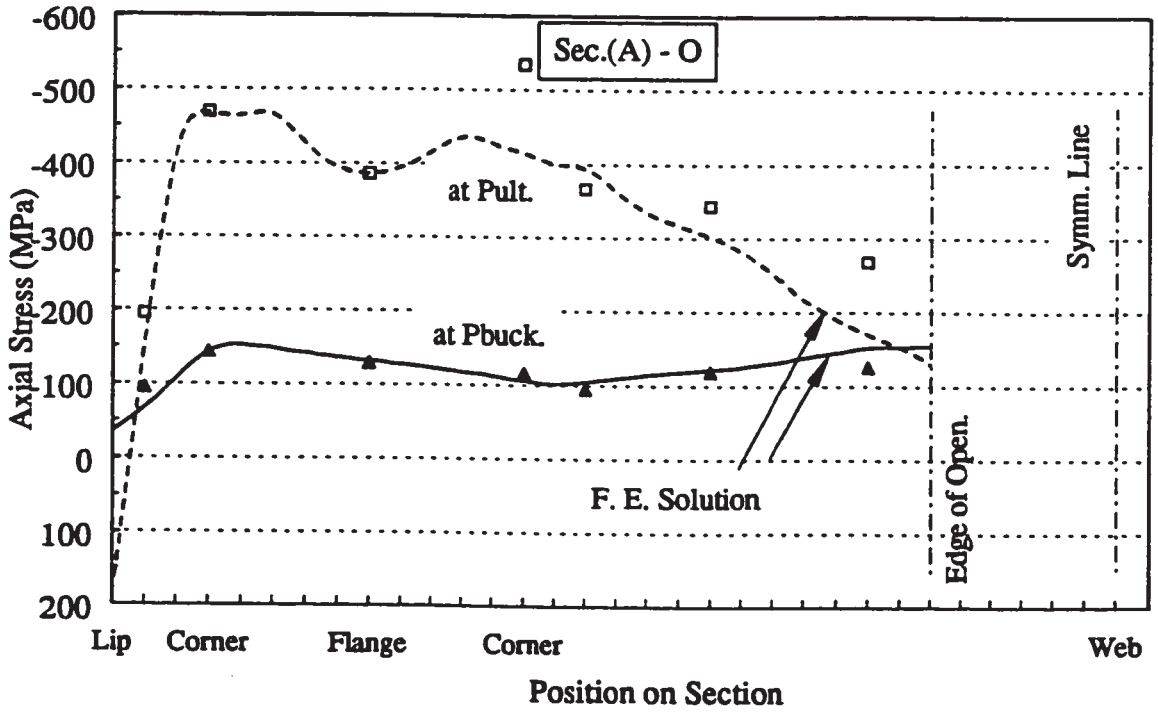

Figure 4.14(d) Measured and predicted F.E. sec. (A) stress distribution (Oval perforation)

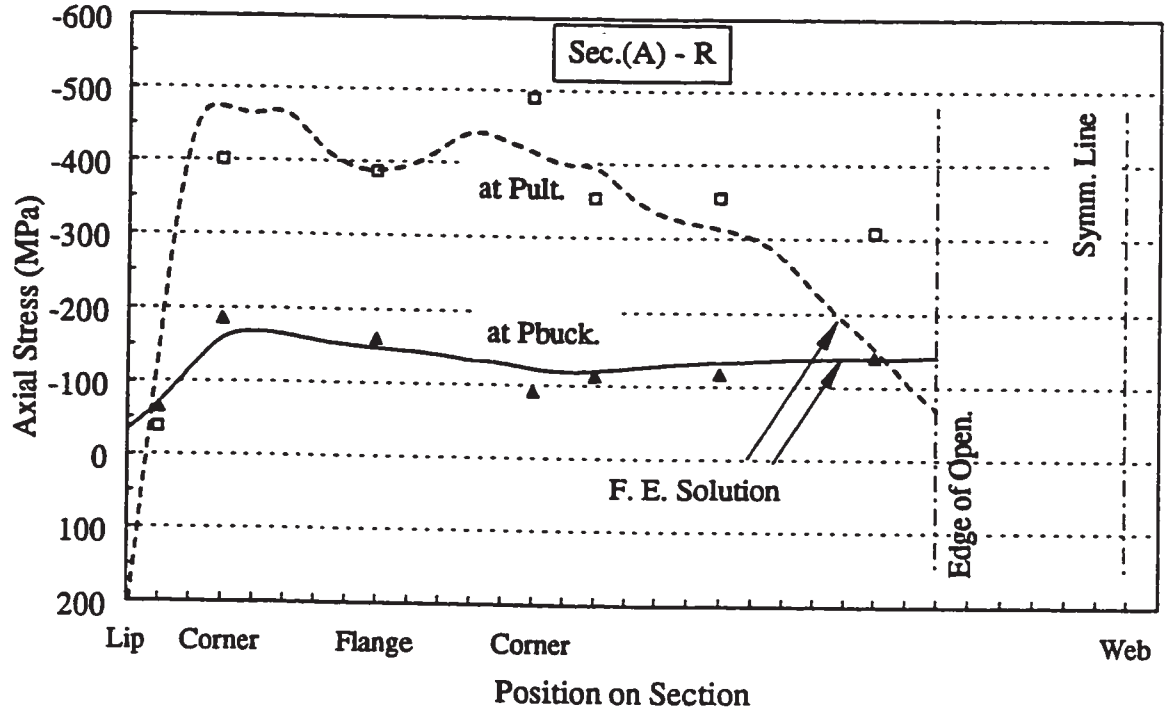

Figure 4.14(e) Measured and predicted F.E. sec. (A) stress distribution (Rectangular perforation)

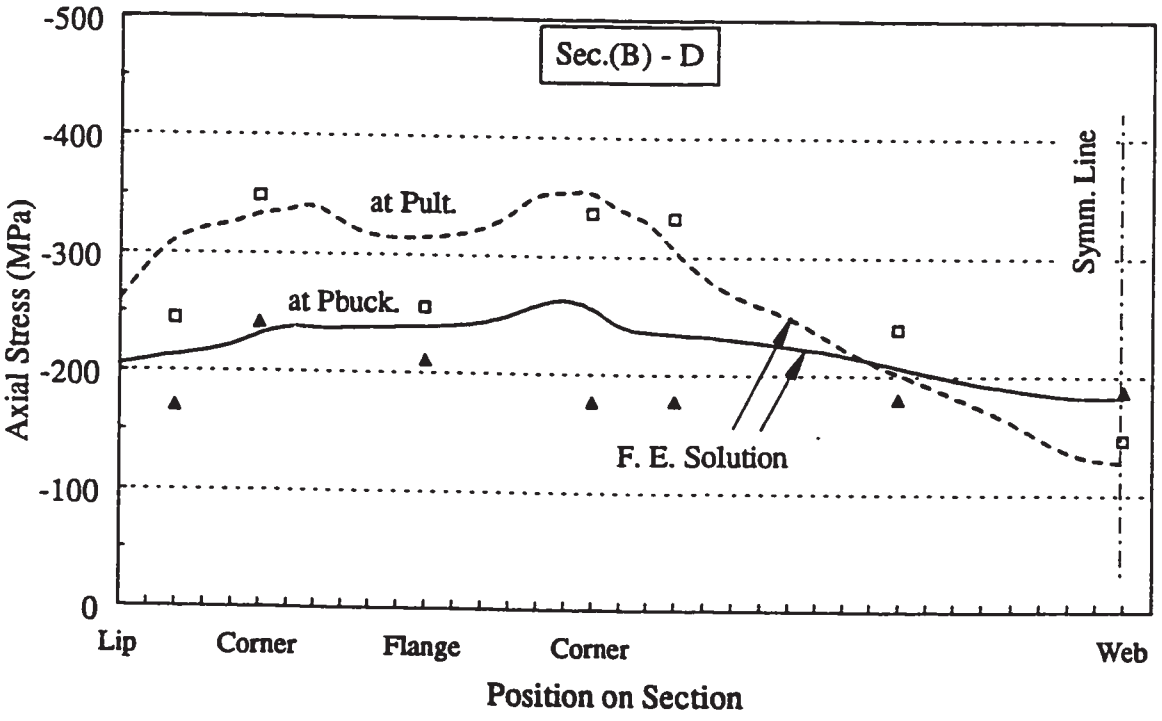

Figure 4.15(a) Measured and predicted F.E. sec. (B) stress distribution (No perforation)

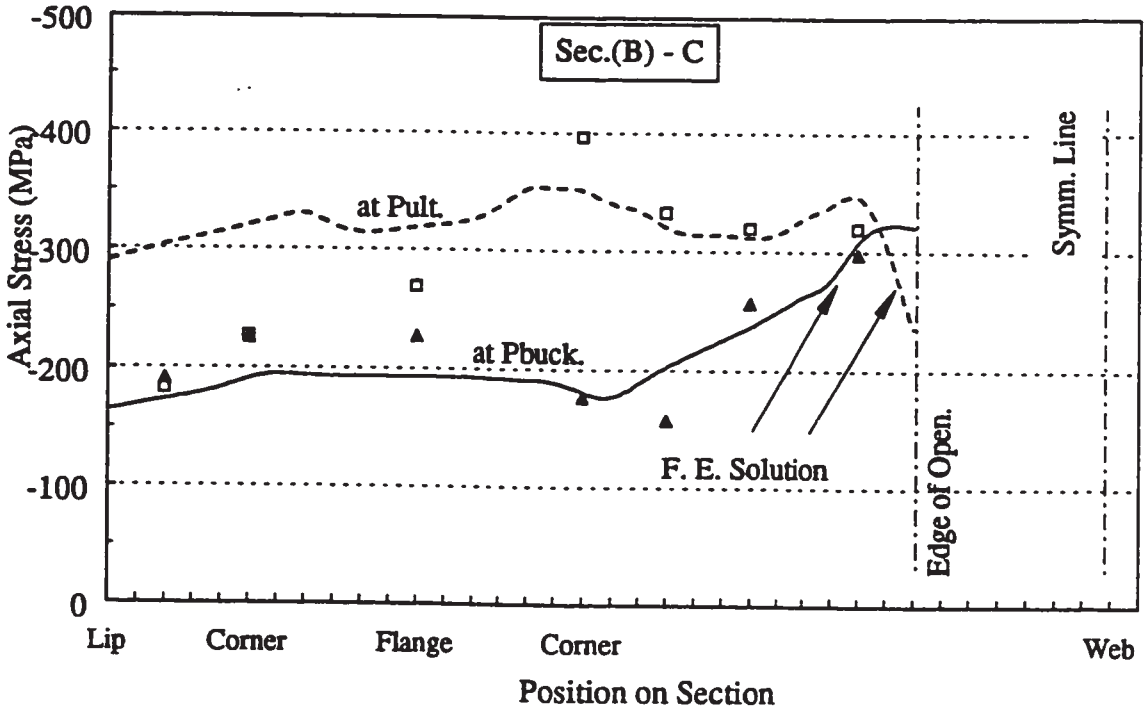

Figure 4.15(b) Measured and predicted F.E. sec. (B) stress distribution (Circular perforation)

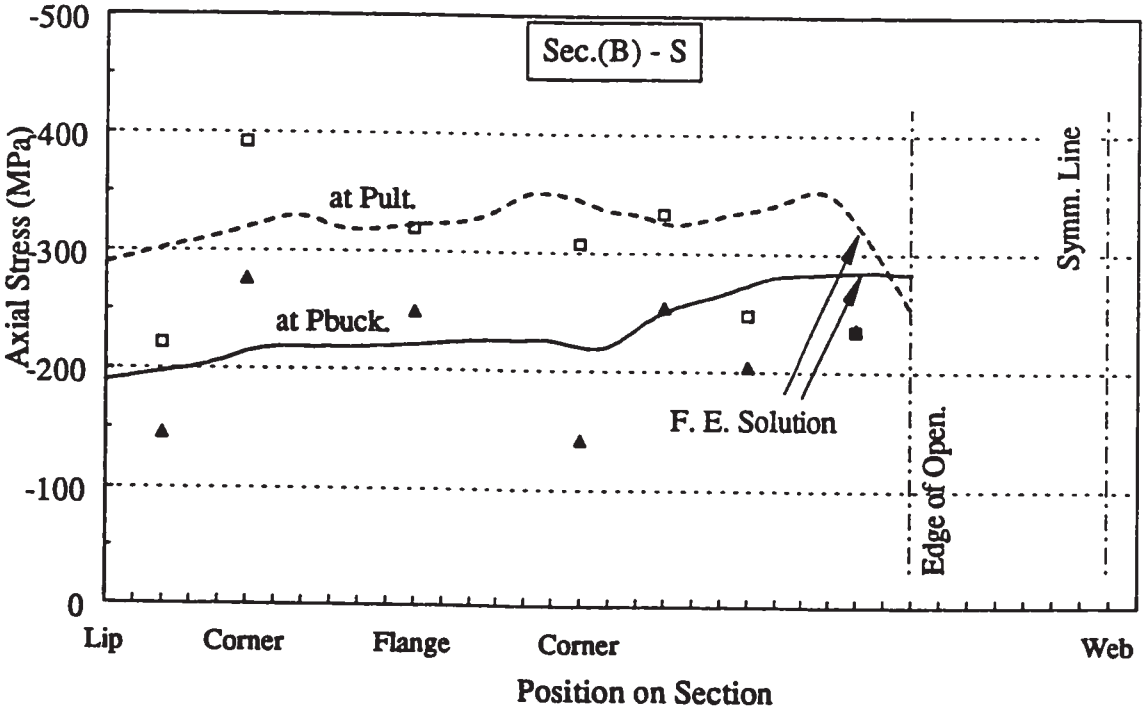

Figure 4.15(c) Measured and predicted F.E. sec. (B) stress distribution (Square perforation)

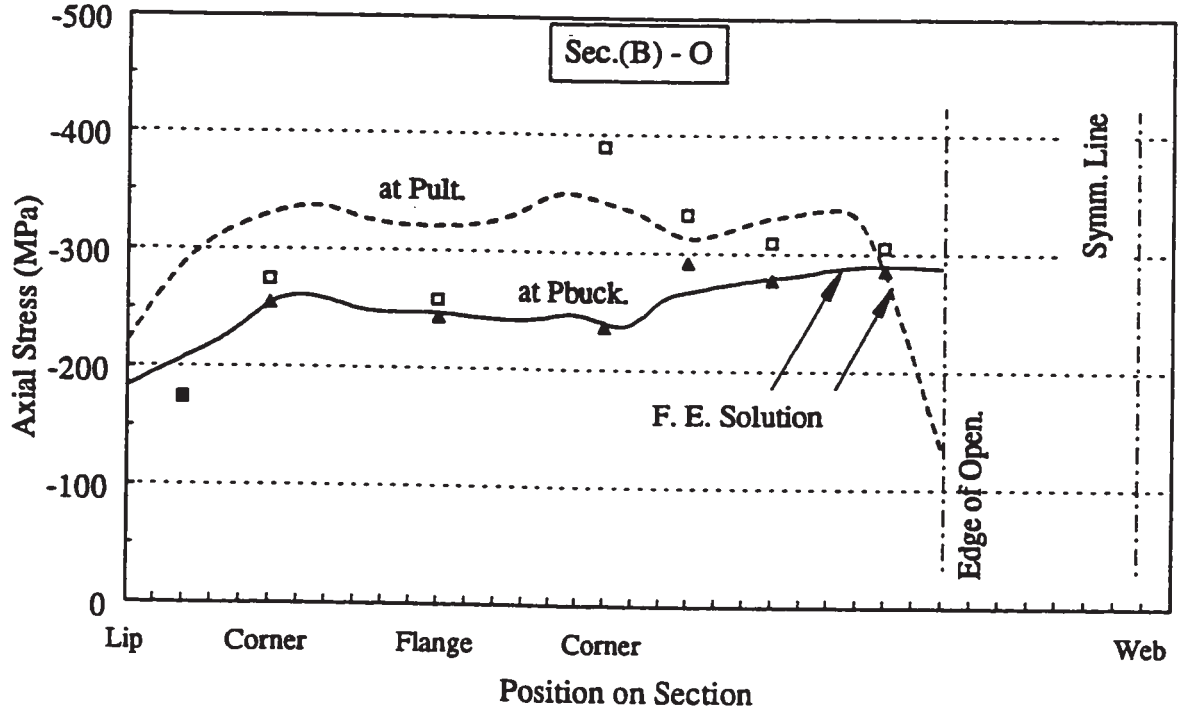

Figure 4.15(d) Measured and predicted F.E. sec. (B) stress distribution (Oval perforation)

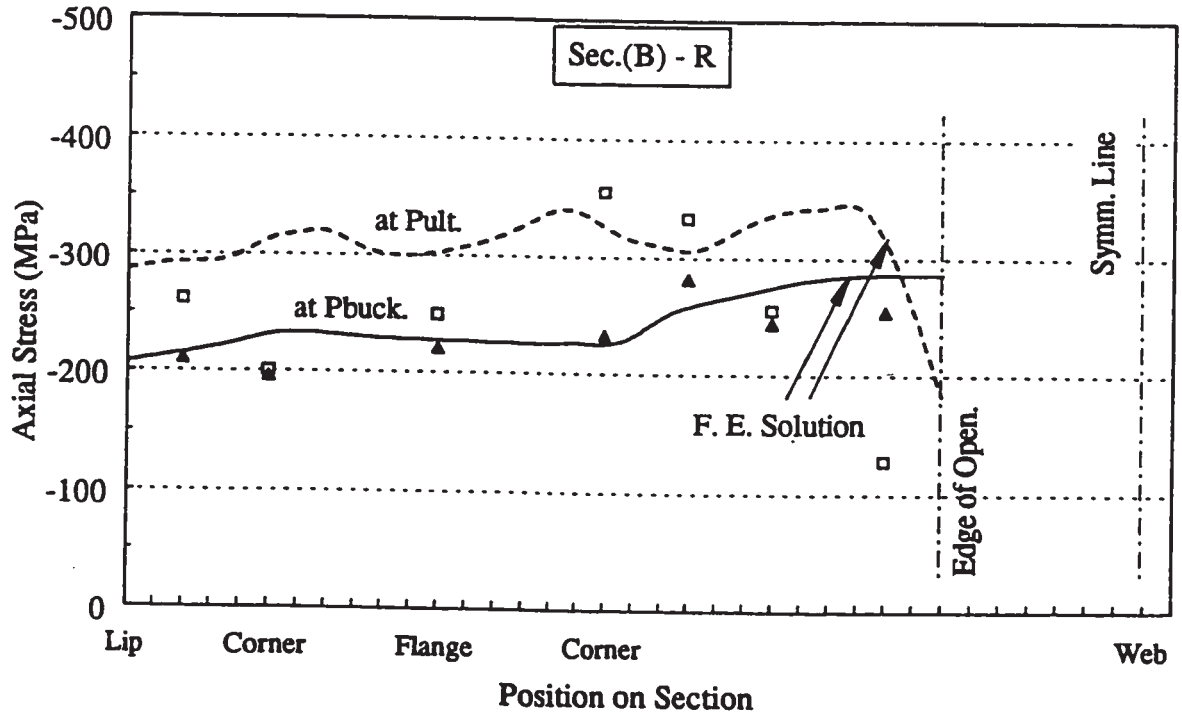

Figure 4.15(e) Measured and predicted F.E. sec. (B) stress distribution (Rectangular perforation)

CHAPTER 5

EFFECTIVE DESIGN WIDTH FOR PERFORATED PLATES OF COLD-FORMED STEEL MEMBERS IN COMPRESSION

5.1 Introduction

The finite element model, developed in Chapter Four for the post-local buckling behaviour of cold-formed steel (CFS) compression members, has been used in this chapter to obtain the axial stress distribution of perforated web plates in compression. The finite element model has been also used to obtain the effective design width of perforated web plates, and consequently the effective design width of perforated CFS compression members.

The parameters of a perforation that affect the ultimate strength of perforated CFS members include the shape of the perforation, the width (a), and the height (h) (see Figure 5.1). These parameters are in addition to the properties of the perforated compression plate itself (dimensions, slenderness ratio, and material properties). In view of the research done on the behaviour and strength of perforated compression plates and perforated CFS compression members, the question whether all perforation parameters have the same important effect on the ultimate strength has not been answered yet. The answer to such a question should reflect on the number of parameters to appear in a design equation for perforated plates.

The first part of this chapter gives the scope and the parameters of the finite element study which was performed on channel-shaped CFS members in compression. The second part presents the analysis results for the CFS compression members and the perforated web plates of the members. The results include the effects of different parameters on the axial stress distribution and the predicted effective design width of the compression plate. The parameters considered in the study are the plate slenderness ratio (w/t), the yield strength (F_y), the perforation width-to-web width ratio (a/w), and the perforation height-to-perforation width ratio (h/a). The third part of the chapter presents two proposed effective design width equations for perforated compression plates with regular (square or circular) and elongated perforations. The equations were obtained based on the current finite element results, and verified using the results of several experimental studies.

5.2 Parameters of Perforations

The experimental studies reviewed in Chapter One emphasized that the primary parameter affecting the ultimate strength of perforated cold-formed steel (CFS) compression members is the perforation width (a). Therefore, the non-dimensional parameter (a/w), where (w) is the web width, was the main parameter in all of the discussed experimental and analytical studies. The effects of the shape of perforation was also studied by Yu and Davis (1973), Narayanan and Chow (1984), and others. It is meant here by the shape of perforation that the perforation is having

either circular or square corners, but having the same overall width and height. It was generally observed that the circular corners shape gives a better distribution of stresses around the perforation than the square corners shape. Also, the ultimate strength of CFS sections with circular perforation shape was found to be slightly higher than the sections with square perforation shape. However, this marginal difference in strength suggests that studying perforation with square shape only might be enough to cover the ultimate strength predictions of perforated sections with circular as well as square shape. As for the effects of the height of perforation (h), it was observed, from the few available experimental studies which considered this parameter, that perforated CFS sections with (h/a) ratio greater than 1.0 have significantly lower ultimate strength than similar sections with (h/a) equal to 1.0.

Based on the above observations from different studies, the current finite element study considers the perforation width-to-web width ratio (a/w), and the perforation height-to-perforation width ratio (h/a) as the study parameters of the perforation. The study also considers the slenderness ratio of the web plate (w/t) and the yield strength (F_y) as the parameters of the CFS sections.

5.3 The Finite Element Study

Lipped channel cold-formed steel (CFS) sections with short flanges were selected for the parametric study on the ultimate strength of CFS compression members with perforated web plates. A lipped channel section has the advantage of

providing a simply supported condition at the two longitudinal edges of the web plate. The lips of the section also act as stiffeners to the flange plates.

5.3.1 Perforated Sections

The analysis was performed on seven different practical channel sections covering a slenderness ratio range of the web plate (w/t) from 31.3 to 194.2. The overall and cross-sectional dimensions of the channel sections are given in Table 5.1. The first three sections had overall dimensions of 101.6 mm (4 in.) for the web, 41.3 mm (1.625 in.) for the flange, and 12.7 mm (0.5 in.) for the lip. The other four sections had overall dimensions of 203.2 mm (8 in.) for the web, 41.3 mm (1.625 in.) for the flange, and 12.7 mm (0.5 in.) for the lip. The inside radius-to-thickness ratio of the corners of all the channel sections was taken as 2. The dimensions of the web, flange, and lip plates, shown in Table 5.1, are the flat dimensions which were calculated by excluding the rounded corners from the overall dimensions of the plates. Different slenderness ratios of the web plate (w/t) were obtained by choosing different values for the thickness of the channel section.

The finite element analysis was performed on ten study cases for each lipped channel section; one case for a non-perforated section and nine cases for perforated sections. The perforated sections were studied with perforation width-to-web width ratios (a/w) equal to 0.2, 0.4, and 0.6. The perforation height-to-perforation width ratio (h/a) was taken equal to 1.0, 2.0, and 3.0 for each perforation width ratio.

These perforation dimensions cover the practical limits for perforated cold-formed steel (CFS) wall studs.

The finite element analysis was performed on the basis of a yield strength (F_y) of the channel sections equal to 345 MPa (50 ksi). However, the effects of the yield strength value on the axial stress distribution, and the effective design width of perforated web plates were investigated by re-analyzing some study cases on the basis of a yield strength value equal to 228 MPa (33 ksi).

5.3.2 The Finite Element Model

Short columns of the channel sections were modelled using the finite element method. The column lengths for study cases of the 101.6 mm (4 in.) section and the 203.2 mm (8 in.) section were taken equal to 300 mm and 600 mm, respectively. The length of the column was chosen large enough to accommodate the desired height of the web perforation, specially for the case of (a/w) ratio of 0.6 and (h/a) ratio of 3.0.

The material properties for cold-formed steel (CFS) channel sections used in the analysis were set according to the material models presented in sections 3.3 and 3.4 of Chapter Three. Increased yield strength (F_{yc}) was utilized in the corner zones of the channel section, while specified yield strength (F_y) was utilized in the other flat zones of the section. The increased yield strength (F_{yc}) was calculated according to Equation 3.3, and found to be 434 MPa for the (F_y) of 345 MPa, and 296 MPa for the (F_y) of 228 MPa. The calculations were based on a specified ratio of the ultimate

tensile strength to the yield strength (F_u / F_y) of 1.30 for (F_y) equal to 345 MPa, and 1.36 for (F_y) equal to 228 MPa (Yu, 1991).

The procedure of choosing the finite element mesh, boundary conditions, and loading technique are explained in sections 4.3.1 and 4.3.3 of Chapter Four. The utilized distributions of the geometric imperfections and the residual stresses are also explained in section 4.3.4. The displacement control algorithm, which was used for the analysis to obtain increments of axial compression displacement rather than axial load, is described in section 4.3.5. The analysis was performed until the ultimate (largest) load of the column is reached and the load started to decrease with more increments of axial displacement.

5.4 Analysis Results

The output results of the finite element analysis on perforated cold-formed steel (CFS) columns include the axial load supported by the column, the nodal displacements in three global directions, and the in-plane element stresses. These results were obtained for every loading step of the incremental displacement solution. Table 5.2 gives the resulting ultimate axial load for every study case of the 70 cases performed on short columns of lipped channel sections. The following part of the study is concerned with discussing the axial stress distributions across non-perforated, and perforated web plates, and the determination of their effective design widths based on the ultimate loads of the short columns. The effects of the parameters of

perforated plates (w/t, a/w, h/a, and F_y) on the shape of the stress distribution and the magnitudes of the effective design width are discussed as well.

5.4.1 Axial Stress Distribution in Web Plates

The axial stress distributions across the mid-height section of the non-perforated web plates are presented in Figure 5.2 for different slenderness ratios (w/t). The axial stress distributions of the perforated web plates of three different channel sections are presented in Figures 5.3, 5.4, and 5.5. These axial stress distributions correspond to a loading level when the yield stress value (F_y) (345 MPa) is first detected across the web plate. The horizontal axis in these figures represents half of the width of the web plate, while the vertical axis represents the normalized axial stress with respect to (F_y) of 345 MPa. The stresses for all distributions were obtained from the mid-plane of the thickness of the web plate. The web plates of the three channel sections under consideration have slenderness ratios (w/t) equal to 31.3, 78.3, and 194.2, respectively. The first slenderness ratio (w/t = 31.3) represents a web plate with a fully effective width at a yield stress (F_y) value of 345 MPa. The other two slenderness ratios (w/t = 78.3 and 194.2) represent web plates with partially effective widths at the same yield stress value.

5.4.1.1 Effects of (w/t) Ratio

The axial stress distributions of the non-perforated web plates of five

slenderness ratios (w/t) are presented in Figure 5.2, which can be used to study the effects of (w/t) ratio. For the (w/t) ratio of 31.3, the axial compressive stress reaches the yield stress value at the edges of the web. However, the stress drops to about $0.9F_y$ next to the edges and remains constant over the whole width of the web plate. The initiation of yielding at the web edges is due to the higher yield and ultimate strengths at the corner zones of cold-formed steel (CFS) sections as discussed earlier in Chapter Three. The constant stress over the width of the web indicates that the web plate is fully effective at that stress level. Any disturbance to that fully effective plate, such as a perforation, will alter the stress distribution and may cause the initiation of yielding to occur inside the plate rather than its edge (see the case in Figure 5.3(a) for (a/w) ratio of 0.2).

As the (w/t) ratio increases to 78.3, the web plate becomes partially effective. The corresponding axial compressive stress distribution shows a gradual decrease from a value of F_y at the edges to a value of $0.5F_y$ at the centre line. This gradual decrease of axial stresses is clearly observed for larger (w/t) ratios of 101.4, 128.7, and 194.2. The axial stress drops to a tensile stress value of $0.07F_y$ at the centre line for (w/t) of 194.2. This gives an evidence that, even though the web plate is under compressive loading, axial tensile stresses develop in its central region when the ratio (w/t) becomes very large. The (w/t) ratio has similar effects on the axial stress distribution of perforated web plates as observed by comparing the corresponding distributions in Figures 5.3, 5.4, and 5.5.

5.4.1.2 Effects of (a/w) Ratio

The axial stress distributions of perforated web plates are presented in Figures 5.3(a) to (c) through 5.5(a) to (c) for different perforation width-to-web width ratios (a/w). Three ratios are shown in each figure; (a/w) equals 0.2, 0.4, and 0.6. The edge of perforation is marked in the figures by a vertical line for each (w/t) ratio. For the (w/t) ratio of 31.3 (Figures 5.3(a) to (c)), it can be noticed that when the perforation is introduced in the web plate, part of the axial compressive stresses supported by the central area of the non-perforated plate appeared to have been transferred to the sides of the perforation. This behaviour can be noticed for all (a/w) ratios, except that the area of the transferred stresses decreases as the (a/w) ratio increases.

On the other hand, the percentage of transferred axial stresses increases with the increase of the slenderness ratio (w/t) of the web plate. This behaviour can be observed by comparing the corresponding stress distributions in Figures 5.3, 5.4, and 5.5. For the (w/t) ratio of 31.3, the plate is fully effective and the area surrounding the perforation could not accommodate much of the stresses lost due to the perforation. For the (w/t) ratio of 78.3, the plate is partially effective and the area surrounding the perforation was capable of carrying a larger percentage of transferred stresses from the perforation area. For the (w/t) ratio of 194.2, the plate is also partially effective but the axial stresses lost due to the perforation are tensile stresses for the case of (a/w) equals 0.2 and little compressive stresses for the cases of (a/w) equals 0.4 and 0.6. As a result, the area of transferred stresses is below the stress

distribution of the non-perforated plate for (a/w) equals 0.2 and little higher for (a/w) equals 0.4 and 0.6.

5.4.1.3 Effects of (h/a) Ratio

The axial stress distributions for different perforation height-to-perforation width ratios (h/a) of perforated web plates are presented under the titles (a) to (c) of Figures 5.3, 5.4, and 5.5. The (h/a) ratios displayed in these figures are 1.0, 2.0, and 3.0. For the (w/t) ratios of 31.3 and 78.3, it can be noticed that the area of axial compressive stresses transferred from the central part of the non-perforated web plate to the sides of the perforation decreases as the (h/a) ratio increases. This suggests that the interaction of the plate elements around the perforation for small (h/a) ratios helps in transferring stresses to the sides of the perforation. However as (h/a) ratio increases, this interaction starts to disappear as the plate becomes divided into two separate segments under compressive loading. This behaviour is quite clear in Figure 5.3(c), where the ratio of (h/a) equals 3.0 results in almost no transfer of axial stresses. Also as (h/a) ratio increases, larger magnitudes of lateral displacements occur at the edges of the perforation, which develop axial tensile stresses in the plate. These tensile stresses reduce the area of transferred compressive stresses to the sides of the perforation. Moreover, the tensile stresses are capable of dominating the compressive stresses for very large lateral displacements. This behaviour can be concluded from Figures 5.5(b) and (c) for the (w/t) ratio of 194.2 when compared to

Figure 5.5(a). The transferred axial stresses in these two figures are dominated by tensile stresses in the areas adjacent to the perforation.

5.4.1.4 Effects of Yield Strength

The effects of two different values of the yield strength (F_y) on the axial stress distributions of non-perforated and perforated web plates were studied. Figure 5.6 shows the axial stress distributions for a web plate (with (w/t) ratio of 78.3) at (F_y) of 228 MPa and 345 MPa. The distributions are shown for non-perforated and perforated plates with (a/w) and (h/a) ratios equal to 0.6 and 1.0, respectively. It can be observed from this figure that the normalized axial stress (F/F_y) changes significantly for non-perforated web plates with the change of (F_y). As the yield strength (F_y) increases from 228 MPa to 345 MPa., the uniformity of axial stresses over the width of the plate disappears and the axial compressive stresses drop in the central part due to the spreading of local buckling mode in the web plate. This behaviour causes the plate to become more partially effective, however, its total load capacity increases due to the increase of (F_y).

For perforated plates, the effects of changing (F_y) are not as significant as that for non-perforated plates as shown in Figure 5.6. The axial stress distribution for the perforated plate with (a/w) of 0.6 has almost the same behaviour when (F_y) changes from 228 MPa to 345 MPa. This is a result of having all the axial stress changes in the plate to start from the central part, and then spread gradually towards the edges.

5.4.2 Effective Design Width of Web Plates

The effective design widths (b) of non-perforated and perforated web plates were determined based on the ultimate loads obtained from the finite element analysis, as presented in Table 5.2. The portion of the ultimate load carried by the web plate (P_w) was first determined by deducting an upper bound load, to be supported by the flanges, lips, and corners of the section, from the total ultimate load (P_u). This was done according to the following procedure:

$$P_w = P_u - [\text{Flat zone eff. areas} \times F_y + \text{Corner zone areas} \times F_{yc}] \qquad (5.1)$$

where the flat and the corner zones of a lipped channel section are as defined in section 3.3 of Chapter Three. The stress (F_y) is the specified flat zone yield strength, and the stress (F_{yc}) is the increased corner zone yield strength. The values of (F_y) and (F_{yc}) are given in section 5.3.2 of this chapter. The effective design width (b) of the web plate was then calculated as:

$$b = \frac{P_w}{F_y\, t} \qquad (5.2)$$

where (t) is the uniform thickness of the channel section. According to the slenderness ratio limits of the design Standards (AISI, 1991 and CSA, 1994), the width of the lip plate was fully effective for all the channel sections under

consideration. However, the width of the flange plate was partially effective for channel sections with (w_f / t) ratios of 28.9 and 35.5 (sections with thickness of 1.22 and 1.02 mm in Table 5.1). The effective design width of the flange plate in such case was calculated according to the procedure provided by the Canadian S136-94 design Standard (CSA, 1994) for non-perforated plates stiffened from one side with a web plate and from the other side with an edge stiffener.

The results for the effective design width are presented in Figure 5.7 for non-perforated web plates and in Figures 5.8(a) to (c) for perforated web plates. The effective design width was normalized with respect to the corresponding web width (w), as shown in the figures, to ease the comparison between different cases.

5.4.2.1 Effects of (w/t) Ratio

The effective design width for non-perforated web plates is presented in Figure 5.7 for different web slenderness ratios (w/t). Both the effective design width results of the approach derived from the present finite element analysis and the Standards predictions (AISI, 1991 and CSA, 1994) are presented. The slenderness ratio limit $(w/t)_{lim}$ of the Standards, which indicates a fully effective plate, is also shown in the figure by a vertical line.

It can be observed from Figure 5.7 that the effective design width (b) of non-perforated plates decreases significantly with the increase of the plate slenderness ratio (w/t). For a plate with (w/t) ratio of about 200, the effective design width is only

20% of the plate width. The behaviour of the effective design width ratio (b/w) created by the finite element results is quite similar to the behaviour of the results of the codes. However, the former behaviour is generally conservative in its predictions than the later one. The reason for the conservative behaviour of the finite element results is the upper bound ultimate load assigned to the flanges, lips, and corners of the channel section as described in the previous section.

The effective design width of the web plate of perforated channel sections has been discussed in the following sections. The effects of the (w/t) ratio on the effective design width of perforated web plates were found similar to that of non-perforated web plates. This can be observed by checking the behaviour of the effective design width ratio (b/w) of the finite element results in Figures 5.8(a) to (c). The effective design width can be less than 10% of the plate width for large (w/t) ratios, when a perforation with (a/w) equals 0.6 and (h/a) equals 3.0 is introduced in the plate.

5.4.2.2 Effects of (a/w) Ratio

The effective design width of perforated web plates is presented in Figures 5.8(a) to (c) for different perforation width-to-web width ratios (a/w). The studied (a/w) ratios cover a range of 0.0 (non-perforated plate) to 0.6 (perforation width is 60% of the plate width). It can be observed from Figure 5.8(a) that the effective width-to-web width ratio (b/w) decreases with an increase of (a/w) ratio. The decrease is more pronounced for webs with small slenderness ratios (w/t) than large

slenderness ratios. This is due to the fact that as (w/t) ratio becomes large, the non-perforated plate becomes partially effective with the central area supporting small area of stresses. Hence, the introduction of a perforation in the centre of the plate causes a marginal reduction in the total area of stresses supported by the plate, and consequently a marginal reduction in the effective design width of the plate. It is also observed in Figure 5.8(a) that for large (w/t) ratios, an (a/w) ratio of 0.2 gives almost no reduction in the effective design width (compared to a/w of 0.0), which confirms the behaviour mentioned in the previous statement.

On the other hand, the loss in the effective design width ratio (b/w) is found close in magnitude to the (a/w) ratio for the channel section with (w/t) ratio of 31.3 in Figures 5.8(a) to (c). In fact, according to the LRFD Specification (AISI, 1991), the loss in the effective design width (Δb) should be equal to the perforation width (a) when (w/t) ratio is less than or equal to the local buckling slenderness ratio limit $(w/t)_{lim}$ shown in Figure 5.7. However, this $(w/t)_{lim}$ was primarily developed for non-perforated plates, and may not be suitable for perforated plates which may have different buckling stresses. This point is further discussed in section 5.5.3 where a proposed effective design width equation for perforated plates is presented.

5.4.2.3 Effects of (h/a) Ratio

The effective design width for different perforation height-to-perforation width ratios (h/a) of perforated web plates is presented in Figures 5.8(a) to (c). The

(h/a) ratios shown in these figures are 1.0, 2.0, and 3.0. The effective width-to-web width ratio (b/w) is generally found to decrease with the increase of (h/a) ratio. However, this decrease is more pronounced for webs with large slenderness ratios (w/t) than for small slenderness ratios. This conclusion can be made by comparing the effective design width results for web plates having (w/t) ratios equal to 31.3 and 194.2, and having similar perforation dimensions. When the first web plate [(w/t) = 31.3] has a perforation with (a/w) of 0.6, and (h/a) increases from 1.0 to 3.0, the loss in (b/w) ratio is only 10%. However, when the second web plate [(w/t) = 194.2] has the same perforation dimension ratios, the loss in (b/w) ratio is 35%. An explanation for the effects of increasing (h/a) ratio was given by Rhodes and Macdonald (1996) based on their experimental findings. They concluded that as the height of the perforation increases, there exists a potential in the material on both sides of the perforation to buckle individually in a column fashion. Based on the current finite element results, it can also be concluded that the individual buckling reduces the effective design width of the web plate, and consequently reduces the ultimate load of the column. Another observation from the current results is that as the slenderness ratio (w/t) of the web plate increases, the tendency for the individual buckling on the sides of the perforation also increases. This is because, as the slenderness ratio of the web plate increases, the slenderness ratio of the whole section also increases and gives more tendency for the individual buckling to occur.

5.4.2.4 Effects of Yield Strength

The effects of two different values of the yield strength (F_y) on the effective design width of non-perforated and perforated web plates were studied. Figure 5.9 shows the effective width-to-web width ratio (b/w) for the web plate at (F_y) equal to 228 MPa and 345 MPa. The effective design width is shown for non-perforated webs and perforated webs with (a/w) and (h/a) ratios equal to 0.6 and 1.0, respectively. It can be observed that the effective design width (b) generally decreases with the increase of the yield strength (F_y). The loss in the effective design width due to the increase of (F_y) is more pronounced for non-perforated plates than for perforated plates. This behaviour is expected as the major loss in the axial stress capacity of the plate is in its central part as discussed earlier in section 5.4.1.4. The slenderness ratio (w/t) of the plate does not seem to have a major effect on the loss in the effective design width due to increase of (F_y), which can be concluded by observing that the loss in (b/w) is fairly constant over the wide range of (w/t) ratio.

5.5 Effective Design Width Equations for Plates with Regular Perforations

In this section, a new proposed equation to predict the loss in the effective design width of a stiffened plate (Δb) due to a regular (circular or square) central perforation is presented. The proposed equation is based on;

[a] The effective design width results of perforated web plates (b), which were obtained from the present finite element analyses for CFS channel sections.

[b] The design equation used by the American cold-formed LRFD Specification (AISI, 1991).

5.5.1 AISI Effective Design Width Procedure

The effective design width equations for non-perforated stiffened compression plates given in the American cold-formed LRFD Specification (AISI, 1991) and the Canadian S136-94 Standard (CSA, 1994) are well-established and quite similar. The equations state that the effective design width (b) is to be calculated as:

$$b = w \qquad \text{for} \quad (w/t) \le (w/t)_{lim} = 0.644 \sqrt{\frac{k\,E}{F_{max}}} \tag{5.3}$$

$$b = 0.95\ t \sqrt{\frac{k\,E}{F_{max}}} \left[1 - 0.208 \left(\frac{t}{w}\right) \sqrt{\frac{k\,E}{F_{max}}} \right] \qquad \text{for } (w/t) > (w/t)_{lim} \tag{5.4}$$

where (k), equal to 4.0, is the buckling coefficient of stiffened plates, and (F_{max}) is the maximum edge stress in the stiffened compression plate.

As for perforated plates, the design procedure given in the American cold-formed LRFD Specification (AISI, 1991) is based on the results of the experimental study of Ortiz-Colberg (1981). This design procedure is only applicable for stiffened compression plates with slenderness ratio (w/t) not greater than 70, and having circular perforation with (a/w) not greater than 0.5. The procedure (in the format of

Equations 5.3 and 5.4) states that:

$$b = w - a \qquad \text{for} \quad (w/t) \le (w/t)_{lim} = 0.644 \sqrt{\frac{k\,E}{F_{max}}} \tag{5.5}$$

$$b = 0.95\ t \sqrt{\frac{k\,E}{F_{max}}} \left[1 - 0.208 \left(\frac{t}{w}\right) \sqrt{\frac{k\,E}{F_{max}}} - \frac{0.8\ a}{w} \right] \quad \text{for} \quad (w/t) > (w/t)_{lim} \tag{5.6}$$

It can be easily concluded, by comparing Equations 5.5 and 5.6 to Equations 5.3 and 5.4, that the loss in the effective design width due to the perforation (Δb) is given by:

$$\Delta b = a \qquad \text{for} \quad (w/t) \le (w/t)_{lim} = 0.644 \sqrt{\frac{k\,E}{F_{max}}} \tag{5.7}$$

$$\Delta b = 1.52 \sqrt{\frac{E}{F_{max}}} \left(\frac{a}{w/t} \right) \qquad \text{for} \quad (w/t) > (w/t)_{lim} \tag{5.8}$$

where (k) is taken equal to 4.0 in Equation 5.8. Equation 5.8 is a slightly conservative modification of the equation proposed by Ortiz-Colberg (1981), which had a constant of 1.46 instead of 1.52.

Equations 5.7 and 5.8 of the LRFD Specification (AISI, 1991) were compared to the present finite element results in Figure 5.10 for the loss in the effective design

width (Δb) due to the perforation. The comparison was done at a maximum stress (F_{max}) equal to a yield stress (F_y) of 345 MPa. Obviously, a larger (Δb) value in the figure means a larger loss in the effective design width due to the perforation. It can be observed from the figure that the code equation is generally highly conservative in the assumption of (Δb). It can also be observed that there exists a discontinuity in the code prediction at the $(w/t)_{lim}$ value due to the use of two different equations at this limit. The code predictions were terminated at a (w/t) ratio of 70 as Equation 5.8 is not applicable beyond this limit. The equation is also not applicable for (a/w) ratios greater than 0.5.

The reasons for the conservative nature of the AISI equation were investigated by reviewing the analysis of Ortiz-Colberg (1981), which is the source of Equation 5.8. It was discovered that Ortiz-Colberg (1981) assumed in his analysis that the slenderness ratio of perforated plates (w/t) is to be calculated based on the overall width rather than the flat width of the plate. The difference between the overall width and the flat width is the width of two rounded corner parts connecting the web plate to the flanges of the cross section. According to that assumption, the above mentioned analysis consistently obtained a (w/t) ratio higher than the correct value for a specific loss in the effective design width (Δb). This behaviour resulted in a shift in all the data towards higher (w/t) ratios, and consequently resulted in a higher regression constant in Equation 5.8.

5.5.2 Proposed Effective Design Width Equation

Figure 5.11 shows the present finite element results for the loss in the effective design width (Δb) due to a square perforation. The results were obtained for perforation width-to-plate width ratios (a/w) of 0.2, 0.4, and 0.6, and for a yield stress (F_y) of 345 MPa. The loss in the effective design width was normalized with respect to the web plate width ($\Delta b/w$).

After investigating different forms of equations for the loss in the effective design width (Δb), an equation of the form of Equation 5.8 was found to represent the perforation effect on (Δb) quite well. The reason was that by dividing both sides of the equation by (w), and considering an unknown constant (C), the equation takes the form:

$$\frac{\Delta b}{w} = C \sqrt{\frac{E}{F_y}} \left(\frac{a/w}{w/t} \right) \qquad (5.9)$$

Equation 5.9 clearly shows the effects of different parameters (a/w, w/t, and F_y) on the normalized loss in the effective design width ($\Delta b/w$) as discussed in section 5.4.2 of this chapter. Moreover, the equation is compatible with the effective design width equation of non-perforated compression plates (Equation 5.4). Hence, Equation 5.9 was used to fit the finite element results presented in Figure 5.11. The constant (C) was selected on the basis of having the equation to represent an upper bound for all the finite element results. This approach resulted in a constant (C) equal to 1.095,

which can be approximated to 1.1 to give the following equation:

$$\frac{\Delta b}{w} = 1.1 \sqrt{\frac{E}{F_y}} \left(\frac{a/w}{w/t} \right) \qquad (5.10)$$

Although the upper bound approach used herein is rather a conservative approach, Equation 5.10 presents a good correlation with the finite element results, as shown in Figure 5.11. The intersections of Equation 5.10 with (a/w) limits are shown in the figure by horizontal lines at a proposed limit for (w/t) ratio. This intersection limit of (w/t) is less than the Standards (CSA, 1994 and AISI, 1991) local buckling limit $[0.644 \sqrt{\frac{k\,E}{F_y}}]$, which was primarily developed for non-perforated plates. This change [reduction] in the limit of (w/t) is logical and in agreement with the experimental findings in this study (Chapter Four) and other studies (Yu and Davis, 1973, and Banwait, 1987). These studies indicated that one of the effects of a perforation on a stiffened compression plate is to reduce its local buckling stress (F_{cr}). The reduction in (F_{cr}) results in an early local buckling of the plate, and eventually less limit of (w/t) ratio.

By combining Equation 5.10 with the effective design width equation for non-perforated plates (Equation 5.4), the following equation was obtained and can be used in replacement of Equations 5.5 and 5.6 combined:

$$b = 0.95\ t \sqrt{\frac{k\ E}{F_{max}}} \left[1 - 0.208 \left(\frac{t}{w}\right) \sqrt{\frac{k\ E}{F_{max}}} - 0.58 \frac{a}{w} \right] \leq (w - a) \qquad (5.11)$$

In other words, Equation 5.11 reads as follows: "the effective design width (b) of a stiffened plate of width (w) subjected to uniform compression, and having a perforation width [diameter] (a) can be calculated using Equation 5.11. This effective design width should not exceed the value of (w-a)". The last term between the brackets (0.58 a/w) in Equation 5.11 would represent the effects of the perforation on the effective design width (b) of the plate.

Equation 5.11 was further verified by comparing the predicted ultimate loads with the current test results (Chapter Four), and the test results of Ortiz-Colberg (1981), Banwait (1987), and Rhodes and Schneider (1994). The properties of the experimental specimens for each of the studies indicated above are given in Appendix D. The predicted (using Equation 5.11) and the experimental ultimate loads (P_p and P_t) for each study are presented in Tables 5.3 through 5.7. The ultimate loads obtained by the AISI Specification (P_{AISI}) (AISI, 1991) using Equations 5.5 and 5.6, and the ultimate loads obtained by the CSA Standard (P_{CSA}) (CSA, 1994) using the unstiffened strip approach are presented in the same tables where applicable, according to the provided limits. The ratios between the experimental ultimate loads and different predicted ultimate loads (P_t / P_p, P_t / P_{CSA}, P_t / P_{AISI}) are also given in the same tables. The percentage drops in the four compared ultimate loads (P_p, P_{CSA},

P_{AISI} , and P_t) due to the perforation are also presented in Tables 5.3 through 5.7. The percentage drop in an ultimate load was calculated as the ratio between the loss in the ultimate load of a specimen due to the perforation, and the ultimate load of the corresponding non-perforated specimen. The percentage drop in the ultimate load is considered another good measure for the current comparison, since it is a measure for the effect of the perforation only, regardless of the strength of the non-perforated specimen.

It can be noticed from Tables 5.3 through 5.7 that the predicted ultimate loads (P_p) are in good agreement with the experimental ultimate loads (P_t). The ultimate loads given by the AISI Specification (P_{AISI}) could not be obtained for many specimens (indicated by N/A in the tables) due to the Specification limits. In the cases where (P_{AISI}) could be obtained, the predicted loads from the current study (P_p) were always closer to the experimental loads (P_t) than (P_{AISI}). The ultimate loads given by the CSA Standard (P_{CSA}) were generally conservative due to the used unstiffened strip approach. The loads (P_{CSA}) could not be obtained for some specimens as well due to the CSA Standard limits. The percentage load drop given by (P_p) was also in better agreement with the percentage given by the experimental load (P_t), than that given by (P_{AISI}) and (P_{CSA}). The mean values and the standard deviations of the ratios (P_t / P_p, P_t / P_{CSA}, P_t / P_{AISI}) for each study, and for all tests, are presented in Table 5.8. It can be concluded from Table 5.8 that the proposed effective design width equation gives the best predictions of the perforated members ultimate loads, when compared to the

predictions of the CSA and AISI Standards. The proposed effective design width equation gives also accurate and safe predictions of the ultimate loads.

5.6 Effective Design Width Equation for Plates with Elongated Perforations

This section presents a proposed equation to predict the loss in the effective design width (Δb) of a stiffened compression plate due to an elongated (oval and rectangular) central perforation. Elongated perforations are generally the perforations with height-to-width ratios (h/a) greater than 1.0. The proposed equation is an extension for the effective design width equation of plates with square perforation (Equation 5.11) presented in section 5.5.2.

The effects of (h/a) ratio on the effective design width (b) of perforated plates were discussed in detail in section 5.4.2.3. It was concluded that (b) decreases with the increase of (h/a) ratio, however that decrease is more pronounced with larger slenderness ratios (w/t) of the plate. Figures 5.12 and 5.13 show the present finite element results for the normalized loss in the effective design width ($\Delta b/w$), for (h/a) ratios equal to 2.0 and 3.0, respectively. The results were obtained for a yield stress (F_y) of 345 MPa.

Based on the finite element results and the conclusions of section 5.4.2.3, the loss in the effective design width (Δb) due to an elongated perforation ($h/a > 1.0$) can be calculated, with reference to (Δb) of a square perforation, as follows:

$$[\Delta b]\ (\text{for } h/a>1.0) = [\Delta b]\ (\text{for } h/a=1.0) \times [1 + D\ (\frac{w}{t})\ (\frac{h}{a} - 1)] \quad (5.12)$$

where (D) is a constant to be determined. In order to maintain simplicity, Equation 5.12 takes into consideration the additional effects of (h/a) and (w/t) ratios on (Δb) in a linear relationship fashion. For a square perforation (h/a = 1.0), the additional term breaks down to a value of 1.0. The constant (D) was determined on the basis of having Equation 5.12 to represent an upper bound for the finite element results as shown in Figures 5.12 and 5.13. This approach resulted in a constant (D) equal to 0.0025, and the following equation for the normalized loss in the effective design width ratio (Δb/w):

$$\frac{\Delta b}{w} = 1.1 \sqrt{\frac{E}{F_y}}\ (\ \frac{a/w}{w/t}\ )\ [1 + 0.0025\ (\frac{w}{t})\ (\frac{h}{a} - 1)] \quad (5.13)$$

An effective design width equation, similar to Equation 5.11, can then be obtained in the following form:

$$b = 0.95\ t \sqrt{\frac{k\ E}{F_{max}}}\ [1 - 0.208\ (\frac{t}{w}) \sqrt{\frac{k\ E}{F_{max}}} - 0.58\ (\frac{a}{w}) - 0.0015\ (\frac{h-a}{t})] \leq (w - a) \quad (5.14)$$

In other words, Equation 5.14 reads as follows: "the effective design width (b) for a stiffened plate of width (w) subjected to uniform compression, and having an elongated perforation of width (a) and height (h), can be calculated using Equation

5.14. This effective design width should not exceed the value of (w-a)". The last term between the brackets $[0.0015(\frac{h - a}{t})]$ in Equation 5.14 would represent the effects of the perforation height on the effective design width (b), while the previous term (0.58 a/w) would represent the effects of the perforation width. The last term would vanish from the equation for a square or circular perforation (h = a).

Equation 5.14 was further verified by comparing the predicted ultimate loads with the current test results (Chapter Four), and the test results of Loov (1984) and Miller and Pekoz (1994). The properties of the experimental specimens for each of the studies indicated above are given in Appendix D. The predicted and experimental ultimate loads (P_p and P_t) for each study are presented in Tables 5.9 through 5.11. The ultimate loads obtained by the CSA Standard (P_{CSA}) (CSA, 1994) using the unstiffened strip approach are presented in the same tables where applicable, according to the Standard limits. No ultimate loads were given by the AISI Specification (AISI, 1991) for the current comparison, as the AISI Specification is only limited to circular perforations. The ratios between the experimental and the predicted ultimate loads (P_t / P_p and P_t / P_{CSA}) are given in the Tables 5.9 through 5.11. The percentage drops in the three compared ultimate loads (P_p , P_{CSA} , and P_t) due to the perforation are also presented in the same tables. The percentage drop in an ultimate load was calculated as described in Section 5.5.2.

It can be noticed from Tables 5.9 through 5.11 that the predicted ultimate loads (P_p) are in good agreement with the experimental loads (P_t). The ultimate loads

given by the CSA Standard (P_{CSA}) are also in good agreement with the experimental loads. However, the loads (P_{CSA}) could not be obtained for some specimens due to the limits of the CSA Standard. The percentage load drop given by (P_p) was also in good agreement with the percentage given by (P_l). The mean values and the standard deviations of the ratios (P_t / P_p and P_t / P_{CSA}) for each study, and for all tests, are presented in Table 5.12. It can be concluded from Table 5.12 that the proposed effective design width equation gives good and safe predictions of the perforated members ultimate loads. Although the CSA Standard procedure also gives good predictions of the ultimate loads, the procedure has some dimension limitations on the perforation width and height.

5.7 Summary

The effects of different perforation parameters on the ultimate strength of perforated cold-formed steel (CFS) compression members have been discussed in this chapter. A finite element study was performed on perforated lipped channel CFS members in compression, using the finite element model developed in chapter Four. The parameters considered in the study were the slenderness ratio of the perforated web plate of the CFS compression member, the perforation width, the perforation height, and the yield strength of the CFS material.

The results of the performed finite element study included the behaviour of the axial stress distribution and the effective design width of the perforated web plate of

the CFS compression members. The effective design width of the perforated plate was predicted based on the finite element ultimate load results of the compression members. The axial compressive stress capacity and the predicted effective design width of the perforated web plate were found to decrease significantly with the increase of perforation width, the plate slenderness ratio, and the yield strength of the material. The perforation height had a similar effect on the axial stress capacity and the effective design width of the perforated plates with relatively large slenderness ratios. One main observation of the study was that a transfer of the axial stresses occur from the central part of the perforated compression plate to the sides of the perforation. This transfer of stresses increased in the case of large slenderness ratio of the plate, and small perforation width and height.

Based on the results of the finite element study, two effective design width equations were developed for perforated compression plates with square and elongated perforations. The efficiency of the two equations in predicting the ultimate strength of perforated CFS compression members was verified through a comparison with the ultimate load results of the experimental study of Chapter Four, and other experimental studies from the literature. The comparison indicated that the proposed equations predict accurate ultimate loads for perforated CFS compression members.

Table 5.1 Overall and cross-sectional dimensions of lipped channel sections

Sec No.	Overall dimensions $w' \times w_f' \times w_l'$	Dimensions (mm) [a]			Thick-ness (t) (mm)	Slenderness ratios		
		Web w	Flange w_f	Lip w_l		w/t	w_f/t	w_l/t
1	101.6x41.3 x12.7	87.6	27.3	5.7	2.8	31.3	9.8	2.0
2		92.1	31.8	7.9	1.91	48.2	16.6	4.1
3		95.5	35.2	9.7	1.22	78.3	28.9	8.0
4	203.2x41.3 x12.7	193.7	31.8	7.9	1.91	101.4	16.6	4.1
5		195.6	33.7	8.9	1.52	128.7	22.2	5.9
6		197.1	35.2	9.7	1.22	161.6	28.9	8.0
7		198.1	36.2	10.2	1.02	194.2	35.5	10.0

[a] Dimensions of flat portions of the section, excluding rounded corners.

Table 5.2 Finite element ultimate loads for 70 study cases of lipped channel sections

Section No.	Ultimate load (P_u) (kN)									
	No perfora-tion	a/w			a/w			a/w		
		0.2	0.4	0.6	0.2	0.4	0.6	0.2	0.4	0.6
		h/a = 1.0			h/a = 2.0			h/a = 3.0		
1	209.7	195.7	182.0	166.7	194.1	180.9	165.6	192.9	181.6	162.8
2	127.2	121.8	115.2	108.3	120.2	115.6	107.7	119.1	116.3	107.1
3	68.9	67.0	63.7	61.6	66.5	63.1	61.2	65.3	63.6	61.0
4	135.6	133.9	124.8	118.4	132.7	120.3	115.6	129.3	118.5	114.3
5	98.1	98.0	92.0	86.9	97.9	88.4	82.6	94.8	86.8	79.8
6	70.7	69.9	67.5	63.1	69.6	64.5	59.2	69.9	63.5	58.3
7	52.6	52.2	50.3	48.6	52.0	49.5	46.9	51.3	49.0	45.4

Table 5.3 Comparison between current predicted and experimental ultimate loads, Author (Chapter 4)

Spec. No.	Predicted load P_p (kN)	CSA load P_{CSA} (kN)	AISI load P_{AISI} (kN)	Test load P_t (kN)	$\frac{P_t}{P_p}$	$\frac{P_t}{P_{CSA}}$	$\frac{P_t}{P_{AISI}}$	% Load drop in			
								P_p	P_{CSA}	P_{AISI}	P_t
A-D	129.7	129.7	129.7	128.5	0.991	0.991	0.991	No perforation			
A-C	118.3	111.2	N/A[a]	117.9	0.997	1.060	N/A	8.8	14.3	N/A	8.2
A-S	118.3	111.2	N/A	119.1	1.007	1.071	N/A	8.8	14.3	N/A	7.3
B-D	64.4	64.4	64.4	65.3	1.014	1.014	1.014	No perforation			
B-C	58.5	56.9	N/A	56.7	0.969	0.996	N/A	9.2	11.6	N/A	13.2
B-S	58.5	56.9	N/A	56.4	0.964	0.991	N/A	9.2	11.6	N/A	13.6

[a] AISI Specification is not applicable for this case.

Table 5.4 Comparison between predicted and experimental ultimate loads, Ortiz-Colberg (1981)

Spec. No.	Predicted load P_p (kN)	CSA load P_{CSA} (kN)	AISI load P_{AISI} (kN)	Test load P_t (kN)	$\frac{P_t}{P_p}$	$\frac{P_t}{P_{CSA}}$	$\frac{P_t}{P_{AISI}}$	% Load drop in			
								P_p	P_{CSA}	P_{AISI}	P_t
I-1,2	66.2	66.2	66.2	66.5	1.005	1.005	1.005	No perforaion			
I-3,9	63.8	59.4	62.9	66.7	1.045	1.123	1.060	3.6	10.3	5.0	-0.3
I-4	62.8	59.2	61.5	62.9	1.002	1.063	1.023	5.1	10.6	7.1	5.4
I-5,10	61.5	58.9	59.7	63.9	1.039	1.085	1.070	7.1	11.0	9.8	3.9
I-6	60.5	58.6	58.3	61.4	1.015	1.048	1.053	8.6	11.5	11.9	7.7
I-7,11	59.3	58.2	56.6	60.4	1.019	1.038	1.067	10.4	12.1	14.5	9.2
I-8	58.1	N/A[a]	N/A[a]	60.5	1.041	N/A	N/A	12.2	N/A	N/A	9.0

[a] CSA and AISI Specifications are not applicable for this case.

Table 5.5 Comparison between predicted and experimental ultimate loads, Banwait (1987) (Series I)

Spec. No.	Predicted load P_p (kN)	CSA load P_{CSA} (kN)	AISI load P_{AISI} (kN)	Test load P_t (kN)	$\frac{P_t}{P_p}$	$\frac{P_t}{P_{CSA}}$	$\frac{P_t}{P_{AISI}}$	% Load drop in			
								P_p	P_{CSA}	P_{AISI}	P_t
I-D	89.4	89.4	89.4	85.3	0.954	0.954	0.954	No perforation			
I-A-2	84.6	79.1	82.9	85.8	1.014	1.085	1.035	5.4	11.5	7.3	-0.6
I-B-2	84.6	79.1	82.9	84.7	1.001	1.071	1.022	5.4	11.5	7.3	0.7
I-A-4	80.0	77.7	76.4	81.7	1.021	1.051	1.069	10.5	13.1	14.5	4.2
I-B-4	80.0	77.7	76.4	81.6	1.020	1.050	1.068	10.5	13.1	14.5	4.3
I-A-6	75.3	N/A	N/A	78.1	1.037	N/A	N/A	15.8	N/A	N/A	8.4
I-B-6	75.3	N/A	N/A	77.7	1.037	N/A	N/A	15.8	N/A	N/A	8.9

Table 5.6 Comparison between predicted and experimental ultimate loads, Banwait (1987) (Series II)

Spec. No.	Predicted load P_p (kN)	CSA load P_{CSA} (kN)	AISI load P_{AISI} (kN)	Test load P_t (kN)	$\frac{P_t}{P_p}$	$\frac{P_t}{P_{CSA}}$	$\frac{P_t}{P_{AISI}}$	% Load drop in			
								P_p	P_{CSA}	P_{AISI}	P_t
II-D	56.4	56.4	56.4	54.0	0.957	0.957	0.957	No perforation			
II-A-2	53.7	49.5	N/A	54.0	1.006	1.091	N/A	4.8	12.2	N/A	0.0
II-B-2	53.7	49.5	N/A	53.2	0.991	1.075	N/A	4.8	12.2	N/A	1.5
II-A-4	51.0	49.1	N/A	53.4	1.047	1.088	N/A	9.6	12.9	N/A	1.1
II-B-4	51.0	49.1	N/A	51.0	1.000	1.039	N/A	9.6	12.9	N/A	5.6
II-A-6	48.3	N/A	N/A	47.1	0.975	N/A	N/A	14.4	N/A	N/A	12.8
II-B-6	48.3	N/A	N/A	47.0	0.973	N/A	N/A	14.4	N/A	N/A	13.0

Table 5.7 Comparison between predicted and experimental ultimate loads, Rhodes and Schneider (1994)

Spec. No.	Predicted load P_p (kN)	CSA load P_{CSA} (kN)	AISI load P_{AISI} (kN)	Test load P_t (kN)	$\frac{P_t}{P_p}$	$\frac{P_t}{P_{CSA}}$	$\frac{P_t}{P_{AISI}}$	% Load drop in			
								P_p	P_{CSA}	P_{AISI}	P_t
I-up	9.23	9.23	9.23	9.38	1.016	1.016	1.016	No perforation			
I-wcl	8.25	7.44	N/A	9.03	1.095	1.214	N/A	10.6	19.4	N/A	3.7
I-wf	8.25	7.44	N/A	8.88	1.076	1.194	N/A	10.6	19.4	N/A	5.3
II-up	21.4	21.4	21.4	22.9	1.070	1.070	1.070	No perforation			
II-wcl	18.9	17.5	17.9	21.9	1.159	1.251	1.223	11.7	18.2	16.4	4.4
II-wf	18.9	17.5	17.9	20.3	1.074	1.160	1.134	11.7	18.2	16.4	11.4
III-up	46.4	46.4	46.4	48.8	1.052	1.052	1.052	No perforation			
III-wcl	40.8	38.0	38.7	47.8	1.172	1.258	1.235	12.1	18.1	16.6	2.0
III-wf	40.8	38.0	38.7	46.5	1.140	1.224	1.202	12.1	18.1	16.6	4.7

Table 5.8 Statistics for comparison between predicted and experimental ultimate loads [a]

Study	Mean			Standard Deviation		
	P_t / P_p	P_t/P_{CSA}	P_t/P_{AISI}	P_t / P_p	P_t/P_{CSA}	P_t/P_{AISI}
Author (Ch. 4)	0.984	1.030	N/A [b]	0.018	0.036	N/A [b]
Ortiz-Colberg (1981)	1.027	1.071 [b]	1.055 [b]	0.016	0.030 [b]	0.017 [b]
Banwait I, II (1987)	1.010	1.069 [b]	1.049 [b]	0.023	0.019 [b]	0.021 [b]
Rhodes, et al. (1994)	1.119	1.217	1.199 [b]	0.039	0.033	0.039 [b]
All	1.033	1.101 [b]	1.097 [b]	0.053	0.076 [b]	0.073 [b]

[a] Excluding non-perforated specimens.

[b] Non applicable specimens were not considered.

Table 5.9 Comparison between current predicted and experimental ultimate loads, (Chapter 4)

Spec. No.	Predic-ted load P_p (kN)	CSA load P_{CSA} (kN)	Test load P_t (kN)	$\frac{P_t}{P_p}$	$\frac{P_t}{P_{CSA}}$	% Load drop in		
						P_p	P_{CSA}	P_t
A-D	129.7	129.7	128.5	0.991	0.991	No perforation		
A-O	116.0	111.3	118.2	1.019	1.062	10.6	14.2	8.0
A-R	116.0	111.3	114.6	0.988	1.030	10.6	14.2	10.8
B-D	64.4	64.4	65.3	1.014	1.014	No perforation		
B-O	56.6	56.9	56.1	0.991	0.986	12.1	11.6	14.1
B-R	56.6	56.9	56.9	1.005	1.000	12.1	11.6	12.8

Table 5.10 Comparison between predicted and experimental ultimate loads, Loov (1984)

Spec. No.	Predicted load P_p (kN)	CSA load P_{CSA} (kN)	Test load P_t (kN)	$\frac{P_t}{P_p}$	$\frac{P_t}{P_{CSA}}$	% Load drop in [a]		
						P_p	P_{CSA}	P_t
1,2,3	97.8	N/A	103.3	1.056	N/A	23.1	N/A	18.8
4,6	71.8	N/A	77.3	1.076	N/A	16.5	N/A	10.1
7,8,9	42.5	N/A	43.8	1.030	N/A	16.7	N/A	14.1
10,11,12	47.3	46.6	47.8	1.011	1.026	10.6	11.9	9.7
13,14,15	79.6	78.4	75.8	0.952	0.967	10.4	11.8	14.7
16,17,18	119.6	117.8	118.5	0.991	1.006	13.3	14.6	14.1
19,20,21	51.2	48.2	52.1	1.018	1.081	6.0	11.5	4.3
22,23,24	85.3	80.4	84.7	0.993	1.053	5.9	11.3	6.5
25,26,27	133.8	125.0	127.8	0.955	1.022	7.6	13.7	11.7
28,29,30	52.3	48.4	48.7	0.931	1.006	4.6	11.7	11.2
31,32,33	87.5	81.1	85.2	0.974	1.051	4.5	11.5	7.0
34,35,36	139.7	127.6	134.0	0.959	1.050	5.5	13.7	9.4

[a] Calculated with respect to code predicted non-perforated sections.

Table 5.11 Comparison between predicted and experimental ultimate loads, Miller and Pekoz (1994)

Spec. No.	Predicted load P_p (kN)	CSA load P_{CSA} (kN)	Test load P_t (kN)	$\frac{P_t}{P_p}$	$\frac{P_t}{P_{CSA}}$	% Load drop in		
						P_p	P_{CSA}	P_t
1:1	109.3	109.3	124.5	1.139	1.139	No perforation		
1:12,13	91.3	91.1	109.6	1.201	1.203	16.5	16.7	12
2:1-5	111.4	111.4	112.8	1.013	1.013	No perforation		
2:11-13	94.3	93.7	98.5	1.045	1.051	15.4	15.9	12.7
1:14-16	29.8	29.8	27.8	0.933	0.933	No perforation		
1:17,19	27.6	26.0	25.3	0.918	0.973	7.5	12.8	9
2:6-10	29.3	29.3	(25.7)	0.877	0.877	No perforation		
2:14-16	27.0	25.5	(26.2)[a]	0.970	1.027	7.8	13.0	(-2.0)

[a] Load is greater than corresponding non-perforated specimen.

Table 5.12 Statistics for comparison between predicted and experimental ultimate loads [a]

Study	Mean		Standard Deviation	
	P_t / P_p	P_t / P_{CSA}	P_t / P_p	P_t / P_{CSA}
Author (Ch. 4)	1.001	1.020	0.012	0.029
Loov (1984)	0.996	1.029[b]	0.042	0.032[b]
Miller & Pekoz (1994)	1.034	1.064	0.107	0.085
All	1.004	1.035[b]	0.060	0.052[b]

[a] Excluding non-perforated specimens.

[b] Non applicable specimens were not considered.

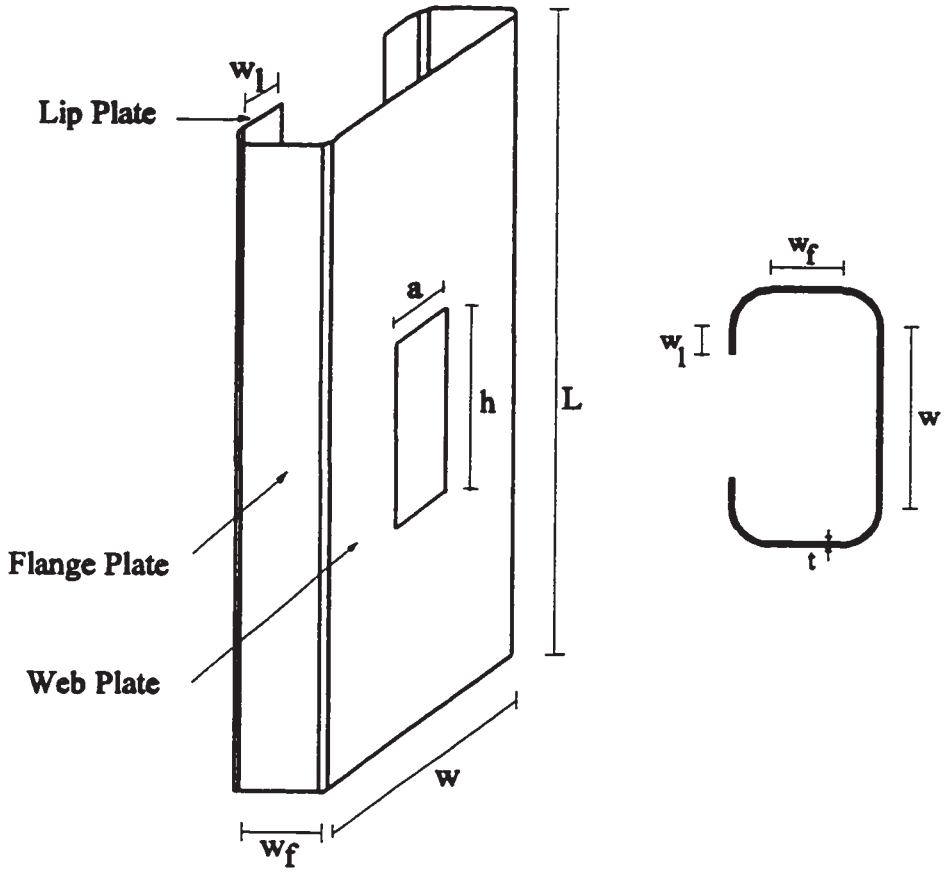

Figure 5.1 Dimensions of perforated cold-formed steel sections

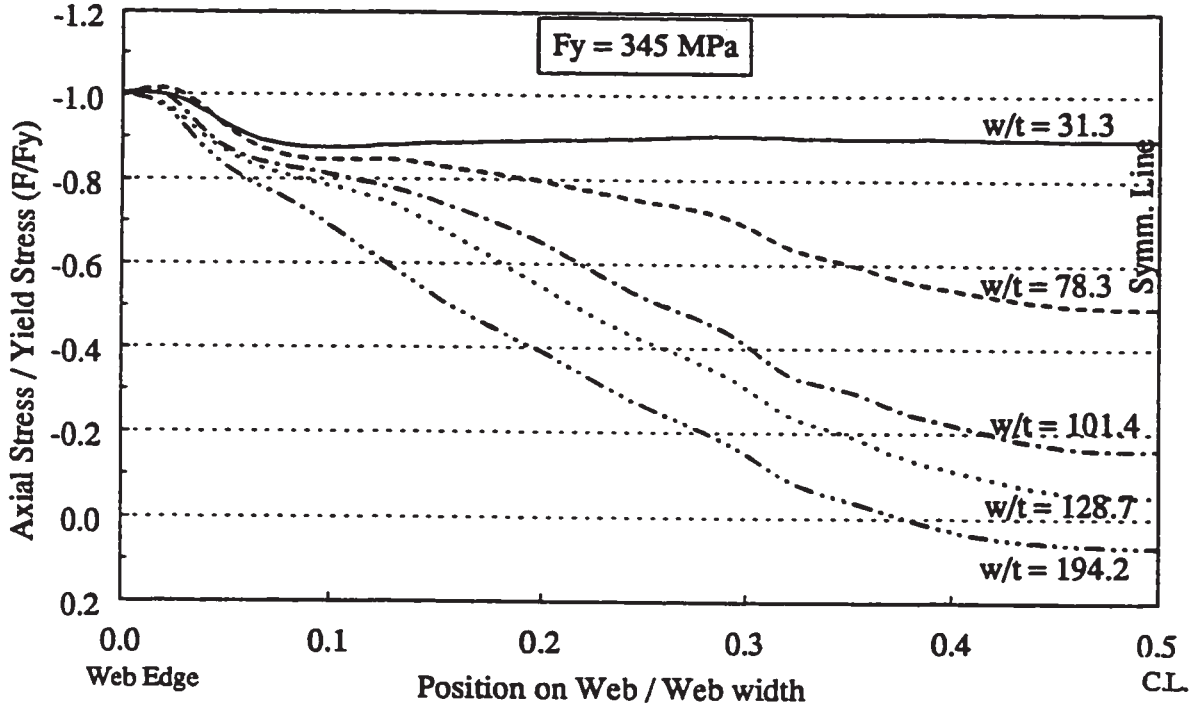

Figure 5.2 Axial stress distributions of non-perforated compression web plates

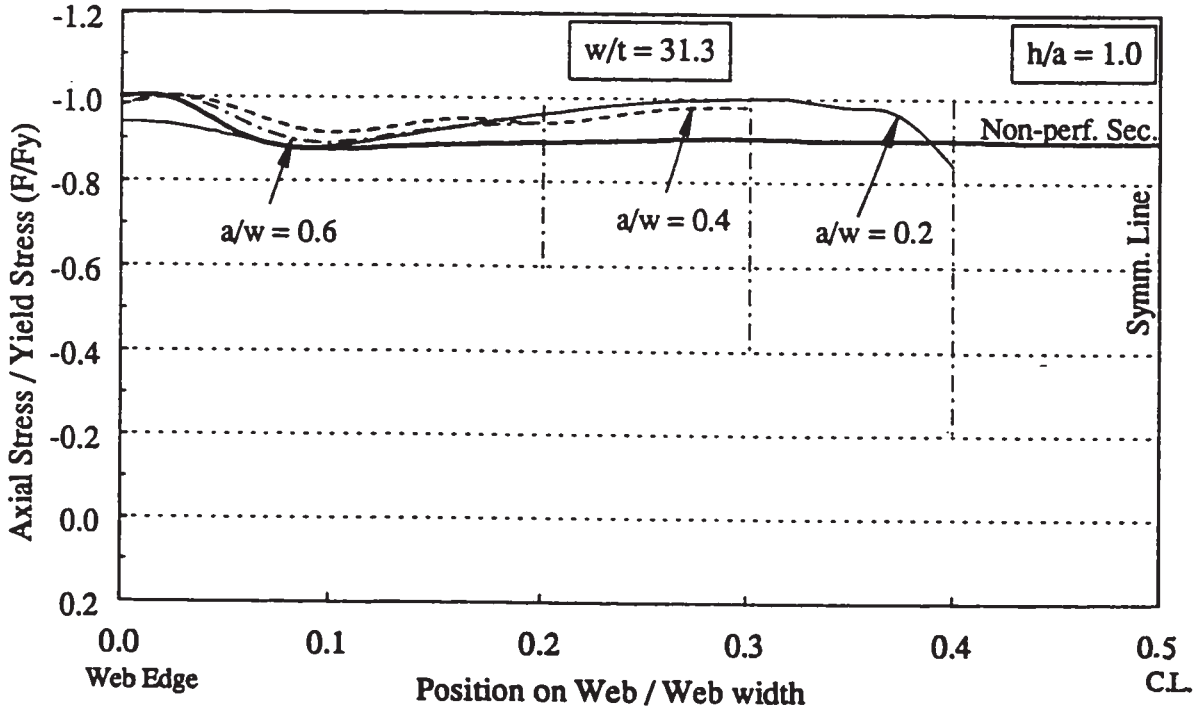

Figure 5.3(a) Axial stress distributions of perforated web plates (w/t=31.3, h/a=1)

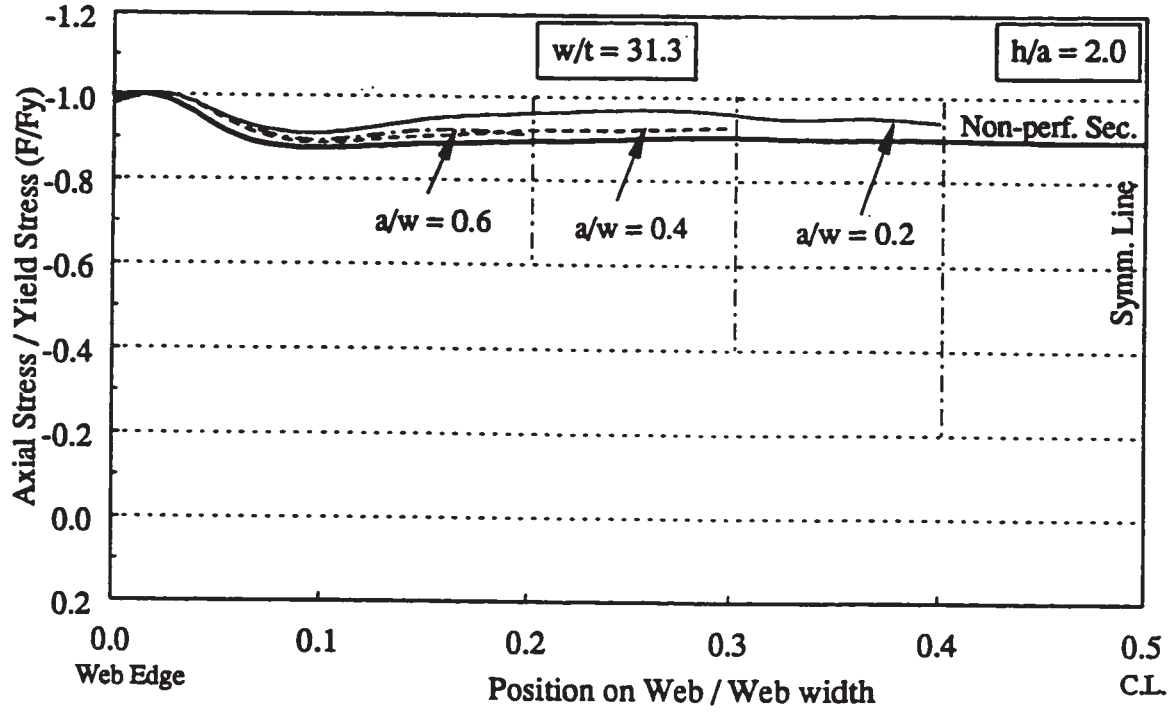

Figure 5.3(b) Axial stress distributions of perforated web plates (w/t=31.3, h/a=2)

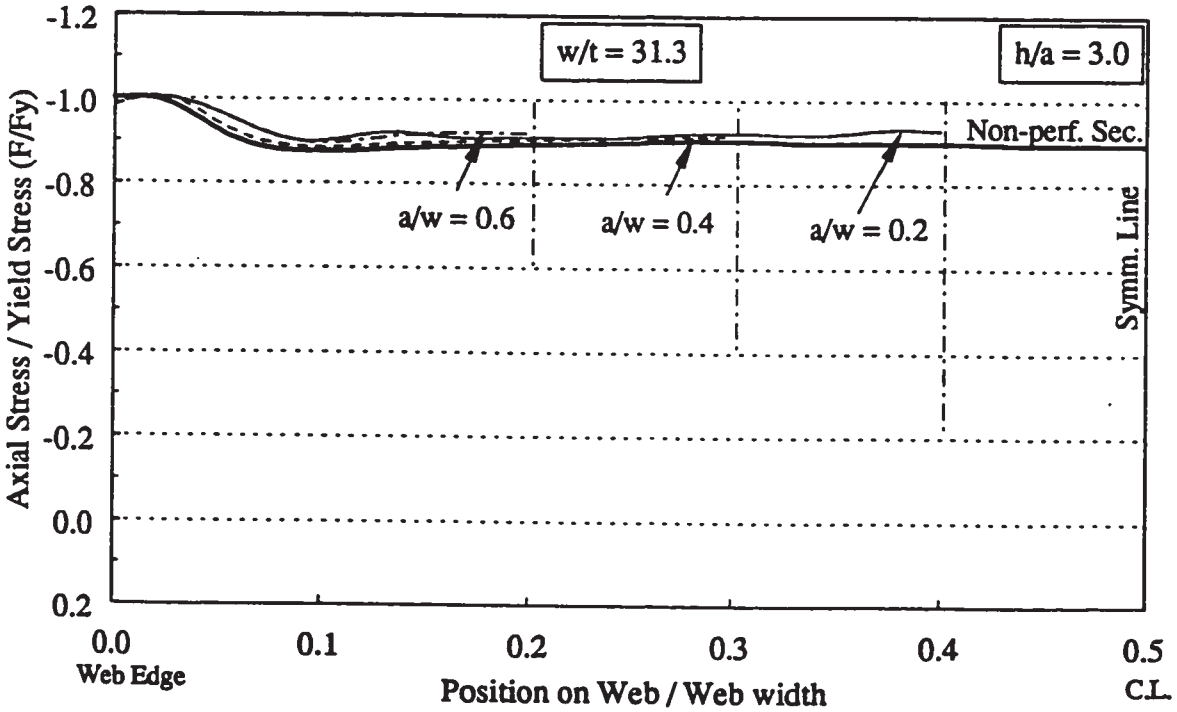

Figure 5.3(c) Axial stress distributions of perforated web plates (w/t=31.3, h/a=3)

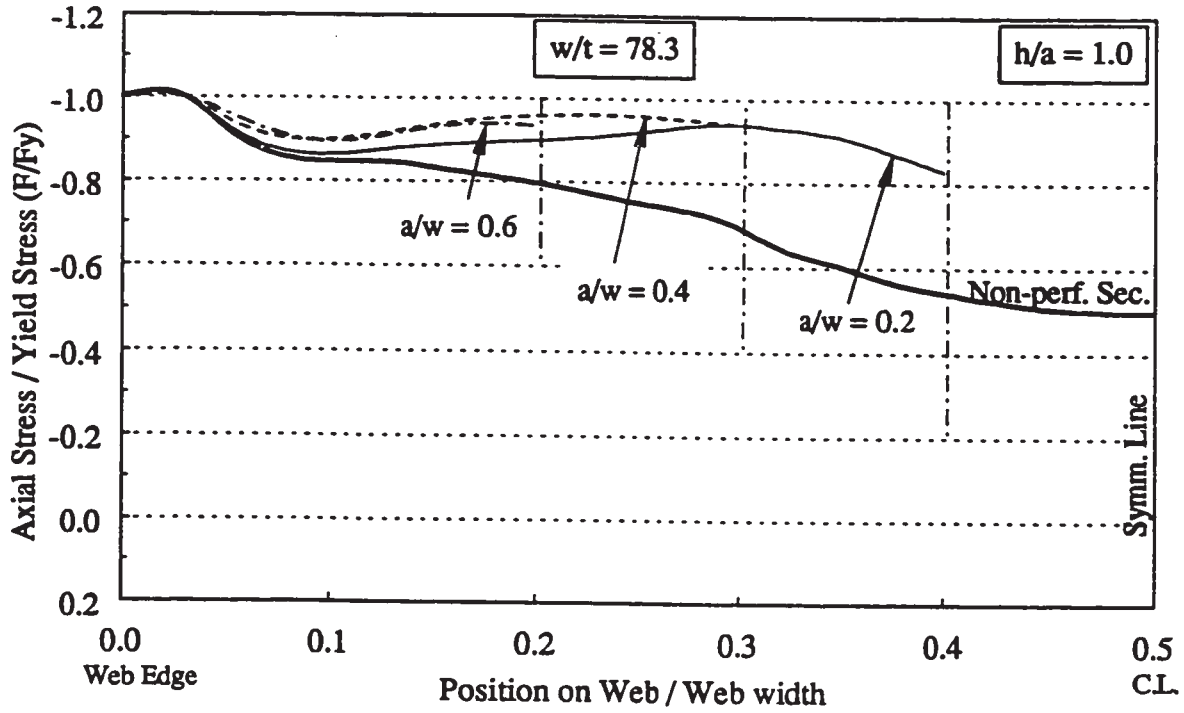

Figure 5.4(a) Axial stress distributions of perforated web plates (w/t=78.3, h/a=1)

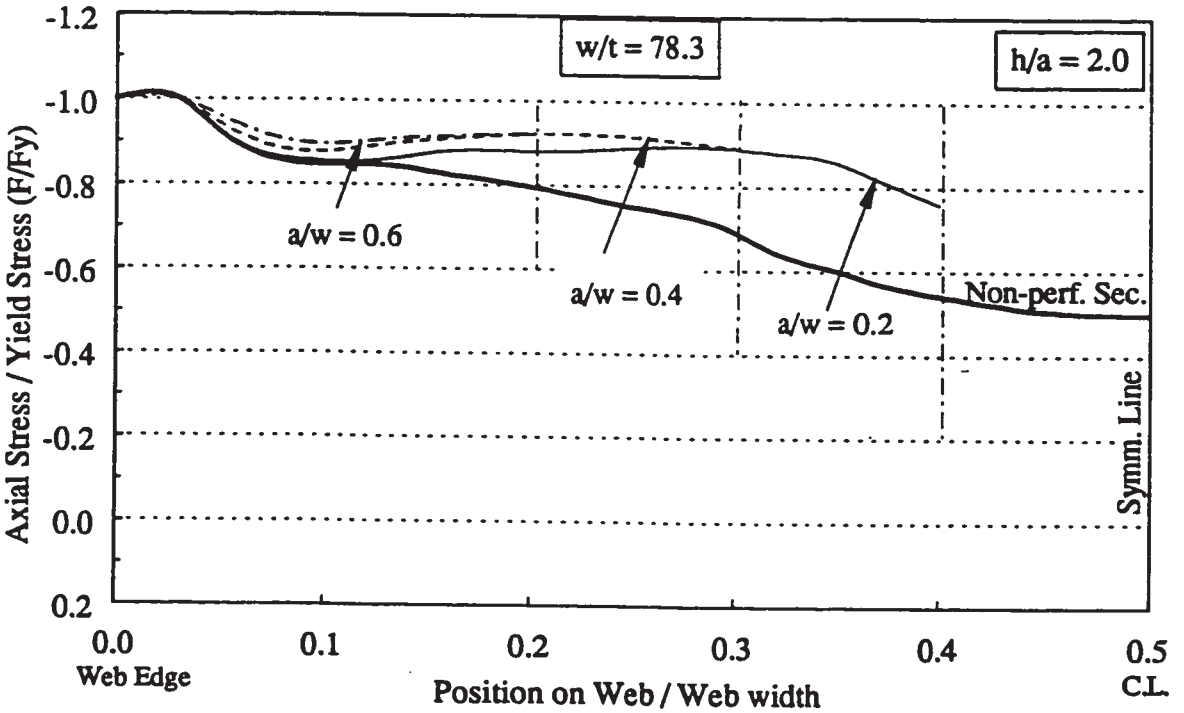

Figure 5.4(b) Axial stress distributions of perforated web plates (w/t=78.3, h/a=2)

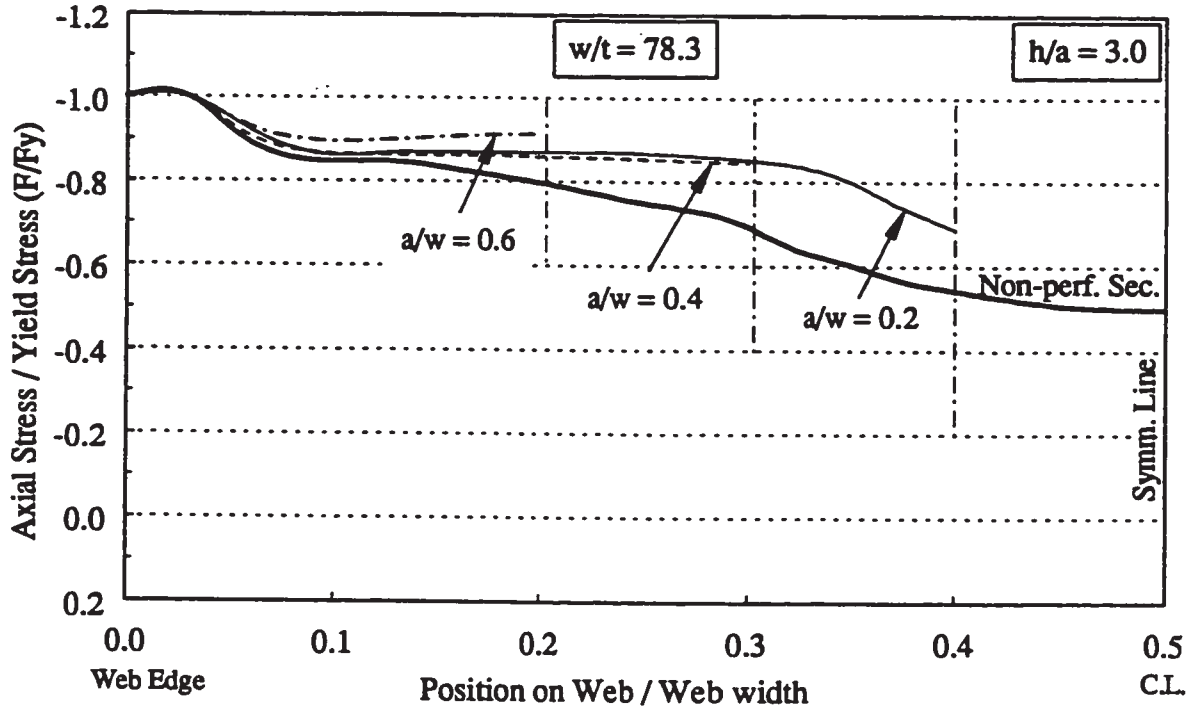

Figure 5.4(c) Axial stress distributions of perforated web plates (w/t=78.3, h/a=3)

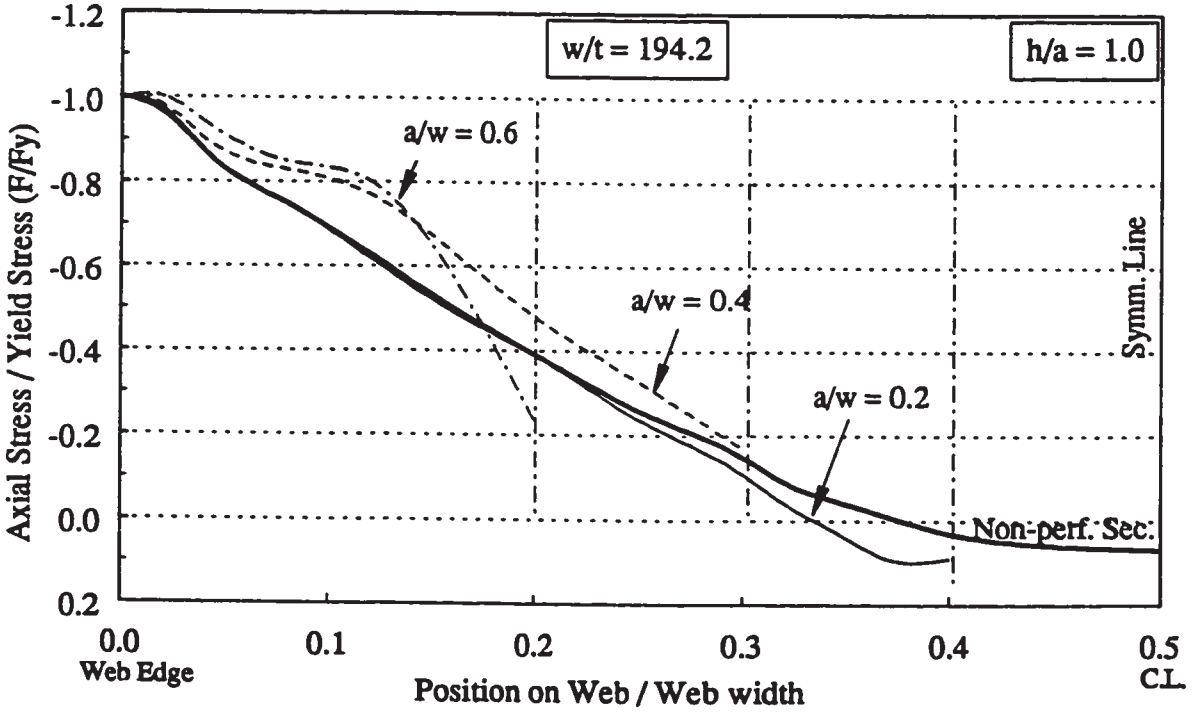

Figure 5.5(a) Axial stress distributions of perforated web plates (w/t=194.2, h/a=1)

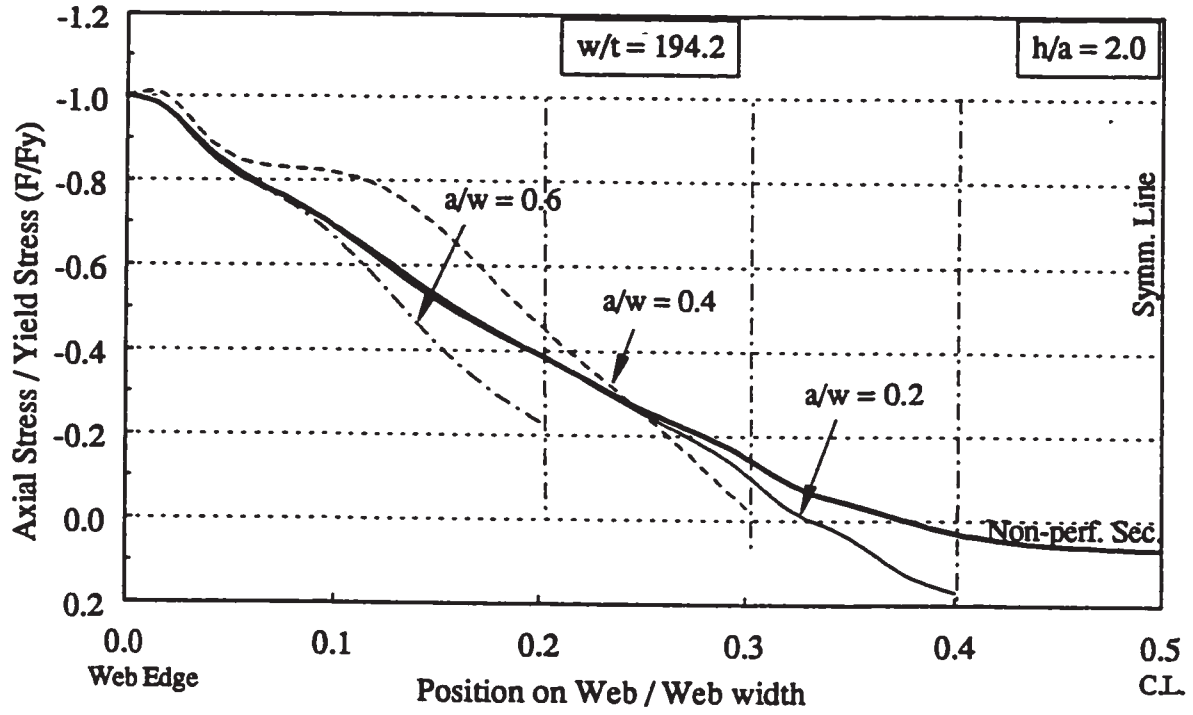

Figure 5.5(b) Axial stress distributions of perforated web plates (w/t=194.2, h/a=2)

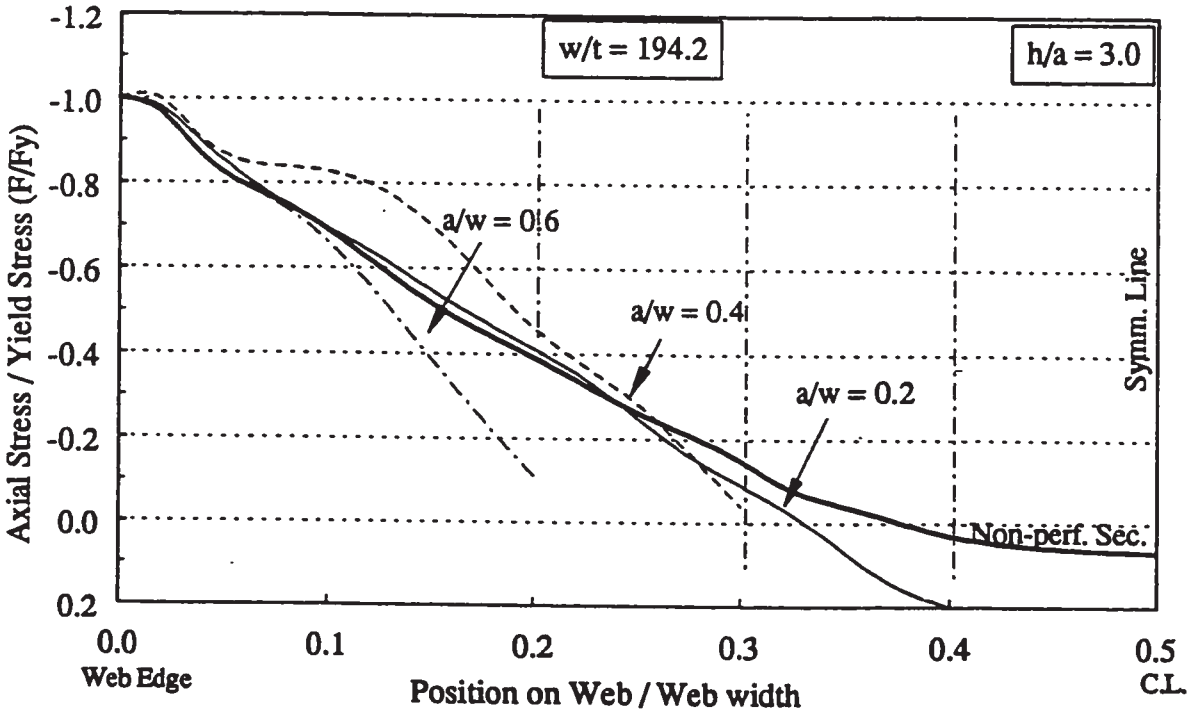

Figure 5.5(c) Axial stress distributions of perforated web plates (w/t=194.2, h/a=3)

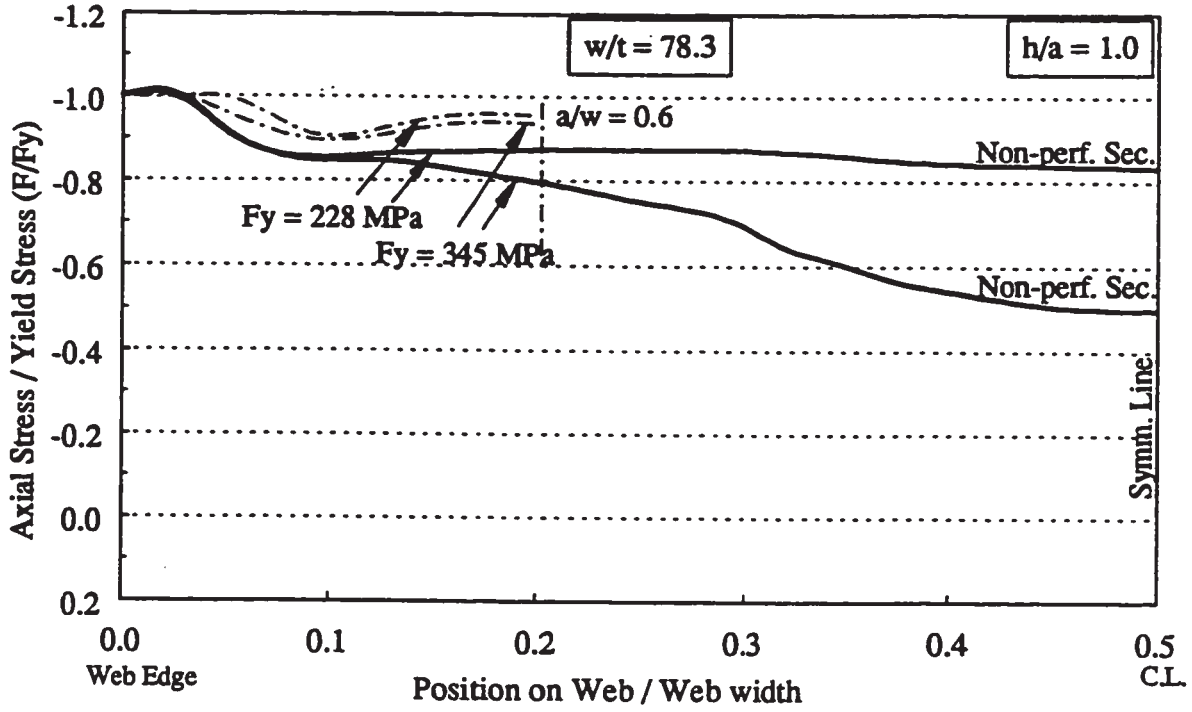

Figure 5.6 Axial stress distributions of compression web plates for different yield strengths

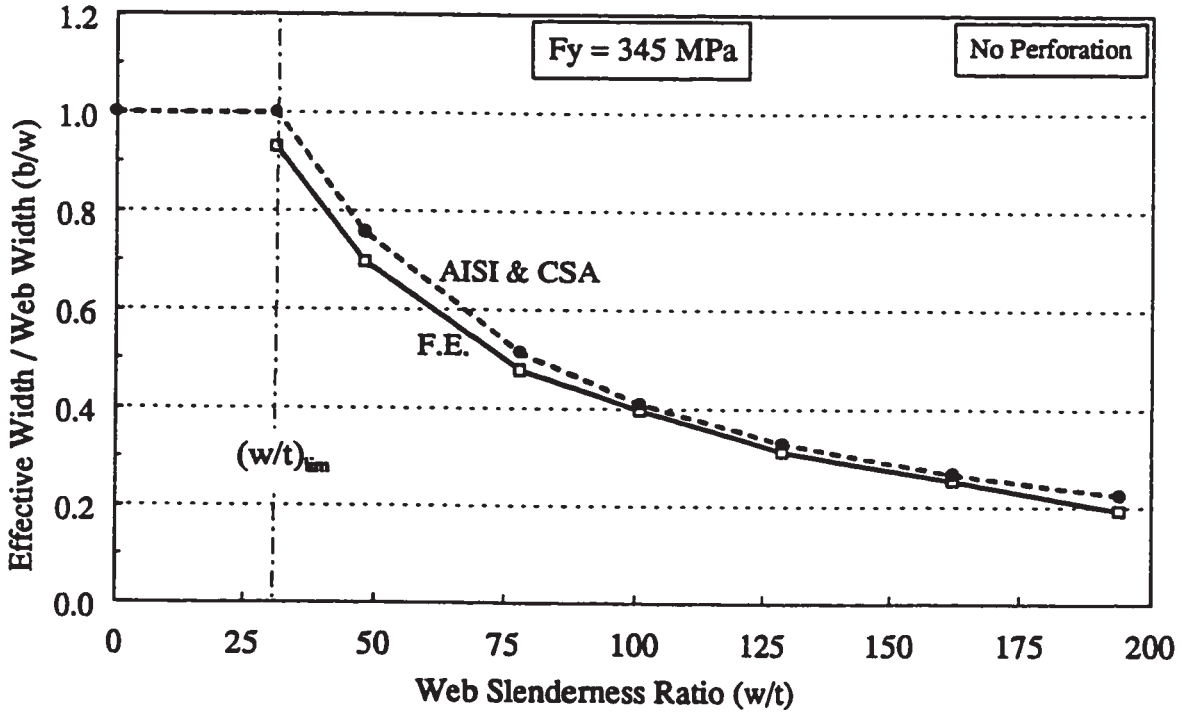

Figure 5.7 Effective design width of non-perforated compression web plates

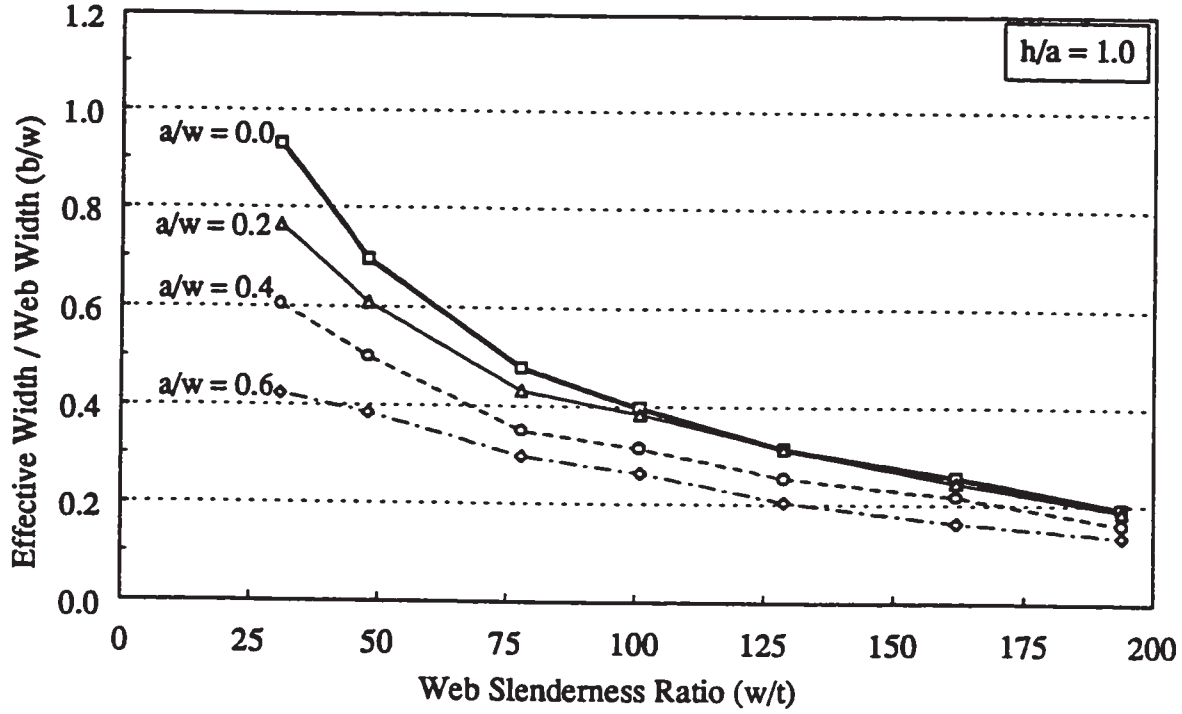

Figure 5.8(a) Effective design width of perforated web plates (h/a=1)

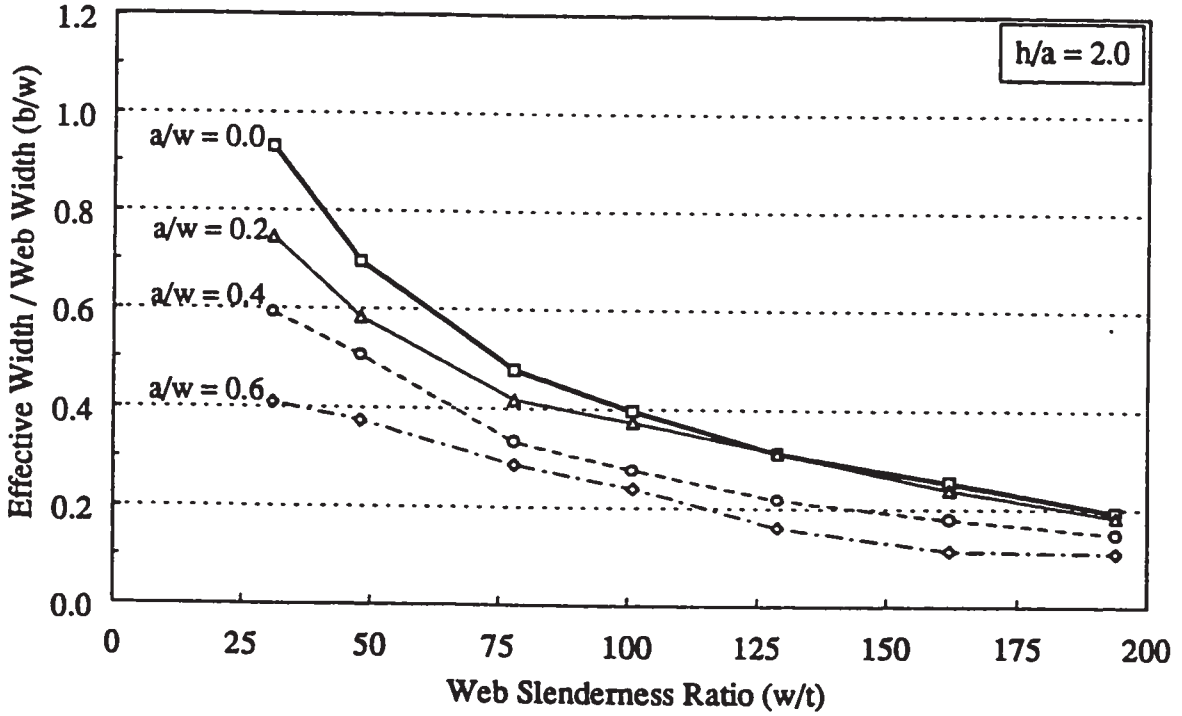

Figure 5.8(b) Effective design width of perforated web plates (h/a=2)

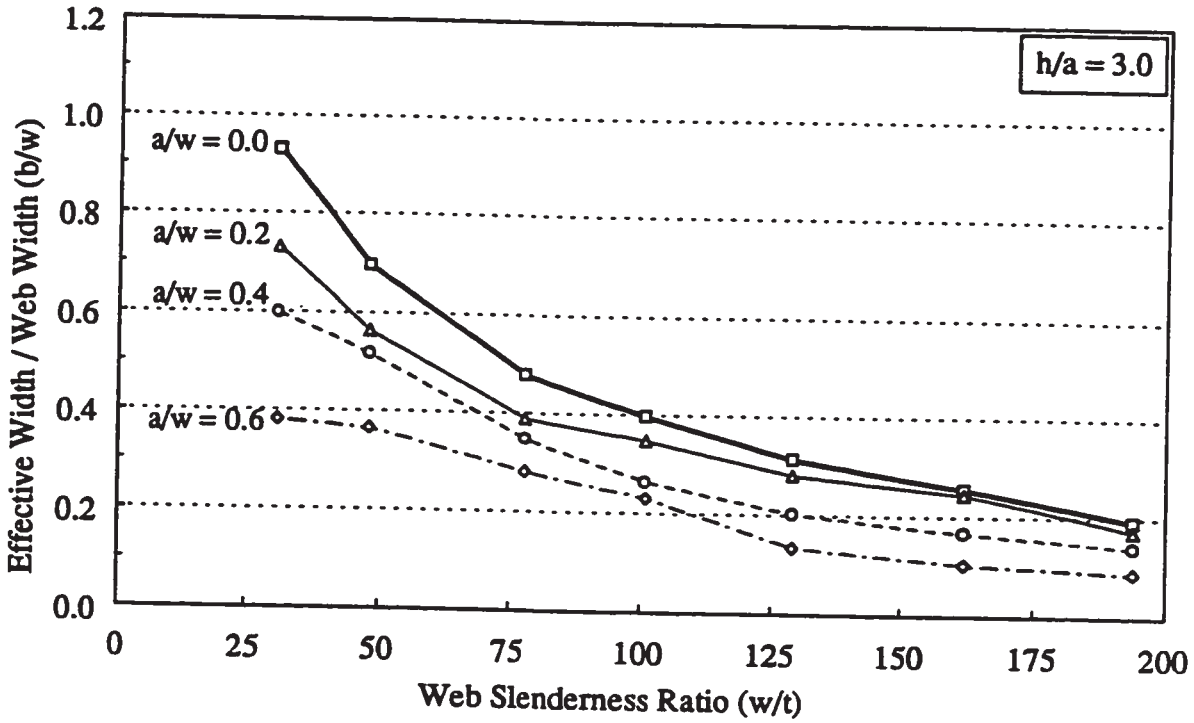

Figure 5.8(c) Effective design width of perforated web plates (h/a=3)

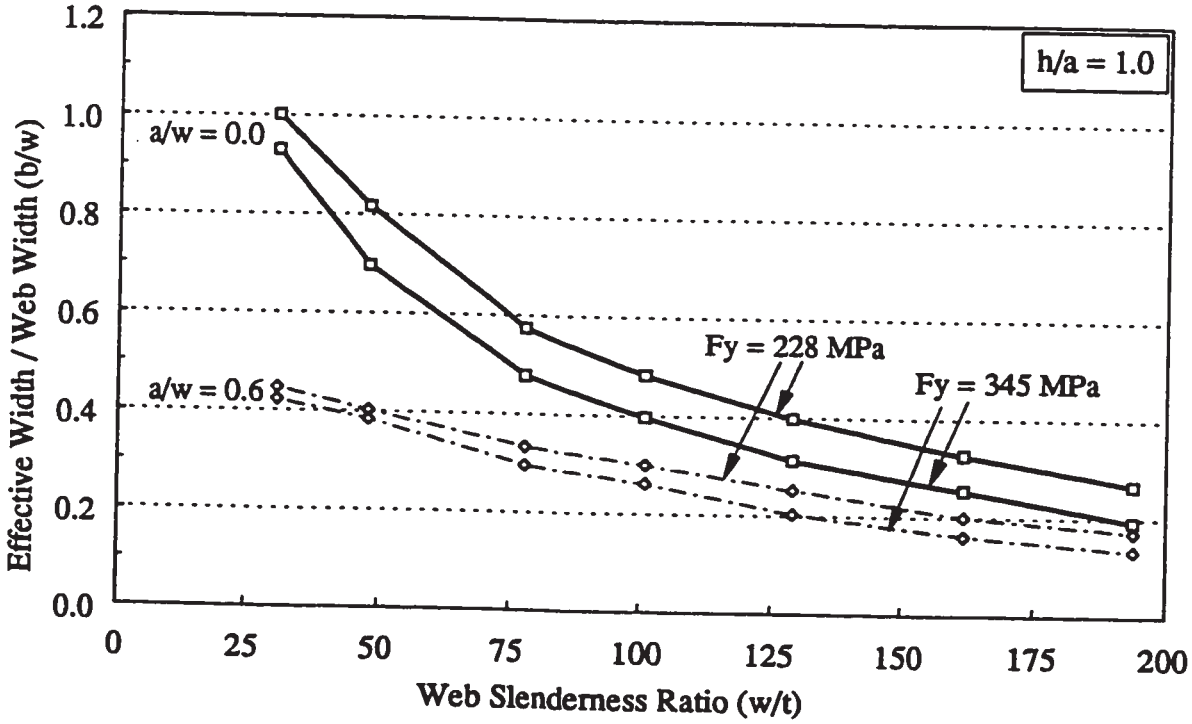

Figure 5.9 Effective design width of compression web plates with different yield strengths

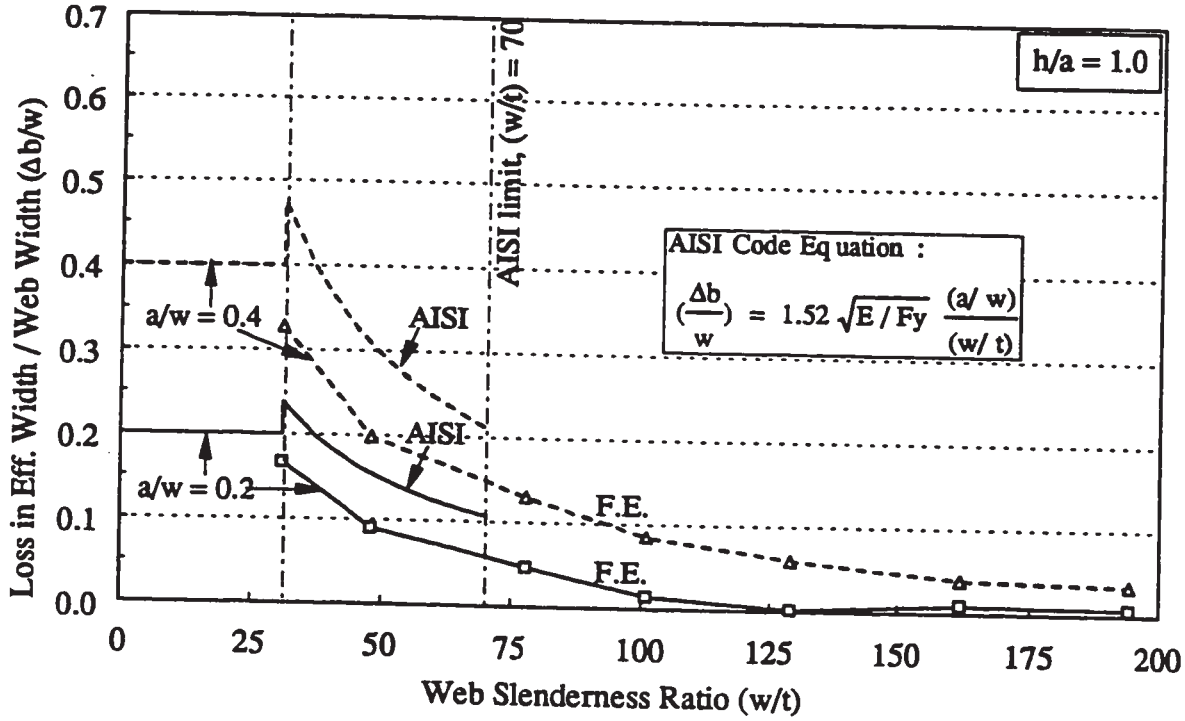

Figure 5.10 Loss in the effective design width of perforated web plates (comparison to AISI)

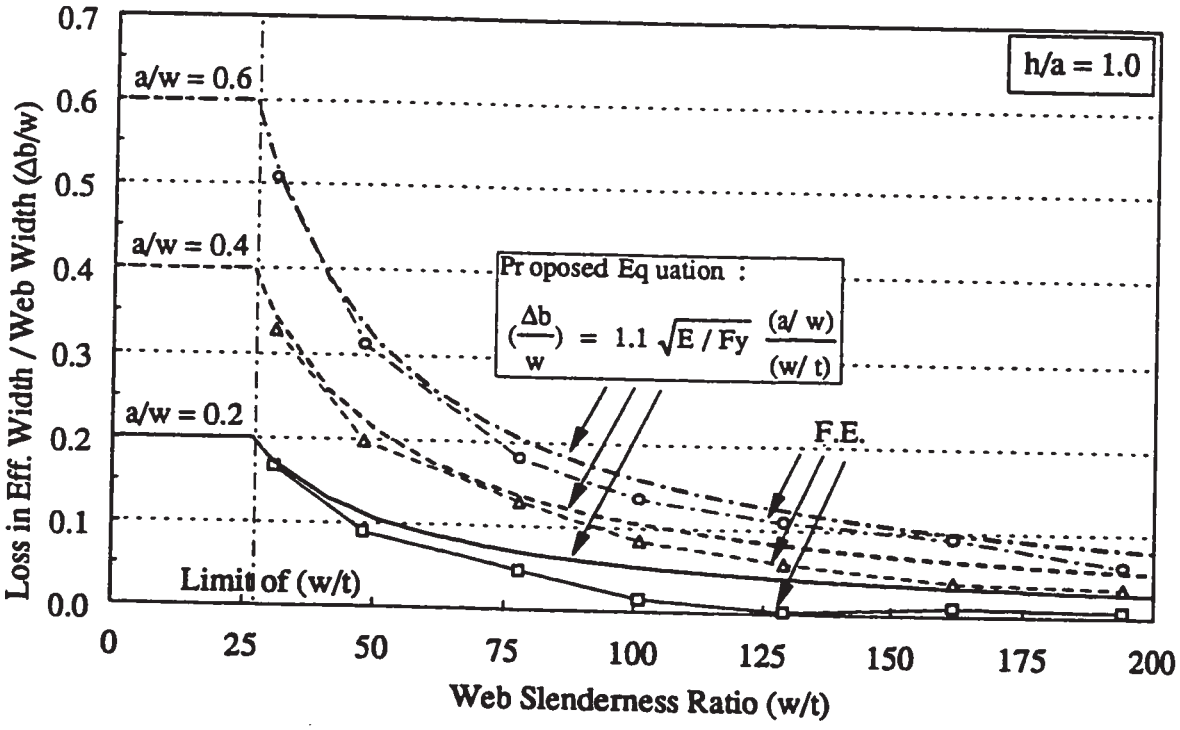

Figure 5.11 Loss in the effective design width of perforated web plates (h/a=1)

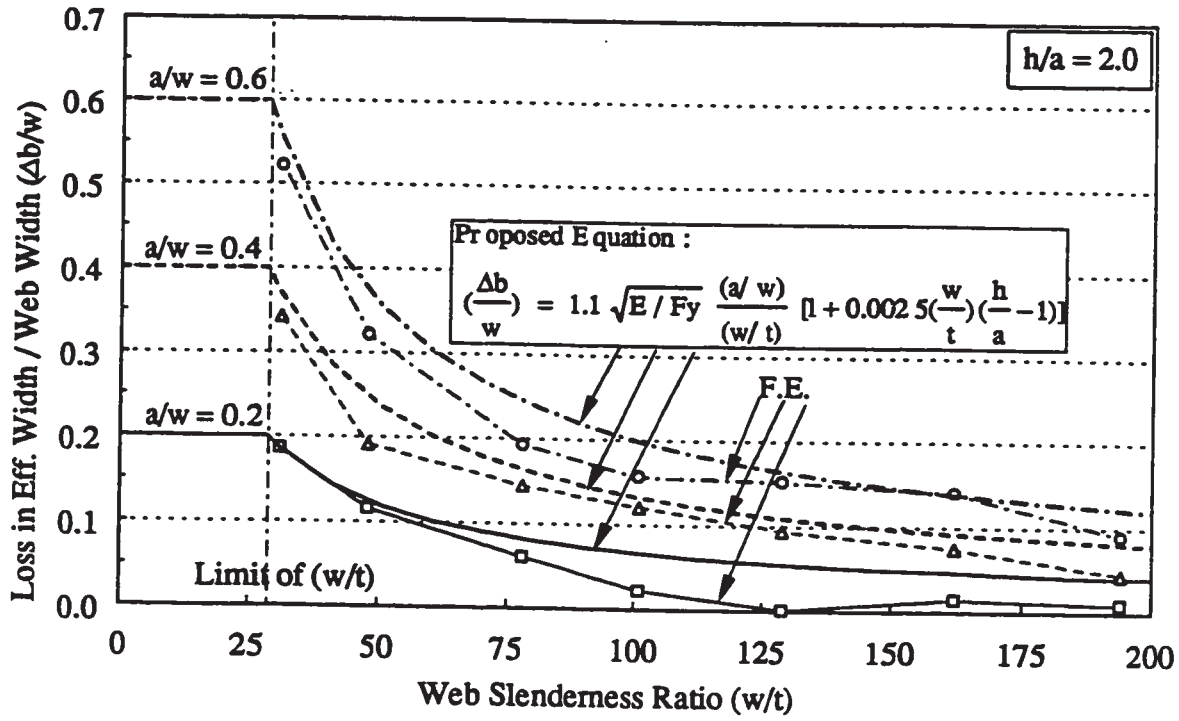

Figure 5.12 Loss in the effective design width of perforated web plates (h/a=2)

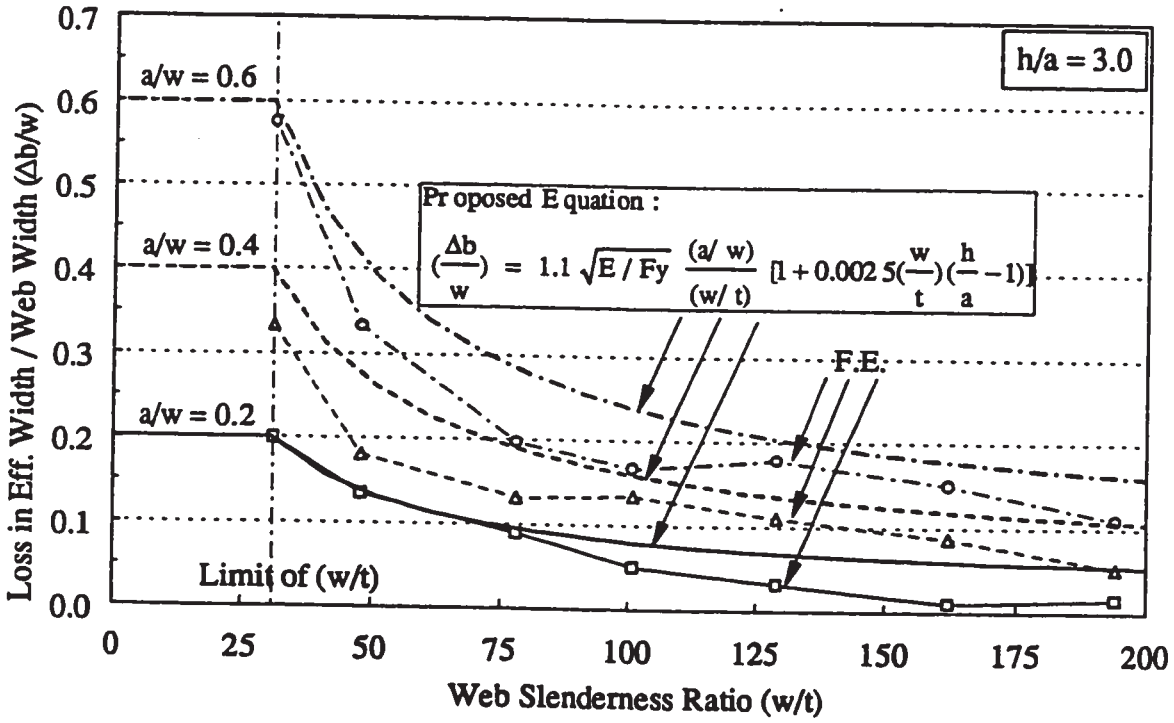

Figure 5.13 Loss in the effective design width of perforated web plates (h/a=3)

CHAPTER 6

SUMMARY AND CONCLUSIONS

6.1 Introduction

The research work accomplished and presented in this thesis is concerned with the local buckling behaviour and the post-local buckling strength of perforated cold-formed steel (CFS) members subjected to axial compressive loading. This research work was motivated by the need for an appropriate analytical technique to predict the behaviour and the ultimate strength of CFS compression members. The objective of developing design equations for perforated CFS members in compression was achieved initially by developing a finite element model for the analysis of CFS members. The model was verified by a comparison with the results of experimental tests, and then used to develop a design procedure for perforated CFS members in compression.

6.2 Summary

A degenerated isoparametric shell finite element was chosen to model cold-formed steel (CFS) sections. The element has nine mid-surface nodes, and applies the Reissner-Mindlin theory where transverse shear deformations are considered and assumed constant through the element thickness. The shell finite element was found

to lock (give over stiff solutions) when applied to very thin shell structures, and shells in pure bending. The method of "assumed strain fields" was implemented in the shell element to eliminate the "transverse shear and membrane locking" problem. A further enhancement of that method was developed in the current study by implementing the "assumed strain fields" method to both linear and nonlinear terms of the stiffness matrix of the 9-node shell element. This enhancement was essential for the large deformation analysis of cold-formed steel members. The accuracy and the efficiency of the new assumed strain shell element was tested with several large deformation and elasto-plastic bench mark problems for plate and shell structures.

A total of 41 tensile coupons was tested in the current study to determine the changes, caused by the cold forming operation, in the mechanical properties and the stress-strain behaviour of the material at different locations of CFS channel sections. The coupons were cut longitudinally from flat parts, corner parts, and near-to-corner parts of the test sections. Based on the test results, analytical models were developed for the distribution of the yield strength and the stress-strain relationship across the CFS channel sections.

Four residual stress tests were performed to measure the longitudinal surface strains along CFS channel sections using electrical resistance strain gauges. The method of the Electrical Discharge Machining (EDM) was used to perform the cutting operation, in order to release the surface strains. Based on the test results, an idealized model for the distribution of residual stresses across CFS channel sections

has been developed.

A finite element model was developed to predict the behaviour of cold-formed steel (CFS) members subjected to axial compressive loading. The model utilized the 9-node assumed strain shell finite element, which includes both geometric and material non-linearities. The model was capable of simulating different material properties, geometric imperfections, and residual stresses. The finite element model was flexible enough to accommodate different shapes of perforations within the CFS members. A uniform axial displacement condition, with the help of a displacement control algorithm, was applied in the finite element model of CFS members in compression.

An experimental study, with a series of 20 non-perforated and perforated CFS channel stub-column tests, was performed to verify the results of the proposed finite element model for CFS members in compression. The tests were also used to investigate the effects of perforations on the deformation behaviour and the strength of CFS members in compression. Finite element models representing the test cases of stub-column specimens were analyzed. The deformation, axial stress, and load capacity results of the finite element analysis were compared to that of the stub-columns.

The developed finite element model for cold-formed steel (CFS) compression members was used to assess the axial stress distributions of the perforated plates of the compression members. The developed model was also used to establish the share of the ultimate load carried out by the perforated plates, and consequently the

effective design widths of the perforated plates. The effects of the plate and the perforation parameters on the axial stress distribution, and the predicted effective design width of the plate, were discussed. The parameters considered were; the plate slenderness ratio (w/t), the perforation width-to-plate width ratio (a/w), the perforation height-to-perforation width ratio (h/a), and the yield strength (F_y) of the CFS compression member. Based on the results of the finite element analysis, two effective design width equations were developed for stiffened compression plates with square and elongated perforations. The equations were verified, for CFS members in compression, by comparing the predicted ultimate loads from the equations with the author's test results and several test results from the literature.

6.3 Conclusions

The following points summarize the main conclusions from the study:

[1] The 9-node degenerated shell finite element suffers from the "transverse shear and membrane locking" problem for thin plate and shell structures, which can be the case for cold-formed steel (CFS) members. The "assumed strain fields" method is an excellent and relatively simple procedure to modify the kinematic formulation of the 9-node shell finite element for thin shell analysis. The enhancement of that method in the current study, by extending it for both linear and nonlinear terms of the element stiffness matrix, resulted in a superior shell finite element, and a complete elimination of the "transverse shear and membrane locking" problem.

[2] A cold-roll forming operation alters the virgin material properties of the steel sheet. The large plastic deformations at and around the corner areas of CFS sections results in increased yield strength (up to 47%) and increased ultimate strength (up to 29%) at the corners, accompanied by a gradual yielding behaviour and a severe decrease in the material elongation. The steel grade (yield strength of the steel sheet) is a main factor affecting the percentage increase of the yield and ultimate strengths. The higher the steel grade, the higher the percentage increase in the yield and ultimate strengths. On the other hand, the forming operation has minor effects on the yield and ultimate strengths of the flat areas of CFS sections.

[3] A cold-roll forming operation results in the generation of residual stresses at both corner and flat areas of CFS sections. Longitudinal residual stresses up to 72% and 30% of the yield strength were measured at the corner areas and at the flat areas, respectively, in the form of residual strains. The longitudinal residual stresses take the form of tensile stresses on the outside surfaces of CFS sections, and equal compressive stresses on the inside surfaces of the sections. Minor transverse residual stresses (less than 1% of the yield strength) were measured at the flat areas of the sections.

[4] Analytical models were developed for the mechanical material properties across CFS channel sections. A channel section was assumed to be divided into a corner zone and a flat zone. The corner zone included all the four curved areas of the section, two equivalent flat areas on both sides of each curved area, and the two lips

of the section. The flat zone included the rest of the flat area of the web and the flanges of the section. A non-uniform distribution model was developed for the yield strength (F_y), based on Karren's model (1967) and the measured flat yield strength (F_y) of the CFS section, as follows:

$$F_y \quad (\underline{\text{flat zone}}) = 1.0\ F_y$$
$$F_y\ (\underline{\text{corner zone}}) = [0.60\ \frac{B_c}{(r/t)^m} + 0.4]\ F_y \qquad \geq F_y \tag{6.1}$$

where,

$$B_c = 3.69\ (\frac{F_u}{F_y}) - 0.819\ (\frac{F_u}{F_y})^2 - 1.79\ , \quad m = 0.192\ (\frac{F_u}{F_y}) - 0.068$$

If the measured yield strength (F_y) of the section is not available, the minimum specified yield strength $(F_y)_{min}$ can be used instead. A multi-linear elasto-plastic stress-strain relationship was also developed, with a bi-linear stress-strain representation of the gradual yielding of the CFS material, and a linear representation of the strain hardening range.

[5] A non-uniform distribution model was developed for the longitudinal residual stress (F_{rl}) across CFS channel sections. The residual stress distribution considered tensile stresses on the outside surface, equal compressive stresses on the inside surface, and a linear variation through the CFS material thickness. The non-uniform distribution is presented as follows:

$$F_{rl} \quad (\underline{\text{flat zone}}) = [0.4 - 0.005\ (\frac{w'}{r})]\ F_y$$
$$F_{rl}\ (\underline{\text{corner zone}}) = 0.4\ F_y \tag{6.2}$$

where (w') is the overall web width and (r) is the inside corner bending radius of the channel section. If the measured yield strength (F_y) of the section is not available, the minimum specified value $(F_y)_{min}$ can be used. The use of the mechanical properties and the residual stress models in the finite element analysis of CFS members assists in obtaining the true deformation and the axial stress behaviour of such members.

[6] The failure of CFS stub-column specimens is usually initiated by local buckling of the web plate. The web of the channel-shaped specimens buckled in a series of longitudinal waves, with a half-wave length value between the web width and the flange width. Perforated CFS steel stub-column specimens had lower axial stiffness, buckling loads, and ultimate loads than the non-perforated specimens. The axial stiffness and the ultimate load were found to decrease with the increase of the perforation width or height. However, a similar effect on the buckling load could not be identified from the experimental study.

[7] A finite element model was developed for perforated CFS members under axial compression. The model gave good predictions for the deformation and the axial stress behaviour of such members. The model was capable of capturing the stress concentrations adjacent to the perforation prior to local buckling. The model was also capable of predicting the large lateral displacements and the transfer of stresses from the centre of the web plate to its edges in the post-local buckling range.

[8] The axial compressive load capacity of non-perforated and perforated web plates of CFS compression members decrease significantly with the increase of the

plate slenderness ratio (w/t). Larger ratios of the perforation width-to-web width (a/w), and the perforation height-to-perforation width (h/a), result in a reduction in the stress continuity and less interaction of the plate elements around the perforation, and consequently a reduction in the axial stress capacity of the plate. Perforations with small (a/w) ratios (up to 0.2) have slight effects on the effective design width and the axial stress capacity of plates with large (w/t) ratios (larger than 100), since the central part of a slender plate is usually not effective in supporting axial stresses.

[9] The predictions of the current effective design width approach for compression plates with circular perforations (provided by the American Cold-Formed LRFD Specification, AISI 1991) are highly conservative, and have a discontinuity at the local buckling slenderness limit $(w/t)_{lim}$. The approach is also limited to (w/t) ratio not greater than 70, and (a/w) ratio not greater than 0.5.

[10] The following two equations are proposed to evaluate the effective design width (b) of stiffened plates under uniform compression, and having central square or elongated perforations, respectively:

$$b = 0.95\ t \sqrt{\frac{k\ E}{F_{max}}} \left[1 - 0.208 \left(\frac{t}{w}\right) \sqrt{\frac{k\ E}{F_{max}}} - 0.58 \frac{a}{w} \right] \leq (w - a) \qquad (6.3)$$

$$b = 0.95\ t \sqrt{\frac{k\ E}{F_{max}}} \left[1 - 0.208 \left(\frac{t}{w}\right) \sqrt{\frac{k\ E}{F_{max}}} - 0.58 \left(\frac{a}{w}\right) - 0.0015 \left(\frac{h-a}{t}\right)\right] \leq (w - a) \qquad (6.4)$$

The proposed equations cover a (w/t) ratio up to 194, (a/w) ratio up to 0.6, and (h/a) ratio up to 3.0. These limits cover the practical limits of perforated web plates of CFS members. The proposed equations give accurate and safe predictions of the effective design width and the ultimate load of perforated CFS members in compression, when compared to the test results of the present study and several test results from the literature.

6.4 Recommendations for Future Research

The following recommendations may be considered in a future research involving tests and analysis of perforated cold-formed steel (CFS) members:

[1] The tensile coupon tests and the residual stress tests of CFS sections, performed in the present study, were limited to channel sections with small rounded corners. Similar tests may be conducted to investigate the effects of the forming operation on the material properties of other shapes of CFS sections, and channel sections with larger rounded corners.

[2] The effects of perforations on the critical buckling stress and the buckling load of perforated CFS compression members need further investigation. Both the perforation width and height were found to affect the buckling load of CFS compression members.

[3] Perforated CFS compression members, with non central perforations and multiple transverse perforations in both the web and flange plates, may be considered

for a finite element analysis similar to the present study. Such members are common nowadays, specially for rack structures.

[4] The assumed strain shell finite element and the CFS material models, presented in this study, may be used to construct finite element models for CFS members under loading conditions other than axial compression. Loading conditions such as; compression and bending, web bearing, and compression and web bearing, may be considered for CFS members.

REFERENCES

Abdel-Rahman, N. and Sivakumaran, K.S. (1997), Material Properties Models for Analysis of Cold-Formed Steel Members, Accepted for Publication in the Journal of Structural Engineering, ASCE.

Abdel-Rahman, N. and Sivakumaran, K. S. (1996), Evaluation and Modelling of the Material Properties for Analysis of Cold-Formed Steel Sections, 13th International Speciality Conference on Cold-Formed Steel Structures, St. Louis, Missouri, U.S.A.

Abdel-Rahman, N. and Sivakumaran, K. S. (1995), Nonlinear Analysis of Cold-Formed Steel Members Using Assumed Strain Shell Finite Elements, Proceedings of the Annual Conference of the Canadian Society for Civil Engineering, CSCE, Vol. IV, Ottawa, Ontario, Canada.

Abdel-Rahman, N. and Sivakumaran, K. S. (1994), Finite Elements for Analysis of Cold-Formed Steel Members, Proceedings of the Annual Conference of the Canadian Society for Civil Engineering, CSCE, Vol. II, Winnipeg, Manitoba, Canada.

Ahmad, S., Irons, B. M., and Zienkiewicz, O. C. (1970), Analysis of Thick and Thin Shell Structures by Curved Finite Elements, International Journal for Numerical Methods in Engineering, Vol. 2, pp. 419-451.

AIJ (1985), Recommendations for the Design and Fabrication of Light Weight Steel Structures, Architectural Institute of Japan, Japan.

AISI (1991), Load and Resistance Factor Design Specification (LRFD) for Cold Formed Steel Structural Members, American Iron and Steel Institute, Washington, D.C., U.S.A.

Alexander, J. M. (1959), An Analysis of the Plastic Bending of Wide Plate and the Effect of Stretching on Transverse Residual Stresses, Proceedings (Institute of Mechanical Engineers), Vol. 173, No. 1, 73.

ASTM Standards (1994a). Iron and Steel Products - Coated Steel Products, American Society for Testing and Materials, A446/A 446M, Philadelphia, U.S.A.

ASTM Standards (1994b). Standard Test Methods and Definitions for Mechanical Testing of Steel Products, American Society for Testing and Materials, A370-92, Philadelphia, U.S.A.

ASTM Standards (1994c). Standard Test Method for Weight of Coating on Iron and Steel Articles with Zinc or Zinc-Alloy coatings, American Society for Testing and Materials, A 90/A 90M, Philadelphia, U.S.A.

Banwait, A. S. (1987), Axial Load Behaviour of Thin Walled Steel Sections with Openings, M. Eng. Thesis, McMaster University, Hamilton, Ontario, Canada.

Bathe, K. J. (1982), Finite Element Procedures in Engineering Analysis, Prentice-Hall Inc., Englewood Cliffs, New Jersy.

Batoz, J. L. and Lardeur, P. (1989), A Discrete Shear Triangular Nine Degree of Freedom Element for the Analysis of Thick to Very Thin Plates, International Journal for Numerical Methods in Engineering, Vol. 28, pp. 533-560.

Chajes, A., Britvec, S. J., and Winter, G. (1963), Effects of Cold-Straining on Structural Sheet Steel, Journal of Structural Division, ASCE, Vol. 89, No. ST4, pp. 1-32.

Chen, W. F. and Han, D. J. (1988), Plasticity for Structural Engineers, Springer-Verlag Inc., New York.

Coetsee, J. S., Van den Berg, G. J., and Van der Merwe, P. (1990), The Effect of Workhardening and Residual Stresses due to Cold Working of Forming on the Strength of Cold-Formed Stainless Steel Lipped Channel Sections, 10th International Specialty Conference on Cold-Formed Steel Structures, St. Louis, Missouri, U.S.A.

Column Research Council (1976), Guide to Stability Design Criteria for Metal Structures, Edited by Johnston, B. G., Wiely-Interscience, New York, U.S.A.

Crisfield, M. A. (1981), A Fast Incremental/Iterative Solution Procedure that Handles "Snap-Through", Computers and Structures, Vol. 13, pp. 55-62.

Crisfield, M. A. (1975), Full-Range Analysis of Steel Plates and Stiffened Plating Under Uniaxial Compression, Proceedings of the Institute of Civil Engineers, Part 2, Vol. 59, pp. 595-624.

CSA (1994), Cold Formed Steel Structural Members, S136-94, Canadian Standards Association, Rexdale, Ontario, Canada.

Dally, J. W. and Riley, W. F. (1978), Experimental Stress Analysis, McGraw-Hill, 2nd. Edition.

El Damatty, A. (1995), Non-Linear Dynamic Extension of Consistent Shell Element and Analysis of Liquid-Filled Conical Tanks, Ph.D. Thesis, McMaster University, Hamilton, Ontario, Canada.

Gilewski, W. and Radwanska, M. (1991), A Survey of Finite Element Models for the Analysis of Moderately Thick Shells, Finite Elements in Analysis and Design, Vol. 9, pp. 1-21.

Hancock, G. J. (1981), Nonlinear Analysis of Thin Sections in Compression, Journal of Structural Division, ASCE, Vol. 25, No. 1, pp. 147-155.

Horrigome, G. (1977), Finite Element Instability Analysis of Free-Form Shells, Division of Structural Mechanics, The Norwegian Institute of Technology, Trondheim, Report No. 77-2.

Huang, H. C. (1987a), Implementation of Assumed Strain Degenerated Shell Elements, Computers and Structures, Vol. 25, No. 1, pp. 147-155.

Huang, H. C. (1987b), Membrane Locking and Assumed Strain Shell Elements, Computers and Structures, Vol. 27, No. 5, pp. 671-677.

Huang, H. C. and Hinton, E. (1986), A New Nine Node Degenerated Shell Element with Enhanced Membrane and Shear Interpolation, International Journal for Numerical Methods in Engineering, Vol. 22, pp. 73-92.

Hughes, T. J. R., Cohen, M., and Haroun, M. (1978), Reduced and Selective Integration Techniques in the Finite Element Analysis of Plates, Nuclear Engineering Design, Vol. 46, pp. 203-222.

INDAP (1987), Incremental Nonlinear Dynamic Analysis Program, Department of Mechanical Engineering, McMaster University, Hamilton, Ontario, Canada.

Ingvarsson, L. (1979), Cold-Forming Residual Stresses in Thin-Walled Structures, International Conference on Thin-Walled Structures, Glasgow, Scotland.

Irons, B. M. (1976), The Semi Loof Shell Elements, Finite Elements for Thin Shells and Curved Members, edited by Ashwell and Gallagher, London.

Kanok-Nukulchai, W. and Ma, H. (1993), A Review of Displacement-Based Degenerate Shell Elements, Past and Present, Second Asian-Pacific Conference on Computational Mechanics, Sydney, Australia.

Kanok-Nukulchai, W. (1990), Development of a Powerful Nonlinear Analysis Package for Small Computers, International Conference on Education, Practice, and Promotion of Computational Methods in Engineering using Small Computers, Macau.

Karren, K. W. (1967), Corner Properties of Cold-Formed Steel Shapes, Journal of the Structural Division, ASCE Proceedings, Vol. 93, No. ST1, pp. 401-432.

Karren, K. W. and Winter, G. (1967), Effects of Cold-Forming on Light-Gage Steel Members, Journal of the Structural Division, ASCE Proceedings, Vol. 93, No. ST1, pp. 433-469.

Kawai, T. and Yoshimura, N. (1969), Analysis of Large Deflection of Plates by the Finite Element Method, International Journal for Numerical Methods in Engineering, Vol. 1, pp. 123-133.

Korol, R. M. (1971), A Model to Represent The Effect of Cold-Bending Wide Sheet on Subsequent Behaviour Under Uniaxial Stressing, International Journal of Mechanical Sciences, Vol. 13, pp. 681-688.

Korol, R. M. and Sherbourne, A. N. (1972), Strength Predictions of Plates in Uniaxial Compression, Journal of the Structural Division, ASCE Proceedings, Vol. 98, No. ST9, pp. 1965-1986.

Koziey, B. L. (1993), Formulation and Applications of Consistent Shell and Beam Elements, Ph.D. Thesis, McMaster University, Hamilton, Ontario, Canada.

Kwon, Y. B. and Hancock, G. J. (1991), Strength Tests of Cold-Formed Channel Sections Undergoing Local and Distortional Buckling, Research Report No. R640, Centre for Advanced Structural Engineering, The University of Sydney, Australia.

Langan, J. E., LaBoube, R. A., and Yu, W. W. (1994), Perforated Webs Subjected to End-One-Flange Loading, 12th International Speciality Conference on Cold-Formed Steel Structures, St. Louis, Missouri, U.S.A.

Lind, N. C. and Schroff, D. K. (1975), Utilization of Cold Work in Cold-Formed Steel, Journal of the Structural Division, ASCE Proceedings, Vol. 101, No. ST1, pp. 67-78.

Loov, R. (1984), Local Buckling Capacity of C-Shaped Cold-Formed Steel Sections with Punched Webs, Canadian Journal of Civil Engineering, Vol. 11, pp. 1-7.

Mackerle, J. (1993), Finite and Boundary Element Analyses of Shells - A Bibliography (1990-1992), Finite Elements in Analysis and Design, Vol. 14, pp. 73-83.

Miller, T. H. and Pekoz, T. (1994), Unstiffened Strip Approach for Perforated Wall Studs, Journal of Structural Engineering, ASCE, Vol. 120, No. 2, pp. 410-421.

Mindlin, R. D. (1951), Influence of Rotary Inertia and Shear on Flexural Motions of Isotropic Elastic Plates, Journal of Applied Mechanics, ASME, Vol. 18, pp. 31-38.

Narayanan, R. and Chow, F. Y. (1984), Ultimate Capacity of Uniaxially Compressed Perforated Plates, Thin-Walled Structures, No. 2, pp. 241-264.

Ortiz-Colberg, R. (1981), The Load Carrying Capacity of Perforated Cold-Formed Steel Columns, M.Sc. Thesis, Cornell University, Ithaca, N.Y., U.S.A.

Parisch, H. (1979), A Critical Survey on the 9-Node Degenerated Shell Element with Special Emphasis on Thin Shell Application and Reduced Integration, Computer Methods in Applied Mechanics and Engineering, Vol. 20, pp. 323-350.

Rhodes, J. and Macdonald, M. (1996), The Effects of Perforation Length on the Behaviour of Perforated Elements in Compression, 13th International Specialty Conference on Cold-Formed Steel Structures, St. Louis, Missouri, U.S.A.

Rhodes, J. and Schneider, F. D. (1994), The Compressional Behaviour of Perforated Elements, 12th International Specialty Conference on Cold-Formed Steel Structures, St. Louis, Missouri, U.S.A.

Roorda, J. and Venkataramaiah, K. R. (1979), Effective Width of Stiffened Cold-Formed Steel Plates, Canadian Journal of Civil Engineering, Vol. 6, pp. 381-389.

Roy, G., Mohamedien, M. A., and Polyzois, D. (1994), Residual Stresses due to Cold Forming, Proceedings of the Annual Conference for the Canadian Society of Civil Engineering, CSCE, Winnipeg, Manitoba, Canada.

Schlack, A. L. (1968), Experimental Critical Loads for Perforated Square Plates, Experimental Mechanics, Feb., pp. 69-74.

Schuster, R. M. (1992), Testing of Perforated C-Stud Sections in Bending, Report for the Canadian Sheet Steel Building Institute, University of Waterloo, Waterloo, Ontario, Canada.

Shan, M. Y., Batson, K. D., LaBoube, R. A., and Yu, W. W. (1994), Local Buckling Flexural Strength of Webs with Openings, Engineering Structures, Vol. 16, No. 5, pp. 317-323.

Sivakumaran, K. S. and Abdel-Rahman, N. (1996), Computer Models for Analysis of Cold-Formed Steel Members, Third Asian-Pacific Conference on Computational Mechanics, APCOM, Seoul, Korea.

Sivakumaran, K. S. and Abdel-Rahman, N. (1995), Implementation of an Advanced Shell Finite Element, Proceedings of the 15th Canadian Congress of Applied Mechanics, CANCAM, Vol. I, Victoria, British Columbia, Canada.

Sivakumaran, K. S. and Zielonka, K. M. (1989), Web Crippling Strength of Thin-Walled Steel Members with Web Opening, Thin-Walled Structures, Vol. 8, pp. 295-319.

Sivakumaran, K. S. (1987a), Load Capacity of Uniformly Compressed Cold-Formed Steel Section with Punched Web, Canadian Journal of Civil Engineering, Vol. 14, pp. 550-558.

Sivakumaran, K. S. (1987b), Analysis for Local Buckling Capacity of Cold-Formed Steel Sections with Web Opening, Computers and Structures, Vol. 26, No. 1/2, pp. 275-282.

Stowell, E. Z., Heimerl, G. J., Libove, C., and Lundquist, E. E. (1951), Buckling Stresses for Flat Plates and Sections, Journal of the Structural Division, ASCE Proceedings, Vol. 77, pp. 545-578.

Von Karman, T., Sechler, E. E., and Donnell, L. H. (1932), The Strength of Thin Plates in Compression, Transactions, ASME, Vol. 54, APM 54-5.

Way, S. (1938), Uniformly Loaded, Clamped, Rectangular Plates with Large Deformation, Proceedings of the 5th. International Congress of Applied Mechanics, Cambridge, Massachusetts, U.S.A.

Weller, E. J. and Haavisto, M. (1984), Nontraditional Machining Processes, Society of Manufacturing Engineers, Dearborn, Michigan, U.S.A.

Weng, C. C. and Pekoz, T. (1990), Residual Stresses in Cold-Formed Steel Members, Journal of Structural Engineering, ASCE, Vol. 116, No. 6, pp. 1611-1625.

Winter, G. (1970), Commentary on the 1968 Edition of the Specification for the Design of Cold-Formed Steel Structural Members, American Iron and Steel Institute, U.S.A.

Winter, G. (1947), Strength of Thin Steel Compression Flanges, Transactions, ASCE, Vol. 112, Paper No. 2305, pp. 527-554.

XFEAP (1990), Extended Version of the Finite Element Analysis Program (FEAP), Division of Structural Engineering and Construction, Asian Institute of Technology, Bangkok, Thailand.

Yamaki, N. (1959), Post-buckling Behaviour of Rectangular Plates with Small Initial Curvature Loaded in Edge Compression, Journal of Applied Mechanics, pp. 407-414.

Yu, W. W. (1991), Cold-Formed Steel Design, John Wiely & Sons Inc., New York.

Yu, W. W. and Davis, C. S. (1973), Cold-Formed Steel Members with Perforated Elements, Journal of the Structural Division, ASCE, Vol. 99, No. ST10, pp. 2061-2077.

Zienkiewicz, O. C., and Taylor, R. L. (1991), The Finite Element Method, Vol. 1 and Vol. 2, Fourth Edition, McGraw-Hill Company, London.

Zienkiewicz, O. C., Taylor, R. L., and Too, J. M. (1971), Reduced Integration Techniques in General Analysis of Plates and Shells, International Journal for Numerical Methods in Engineering, Vol. 3, pp. 275-290.

APPENDIX A

INTERPOLATION FUNCTIONS FOR THE 9-NODE SHELL ELEMENT

The general form of the mid-surface interpolation functions for the 9-node shell finite element, at a node (k), can be written as follows:

$$N^k = [\xi\xi^k(1+\xi\xi^k)/2 + (1-\xi^2)(1-(\xi^k)^2)]\,[\eta\eta^k(1+\eta\eta^k)/2 + (1-\eta^2)(1-(\eta^k)^2)] \quad (A.1)$$

Based on Equation A.1, the nodal interpolation functions in the natural coordinate system can be listed as follows:

Nodal point	ξ value	η value	Interpolation function (N)
1	+1	+1	$\frac{1}{4}\xi\eta(1+\xi)(1+\eta)$
2	-1	+1	$-\frac{1}{4}\xi\eta(1-\xi)(1+\eta)$
3	-1	-1	$\frac{1}{4}\xi\eta(1-\xi)(1-\eta)$
4	+1	-1	$-\frac{1}{4}\xi\eta(1+\xi)(1-\eta)$
5	0	+1	$\frac{1}{2}\eta(1-\xi^2)(1+\eta)$
6	-1	0	$-\frac{1}{2}\xi(1-\xi)(1-\eta^2)$
7	0	-1	$-\frac{1}{2}\eta(1-\xi^2)(1-\eta)$
8	+1	0	$\frac{1}{2}\xi(1+\xi)(1-\eta^2)$
9	0	0	$(1-\xi^2)(1-\eta^2)$

APPENDIX B

TRANSFORMATION MATRICES BETWEEN DIFFERENT COORDINATE SYSTEMS

The Transformation between Local and Global Coordinate Systems

The transformation between the local Cartesian coordinate system (x′, y′, z′) and the global Cartesian coordinate system (x, y, z) can be established through the matrix of direction cosines [θ] between the local and global axes at a particular point in the element. The matrix [θ] is defined as:

$$[\theta] = \begin{bmatrix} l_1 & m_1 & n_1 \\ l_2 & m_2 & n_2 \\ l_3 & m_3 & n_3 \end{bmatrix} \qquad \text{(B.1)}$$

where (l_1) through (n_3) are the direction cosines of the (x′, y′, z′) coordinate axes measured in the (x, y, z) coordinate directions. If the strain vector (∈) is defined as:

$$\epsilon^T = [\, \epsilon_{xx}\ \epsilon_{yy}\ \epsilon_{zz}\ \epsilon_{xy}\ \epsilon_{yz}\ \epsilon_{xz}\,]^T \qquad \text{(B.2)}$$

then (∈) can be transformed from the global to the local coordinate systems as follows:

$$\epsilon' = \theta\, \epsilon\, \theta^T = T\, \epsilon \tag{B.3}$$

where the transformation matrix [T] can be evaluated as:

$$[T] = \begin{bmatrix} l_1^2 & m_1^2 & n_1^2 & 2l_1m_1 & 2m_1n_1 & 2n_1l_1 \\ l_2^2 & m_2^2 & n_2^2 & 2l_2m_2 & 2m_2n_2 & 2n_2l_2 \\ l_3^2 & m_3^2 & n_3^2 & 2l_3m_3 & 2m_3n_3 & 2n_3l_3 \\ l_1l_2 & m_1m_2 & n_1n_2 & l_1m_2+l_2m_1 & m_1n_2+m_2n_1 & n_1l_2+n_2l_1 \\ l_2l_3 & m_2m_3 & n_2n_3 & l_2m_3+l_2m_3 & m_2n_3+m_3n_2 & n_2l_3+n_3l_2 \\ l_3l_1 & m_3m_1 & n_3n_1 & l_3m_1+l_1m_3 & m_3n_1+m_1n_3 & n_3l_1+n_1l_3 \end{bmatrix} \tag{B.4}$$

However, if the strain vector (ϵ) is defined using the engineering strains, i.e.:

$$\epsilon^T = [\, \epsilon_{xx}\, \epsilon_{yy}\, \epsilon_{zz}\, \gamma_{xy}\, \gamma_{yz}\, \gamma_{xz}\,]^T \tag{B.5}$$

then the transformation matrix [T] in Equation B.3 should be replaced by the matrix [T′], where:

$$\text{If } [T] = \begin{bmatrix} [T_{11}] & [T_{12}] \\ [T_{21}] & [T_{22}] \end{bmatrix}, \quad \text{then } [T'] = \begin{bmatrix} [T_{11}] & [\tfrac{1}{2}T_{12}] \\ [2T_{21}] & [T_{22}] \end{bmatrix} \tag{B.6}$$

The transformation matrices for the inverse transformation of Equation B.3, from the local to the global coordinate system, can be easily established by knowing the following facts:

$$[T]^{-1} = [T']^{T},$$

$$[T']^{-1} = [T]^{T} \tag{B.7}$$

where $[T]^{-1}$ and $[T']^{-1}$ are the inverse matrices of the transformation matrices [T] and [T′], respectively.

The transformation of the strain-displacement matrix [B] between the local and the global Cartesian coordinate systems follows identically the same rules as the transformation of the strain vector (ϵ). However, as the matrix [B] is usually defined with respect to the engineering strains, the transformation matrix [T′] and its inverse matrix $[T']^{-1}$ are usually used to obtain the required transformations.

The Transformation between natural and Global Coordinate Systems

The transformation of the strains from the global Cartesian coordinate system (x, y, z) to the natural coordinate system (ξ,η,ζ) can be established through the following tensorial relationship:

$$\epsilon^{\xi}_{kl} = \frac{\partial x_i}{\partial \xi_k} \frac{\partial x_j}{\partial \xi_l} \epsilon_{ij} \tag{B.8}$$

where (ϵ_{ij}) and (ϵ^{ξ}_{kl}) are the strain tensors in the global Cartesian and natural coordinate systems, respectively. The derivative operator ($\partial x_i / \partial \xi_k$) represents the Jacobian matrix, which relates the derivatives in the natural coordinate system to the

derivatives in the global Cartesian coordinate system. Therefore, the Jacobian matrix [J] is defined as:

$$[J] = \begin{bmatrix} \frac{\partial x}{\partial \xi} & \frac{\partial y}{\partial \xi} & \frac{\partial z}{\partial \xi} \\ \frac{\partial x}{\partial \eta} & \frac{\partial y}{\partial \eta} & \frac{\partial z}{\partial \eta} \\ \frac{\partial x}{\partial \zeta} & \frac{\partial y}{\partial \zeta} & \frac{\partial z}{\partial \zeta} \end{bmatrix} \tag{B.9}$$

Using the expression of the Jacobian matrix [J], the tensorial relationship in Equation B.8 can be written in a matrix form as follows:

$$\epsilon^{\xi} = TJ \ \epsilon \tag{B.10}$$

where the transformation matrix [TJ] can be evaluated as:

$$[TJ] = \begin{bmatrix} J_{11}^2 & J_{12}^2 & J_{13}^2 & 2J_{11}J_{12} & 2J_{12}J_{13} & 2J_{13}J_{11} \\ J_{21}^2 & J_{22}^2 & J_{23}^2 & 2J_{21}J_{22} & 2J_{22}J_{23} & 2J_{23}J_{21} \\ J_{31}^2 & J_{32}^2 & J_{33}^2 & 2J_{31}J_{32} & 2J_{32}J_{33} & 2J_{33}J_{31} \\ J_{11}J_{21} & J_{12}J_{22} & J_{13}J_{23} & J_{11}J_{22}+J_{21}J_{12} & J_{12}J_{23}+J_{22}J_{13} & J_{13}J_{21}+J_{23}J_{11} \\ J_{21}J_{31} & J_{22}J_{32} & J_{23}J_{33} & J_{21}J_{32}+J_{31}J_{22} & J_{22}J_{33}+J_{32}J_{23} & J_{23}J_{31}+J_{33}J_{21} \\ J_{31}J_{11} & J_{32}J_{12} & J_{33}J_{13} & J_{31}J_{12}+J_{32}J_{11} & J_{32}J_{13}+J_{33}J_{12} & J_{33}J_{11}+J_{13}J_{31} \end{bmatrix} \tag{B.11}$$

If the engineering strains are defined, as in Equation B.5, the transformation matrix [TJ] in Equation B.10 should be replaced by the matrix [TJ'], where:

$$\text{If } [TJ] = \begin{bmatrix} [TJ_{11}] & [TJ_{12}] \\ [TJ_{21}] & [TJ_{22}] \end{bmatrix}, \quad \text{then } [TJ'] = \begin{bmatrix} [TJ_{11}] & [\tfrac{1}{2}TJ_{12}] \\ [2TJ_{21}] & [TJ_{22}] \end{bmatrix} \qquad \text{(B.12)}$$

The inverse transformation in Equation B.8 should be established through the inverse derivative operator ($\partial \xi_i / \partial x_k$), which represents the inverse Jacobian matrix $[J]^{-1}$. An inverse transformation matrix $[TJ]^{-1}$ can be constructed by replacing the terms of the matrix [TJ], in Equation B.11, by the corresponding terms of the inverse Jacobian matrix $[J]^{-1}$. Also, an inverse transformation matrix $[TJ']^{-1}$ for the transformation of the engineering strains can be constructed from the matrix $[TJ]^{-1}$ using similar relationship to that in Equation B.12.

The transformation of the strain-displacement matrix [B] between the natural and the global Cartesian coordinate systems follows identically the same rules of the transformation of the strain vector (ϵ). However, as the matrix [B] is usually defined with respect to the engineering strains, the transformation matrix [TJ'] and its inverse matrix $[TJ']^{-1}$ are usually used to obtain the required transformations.

APPENDIX C

UNIFIED CONSTRAINT ALGORITHM

The equilibrium equations of a discrete non-linear finite element system are generally expressed as a system of (n) simultaneous nonlinear equations in terms of (n+1) unknowns, [i.e., (n) components of the displacement vector (u) and a loading intensity (λ)]. The general equilibrium equation is:

$$K\,u - \lambda\,F = 0 \qquad \text{(C.1)}$$

where (K u) is the internal force vector which is a non-linear function of (u), and (F) is a constant reference load vector. In the unified constraint algorithm, Equation C.1 is solved for (n+1) unknowns by introducing an additional constraint equation in the form of:

$$\sum_{k=1}^{n} \beta_k \left(u_k^m - u_k^{m-1} \right)^2 + \beta_{n+1}\,\alpha^2 \left(\lambda^m - \lambda^{m-1} \right)^2 = c^2 \qquad \text{(C.2)}$$

where (β_k's) (k = 1, 2, ..., n+1) are the algorithm control parameters, the quantities with superscript (m) correspond to the converged solution at the current (m) solution step, (α) is a load coefficient used to normalize the dimension of load to that of displacement, and (c) is the prescribed increment value between the (m) and the (m-1)

solution steps. The control parameters (β_k's) lead to the required control technique as follows:

1) $\beta_k = 0$ (k = 1 to n) and $\beta_{n+1} = 1$ ➞ leads to a load control algorithm.

2) $\beta_k = 1$ and $\beta_i = 0$ ($i \neq k$) ➞ leads to a displacement control algorithm.

3) All β_k's $\neq 0$ ➞ leads to an arc-length control algorithm.

According to the Newton-Raphson iteration technique, the linearization of Equations C.1 and C.2 with respect to the displacement vector (u) and the intensity (λ) about the previous solution ($u^{i,m}$, $\lambda^{i,m}$) leads to the linearized equilibrium and constraint equation as follows:

$$\begin{bmatrix} K(u^{i,m}) & F \\ 2\beta_1(u_1^{i,m} - u_1^{*,m-1}) \;..\; 2\beta_n(u_n^{i,m} - u_n^{*,m-1}) & 2\beta_{n+1}\,\alpha^2(\lambda^{i,m} - \lambda^{*,m-1}) \end{bmatrix} \begin{bmatrix} \Delta u^{i,m} \\ \Delta\lambda^{i,m} \end{bmatrix} = \begin{bmatrix} R(u^{i,m}) \\ r^{i,m} \end{bmatrix} \tag{C.3}$$

where $[K(u^{i,m})]$ is the tangent stiffness about the known displacement vector ($u^{i,m}$), and the unbalanced force vector is $R(u^{i,m}) = [K]\,(u^{i,m}) - \lambda^{i,m}\,(F)$. The residual of the constraint equation is:

$$r^{i,m} = c^2 - \sum_{k=1}^{n} \beta_k\,(u_k^{i,m} - u_k^{*,m-1})^2 - \beta_{n+1}\,\alpha^2\,(\lambda^{i,m} - \lambda^{*,m-1})^2 \tag{C.4}$$

Note that the superscript (m) refers to the current solution step, and the superscript (i) refers to the previous iteration just completed. The superscript (∞) replaces (i) to refer to a converged solution of the step. Equation C.3 is solved for ($\Delta u^{i,m}$, $\Delta \lambda^{i,m}$) in order to update the solution, i.e.:

$$\begin{aligned} u^{i+1,m} &= u^{i,m} + \Delta u^{i,m} \\ \lambda^{i+1,m} &= \lambda^{i,m} + \Delta \lambda^{i,m} \end{aligned} \qquad \text{(C.5)}$$

APPENDIX D

PROPERTIES OF THE EXPERIMENTAL SPECIMENS OF DIFFERENT STUDIES

For all the cold-formed steel channel section specimens of the experimental studies presented below, the dimensions shown are the dimensions of the flat portions of the section, excluding the rounded corners. The flange and the lip plates of all the specimens are fully effective, unless otherwise indicated.

The Properties of the Experimental Specimens for the Comparison in Section 5.5.3 (Square or Circular Perforation)

Table D.1 Properties of current experimental specimens, (Chapter 4)

Spec. No.	Dimensions (mm)				Perf. (a) (mm)	F_y (MPa)	Ratios	
	Web (w)	Fl. (w_f)	Lip (w_l)	Thick. (t)			w/t	a/w
A-D	191.7	30.3	7.4	1.88	0.0	385	102.0	0.0
A-C,S	191.7	30.3	7.4	1.88	63.5	385	102.0	0.33
B-D	93.9	34.0	9.4	1.27	0.0	319	73.9	0.0
B-C,S	93.9	34.0	9.4	1.27	38.1	319	73.9	0.41

Table D.2 Properties of experimental specimens, Ortiz-Colberg (1981)

Spec. No.	Dimensions (mm)				Perf. (a) (mm)	F_y (MPa)	Ratios	
	Web (w)	Fl. (w_f)	Lip (w_l)	Thick. (t)			w/t	a/w
I-1,2	81.4	33.7	8.4	1.27	0.0	339	64.1	0.0
I-3,9	81.4	33.7	8.4	1.27	12.7	339	64.1	0.16
I-4	81.4	33.7	8.4	1.27	19.1	339	64.1	0.23
I-5,10	81.4	33.7	8.4	1.27	26.4	339	64.1	0.32
I-6	81.4	33.7	8.4	1.27	31.8	339	64.1	0.39
I-7,11	81.4	33.7	8.4	1.27	38.1	339	64.1	0.47
I-8	81.4	33.7	8.4	1.27	44.5	339	64.1	0.55

Table D.3 Properties of experimental specimens, Banwait (1987) (Series I)

Spec. No.	Dimensions (mm)				Perf. (a) (mm)	F_y (MPa)	Ratios	
	Web (w)	Fl. (w_f)	Lip (w_l)	Thick. (t)			w/t	a/w
I-D	82.5	31.7	7.9	1.6	0.0	341	51.5	0.0
I-A-2	82.5	31.7	7.9	1.6	16.5	341	51.5	0.2
I-B-2	82.5	31.7	7.9	1.6	16.5	341	51.5	0.2
I-A-4	82.5	31.7	7.9	1.6	33.0	341	51.5	0.4
I-B-4	82.5	31.7	7.9	1.6	33.0	341	51.5	0.4
I-A-6	82.5	31.7	7.9	1.6	49.5	341	51.5	0.6
I-B-6	82.5	31.7	7.9	1.6	49.5	341	51.5	0.6

Table D.4 Properties of experimental specimens, Banwait (1987) (Series II)

Spec. No.	Dimensions (mm)				Perf. (a) (mm)	F_y (MPa)	Ratios	
	Web (w)	Fl. (w_f)	Lip (w_l)	Thick. (t)			w/t	a/w
II-D	144.7	33.6	8.8	1.29	0.0	263	112.4	0.0
II-A-2	144.7	33.6	8.8	1.29	29.0	263	112.4	0.2
II-B-2	144.7	33.6	8.8	1.29	29.0	263	112.4	0.2
II-A-4	144.7	33.6	8.8	1.29	58.0	263	112.4	0.4
II-B-4	144.7	33.6	8.8	1.29	58.0	263	112.4	0.4
II-A-6	144.7	33.6	8.8	1.29	87.0	263	112.4	0.6
II-B-6	144.7	33.6	8.8	1.29	87.0	263	112.4	0.6

Table D.5 Properties of experimental specimens, Rhodes and Schneider (1994)

Spec. No.	Dimensions (mm)			Perf. (a) (mm)	F_y (MPa)	Ratios	
	Web (w)	Fl.[a] (w_f)	Thick. (t)			w/t	a/w
I-up	61.2	30.8	0.75	0.0	184	81.6	0.0
I-wcl	61.2	30.8	0.75	2x8.0	184	81.6	0.26
I-wf	61.2	30.8	0.75	2x8.0	184	81.6	0.26
II-up	62.0	30.7	1.19	0.0	190	52.1	0.0
II-wcl	62.0	30.7	1.19	2x8.0	190	52.1	0.26
II-wf	62.0	30.7	1.19	2x8.0	190	52.1	0.26
III-up	61.5	30.9	1.60	0.0	289	38.4	0.0
III-wcl	61.5	30.9	1.60	2x8.0	289	38.4	0.26
III-wf	61.5	30.9	1.60	2x8.0	289	38.4	0.26

[a] Flanges of all specimens are not fully effective - sections with no lips.

The Properties of the Experimental Specimens for the Comparison in Section 5.6 (Elongated Perforation)

Table D.6 Properties of current experimental specimens, (Chapter 4)

Spec. No.	Dimensions (mm)				Perforation		F_y (MPa)	Ratios		
	Web (w)	Fl. (w_f)	Lip (w_l)	Thick. (t)	a (mm)	h (mm)		w/t	a/w	h/a
A-D	191.7	30.3	7.4	1.88	0.0	0.0	385	102.0	0.0	0.0
A-O,R	191.7	30.3	7.4	1.88	63.5	114.3	385	102.0	0.33	1.8
B-D	93.9	34.0	9.4	1.27	0.0	0.0	319	73.9	0.0	0.0
B-O,R	93.9	34.0	9.4	1.27	38.1	101.6	319	73.9	0.41	2.7

Table D.7 Properties of experimental specimens, Loov (1984)[a]

Spec. No.	Dimensions (mm)				Perforation		F_y (MPa)	Ratios		
	Web (w)	Fl. (w_f)	Lip (w_l)	Thick. (t)	a (mm)	h (mm)		w/t	a/w	h/a
1,2,3	53.4	34.2	8.3	2.01	38.1	44.5	384	26.6	0.71	1.17
4,6	54.5	34.4	9.1	1.42	38.1	44.5	383	38.4	0.70	1.17
7,8,9	54.7	34.8	8.3	1.21	38.1	44.5	268	45.2	0.70	1.17
10,11,12	83.5	34.6	8.7	1.21	38.1	44.5	268	69.0	0.46	1.17
13,14,15	82.9	34.4	9.1	1.42	38.1	44.5	383	58.4	0.46	1.17
16,17,18	82.0	34.0	8.6	2.01	38.1	44.5	384	40.8	0.46	1.17
19,20,21	144.0	34.5	8.9	1.21	38.1	44.5	268	119.0	0.26	1.17
22,23,24	143.3	34.1	8.9	1.42	38.1	44.5	383	100.9	0.26	1.17
25,26,27	142.2	33.8	8.7	2.01	38.1	44.5	384	70.7	0.27	1.17
28,29,30	194.9	34.5	8.7	1.21	38.1	44.5	268	161.1	0.20	1.17
31,32,33	193.8	34.1	9.0	1.42	38.1	44.5	383	136.5	0.20	1.17
34,35,36	193.6	34.3	8.7	2.01	38.1	44.5	384	96.3	0.20	1.17

[a] No reference non-perforated specimens for all tests.

Table D.8 Properties of experimental specimens, Miller and Pekoz (1994)

Spec. No.	Dimensions (mm)				Perforation		F_y (MPa)	Ratios		
	Web (w)	Fl.[a] (w_f)	Lip (w_l)	Thick. (t)	a (mm)	h (mm)		w/t	a/w	h/a
1:1	83.4	28.4	7.7	1.91	0.0	0.0	358	43.7	0.0	0.0
1:12,13	83.4	28.4	7.7	1.91	41.0	70.0	358	43.7	0.49	1.7
2:1-5	83.4	28.4	7.7	1.91	0.0	0.0	366	43.7	0.0	0.0
2:11-13	83.4	28.4	7.7	1.91	38.0	65.0	366	43.7	0.46	1.7
1:14-16	145.4	28.4	4.7	0.89	0.0	0.0	309	163.4	0.0	0.0
1:17,19	145.4	28.4	4.7	0.89	40.0	57.0	309	163.4	0.28	1.43
2:6-10	145.4	28.4	4.7	0.89	0.0	0.0	302	163.4	0.0	0.0
2:14-16	145.4	28.4	4.7	0.89	40.0	57.0	302	163.4	0.28	1.43

[a] Flanges of specimens with t=0.89 mm are not fully effective.

IMAGE EVALUATION TEST TARGET (QA-3)

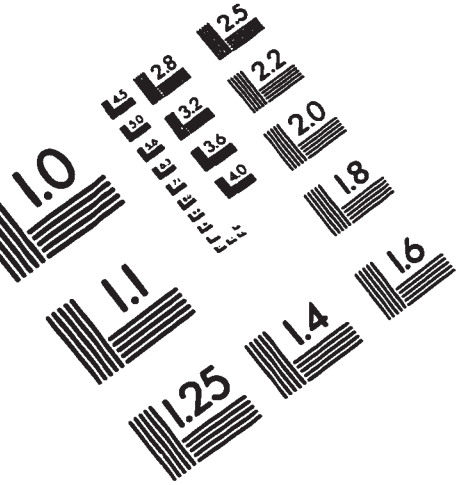

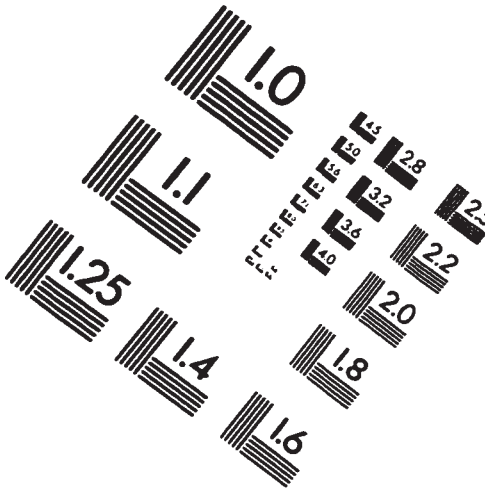

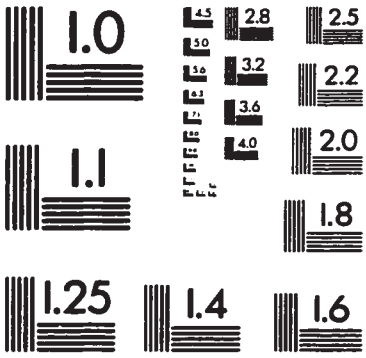

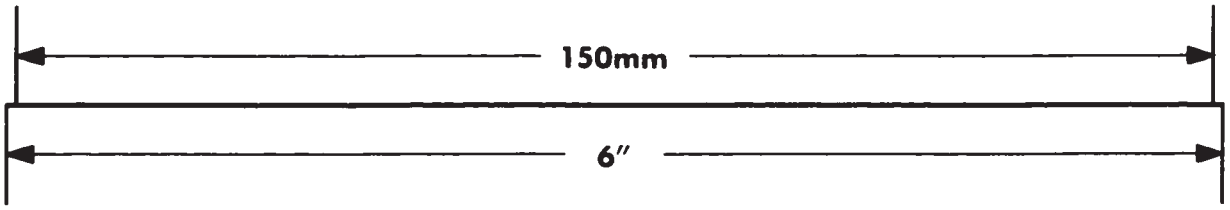

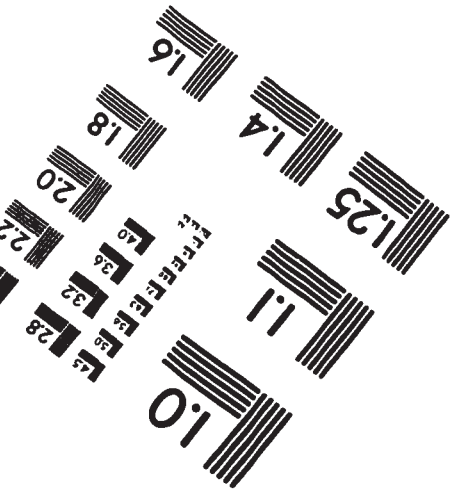

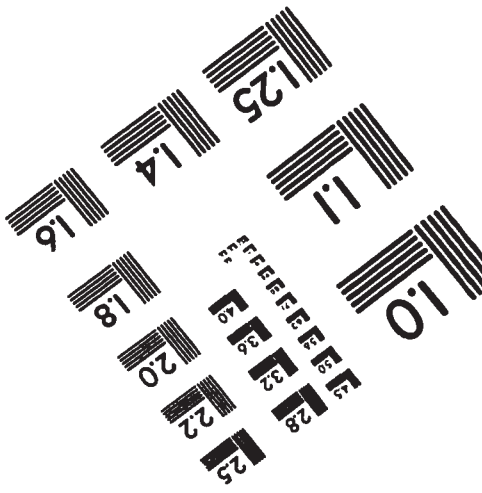

APPLIED IMAGE, Inc
1653 East Main Street
Rochester, NY 14609 USA
Phone: 716/482-0300
Fax: 716/288-5989